ORIGINAL RESEARCH

Protein nanocoatings on synthetic polymeric nanofibrous membranes designed as carriers for skin cells

Marketa Bacakova[1,2]
Julia Pajorova[1,2]
Denisa Stranska[3]
Daniel Hadraba[1,4]
Frantisek Lopot[4]
Tomas Riedel[5]
Eduard Brynda[5]
Margit Zaloudkova[6]
Lucie Bacakova[1]

[1]Department of Biomaterials and Tissue Engineering, Institute of Physiology, Czech Academy of Sciences, [2]Second Faculty of Medicine, Charles University, Prague, [3]InStar Technologies, Liberec, [4]Department of Anatomy and Biomechanics, Faculty of Physical Education and Sport, Charles University, [5]Department of Chemistry and Physics of Surfaces and Biointerfaces, Institute of Macromolecular Chemistry, [6]Department of Composites and Carbon Materials, Institute of Rock Structure and Mechanics, Czech Academy of Sciences, Prague, Czech Republic

Correspondence: Marketa Bacakova
Department of Biomaterials and Tissue Engineering, Institute of Physiology, Czech Academy of Sciences, 1083 Vídeňská, Prague 4 14220, Czech Republic
Tel +420 296 443 765
Email marketa.bacakova@fgu.cas.cz

Abstract: Protein-coated resorbable synthetic polymeric nanofibrous membranes are promising for the fabrication of advanced skin substitutes. We fabricated electrospun polylactic acid and poly(lactide-*co*-glycolic acid) nanofibrous membranes and coated them with fibrin or collagen I. Fibronectin was attached to a fibrin or collagen nanocoating, in order further to enhance the cell adhesion and spreading. Fibrin regularly formed a coating around individual nanofibers in the membranes, and also formed a thin noncontinuous nanofibrous mesh on top of the membranes. Collagen also coated most of the fibers of the membrane and randomly created a soft gel on the membrane surface. Fibronectin predominantly adsorbed onto a thin fibrin mesh or a collagen gel, and formed a thin nanofibrous structure. Fibrin nanocoating greatly improved the attachment, spreading, and proliferation of human dermal fibroblasts, whereas collagen nanocoating had a positive influence on the behavior of human HaCaT keratinocytes. In addition, fibrin stimulated the fibroblasts to synthesize fibronectin and to deposit it as an extracellular matrix. Fibrin coating also showed a tendency to improve the ultimate tensile strength of the nanofibrous membranes. Fibronectin attached to fibrin or to a collagen coating further enhanced the adhesion, spreading, and proliferation of both cell types.

Keywords: skin-tissue engineering, nanocoating, nanofibers, skin cells, fibrin, collagen

Introduction

Advanced skin substitutes should mimic the morphology, composition, and functions of the original tissue. They have to accelerate tissue regeneration, ie, they have to support the formation of dermis and epidermis layers with a well-developed extracellular matrix (ECM). Moreover, they should enable nutrition supply and not cause unwanted immune reactions. However, clinically used skin substitutes have not yet met all these requirements, and they have several limiting factors. These substitutes mostly serve as temporary wound coverage or as carriers for skin cells, and ultimately they are rejected by the organism.[1] This transplant rejection is caused mainly by the use of nonresorbable materials or allogenic cells that are subject to inflammatory reactions.

Advanced tissue engineering lays emphasis on the formation of two of the most important layers of natural skin: the dermis and the epidermis. Fibrous or porous membranes or films of nanoscale thickness can be advantageously used for developing a bilayer of fibroblasts and keratinocytes. The pores in the carriers can enable physical and biochemical communication between fibroblasts and keratinocytes. Moreover, the pores can ensure the supply of cells with active biological molecules, mainly with nutrients and growth factors from the cell culture medium or from the

surrounding tissue.[2] Nanostructured materials also mimic the nanofibrous component of the ECM in natural tissues better than conventional flat materials.[3] They enable the adsorption of cell adhesion-mediating ECM molecules from body fluid or from cell culture media in an appropriate spatial orientation. This conformation of ECM molecules is important for binding their specific bioactive amino acid sequences by cell adhesion receptors, eg, integrins.[4]

Synthetic polymers or natural polymers have been used for constructing carriers for skin cells.[5] However, these two types of materials are rarely applied in combination. Degradable synthetic polymers, mainly polyesters (polylactide, polylactide-*co*-glycolide, polycaprolactone), are relatively easily spinnable, eg, nanofibers can be formed by a process referred to as electrospinning.[6] Moreover, nanofibrous membranes made of these synthetic polymers can provide stable mechanical support for cells. However, synthetic polymers in their pristine state are unable to provide sufficient support for cellular adhesion, proliferation, and deposition of an ECM.[7,8] In these cases, synthetic polymers could be combined with molecules physiologically present in the skin, such as collagen, fibronectin, and hyaluronan, or with molecules occurring during wound healing, particularly fibrin. These molecules improve the colonization of matrices by cells.[9] In addition, natural molecules, eg, fibrinogen as the precursor of fibrin, can be isolated in an autologous form from the patient's body fluids or tissues to prevent immune rejection of the implant.[10]

Collagen is an important component of the ECM in the skin dermis. It is mainly produced by fibroblasts and is organized into fibers running throughout the dermis.[11] In skin substitutes, collagen is often applied in the form of a gel,[12,13] or it is used in composites with other natural or synthetic materials.[14,15] Previous studies have revealed that collagen supports wound healing. Niiyama and Kuroyanagi combined collagen with hyaluronic acid and functionalized this composite with EGF.[16] Butler and Orgill observed improved growth of epidermal keratinocytes on a collagen–glycosaminoglycan matrix.[17] Wang et al prepared collagen/chitosan-based scaffolds with VEGF and gentamicin encapsulated into poly(lactide-*co*-glycolic acid) (PLGA) microspheres and observed positive effects of these scaffolds on the adhesion and growth of mouse fibroblasts.[18] Collagen has also been widely applied in clinically used skin substitutes. For example, Integra (Integra LifeSciences, Plainsboro, NJ, USA), which is used for treating severe full-thickness burns, consists of a silicone layer on top of a porous matrix comprising a chemically cross-linked coprecipitate of bovine collagen and shark-derived chondroitin-6-sulfate. The pore size of 20–125 µm allows ingrowth of fibroblasts and revascularization. After that, keratinocytes can be applied on the material surface. Apligraf (Organogenesis Inc, Canton, MA,USA) is a bilayered skin substitute used for treating venous ulcers, diabetic ulcers, donor-site wounds, epidermolysis bullosa, and cutis aplasia. Apligraf consists of allogeneic neonatal fibroblasts cultivated on a bovine type I collagen matrix. Keratinocytes are cultured on the top of this dermal layer.[19,20]

Fibrin is a provisional matrix molecule that plays an important role during wound healing. Fibrin fibers are formed from fibrinogen, a soluble precursor, in the last step of the coagulation cascade.[21] Cells can bind directly to fibrin(ogen) via integrin cell adhesion receptors or via non-integrin receptors (eg, VE-cadherin, ICAM1, or P-selectin). Fibrin is also able to bind cell adhesion-mediating proteins (eg, fibronectin and vitronectin) or growth factors.[22] Fibrin has often been applied in the form of a glue, gel, or microbeads.[23–25] For better regenerative potential and mechanical stability, fibrin matrices have been combined with other biological or synthetic molecules, eg, collagen,[26,27] hyaluronic acid with a cell adhesion-promoting peptide,[28] basic FGF,[29] or EGF.[30] Fibrin has relatively rarely been deposited on supporting substrates, although fibrin self-supporting matrices are usually fragile. In our previous study, we deposited a fibrin nanocoating on polylactide nanofibrous membranes and observed its positive influence on the behavior of dermal fibroblasts.[9] Fibrin has also been used in commercially available skin substitutes. For example, ICX-SKN (Intercytex, Manchester, UK), a fibrin matrix seeded with neonatal human fibroblasts, is promising for ulcer treatment.[20]

In our study, we prepared electrospun polylactic acid (PLA) and PLGA nanofibrous membranes, coated them with fibrin or collagen I, and then with fibronectin attached to the surface of these proteins. Firstly, we compared the behavior of human dermal fibroblasts and human HaCaT keratinocytes on these two protein-modified biodegradable polymer matrices. Although the physical and chemical properties and the biocompatibility of PLA and PLGA are generally considered very close, some differences have been reported between these polymers as regards their degradability, mechanical integrity,[31] porosity, wettability, protein adsorption,[32] and cell behavior on their surfaces;[33,34] therefore, differences in cell adhesion and growth for these polymers were also expected in this study. Secondly, we evaluated the influence of newly developed protein nanocoatings,

ie, fibrin, collagen, and fibronectin, on the adhesion and growth of dermal fibroblasts and HaCaT keratinocytes on the nanofibrous PLA and PLGA scaffolds.

Materials and methods
Preparation of nanofibrous membranes

Experiments were carried out on nanofibrous membranes made of a PLGA copolymer (ratio 85:15, Purasorb® PLG 8531; Corbion, Amsterdam, the Netherlands) or made of PLA (Ingeo™ Biopolymer 4032D; NatureWorks, Minnetonka, MN, USA). The solution for the polymers was prepared and the electrospinning process carried out as presented in our previous work.[9] Both polymers were dissolved in chloroform. Solvents – dichloroethane and ethyl acetate – were added into a PLA solution to a final concentration of 7 wt% of PLA. The volume ratio of the chloroform, dichloroethane, and ethyl acetate solvents was 61:29:10. The solution of the two polymers was made electrically conductive with the use of tetraethylammonium bromide. This chemical was first dissolved in dimethylformamide to a concentration of 3 wt%. Then, 3 g of this solution was added to 100 g of the PLGA or PLA solution.

Nanospider needle-free electrospinning technology (Elmarco, Liberec, Czech Republic) was used for preparing the nanofibrous membranes. The process conditions were electrode distance 145–180 mm, voltage 50–60 kV, relative humidity 20%–30%, and room temperature. Fiber density, ie, the area weight of the prepared nanofibers, was 10.5–19.6 g/m^2 for PLGA and 13–15 g/m^2 for PLA. The thickness of the membranes was in the range of 47–97 µm for PLGA and 125–190 µm for PLA.[9]

Preparation of fibrin and collagen nanocoating with attached fibronectin

The fibrin nanocoating on the polymeric nanofibrous membranes was formed by activating human fibrinogen (341576; EMD Millipore, Billerica, MA, USA) with human thrombin (T6884; Sigma-Aldrich Co, St Louis, MO, USA), as described in detail in our previous papers.[9,35] Fibrinogen at a concentration of 10 µg/mL in Tris buffer (consisting of 50 mM Tris-HCl, 100 nM NaCl, and 2.5 mM CaCl$_2$) was adsorbed on the membrane surface for 1 hour. After being rinsed with Tris buffer, the adsorbed fibrinogen was activated with thrombin (2.5 U/mL in Tris buffer) for 15 minutes. The samples were rinsed with Tris buffer, and a solution of 200 µg/mL of fibrinogen in Tris buffer and 0.5 U/mL of antithrombin III in deionized water was added to the membranes for 1 hour. A fibrin network was formed by a catalytic reaction of the surface-attached thrombin with the ambient fibrinogen solution. The antithrombin III blocked the unreacted thrombin, in order to form a 2-D fibrin layer (Figure 1).

The collagen nanocoating was formed from a collagen solution by changing the pH. The collagen solution (rat tail, 3.37 mg/mL; Corning Incorporated, Corning, NY, USA) was diluted in 0.02 M acetic acid to a final concentration of 200 µg/mL, and was applied to the samples. The samples were immersed in ammonia vapor for 10 minutes to change the acid pH to basic pH. After collagen precipitation, the solution was sucked out and the samples rinsed with deionized water (Figure 1).

Fibronectin was attached to the surface of the fibrin and collagen nanocoating. Fibronectin powder (human, 11051407001; Hoffman-La Roche Ltd, Basel, Switzerland) was dissolved in deionized water at a concentration of 1 mg/mL. The fibronectin solution was subsequently diluted in phosphate-buffered saline (PBS; Sigma-Aldrich) to a final concentration of 50 µg/mL and incubated with the samples overnight at 4°C. The samples were then rinsed twice with PBS.

Morphology of nanofibrous membranes

The morphology of the PLGA and PLA nanofibrous membranes in their pristine state (ie, uncoated membranes) was studied by scanning electron microscopy (SEM). The measurements were carried out in accordance with a previously published protocol:[9] the membranes were sputter-coated with gold and evaluated by SEM (Quanta 450; Thermo Fisher Scientific, Waltham, MA, USA) in high vacuum mode. The images were taken using an Everhart–Thornley detector in secondary electron mode at high voltage (20 kV) and magnification 2,000× and 10,000×. The thickness of the membranes was determined from SEM images of a vertical section of the membrane. The diameter of the fibers was measured on the SEM images using Atlas software (Tescan, Brno, Czech Republic).

Membrane puncture testing

Nanofibrous membranes in CellCrown inserts (n=6 for each group of scaffolds; Scaffdex Oy, Tampere, Finland) were placed into the manufactured holder and secured against a tilt. Then, the holder was fastened in the standard microscope stage (DM2500; Leica Microsystems, Wetzlar, Germany) and the microscope condenser replaced with a manufactured tooling that carried a low-level force sensor (9203; Kistler, Winterthur, Switzerland) with a spherical cup
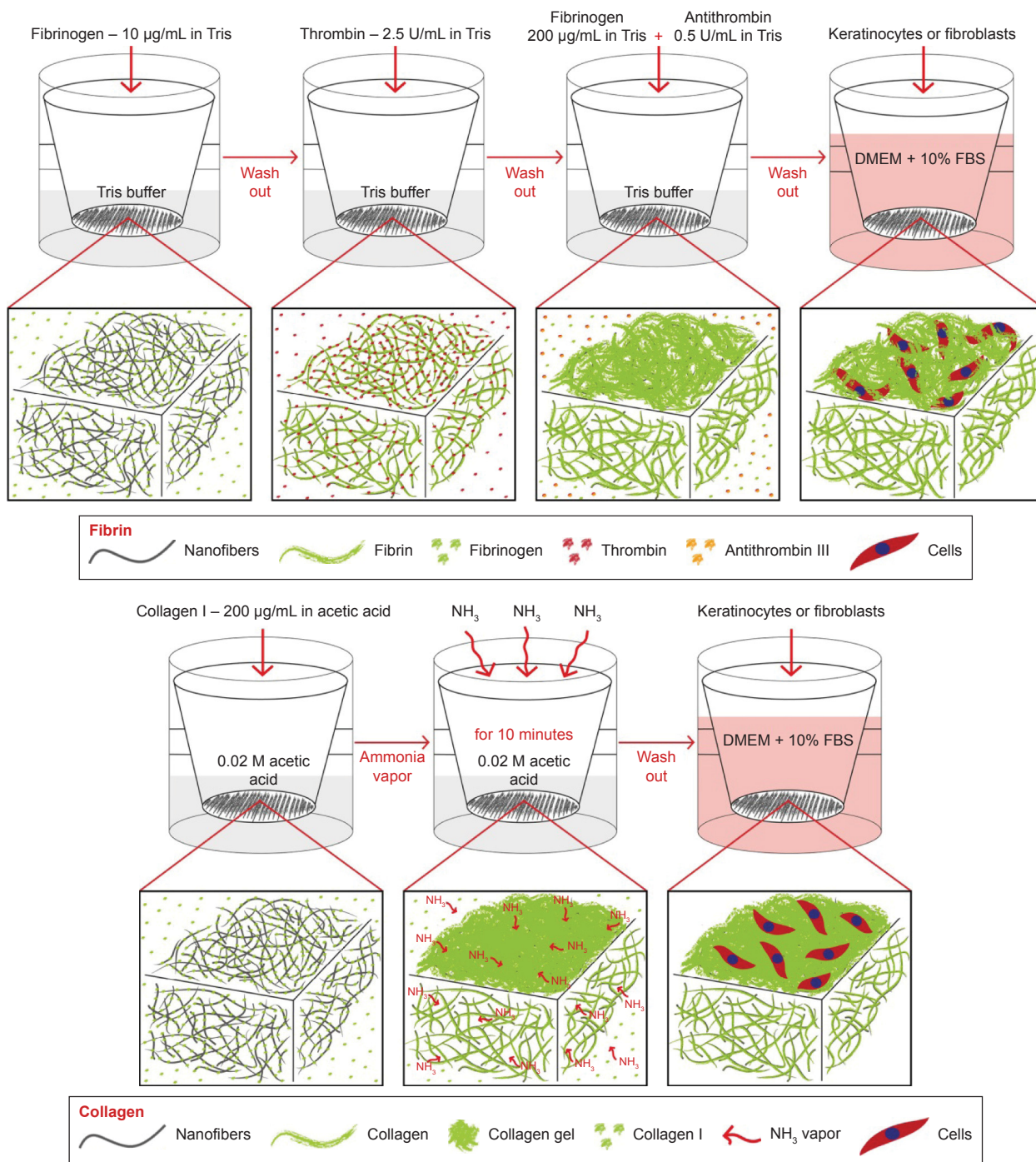
Figure 1 Schematic representation of a preparation of fibrin and collagen nanocoating on nanofibrous membrane.
Abbreviations: FBS, fetal bovine serum; DMEM, Dulbecco's Modified Eagle's Medium.

probe (Figure 2). Due to the construction of the DM2500 microscope, the force sensor can be moved independently on the stage in respect to the focal plane. First, the membranes were focused and imaged by the confocal microscope (magnification 4×, image resolution 1,024×1,024, pixel size 1.8 μm) to verify their structural integrity. Second, the camera started capturing the calibrated images (image resolution 1,920×1,440, pixel size 0.05 mm) of the membrane at

10 Hz repetition rate, and the force sensor recorded the force changes at 100 Hz repetition rate. Finally, the force sensor with the probe moved toward the sample at a speed of 0.2 mm/s until the force value returned to zero.

The deformation u_z of the nanofibrous membranes was evaluated in MatLab 2015A (MathWorks, Natick, MA, USA) by image segmentation (thresholding and edge detection using a Sobel filter). The stress in the membrane σ_t is based
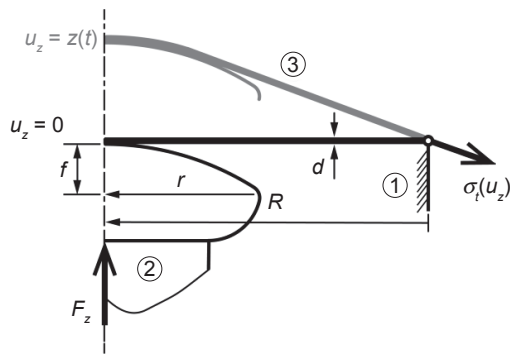
Figure 2 The puncture testing protocol.
Notes: The CellCrown membrane insert ① with radius R represents the pinned joint. The probe ② with radius r and head-high f deforms the membrane ③ of measured thickness d until rupture. The dimensions are used to calculate the membrane stress σ_t.

on static equilibrium, and calculated from the force data F_z and deformation u_z as

$$\sigma_t(u_z \leq a) = \frac{F_z}{2\pi R d \tan^{-1}\left(\dfrac{R}{u_z}\right)} \qquad (1)$$

or

$$\sigma_t(u_z > a) = \frac{F_z}{2\pi R d \tan^{-1}\left(\dfrac{R-r}{u_z - f}\right)} \qquad (2)$$

for the geometrical contact ratio a:

$$a = \frac{f}{r} R \qquad (3)$$

Cell culture

The nanofibrous membranes were fixed in CellCrown inserts, in order to prevent them floating in the cell culture medium, and inserted into the wells of 24-well plates (well diameter 1.56 cm; TPP Techno Plastic Products AG, Trasadingen, Switzerland). Samples were seeded with neonatal human dermal fibroblasts, purchased from Lonza (Basel, Switzerland), passage 3–6, or with human keratinocytes of the line HaCaT, purchased from CLS Cell Lines Service (Eppelheim, Germany).[36] The HaCaT cell line consists of spontaneously transformed and immortal human epidermal keratinocytes, but it remains nontumorigenic and maintains full epidermal differentiation capacity. In contrast to normal keratinocytes, HaCaT cells are able to adhere to various materials without requiring a fibroblast feeder layer

for their adhesion and growth. This property of HaCaT cells can be regarded as advantageous for studies on the suitability of various synthetic and biological scaffolds for skin tissue engineering and was also used for this purpose in our study.

Cells were seeded at a density of approximately 10,000 cells/cm² (ie, 20,000 cells/well) and were cultivated in Dulbecco's Modified Eagle's Medium (Sigma-Aldrich) with 10% of fetal bovine serum (Sebak GmbH, Aidenbach, Germany) and 40 µg/mL of gentamicin (Novartis International AG, Basel, Switzerland). The volume of cell culture medium was 1.5 mL/well. Cells were cultivated for three time periods (1, 3, and 7 days) in a cell incubator at 37°C and in a humidified atmosphere with 5% CO_2. Polystyrene culture wells (24-well plates) were used as a control material.

Morphology of protein nanocoatings

The morphology of the fibrin, collagen, and fibronectin nanocoatings was studied by immunofluorescence staining on freshly prepared samples, on cell-free samples incubated for two periods (ie, on days 3 and 7) in Dulbecco's Modified Eagle's Medium under the conditions used for cell cultivation, and on samples with cells on days 3 or 7 after seeding. Uncoated membranes were used as control samples to evaluate possible nonspecific binding of the primary and secondary antibodies. Two samples of each experimental group for each time period were used.

The membranes were treated with 1% bovine serum albumin in PBS for 20 minutes, and then with 1% Tween (Sigma-Aldrich Co) in PBS for 20 minutes at room temperature to block nonspecific binding sites. The samples were subsequently incubated overnight at 4°C with primary antibodies against human fibrinogen (polyclonal rabbit antibody; Dako Denmark A/S, Glostrup, Denmark), collagen I (monoclonal mouse antibody; Sigma-Aldrich), or fibronectin (monoclonal mouse antibody; Sigma-Aldrich) diluted in PBS at a ratio of 1:200. The samples were then rinsed twice with PBS and incubated with secondary antibodies, namely goat antirabbit or goat antimouse F(ab′)$_2$ fragments of IgG (H + L [Heavy and Light chains]), conjugated with Alexa Fluor® 488 (diluted in PBS at a ratio of 1:400; Thermo Fisher Scientific) for 1 hour at room temperature in the dark.

The fibrin- or collagen-coated membranes with attached fibronectin were also stained for fibrin + fibronectin or collagen + fibronectin on the same sample. The samples were incubated overnight at 4°C with primary antibodies against human fibrinogen (rabbit polyclonal antibody; Dako) or with collagen I (rabbit polyclonal antibody; Cosmo Bio Co Ltd, Tokyo, Japan) diluted in PBS at a ratio of 1:200.

Subsequently, after being rinsed with PBS, the primary antibody against fibronectin (mouse monoclonal antibody; Sigma-Aldrich) was added for 3 hours. The samples were rinsed with PBS and incubated with a secondary antibody goat antirabbit F(ab′)$_2$ fragment of IgG (H + L), conjugated with Alexa Fluor 488 (diluted in PBS at a ratio of 1:400) for 1 hour (in order to visualize the fibrin or collagen), and then with a secondary antibody goat antimouse F(ab′)$_2$ fragment of IgG (H + L), conjugated with Alexa Fluor 633 (diluted in PBS at a ratio of 1:400) for 1 hour (in order to visualize the fibrinogen). The samples were rinsed with PBS and scanned using the Leica TCS SPE DM2500 upright confocal microscope, magnification 40×/1.15 NA oil.

Cell spreading and morphology

The spreading and morphology of the cells on uncoated or protein-coated nanofibrous membranes were visualized on days 1, 3, and 7 after seeding by staining the cells with a combination of fluorescent dyes diluted in PBS (5 µg/mL Hoechst 33258 cell nucleus dye; Sigma-Aldrich; and 20 ng/mL Texas red C$_2$-maleimide cell membrane dye; Thermo Fisher Scientific) for 1 hour at room temperature in the dark. Instead of Texas red staining, the F-actin cytoskeleton of the cells was stained with phalloidin conjugated with tetramethylrhodamine isothiocyanate fluorescent dye (Sigma-Aldrich), diluted in PBS to a final concentration of 5 µg/mL, for 1 hour at room temperature in the dark. Before staining, the cells were rinsed with PBS and were fixed with −20°C cold ethanol for 10 minutes. Images of the cells were taken using epifluorescence microscopy (magnification 10×, IX 51; Olympus, Tokyo, Japan) equipped with a digital camera (DP 70), or using the Leica TCS SPE DM2500 upright confocal microscope, magnification 40×/1.15 NA oil. On day 1 after seeding of the cells, the spreading area of islands formed by human HaCaT keratinocytes was measured on images taken under fluorescence microscopy using the Atlas software.

Cell mitochondrial activity

The activity of mitochondrial enzymes was measured at three points of cell cultivation (on days 1, 3, and 7 after cell seeding) for the dermal fibroblasts and at two points (on days 3 and 7 after cell seeding) for the HaCaT keratinocytes with CellTiter 96® Aqueous One solution cell proliferation assay (MTS; Promega Corporation, Fitchburg, WI, USA) on samples of nanofibrous membranes incubated in 24-well cell culture plates. The mitochondrial activity of the HaCaT keratinocytes was measured only on days 3 and 7, but not on day 1 after cell seeding. The reason was that our preliminary measurements, using the MTS assay, revealed that on day 1 after seeding, when cell numbers were relatively low, the measured absorbance was on the limit of detection and showed no significant differences among the tested samples. This was probably due to the relatively low activity of the mitochondrial enzymes in the HaCaT cells. In cell culture and human skin sections, the activities of mitochondrial enzymes were lower in keratinocytes than in fibroblasts.[37] The principle of an MTS assay is based on cleavage of the yellow tetrazolium salt MTS and on the formation of a water-soluble brown formazan salt by the activity of mitochondrial enzymes (ie, dehydrogenases) in the cells. The formazan dye produced by the cells was then quantified by measuring the absorbance using a spectrophotometer (ie, an enzyme-linked immunosorbent assay [ELISA] reader).

Membrane samples were moved into fresh 24-well plates to avoid the influence of the cells adhered to the bottom of the well. The assay was performed according to the manufacturer's protocol. Absorbance was measured using the VersaMax ELISA microplate reader (Molecular Devices LLC, Sunnyvale, CA, USA) in Nunc-Immuno MicroWell 96-well cell culture plates (Sigma-Aldrich) with wavelength 490 nm. Three independent samples for each experimental group and time point were used. One sample without cells for each experimental group and time point was used as a control to set the background for the measured absorbance. A polystyrene culture dish (24-well plate) was used as a control material for the cell mitochondrial activity.

Cell viability

The cell viability was determined using a Live/Dead viability/cytotoxicity kit (Thermo Fisher Scientific). The principle of this assay is based on the different ability of two fluorescent dyes to penetrate the cell membrane of live and dead cells. Calcein AM penetrates live cells, where it is converted by esterases to calcein, which emits green fluorescence. Ethidium homodimer 1 penetrates the membrane of the dead cells and stains them with red fluorescence.

The samples were carefully rinsed with PBS and stained with a solution of 2×10^{-3} µM calcein AM and 6×10^{-3} µM ethidium homodimer 1. After 10 minutes of incubation in the cell incubator, the cells were rinsed with PBS and evaluated using epifluorescence microscopy (IX 51) equipped with a digital camera (DP 70).

Statistics

Quantitative data are presented as mean ± standard deviation values or standard error of the mean from three independent

samples for each experimental group and time point. Statistical significance was evaluated using analysis of variance, Student–Newman–Keuls method or nonparametric Kruskal–Wallis test, and Mann–Whitney U test. Values of $P \leq 0.05$ were considered significant.

Results
Morphology and mechanical properties of nanofibrous membranes

Fibers of both types of nanofibrous membranes were mostly straight and randomly oriented. The diameter of the fibers was within a large range, from tens of nm to more than 1 μm. The average fiber diameter was more than 300 nm (Figure 3), similarly to our earlier study.[9] The material nanostructures were defined to be equal to or less than 100 nm in at least one dimension. The fiber diameter in our study was thus in submicron and micron scale rather than in nanoscale. However, such fibers are frequently referred to in the literature as nanofibers.[4,38–40]

Puncture testing revealed a faster mechanical response of the PLA membranes. At about 1 mm deformation, the stress/strain direction changed dramatically and the PLA response stayed linear until rupture. On the other hand, the PLGA membranes reacted to loading gradually and reached significantly lower ultimate strength than the PLA groups (Mann–Whitney U test, $P=0.032$). After collagen modification, the membranes seemed to become brittle. Fibrin modification caused an upward trend in ultimate strength. However, there was no significant difference in ultimate strength when comparing all the modifications (Kruskal–Wallis test, $P=0.177$) (Figure 4, Table 1).

Morphology of protein nanocoating and its stability and degradation during cell cultivation

Fibrin regularly formed a coating around individual nanofibers, and also formed a thin nanofibrous mesh on the membrane surface. However, this mesh did not form homogeneously on the whole surface of the membrane. Collagen also coated most of the fibers in the membranes, but not regularly. Moreover, collagen randomly formed a soft gel on the membrane surface (Figure 5). Fibronectin was bound on the fibrin and collagen nanocoating. Fibronectin formed an additional nanofibrous mesh on the thin fibrin mesh or on the collagen gel (Figure 6). Fibronectin also adsorbed on fibers coated with fibrin or collagen, but it was hardly visible using immunofluorescence. There was no apparent difference in the morphology of the protein nanocoating on PLGA and PLA membranes (Figure 5).

The durability of the protein nanocoatings on the nanofibrous membranes was tested during 7 days under the same conditions as those used for cell cultivation. The results showed that the fibrin, collagen, or fibronectin nanocoatings on both polymer membranes were stable in a cell-free environment, and their morphology was almost unchanged after 1 week (Figure 5).

However, the cells altered the morphology of the protein nanocoatings during their cultivation. Both types of cells degraded and reorganized the protein nanocoating (Figure 7). Fibroblasts penetrated into the fibrin mesh and gradually degraded the fibrin nanocoating. Nevertheless, on day 7, some fibrin-coated fibers and some remains of the thin fibrin nanofibrous mesh were still apparent. Collagen was less degraded than fibrin by fibroblasts. However, the collagen
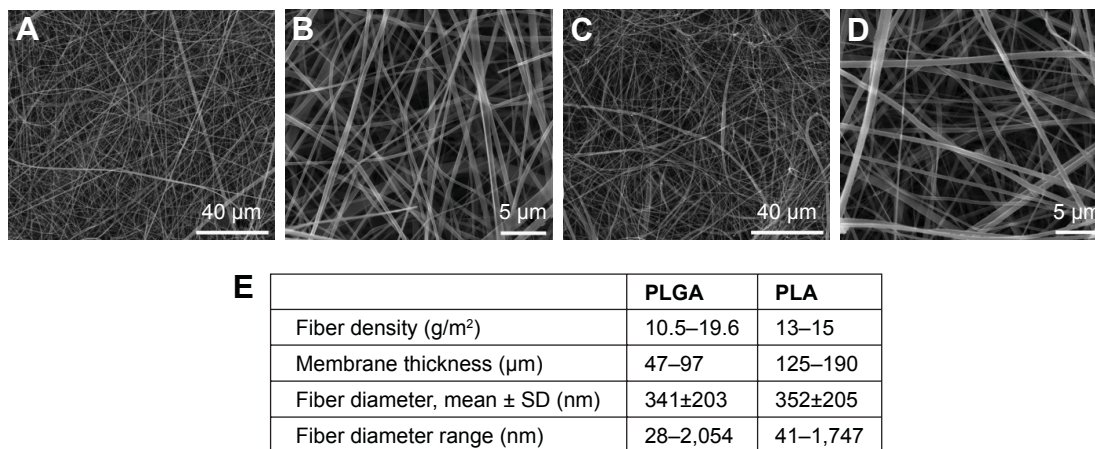

E		PLGA	PLA
Fiber density (g/m^2)		10.5–19.6	13–15
Membrane thickness (μm)		47–97	125–190
Fiber diameter, mean ± SD (nm)		341±203	352±205
Fiber diameter range (nm)		28–2,054	41–1,747

Figure 3 SEM images of unmodified PLGA membranes (**A**, **B**) and PLA membranes (**C**, **D**).
Notes: Quanta 450 scanning electron microscope, original magnification 2,000× (**A**, **C**) or 10,000× (**B**, **D**). Morphological parameters of PLGA and PLA membranes (**E**). Fiber diameter: mean ± SD from 12 SEM images (1,748 measurements in total).
Abbreviations: SEM, scanning electron microscopy; PLGA, poly(lactide-*co*-glycolic acid); PLA, polylactic acid; SD, standard deviation.
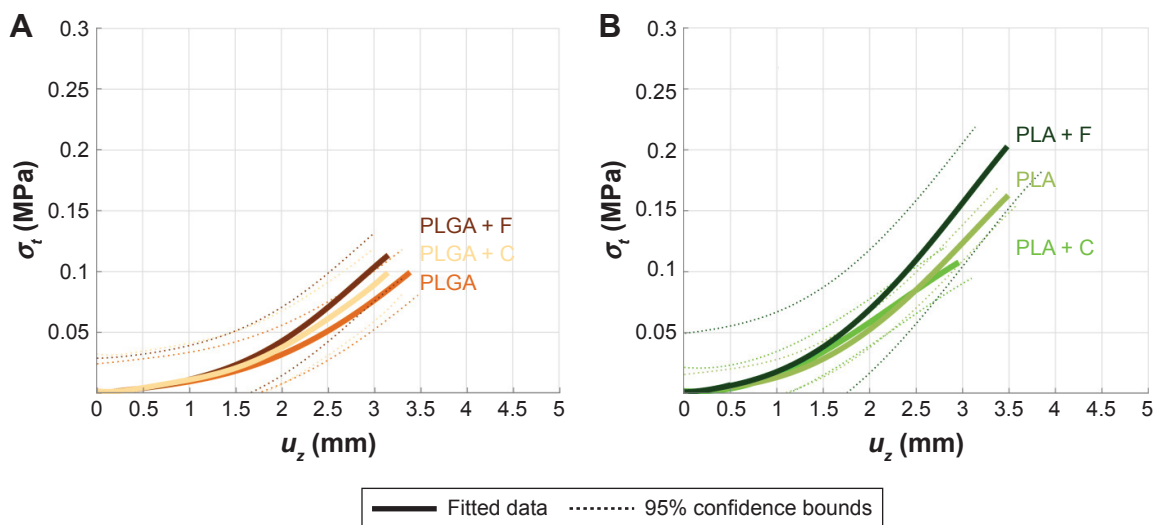
Figure 4 Puncture mechanical testing.
Notes: The membrane's mechanical response was plotted for the unmodified PLGA (**A**) or PLA (**B**) membrane and for each modification of the membranes as a polynomial up to the maximum mean values of stress and strain (thick colored line) and as the confidence bounds of the fit (thin dashed line).
Abbreviations: PLGA, poly(lactide-*co*-glycolic acid); PLA, polylactic acid; F, fibrin; C, collagen.

gel that formed on the membrane surface appeared to be too soft for the adhesion and growth of fibroblasts, and the cells were often detached from the surface of the material. The fibronectin mesh degraded faster on the fibrin nanocoatings than on the collagen nanocoatings. In addition, the fibrin-coated membranes apparently stimulated the fibroblasts to produce fibronectin and to deposit it as ECM in the cell surroundings (Figure 8).

HaCaT keratinocytes degraded the protein nanocoating in a different way. Thin nanofibrous fibrin and fibronectin meshes on the fibrin-coated membranes were almost completely degraded on day 3 after seeding. Only fibers coated with fibrin and the remains of fibronectin meshes remained until day 7 of seeding. The degradation process had started already on day 1 of cell cultivation (data not shown here). In Figure 7, it is apparent that the keratinocytes adhered on the membrane surface did not penetrate the membrane, but remained on the surface of the fibrin or fibronectin meshes, and these meshes were pulled down, probably by cell traction forces. Surprisingly, the fibronectin attached to the collagen gel was not degraded in a similar manner as the fibronectin on the fibrin. The fibronectin attached to the collagen,

and also the collagen itself, was only slightly changed and degraded after 7 days of cell cultivation.

Cell adhesion, spreading, and morphology

Differences in cell morphology among the various types of samples and cells were observed. On the coated samples, the fibroblasts were well spread with a spindle-like or polygonal shape already on day 1 after cell seeding. However, on the uncoated membranes, the cells tended to be round and not well adhered (Figure 9). After 1 week of cell cultivation, the fibroblasts on the fibrin-coated samples, and also on the collagen-coated samples, were almost confluent. On the uncoated membranes, however, there were considerably large free spaces among the cells. On the membranes with fibrin, the cells were able to penetrate into the fibrin mesh and into deeper layers of the membrane (seen mainly on day 7 after seeding). By contrast, on membranes with collagen, the cells adhered only on the surface of the protein nanocoating or on the surface of the membrane (Figure 7).

The morphology of the keratinocytes also varied among the different types of samples. On membranes coated with collagen, the cells were well spread and formed larger cell

Table I Variables σ_t and u_z at the mean maximum

	PLGA + F	**PLGA + C**	**PLGA**	**PLA + F**	**PLA + C**	**PLA**
$\sigma_t(US)$ MPa	0.116±0.032	0.102±0.04	0.101±0.036	0.2±0.086	0.118±0.039	0.161±0.068
$u_z(US)$ (mm)	3.24±0.49	3.29±0.22	3.48±0.33	3.5±0.45	2.87±0.61	3.5±0.79

Note: Values stated as mean maximum ± standard deviation.
Abbreviations: PLGA, poly(lactide-*co*-glycolic acid); PLA, polylactic acid; F, fibrin; C, collagen.
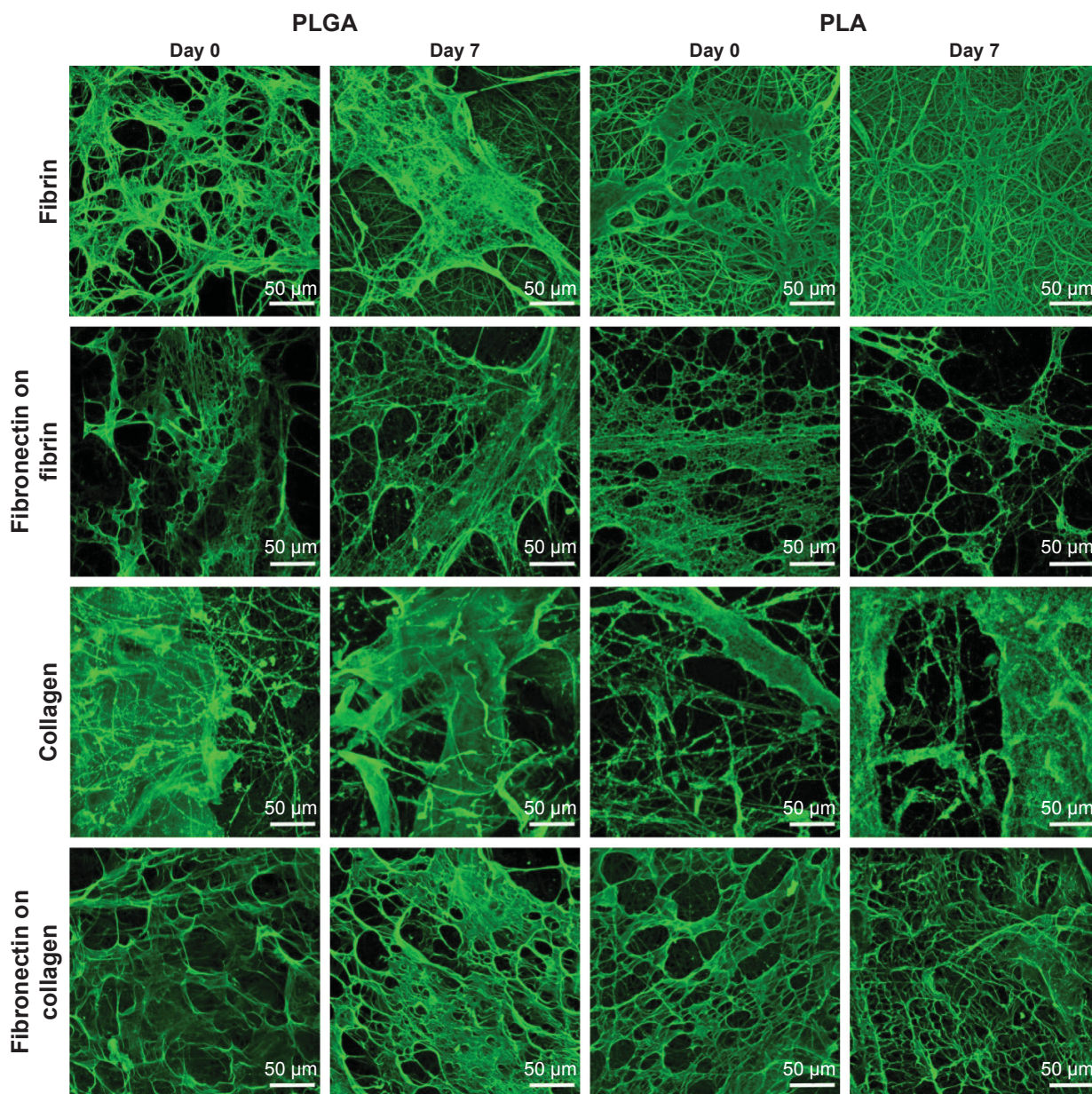
Figure 5 Immunofluorescence staining of protein nanocoating on membrane.
Notes: Fibrin (row 1), fibronectin deposited on fibrin (row 2), collagen I (row 3), and fibronectin deposited on collagen (row 4), freshly prepared on PLGA and PLA membranes (day 0) or after 7 days of incubation in DMEM at 37°C and 5% CO_2 (day 7). Leica TCS SPE DM2500 confocal microscope, magnification 40×/1.15 NA oil.
Abbreviations: PLGA, poly(lactide-*co*-glycolic acid); PLA, polylactic acid; DMEM, Dulbecco's Modified Eagle's Medium.

clusters (islands) than on membranes coated with fibrin or on uncoated membranes (Figures 7 and 9). The size of the cell cluster spreading area on day 1 was larger on membranes with collagen than on uncoated membranes or on membranes with fibrin. Fibronectin improved cell attachment on the protein nanocoatings, mainly on the collagen nanocoating, where the largest cell cluster area was observed. The cluster area of keratinocytes on the fibrin nanocoating was only slightly and insignificantly larger than on the uncoated membranes (Figure 10).

Cell proliferation and viability

Cell proliferation was estimated by measuring cell mitochondrial activity. At all culture time points, the mitochondrial activity of dermal fibroblasts was significantly higher on protein-coated membranes (with the exception of the collagen-coated membranes) than on uncoated (pristine) membranes (Figure 11). On membranes with collagen nanocoating, cell mitochondrial activity was mostly comparable with the metabolic activity of the cells growing on uncoated membranes (with the exception of PLA membranes on day 7
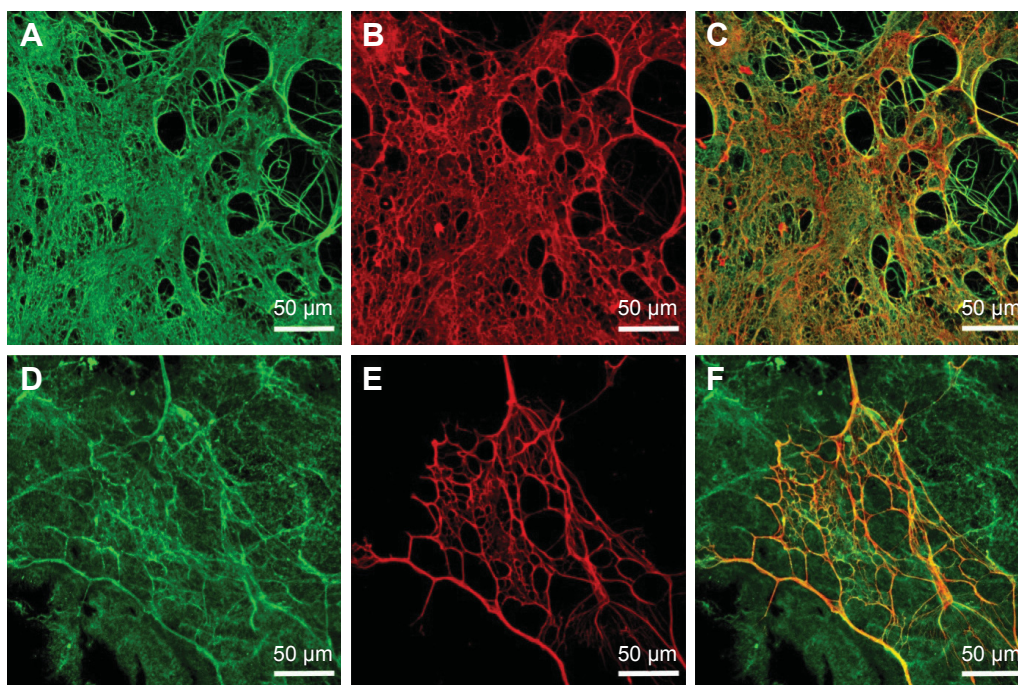
Figure 6 Immunofluorescence staining of protein nanocoating on membrane.
Notes: Fibrin nanocoating (**A**), collagen nanocoating (**D**), fibronectin on fibrin nanocoating (**B**), fibronectin on collagen nanocoating (**E**), freshly deposited on poly(lactide-co-glycolic acid) membranes. Image **A** was merged with **B** (**C**), and image **D** with **E** (**F**). Secondary antibodies were conjugated with Alexa 488 (fibrin, collagen, green fluorescence) or with Alexa 633 (fibronectin, red fluorescence). Leica TCS SPE DM2500 confocal microscope, magnification 40×/1.15 NA oil.

after cell seeding, where mitochondrial activity was higher). Fibronectin attached to the collagen nanocoating greatly improved fibroblast proliferation. Cell mitochondrial activity on samples of this type was significantly higher than on membranes coated only with collagen. The highest metabolic activity of fibroblasts was found on membranes with fibrin nanocoating. Fibronectin attached to the fibrin nanocoating promoted the attachment of fibroblasts, and further increased their mitochondrial activity. This was apparent mainly on day 3 after seeding.

In comparison with dermal fibroblasts, HaCaT keratinocytes adhered and proliferated better on membranes with a collagen nanocoating than on membranes with a fibrin nanocoating (Figure 12). Cell mitochondrial activity was significantly higher on membranes coated with collagen than on non-coated membranes and on membranes coated with fibrin. Cell mitochondrial activity on fibrin was mostly comparable with activity on uncoated membranes. On fibrin-coated PLGA membranes further modified with fibronectin, cell mitochondrial activity was even lower than on pristine PLGA membranes (Figure 12A). In general, however, there were no major differences in cell adhesion, in mitochondrial activity, or in proliferation between the two types of polymeric membranes, ie, PLGA and PLA membranes (Figures 11 and 12). The viability of both cell types – dermal fibroblasts and HaCaT keratinocytes – was

high and reached almost 100% on both coated and uncoated membranes. The lower adhesion and proliferation rate of the cells on uncoated membranes did not affect cell viability (Figure 13).

Discussion

Nanofibrous membranes made from bioresorbable polymers are promising carriers of skin cells for treating acute or chronic wounds. However, the synthetic polymers used for fabricating nanofibrous cell carriers often do not provide sufficient support for cell adhesion, proliferation, or deposition of ECM. Desirable cell behavior can be achieved by modifying the polymer carrier physically or chemically. In our previous studies, modification of PLA membranes by plasma treatment enhanced the adhesion and growth of human keratinocytes,[8] and fibrin nanocoating on PLA membranes improved the adhesion and proliferation of human fibroblasts, and also collagen synthesis and deposition by these cells as ECM.[9] Modifying nanofibrous carriers of skin cells by biomolecules naturally occurring in the skin or during skin regeneration could thus be promising for the development of desirable skin substitutes. In this study, we focused on fabricating fibrin, collagen, and fibronectin nanocoatings on nanofibrous PLGA and PLA membranes in order to enhance adhesion, proliferation, and ECM synthesis in skin cells.
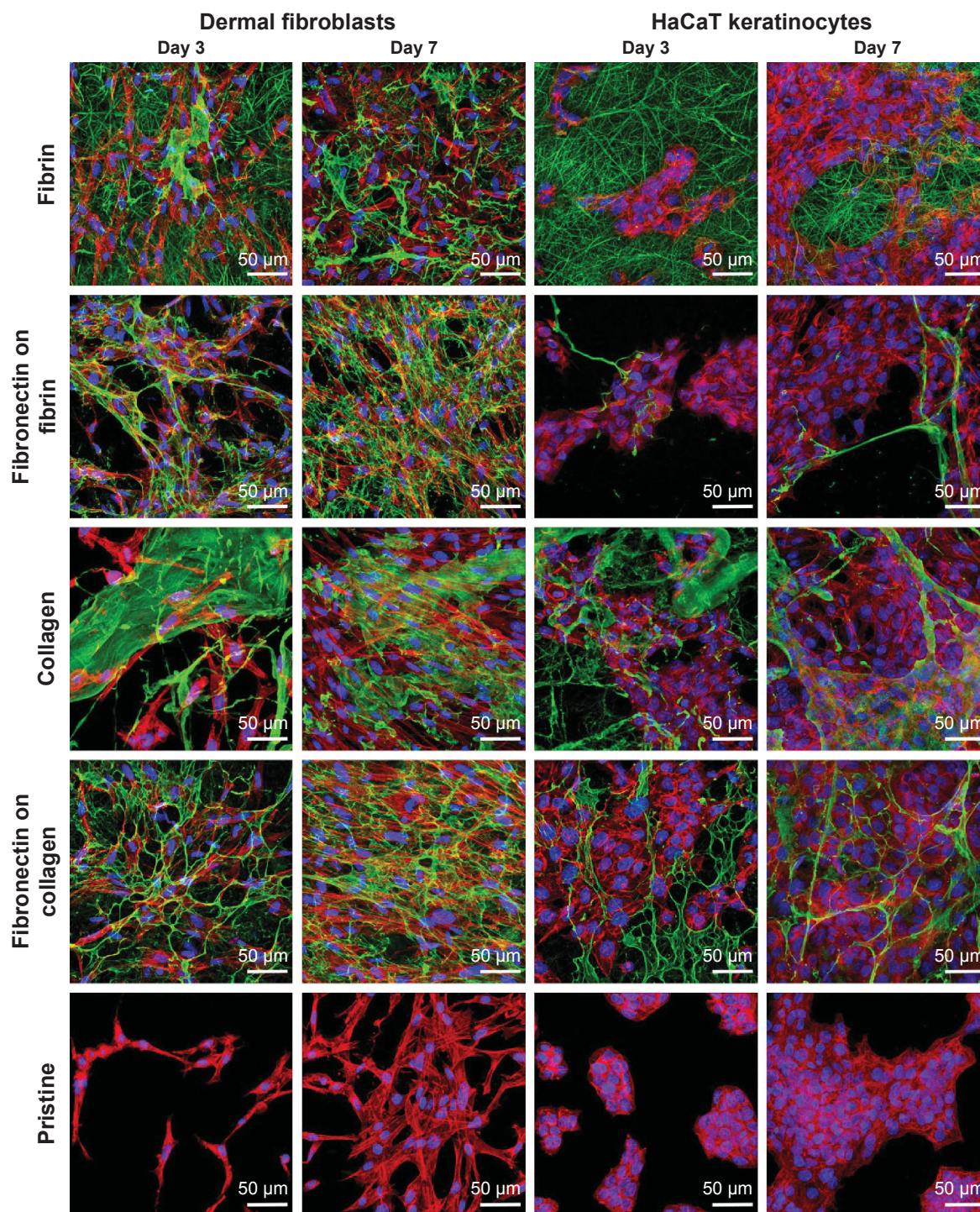
Figure 7 Human dermal fibroblasts and HaCaT keratinocytes on protein-coated membranes.
Notes: Fibrin (row 1), fibronectin deposited on fibrin (row 2), collagen I (row 3), and fibronectin deposited on collagen (row 4) on poly(lactide-*co*-glycolic acid) membranes after 3 and 7 days of cultivation of human dermal fibroblasts and HaCaT keratinocytes. Row 5: control cells on pristine uncoated membranes. The protein nanocoating was immunofluorescence stained (green) with primary and secondary antibody conjugated with Alexa 488. The cells were stained with phalloidin–tetramethylrhodamine isothiocyanate (red; actin cytoskeleton) and with Hoechst 33258 (blue; cell nuclei). Leica TCS SPE DM2500 confocal microscope, magnification 40×/1.15 NA oil.

Fibrin deposited on membrane nanofibers greatly improved the adhesion, spreading, and proliferation of dermal fibroblasts. In some places on the membranes, moreover, fibrin formed a thin nanofibrous mesh, mimicking ECM and promoting more cell adhesion and spreading than was observed on unmodified membranes. These results were similar to those obtained in our previous work. As we discussed there, fibrin enabled the cell adhesion receptors to bind to its molecule, and further supported cell adhesion by attracting cell adhesion-mediating molecules (such as
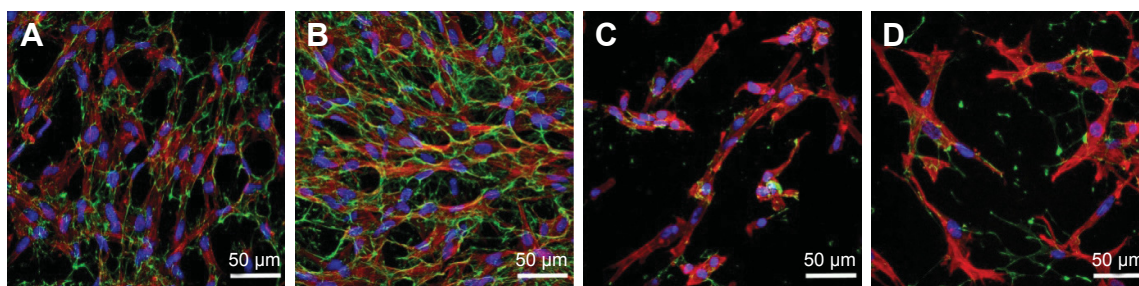
Figure 8 Immunofluorescence staining of fibronectin produced by dermal fibroblasts.
Notes: Fibronectin (green) produced by dermal fibroblasts on poly(lactide-co-glycolic acid) (PLGA) membranes with a fibrin nanocoating (**A**, **B**) or on uncoated PLGA membranes (**C**, **D**) on day 3 (**A**, **C**) and on day 7 (**B**, **D**) after seeding. Cells were stained with phalloidin–tetramethylrhodamine isothiocyanate (red; actin cytoskeleton) and with Hoechst 33258 (blue; cell nuclei). Leica TCS SPE DM2500 confocal microscope, magnification 40×/1.15 NA oil.

fibronectin or vitronectin) from the serum supplement of the cell culture medium. We showed that fibrin enhanced the development of focal adhesion plaques containing β_1-integrins in dermal fibroblasts.[9] Studies by other authors have also shown similar positive effects of fibrin on the adhesion and growth of fibroblasts.[41,42]

However, our results showed that (unlike in the case of fibroblasts) there was not significantly greater proliferation of keratinocytes on fibrin-coated membranes than on uncoated membranes. The explanation for this could be that keratinocytes, unlike fibroblasts, do not naturally come into direct contact with fibrin. During wound healing, fibroblasts migrate into the fibrin clot, start to produce ECM, and are the first to contribute to wound healing. Keratinocytes then migrate to the wound, attach to the ECM matrix, and form new cell layers of epidermis. Many previous studies have attempted to reveal the role of fibrin in the adhesion and proliferation of keratinocytes, but they have not reached consistent conclusions. Sese et al reported that keratinocyte proliferation in three-dimensional fibrin constructs was influenced by thrombin concentration. These authors found that the optimal thrombin concentration in fibrin matrices for stimulating keratinocyte proliferation was about 1 U/mL,[43] while the proliferation of fibroblasts was not strongly dependent
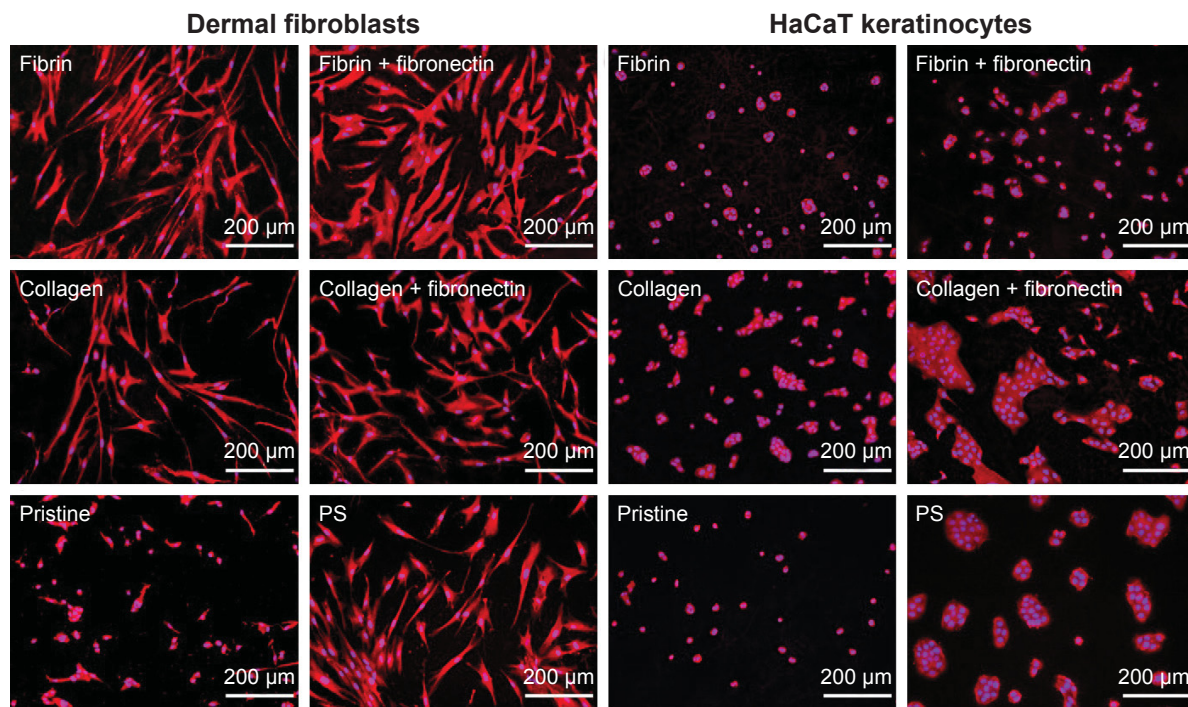

Figure 9 Morphology of human dermal fibroblasts and human HaCaT keratinocytes.
Notes: Day 1 after seeding on poly(lactide-co-glycolic acid) (PLGA) membranes coated with fibrin, fibrin + fibronectin, collagen, or collagen + fibronectin, and on uncoated PLGA membranes (pristine). Polystyrene (PS) culture dishes were used as reference material. Cells stained with Texas red C_2-maleimide and Hoechst 33258. Olympus IX 51 microscope, magnification 10×, DP 70 digital camera.
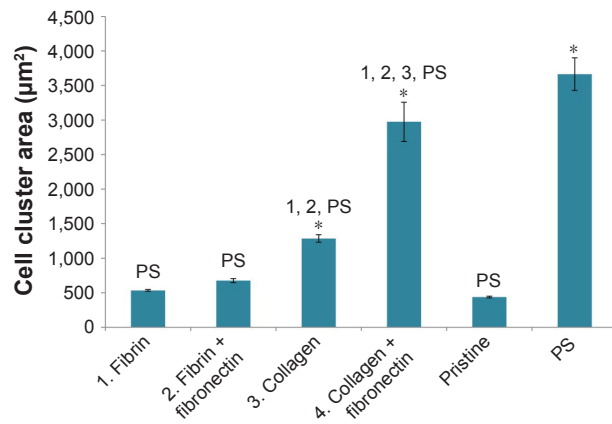
Figure 10 Cell cluster spreading area of HaCaT keratinocytes.
Notes: Day 1 after seeding on poly(lactide-co-glycolic acid) membranes in modified states (1–4) or in an unmodified state (pristine). Polystyrene (PS) culture dishes were used as reference material. Arithmetic mean ± standard error of mean from 283–779 measurements. Analysis of variance, Student–Newman–Keuls method, statistical significance $P \leq 0.05$. 1–4, PS in comparison with experimental group of same label; *compared to pristine sample.

on thrombin concentration. Fibroblasts proliferated well within three-dimensional fibrin clots containing 1–167 U/mL of thrombin.[44] In our study, we used thrombin in a concentration of 2.5 U/mL to fabricate a fibrin nanocoating. This concentration was optimal for forming the nanocoating on the membrane and for supporting the proliferation of fibroblasts, but it was probably not convenient for the growth of keratinocytes. Gugerell et al reported that high concentrations (about 820 U/mL) of thrombin activated apoptotic mechanisms in keratinocytes, and also decreased their attachment and spreading on fibrin sealants.[45] Kubo et al showed that fibrin and fibrinogen were nonadhesive for keratinocytes, due

to a lack in these cells of $\alpha_v\beta_3$ integrin receptors, which are important for binding cells to fibrin molecules.[46] In our study, the HaCaT keratinocytes were able to adhere to fibrin-coated membranes, though they were not so well flattened as on collagen-coated membranes. This may be explained by the relatively long exposure of the fibrin coatings to the adhering keratinocytes, ie, more than 24 hours, which is sufficient time for these cells to alter or to remove the protein coating in order to enhance their adhesion.[46] In addition, the adhesion and proliferation of keratinocytes on fibrin matrices can be improved by cross-linking them, eg, by factor XII, and also by adding fibronectin.[47] It cannot be excluded that fibronectin, which is present in the serum supplement of the culture medium, was bound onto our fibrin matrices through their αC domains,[22] and was then recognized by the $\alpha_5\beta_1$, $\alpha_v\beta_1$, and $\alpha_v\beta_6$ integrin-adhesion receptors present on keratinocytes, including HaCaT.[48] However, in our study, the attachment of fibronectin to fibrin coatings did not significantly improve the adhesion or growth of keratinocytes, although this cell behavior was expected.

Our experiments also suggested that fibrin stimulated fibroblasts to synthesize fibronectin and deposit it as ECM in the cell surroundings. On the fibrin coating, the amount of fibronectin in the cell surroundings increased markedly from day 3 to day 7, and the fibronectin was clearly associated with the cells, ie, it was localized in the immediate vicinity of the cell membrane. This was particularly apparent on day 7, when fibronectin clearly contoured the cells (Figure 8). This pattern could be attributed to de novo synthesis of fibronectin by the cells, rather than to its spontaneous adsorption or binding
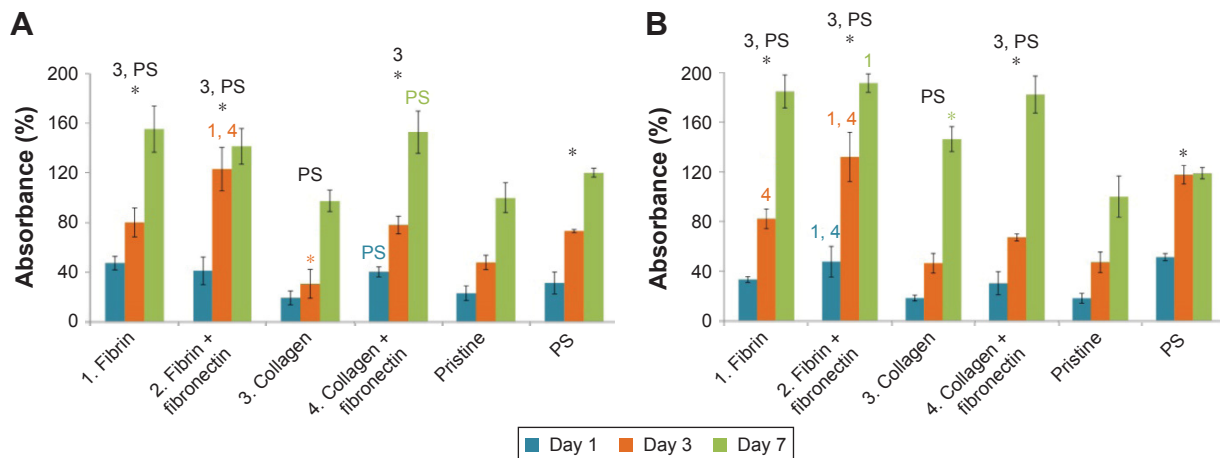

Figure 11 Mitochondrial activity in human dermal fibroblasts determined by MTS assay at three time points (on days 1, 3, and 7 after cell seeding).
Notes: On a poly(lactide-co-glycolic acid) membrane (**A**) or polylactic acid membrane (**B**) in modified states (1–4) or in an unmodified state (pristine). Polystyrene (PS) culture dishes were used as reference material. Arithmetic mean ± standard deviation values from 12 measurements made on three independent samples for each experimental group and time point. Analysis of variance, Student–Newman–Keuls method, statistical significance $P \leq 0.05$. 1–4, PS in comparison with experimental group of same label; *compared to pristine sample at all three time points (black label) or at particular points (color label).
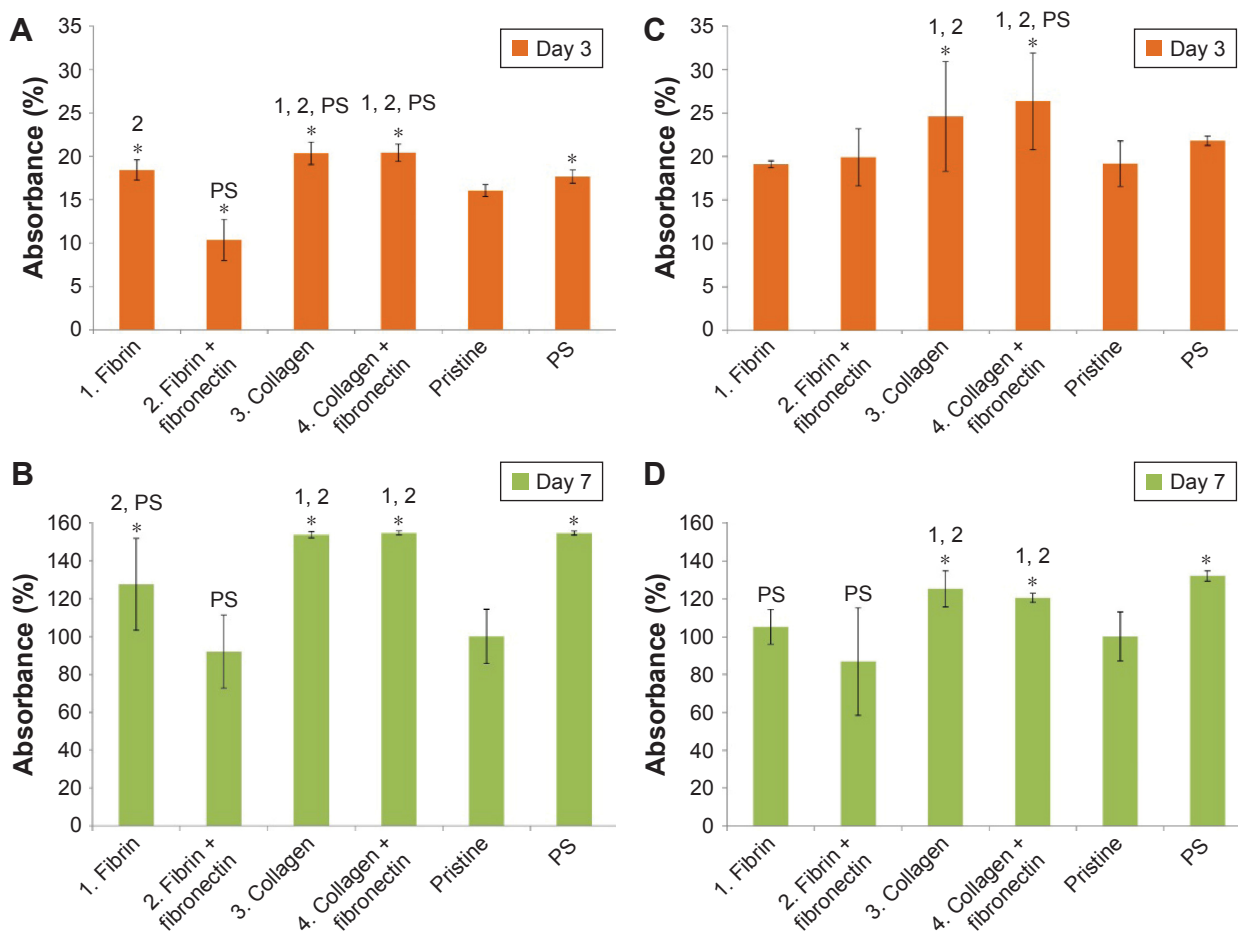
Figure 12 Mitochondrial activity in human HaCaT keratinocytes determined by MTS assay at two time points (on days 3 and 7 after cell seeding).
Notes: On poly(lactide-*co*-glycolic acid) (**A**, **B**) or polylactic acid membranes (**C**, **D**) in modified states (1–4) or in an unmodified state (pristine). Polystyrene (PS) culture dishes were used as control material. Arithmetic mean ± standard deviation values from 12 measurements made on three independent samples for each experimental group and time point. Analysis of variance, Student–Newman–Keuls method, statistical significance $P \leq 0.05$. 1–4, PS in comparison with experimental group of same label; *compared to pristine sample.

to fibrin from the serum of the culture medium. A similar pattern of fibronectin deposition was observed in cardiac fibroblasts cultured on three-dimensional fibrin gels.[49] In our previous study, we showed that fibroblasts were stimulated by a fibrin nanocoating to produce collagen ECM fibers.[9] Studies by other authors have also described a stimulatory effect of fibrin on ECM synthesis (mainly collagen I) by fibroblasts.[42,50]

Collagen deposited on the membranes also enhanced adhesion, spreading, and proliferation of the cells, particularly of HaCaT keratinocytes. Collagen is a major component of ECM, and most of the cells bind to its oligopeptide sequence DGEA (Asp-Gly-Glu-Ala), mainly by $\alpha_2\beta_1$ or $\alpha_3\beta_1$ integrin receptors.[51,52] These receptors are also expressed in HaCaT keratinocytes.[53] The HaCaT keratinocytes in our study adhered, spread, and proliferated faster on collagen-coated membranes than on fibrin-coated or uncoated membranes.

After skin injury, keratinocytes physiologically migrate into the wound and interact through their integrin receptors with ECM molecules, mainly with collagen I nanofibers.[11] It seems to be beneficial to modify nanofibrous scaffolds by collagen or directly to fabricate collagen nanofibrous scaffolds.[38,40] The native ECM in the dermis consists of collagen nanofibers less than 100 nm in diameter. However, the diameter of collagen fibers in nanofibrous matrices is usually greater than 100 nm.[39] For this reason, Fu et al developed composite polycaprolactone–collagen nanofibrous matrices coated with a thin layer of collagen gel, forming a secondary ultrafine network of nanofibers (55±26 nm in diameter), in order to simulate natural conditions better. This ultrafine collagen fibrous network significantly increased the adhesion and migration of keratinocytes in comparison with unmodified polycaprolactone–collagen composite fibers, which were 331±112 nm in diameter.[39] Therefore, the improvement in the adhesion and growth of keratinocytes on our
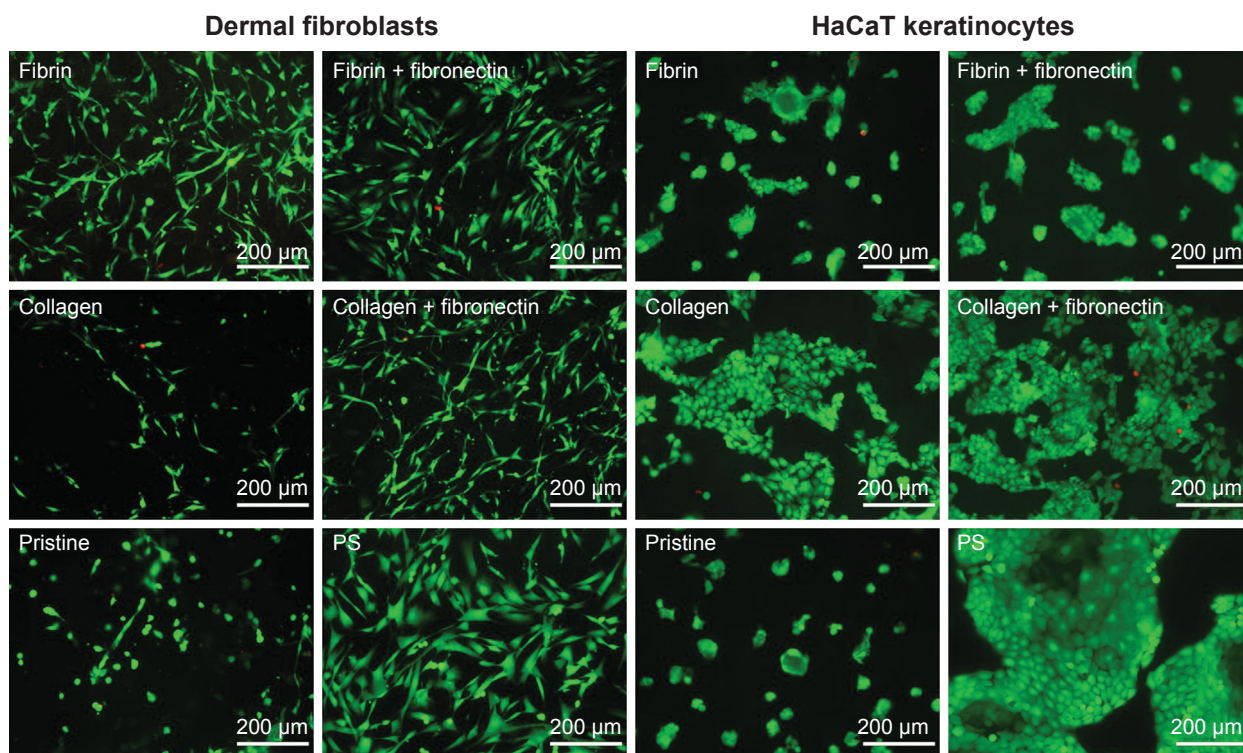
Figure 13 Viability of human dermal fibroblasts and human HaCaT keratinocytes determined by a live/dead kit.
Notes: Day 1 after seeding on poly(lactide-*co*-glycolic acid) (PLGA) membranes coated with fibrin, fibrin + fibronectin, collagen, or collagen + fibronectin, and on uncoated PLGA membranes (pristine). Polystyrene (PS) culture dishes used as reference material. Cells stained with calcein AM (green, live cells) and with ethidium homodimer 1 (red, dead cells). Olympus IX 51 microscope, magnification 10×, DP 70 digital camera.

collagen-modified PLA and PLGA nanofibrous membranes can be explained by the formation of a soft collagen gel on the membrane surface, rather than to the collagen coating of the individual fibers in the membranes.

In contrast to keratinocytes, the adhesion and proliferation of dermal fibroblasts on collagen-coated membranes was usually similar to the adhesion and proliferation on uncoated membranes. Dermal fibroblasts naturally generate contractile forces that affect the surrounding tissue. During wound healing, the fibroblasts produce strong ECM fibers made of collagen and elastin, which resist the traction forces of the cells. Similarly, when cells are seeded on a biomaterial support in vitro, the cells subject this support to traction forces generated by the actin cytoskeleton during cell adhesion, spreading, and migration.[4,54] However, on our membranes, the collagen mostly formed a gel that was probably too soft and was deformed by the traction forces generated by the fibroblasts. In addition, the collagen coating did not improve mechanical properties compared to the fibrin coating, which showed an increase in membrane stiffness. Therefore, the fibrin coating was able to resist contractile forces from fibroblasts better than the collagen gel. The collagen gel was thus probably not able to provide an appropriate substrate

for the attachment and migration of dermal fibroblasts. This was suggested by the fibroblast peeling of the collagen gel observed in our study.

Eastwood et al made a systematic study of the generation of contractile forces by dermal fibroblasts on a collagen gel. They found that most of the forces were induced during attachment and spreading of the cells, and different groups of fibroblasts might vary in their contraction activity.[55] The different behavior of the fibroblasts and the keratinocytes on our collagen-coated membranes was probably due to the different contraction forces generated by these cells on the collagen gel. Agis et al compared fibroblast behavior on a collagen gel and on a collagen porous sponge. They found that the collagen sponge provided better support for cell migration, proliferation, and ECM production than the collagen gel.[56] These results suggest that for the fibroblast component of a skin substitute, it would be better to use nanofibrous scaffolds made of pure collagen, or collagen combined with other degradable materials, as mentioned earlier.[38,40] Mateos-Timoneda et al fabricated polylactide films and fibers covalently bond with collagen. In contrast to our results, they observed significant positive effects on adhesion and proliferation of dermal fibroblasts. The covalently

bond collagen probably was able to better resist contractile forces of fibroblasts, and provide them with a more stable substrate for adhesion.[57]

Fibronectin was deposited on a fibrin or collagen nanocoating in order to enhance the attachment and spreading of the cells. Fibronectin is the main adhesive protein of the ECM and is bound by cell integrin-adhesion receptors through the RGD amino acid sequence (Arg-Gly-Asp).[58] Fibronectin attached to collagen-coated membranes improved the adhesion and spreading of HaCaT keratinocytes. The measured cell cluster area, ie, the size of the keratinocyte islands formed on day 1 after seeding, was larger on fibronectin–collagen-coated membranes than on collagen-only-coated membranes. Moreover, fibronectin attached to a collagen and fibrin nanocoating enhanced the proliferation of dermal fibroblasts. This positive effect was more pronounced on collagen-coated membranes, ie, on a material where the adhesion and growth of fibroblasts were less stimulated than on fibrin. The enhancement of fibroblast proliferation by fibronectin was probably due to better primary attachment of the cells.

The way in which the cells degraded and reorganized the protein nanocoatings differed between fibroblasts and keratinocytes. The fibroblasts slowly and continuously degraded and reorganized all types of protein nanocoatings during cultivation, whereas the effects of HaCaT keratinocytes were different on fibrin-based nanocoatings and on collagen-based nanocoatings. The morphology of the collagen nanocoating was not significantly changed by the keratinocyte behavior. However, the morphology of the thin fibrous mesh of a fibrin nanocoating was strongly altered by keratinocytes already 24 hours after cell seeding. Interestingly, while fibronectin attached to fibrin was significantly degraded by keratinocytes, fibronectin attached to collagen was not significantly degraded. During the attachment, spreading, and migration of keratinocytes, the cells develop traction forces that affect the ECM. The thin fibrous fibrin mesh was probably not able to resist these contractile forces, and was pulled down at an early stage, together with the attached fibronectin. However, the collagen coating probably provided a firmer surface for keratinocyte adhesion and migration. In addition, the collagen gel that formed on the surface of the nanofibrous membranes provided a relatively flat growth support, which may be more convenient for the adhesion of keratinocytes, ie, flat and polygonal epithelial cells. Last but not least, keratinocytes lack $\alpha_v\beta_3$ integrin receptors, which are important for binding to fibrin molecules. They thus did not use the fibrin molecules as a substrate

for their adhesion, migration, or growth, and they tried to reorganize or even remove this coating. From physiological wound healing in vivo, it is known that keratinocytes slough the fibrin eschar from the newly formed epidermis.[46]

On the PLA and PLGA membranes, there was no apparent difference in the morphology of the protein nanocoatings nor in the cell behavior on these coatings. Cell behavior was also similar on both types of nanofibrous membranes. Both PLA and PLGA are degradable polyesters widely used in tissue engineering and in other biotechnologies, eg, for drug delivery. However, certain differences have been reported in the behavior of the two polymers in the biological environment. For example, when prepared in the form of microspheres for drug delivery, PLA has a longer degradation time than PLGA, and the degradation time of PLGA decreases with a decreasing percentage of PLA in this copolymer.[59] Accordingly, the loss of mechanical integrity is faster in PLGA than in PLA.[31] PLA microspheres show a more porous and hydrophobic surface than PLGA, which results in differences in protein adsorption on these polymers, including fibrinogen. PLA adsorbs slightly more fibronectin, but also more albumin, which is nonadhesive for cells.[32] The adhesion and proliferation of porcine chondrocytes is better on PLGA films (ratio 85:15) than on PLA films.[34] Similarly, rat osteoblasts cultured on PLGA films (ratio 75:25) show increased activity of alkaline phosphatase, ie, a marker of osteogenic cell differentiation, than cells on PLA films.[33] In serum free-medium, pristine PLA and PLGA, in forms of both films and fibers, strongly reduce the adhesion of human dermal fibroblasts in comparison with tissue-culture polystyrene, and this adhesion is markedly improved when the polymer materials are covalently bound with collagen I.[57]

Conclusion and future perspectives

The protein nanocoatings developed in our study on nanofibrous PLGA and PLA membranes had a major influence on the behavior of skin cells. The behavior of the cells was different on fibrin than on collagen nanocoating. Fibrin enhanced the adhesion, spreading, proliferation, and fibronectin ECM synthesis of human dermal fibroblasts. In contrast to fibroblasts, HaCaT keratinocytes adhered, spread, and proliferated more quickly on collagen-coated membranes than on fibrin-coated or uncoated membranes. Fibronectin attached to fibrin or to a collagen nanocoating further enhanced cell adhesion and spreading. Moreover, fibronectin increased fibroblast proliferation. No differences were observed in the adhesion or growth of the cells on PLGA and PLA membranes.

Taken together, a degradable nanofibrous membrane with protein nanocoating could be promising for the construction of a bilayered skin substitute. On one side of the membrane, the fibrin-coated nanofibers could support the adhesion, proliferation, and ECM synthesis of fibroblasts. With its collagen nanocoating, the opposite side of the membrane could serve as an appropriate carrier for keratinocytes.

Acknowledgments

Disclosure

The authors report no conflicts of interest in this work.

References

1. Eisenbud D, Huang NF, Luke S, Silberklang M. Skin substitutes and wound healing: current status and challenges. *Wounds*. 2004; 16(1):2–17.
2. McMillan JR, Akiyama M, Tanaka M, et al. Small-diameter porous poly(ε-caprolactone) films enhance adhesion and growth of human cultured epidermal keratinocyte and dermal fibroblast cells. *Tissue Eng*. 2007;13(4):789–798.
3. Sun L, Stout DA, Webster TJ. The nano-effect: improving the long-term prognosis for musculoskeletal implants. *J Long Term Eff Med Implants*. 2012;22(3):195–209.
4. Bacakova L, Filova E, Parizek M, Ruml T, Svorcik V. Modulation of cell adhesion, proliferation and differentiation on materials designed for body implants. *Biotechnol Adv*. 2011;29(6):739–767.
5. Groeber F, Holeiter M, Hampel M, Hinderer S, Schenke-Layland K. Skin tissue engineering: in vivo and in vitro applications. *Adv Drug Deliv Rev*. 2011;63(4–5):352–366.
6. Kai D, Liow SS, Loh XJ. Biodegradable polymers for electrospinning: towards biomedical applications. *Mater Sci Eng C Mater Biol Appl*. 2014;45:659–670.
7. Hoveizi E, Nabiuni M, Parivar K, Rajabi-Zeleti S, Tavakol S. Functionalisation and surface modification of electrospun polylactic acid scaffold for tissue engineering. *Cell Biol Int*. 2014;38(1): 41–49.
8. Bacakova M, Lopot F, Hadraba D, et al. Effects of fiber density and plasma modification of nanofibrous membranes on the adhesion and growth of HaCaT keratinocytes. *J Biomater Appl*. 2015;29(6): 837–853.
9. Bacakova M, Musilkova J, Riedel T, et al. The potential applications of fibrin-coated electrospun polylactide nanofibers in skin tissue engineering. *Int J Nanomedicine*. 2016;11:771–789.
10. Rajangam T, An SS. Fibrinogen and fibrin based micro and nano scaffolds incorporated with drugs, proteins, cells and genes for therapeutic biomedical applications. *Int J Nanomedicine*. 2013;8:3641–3662.
11. O'Toole EA. Extracellular matrix and keratinocyte migration. *Clin Exp Dermatol*. 2001;26(6):525–530.
12. Auxenfans C, Fradette J, Lequeux C, et al. Evolution of three dimensional skin equivalent models reconstructed in vitro by tissue engineering. *Eur J Dermatol*. 2009;19(2):107–113.
13. Nuutila K, Peura M, Suomela S, et al. Recombinant human collagen III gel for transplantation of autologous skin cells in porcine full-thickness wounds. *J Tissue Eng Regen Med*. 2015;9(12):1386–1393.
14. Sarkar SD, Farrugia BL, Dargaville TR, Dhara S. Chitosan-collagen scaffolds with nano/microfibrous architecture for skin tissue engineering. *J Biomed Mater Res A*. 2013;101(12):3482–3492.
15. Peh P, Lim NS, Blocki A, et al. Simultaneous delivery of highly diverse bioactive compounds from blend electrospun fibers for skin wound healing. *Bioconjug Chem*. 2015;26(7):1348–1358.
16. Niiyama H, Kuroyanagi Y. Development of novel wound dressing composed of hyaluronic acid and collagen sponge containing epidermal growth factor and vitamin C derivative. *J Artif Organs*. 2014;17(1): 81–87.
17. Butler CE, Orgill DP. Simultaneous in vivo regeneration of neodermis, epidermis, and basement membrane. *Adv Biochem Eng Biotechnol*. 2005;94:23–41.
18. Wang F, Wang M, She Z, et al. Collagen/chitosan based two-compartment and bi-functional dermal scaffolds for skin regeneration. *Mater Sci Eng C Mater Biol Appl*. 2015;52:155–162.
19. Anish S. Skin substitutes in dermatology. *Indian J Dermatol Venereol Leprol*. 2015;81(2):175–178.
20. Debels H, Hamdi M, Abberton K, Morrison W. Dermal matrices and bioengineered skin substitutes: a critical review of current options. *Plast Reconstr Surg Glob Open*. 2015;3(1):e284.
21. Mutsaers SE, Bishop JE, McGrouther G, Laurent GJ. Mechanisms of tissue repair: from wound healing to fibrosis. *Int J Biochem Cell Biol*. 1997;29(1):5–17.
22. Laurens N, Koolwijk P, de Maat MP. Fibrin structure and wound healing. *J Thromb Haemost*. 2006;4(5):932–939.
23. Gorodetsky R, Clark RA, An J, et al. Fibrin microbeads (FMB) as biodegradable carriers for culturing cells and for accelerating wound healing. *J Invest Dermatol*. 1999;112(6):866–872.
24. Fabris G, Trombelli L, Schincaglia GP, Cavallini R, Calura G, del Senno L. Effects of a fibrin-fibronectin sealing system on proliferation and type I collagen synthesis of human PDL fibroblasts in vitro. *J Clin Periodontol*. 1998;25(1):11–14.
25. Ahmed TA, Dare EV, Hincke M. Fibrin: a versatile scaffold for tissue engineering applications. *Tissue Eng Part B Rev*. 2008;14(2): 199–215.
26. Braziulis E, Biedermann T, Hartmann-Fritsch F, et al. Skingineering I: engineering porcine dermo-epidermal skin analogues for autologous transplantation in a large animal model. *Pediatr Surg Int*. 2011;27(3): 241–247.
27. Mazzone L, Pontiggia L, Reichmann E, Ochsenbein-Kölble N, Moehrlen U, Meuli M. Experimental tissue engineering of fetal skin. *Pediatr Surg Int*. 2014;30(12):1241–1247.
28. Monteiro IP, Gabriel D, Timko BP, et al. A two-component pre-seeded dermal-epidermal scaffold. *Acta Biomater*. 2014;10(12):4928–4938.
29. de la Puente P, Ludena D, Fernandez A, Aranda JL, Varela G, Iglesias J. Autologous fibrin scaffolds cultured dermal fibroblasts and enriched with encapsulated bFGF for tissue engineering. *J Biomed Mater Res A*. 2011;99(4):648–654.
30. Sivan U, Jayakumar K, Krishnan LK. Constitution of fibrin-based niche for in vitro differentiation of adipose-derived mesenchymal stem cells to keratinocytes. *Biores Open Access*. 2014;3(6):339–347.
31. Kranz H, Ubrich N, Maincent P, Bodmeier R. Physicomechanical properties of biodegradable poly(D,L-lactide) and poly(D,L-lactide-co-glycolide) films in the dry and wet states. *J Pharm Sci*. 2000;89(12): 1558–1566.
32. Lück M, Pistel KF, Li YX, Blunk T, Müller RH, Kissel T. Plasma protein adsorption on biodegradable microspheres consisting of poly(D,L-lactide-co-glycolide), poly(L-lactide) or ABA triblock copolymers containing poly(oxyethylene): influence of production method and polymer composition. *J Control Release*. 1998;55(2–3):107–120.
33. Ishaug SL, Yaszemski MJ, Bizios R, Mikos AG. Osteoblast function on synthetic biodegradable polymers. *J Biomed Mater Res*. 1994;28(12): 1445–1453.
34. Tsai WB, Chen CH, Chen JF, Chang KY. The effects of types of degradable polymers on porcine chondrocyte adhesion, proliferation and gene expression. *J Mater Sci Mater Med*. 2006;17(4):337–343.

35. Riedel T, Brynda E, Dyr JE, Houska M. Controlled preparation of thin fibrin films immobilized at solid surfaces. *J Biomed Mater Res A*. 2009;88(2):437–447.

36. Boukamp P, Petrussevska RT, Breitkreutz D, Hornung J, Markham A, Fusenig NE. Normal keratinization in a spontaneously immortalized aneuploid human keratinocyte cell line. *J Cell Biol*. 1988;106(3): 761–771.

37. Hornig-Do HT, von Kleist-Retzow JC, Lanz K, et al. Human epidermal keratinocytes accumulate superoxide due to low activity of Mn-SOD, leading to mitochondrial functional impairment. *J Invest Dermatol*. 2007; 127(5):1084–1093.

38. Rho KS, Jeong L, Lee G, et al. Electrospinning of collagen nanofibers: effects on the behavior of normal human keratinocytes and early-stage wound healing. *Biomaterials*. 2006;27(8):1452–1461.

39. Fu X, Xu M, Liu J, Qi Y, Li S, Wang H. Regulation of migratory activity of human keratinocytes by topography of multiscale collagen-containing nanofibrous matrices. *Biomaterials*. 2014;35(5):1496–1506.

40. Mahjour SB, Fu X, Yang X, Fong J, Sefat F, Wang H. Rapid creation of skin substitutes from human skin cells and biomimetic nanofibers for acute full-thickness wound repair. *Burns*. 2015;41(8):1764–1774.

41. Mazlyzam AL, Aminuddin BS, Fuzina NH, et al. Reconstruction of living bilayer human skin equivalent utilizing human fibrin as a scaffold. *Burns*. 2007;33(3):355–363.

42. Nair RP, Joseph J, Harikrishnan VS, Krishnan VK, Krishnan L. Contribution of fibroblasts to the mechanical stability of in vitro engineered dermal-like tissue through extracellular matrix deposition. *Biores Open Access*. 2014;3(5):217–225.

43. Sese N, Cole M, Tawil B. Proliferation of human keratinocytes and cocultured human keratinocytes and fibroblasts in three-dimensional fibrin constructs. *Tissue Eng Part A*. 2011;17(3–4):429–437.

44. Cox S, Cole M, Tawil B. Behavior of human dermal fibroblasts in three-dimensional fibrin clots: dependence on fibrinogen and thrombin concentration. *Tissue Eng*. 2004;10(5–6):942–954.

45. Gugerell A, Schossleitner K, Wolbank S, et al. High thrombin concentrations in fibrin sealants induce apoptosis in human keratinocytes. *J Biomed Mater Res A*. 2012;100(5):1239–1247.

46. Kubo M, Van de Water L, Plantefaber LC, et al. Fibrinogen and fibrin are anti-adhesive for keratinocytes: a mechanism for fibrin eschar slough during wound repair. *J Invest Dermatol*. 2001;117(6):1369–1381.

47. Weiss E, Yamaguchi Y, Falabella A, Crane S, Tokuda Y, Falanga V. Un-cross-linked fibrin substrates inhibit keratinocyte spreading and replication: correction with fibronectin and factor XIII cross-linking. *J Cell Physiol*. 1998;174(1):58–65.

48. Koivisto L, Larjava K, Häkkinen L, Uitto VJ, Heino J, Larjava H. Different integrins mediate cell spreading, haptotaxis and lateral migration of HaCaT keratinocytes on fibronectin. *Cell Adhes Commun*. 1999; 7(3):245–257.

49. Trombetta-Esilva J, Eadie EP, Zhang Y, Norris RA, Borg TK, Bradshaw AD. The effects of age and the expression of SPARC on extracellular matrix production by cardiac fibroblasts in 3-D cultures. *PLoS One*. 2013;8(11):e79715.

50. Tuan TL, Song A, Chang S, Younai S, Nimni ME. In vitro fibroplasia: matrix contraction, cell growth, and collagen production of fibroblasts cultured in fibrin gels. *Exp Cell Res*. 1996;223(1):127–134.

51. Marchisio PC, Cancedda R, De Luca M. Structural and functional studies of integrin receptors in cultured human keratinocytes. *Cell Differ Dev*. 1990;32(3):355–359.

52. Staatz WD, Fok KF, Zutter MM, Adams SP, Rodriguez BA, Santoro SA. Identification of a tetrapeptide recognition sequence for the $\alpha_2\beta_1$ integrin in collagen. *J Biol Chem*. 1991;266(12):7363–7367.

53. Scharffetter-Kochanek K, Klein CE, Heinen G, et al. Migration of a human keratinocyte cell line (HACAT) to interstitial collagen type I is mediated by the $\alpha_2\beta_1$-integrin receptor. *J Invest Dermatol*. 1992; 98(1):3–11.

54. Engler A, Bacakova L, Newman C, Hategan A, Griffin M, Discher D. Substrate compliance versus ligand density in cell on gel responses. *Biophys J*. 2004;86(1 Pt 1):617–628.

55. Eastwood M, Porter R, Khan U, McGrouther G, Brown R. Quantitative analysis of collagen gel contractile forces generated by dermal fibroblasts and the relationship to cell morphology. *J Cell Physiol*. 1996; 166(1):33–42.

56. Agis H, Collins A, Taut AD, et al. Cell population kinetics of collagen scaffolds in ex vivo oral wound repair. *PLoS One*. 2014;9(11): e112680.

57. Mateos-Timoneda MA, Castano O, Planell JA, Engel E. Effect of structure, topography and chemistry on fibroblast adhesion and morphology. *J Mater Sci Mater Med*. 2014;25(7):1781–1787.

58. Ruoslahti E, Pierschbacher MD. New perspectives in cell adhesion: RGD and integrins. *Science*. 1987;238(4826):491–497.

59. Shive MS, Anderson JM. Biodegradation and biocompatibility of PLA and PLGA microspheres. *Adv Drug Deliv Rev*. 1997;28(1):5–24.

ORIGINAL RESEARCH

Morphology of a fibrin nanocoating influences dermal fibroblast behavior

Julia Pajorova[1]
Marketa Bacakova[1]
Jana Musilkova[1]
Antonin Broz[1]
Daniel Hadraba[1,2]
Frantisek Lopot[2]
Lucie Bacakova[1]

[1]Department of Biomaterials and Tissue Engineering, Institute of Physiology of the Czech Academy of Sciences, Prague, Czech Republic; [2]Department of Anatomy and Biomechanics, Faculty of Physical Education and Sport, Charles University, Prague, Czech Republic

Background: Our study focuses on the fabrication of appropriate scaffolds for skin wound healing. This research brings valuable insights into the molecular mechanisms of adhesion, proliferation, and control of cell behavior through the extracellular matrix represented by synthetic biodegradable nanofibrous membranes coated by biomolecules.

Methods: Nanofibrous polylactic acid (PLA) membranes were prepared by a needle-less electrospinning technology. These membranes were coated with fibrin according to two preparation protocols, and additionally they were coated with fibronectin in order to increase the cell affinity for colonizing the PLA membranes. The adhesion, growth, and extracellular matrix protein production of neonatal human dermal fibroblasts were evaluated on the nanofibrous membranes.

Results: Our results showed that fibrin-coated membranes improved the adhesion and proliferation of human dermal fibroblasts. The morphology of the fibrin nanocoating seems to be crucial for the adhesion of fibroblasts, and consequently for their phenotypic maturation. Fibrin either covered the individual fibers in the membrane (F1 nanocoating), or covered the individual fibers and also formed a fine homogeneous nanofibrous mesh on the surface of the membrane (F2 nanocoating), depending on the mode of fibrin preparation. The fibroblasts on the membranes with the F1 nanocoating remained in their typical spindle-like shape. However, the cells on the F2 nanocoating were spread mostly in a polygon-like shape, and their proliferation was significantly higher. Fibronectin formed an additional mesh attached to the surface of the fibrin mesh, and further enhanced the cell adhesion and growth. The relative gene expression and protein production of collagen I and fibronectin were higher on the F2 nanocoating than on the F1 nanocoating.

Conclusion: A PLA membrane coated with a homogeneous fibrin mesh seems to be promising for the construction of temporary full-thickness skin tissue substitutes.

Keywords: nanofibers, fibrin, nanocoating, dermal fibroblasts, extracellular matrix synthesis, skin substitute, polylactic acid

Introduction

Fibrin is a biomolecule that is physiologically formed after a skin injury. It plays an important role during the healing process of a skin wound. After a tissue injury, the coagulation cascade is activated, and as a result, water-soluble fibrinogen is converted into insoluble fibrin. The fibrin forms a network of fibers that stabilizes the platelet plug by binding platelets to fibrin fibers. The platelets secrete growth factors, mainly platelet-derived growth factor and transforming growth factor beta. These growth factors stimulate the fibroblasts to migrate into the wound, proliferate, and produce extracellular matrix (ECM) proteins, mainly collagen I and fibronectin (Fn). The synthesized extracellular proteins finally replace the fibrin network.[1,2] Through the cell adhesion receptors, the fibrin binds the fibroblasts and the other cell types participating in the

Correspondence: Julia Pajorova
Institute of Physiology, Academy of Sciences of the Czech Republic, Videnska 1083, Prague 4, 14220, Czech Republic
Tel +420 296 443 765
Email julia.pajorova@fgu.cas.cz

wound healing process, such as endothelial cells, smooth muscle cells, leukocytes, fibroblasts, and keratinocytes.[3] The fibrin molecule also binds growth factors and ECM proteins Fn and vitronectin, which are important for cell adhesion.[1]

Fibrin is often applied in regenerative medicine to support wound healing. To accelerate wound healing, fibrin is mostly used in the form of a sealant,[4,5] a gel,[6–8] a glue,[9,10] or microbeads.[11] It is directly applied into the wound and is seeded with skin cells. However, the fibrin is relatively rarely combined with other supporting substrates, although this could improve the stability of various matrices. In our previous studies, we fabricated fibrin-coated polylactic acid (PLA) or polylactide-*co*-glycolide (PLGA) nanofibrous membranes, and we observed a positive influence of fibrin on the behavior of dermal fibroblasts. Moreover, the coated nanofibrous membrane showed good mechanical properties for withstanding the traction forces generated by fibroblasts.[12,13]

In this study, we prepared electrospun PLA membranes with fibrin nanocoatings of various structures. The first nanocoating only coated each individual membrane fiber. The second nanocoating covered the individual fibers, and in addition it formed a fine nanofibrous mesh on top of the membrane and filled the pores between the fibers. In addition, we attached Fn to the fibrin nanocoating to enhance cell adhesion.[13] The purpose of this study was to compare the behavior of human dermal fibroblasts on fibrin-coated membranes depending on the different structure of the fibrin nanocoating. We observed the fibroblast adhesion, spreading, proliferation, and synthesis of ECM proteins – collagen I and Fn. It is known that fibroblasts secrete ECM proteins during wound healing, mainly collagens of type I and type III, the most abundant proteins in skin dermis. The synthesis of extracellular collagen is enhanced by 2-phospho-L-ascorbic acid trisodium salt (AA). AA plays an important role in the formation of stable mature collagen with a triple-helix structure. AA serves as a cofactor for enzymes catalyzing the synthesis of hydroxyproline and hydroxylysine. These amino acids are important for intermolecular crosslinking in the collagen structure.[14,15] In our previous study, we reported that dermal fibroblasts cultivated on fibrin-coated membranes deposited type I extracellular collagen on the surface of the membrane. In addition, fibrin significantly increased the synthesis of extracellular collagen, as determined by an increasing expression of mRNA and an increasing amount of protein deposited on the membrane.[12] In a subsequent study, we observed that fibrin increased the synthesis of another extracellular protein, Fn.[13]

In recent times, nanostructured materials have been applied increasingly in the fabrication of tissue substitutes. In our studies, we also use biodegradable nanofibrous membranes for cell cultivation, because these materials can provide more support for cell adhesion, proliferation, and differentiation than flat and microstructured surfaces.[16] The nanostructure of the materials mimics the nanoarchitecture of the natural ECM, and thus enhances the cell–material interaction. Cell adhesion is mediated through cell integrin receptors, which bind ECM proteins. For successful cell adhesion, the ECM proteins should be adsorbed on the substrate from the body fluid or from the cell culture medium in a sufficient amount, and particularly in an appropriate spatial conformation. The spatial conformation of ECM molecules is important for their interaction with cell adhesion receptors. Nanostructured materials are able to adsorb ECM adhesion-mediating molecules in an appropriate spatial conformation, and thus they enable the cells to attach and spread on the substrate.[16,17]

Materials and methods
Preparation of nanofibrous membranes
Nanofibrous PLA membranes were prepared by the electrospinning process, as was described in our earlier paper.[12] PLA Ingeo™ Biopolymer 4032D (NatureWorks, Minnetonka, MN, USA) was dissolved in chloroform. Dichloroethane and ethyl acetate were added into the PLA solution to a final concentration of 7 wt% of PLA. Tetraethylammonium bromide was added to the PLA solution to make the polymer solution electrically conductive.

A PLA nanofibrous membrane was prepared using Novel Nanospider needle-free electrospinning technology (NS Lab 500, Liberec, Czech Republic). The process was carried out under the following conditions: electrode distance: 180 mm; voltage: 60–10 kV; the spinning electrode rotated at 4 rpm; relative humidity: 25%–30%, and room temperature. The membranes were prepared at a fiber density of 17 g/m², that is, the area weight of the prepared nanofibers.

Preparation of fibrin nanocoatings with attached Fn
The fibrin nanocoatings on the PLA nanofibrous membranes were formed by activation of water-soluble human fibrinogen (341576; EMD Millipore, Billerica, MA, USA) with human thrombin (T6884; Sigma-Aldrich Co, St Louis, MO, USA), in accordance with a previously published work.[18]

Two different types of fibrin nanocoatings were prepared on the membranes. Ten micrograms per milliliter of fibrinogen diluted in Tris buffer (consisting of 50 mM Tris–HCl, 100 nM NaCl, and 2.5 mM CaCl₂) was adsorbed on the membrane for 1 hour. After rinsing with Tris buffer, the adsorbed

fibrinogen was activated with thrombin (2.5 U/mL in Tris buffer) for 15 minutes. These first two preparation steps were the same for both types of fibrin nanocoatings. The subsequent steps differed according to the type of nanocoating. The first type of fibrin nanocoating covered the individual fibers in the membrane (F1 nanocoating). The second type of fibrin nanocoating covered the individual fibers in the membrane and, in addition, it formed a fine homogeneous fibrin mesh on the surface of the membrane and filled the pores between the membrane fibers (F2 nanocoating).

When preparing the F1 nanocoating, the thrombin-activated membranes were incubated in Tris buffer for 30 minutes in order to wash out the unreacted thrombin. Then a solution of 200 µg/mL of fibrinogen in Tris buffer and 0.5 U/mL of anti-thrombin III (Chromogenix, Milano, Italy) in deionized water was added to the membranes for 1 hour to form a stable fibrin nanocoating. The antithrombin III blocked the rest of the unreacted thrombin to prevent the formation of a three-dimensional (3-D) fibrin gel. The F2 nanocoating was prepared directly after thrombin activation, without the incubation step in Tris buffer, that is, without washing out the unreacted thrombin. In this case, the unreacted thrombin reacted with the ambient fibrinogen and a fine nanofibrous fibrin mesh was formed.

To enhance fibroblast adhesion, we attached Fn to the surface of fibrin nanocoating. Human Fn powder (11051407001; Roche, Basel, Switzerland) was dissolved in deionized water at a concentration of 1 mg/mL. The Fn solution with a final concentration of 50 µg/mL in phosphate-buffered saline (PBS; Sigma-Aldrich Co) was added to the samples and was incubated overnight at 4°C. The samples were then rinsed twice with PBS.

Membrane puncture testing

The wet pristine membrane and the membrane with an F1 or F2 nanocoating were tested using the puncture testing protocol, described in detail in our earlier study.[13] Six samples were used for each experimental group. In brief, the samples were placed in a customized holder and were punctured with a spherical cup probe at a constant speed of 0.3 mm/s (stepper motor PD28-3-1021; Trinamic, Hamburg, Germany) while the force was being recorded (1,000 Hz, Force sensor Kistler 9203; Kistler, Winterthur, Switzerland). The structural integrity of the membranes was optically checked at microscale level, using reflectance confocal microscopy (xyt scan, C PLAN magnification 4.0×/0.10 numerical aperture [NA] dry, 256×256 pixels, pixel size 3.6 µm, Leica TCS SPE coupled to Leica DM2500 [Leica Microsystems, Wetzlar, Germany]) and, at macroscale level, by a digital camera (1,504×880 pixels, pixel size 0.015 mm, M5; Integrated Design Tools, Inc., Hitchin, UK).

As the membranes were from a single batch, the evaluation was made using Hooke's law, that is, $F = -kx$, where F is the detected force, x is the membrane extension, and k represents the stiffness of the membrane. In addition, the maximum force F_{max}, the extension at maximum force x_{Fmax}, and the work W that was necessary to completely tear the membrane were also calculated for a statistical comparison (Matlab 2017; Mathworks, Natick, MA, USA).

Cell culture

Before the fibrin nanocoating was prepared and the membranes were seeded with cells, the nanofibrous membranes were fixed in Cell Crown inserts (Scaffdex Ltd, Tampere, Finland) in order to prevent the sample floating in the cell culture medium. The samples were sterilized in 70% ethanol for 30 minutes and were rinsed in sterilized deionized water for 2 days. Then the samples were inserted into the wells of 24-, 12-, or 6-well plates (TPP Techno Plastic Products AG, Trasadingen, Switzerland).

The membranes were seeded with neonatal human dermal fibroblasts, purchased from Lonza (Basel, Switzerland), in passages 2–6, at a density of 10,000 cells/cm². The cells were cultivated in DMEM (Sigma-Aldrich Co) with 10% of fetal bovine serum (FBS; Sebak GmbH, Aidenbach, Germany) and 40 µg/mL of gentamicin (Lek, Ljubljana, Slovenia). The cells were incubated for various time intervals, depending on the given experiment, in a humidified atmosphere with 5% of CO_2 in the air. Polystyrene (PS) culture wells were used as a reference material. On day 1 after cell seeding, the culture medium was supplemented with AA at a concentration of 50 µg/mL in order to stimulate the cells to synthesize extracellular collagen.

Morphology of the fibrin nanocoatings

The morphology of the fibrin F1 and F2 nanocoatings (with or without attached Fn) was studied using fluorescence confocal microscopy. The different fibrin morphology of the F1 and F2 nanocoatings was immunofluorescence stained on freshly prepared cell-free samples and on samples with cells cultivated on membranes for 1, 3, and 7 days. A noncoated membrane was used as a control sample to evaluate possible nonspecific binding of the primary and secondary antibodies.

The membranes were treated with 1% bovine serum albumin in PBS (Sigma-Aldrich Co) for 20 minutes, and then with 1% Tween (Sigma-Aldrich Co) in PBS for 20 minutes at room temperature to block nonspecific binding sites. Then the samples were incubated overnight at 4°C with primary antibody against human fibrinogen (A0080, polyclonal

rabbit antibody; Dako Denmark A/S, Glostrup, Denmark) or with Fn (F0791, mouse monoclonal antibody; Sigma-Aldrich Co), diluted in PBS in a ratio of 1:200. On the next day, the samples were rinsed with PBS and were incubated with secondary antibodies goat anti-rabbit or goat anti-mouse F(ab′)2 fragments of immunoglobulin G (IgG; H+L) conjugated with Alexa Fluor® 488 (A11070 and A11017, Molecular Probes, Thermo Fisher Scientific, Waltham, MA, USA). The incubation time was 1 hour at room temperature in the dark, and the dilution was 1:400 in PBS.

The fibrin-coated membranes with attached Fn were simultaneously stained for fibrin and Fn on the same sample. In this case, the samples were incubated with a primary antibody against fibrinogen overnight at 4°C. On the next day, after the samples had been rinsed with PBS, the primary antibody against Fn was added to the samples for 3 hours. Both primary antibodies were diluted in a ratio of 1:200. Finally, the samples were incubated with secondary antibody goat anti-rabbit F(ab′)2 fragment of IgG (H+L) conjugated with Alexa Fluor 488 and then with secondary antibody goat anti-mouse F(ab′)2 fragment of IgG (H+L) conjugated with Alexa Fluor 633 (A11070 and A21053, Molecular Probes, Thermo Fisher Scientific). The incubation time for both secondary antibodies was 1 hour in the dark, and the dilution was 1:400 in PBS.

The samples were scanned on a Leica TCS SPE DM2500 upright confocal microscope, magnification 40×/1.15 NA oil, and on a Leica TCS SP8, objective HCX PL APO, magnification 40×/1.25–0.75 NA Oil CS. The signal intensity profiles of the immunofluorescence-stained fibrin nanocoating with attached Fn were plotted using data obtained by the "Plot Z-axis Profile" function in Fiji (ImageJ) open-source image analysis software.[19] This software function plots the average image plane intensity in a given color channel versus the z-axis (depth) of a confocal z-stack image.

Cell spreading

The spreading and the shape of the cells were evaluated by staining the cell F-actin cytoskeleton and the cell nuclei. The F-actin was stained with phalloidin conjugated with tetramethylrhodamine fluorescent dye (Sigma-Aldrich Co), and the cell nuclei were stained with Hoechst #33258 (Sigma-Aldrich Co) for 1 hour at room temperature in the dark. Both dyes were diluted in PBS to concentration 5 µg/mL. Before the cells were stained with fluorescent dyes, they were rinsed in PBS and were fixed with −20°C cold ethanol for 10 minutes. The images were taken using a Leica TCS SPE DM2500 upright confocal microscope using magnification 40×/1.15 NA oil.

Cell mitochondrial activity

The activity of cell mitochondrial enzymes was measured on days 1, 3, and 7 after cell seeding as a marker of cell proliferation and viability. The metabolic activity was determined by a CellTiter 96® AQueous One Solution Cell Proliferation Assay (MTS; Promega Corporation, Madison, WI, USA). The membrane samples were moved into fresh cell culture wells to avoid the influence of cells adhered to the bottom of the well. The assay was performed according the manufacturer's protocol. The formazan dye produced by the cells after 3 hours of incubation was quantified by measuring the absorbance using a VersaMax ELISA Microplate Reader spectrophotometer (Molecular Devices Corporation, Sunnyvale, CA, USA). The absorbance was measured with wavelength 490 nm and with reference wavelength 650 nm. Three independent samples were used for each experimental group and time interval. The experiment was performed three times.

Immunofluorescence staining of extracellular collagen I and Fn

The extracellular collagen I and Fn deposited by the cells on the surface of the membrane were immunofluorescently stained on days 4, 7, and 14 after cell seeding. The samples were rinsed with 5% FBS in PBS. The membranes were then incubated in primary antibodies against collagen I (C2456, mouse monoclonal antibody; Sigma-Aldrich Co) or Fn (F0791, mouse monoclonal antibody; Sigma-Aldrich Co) diluted in PBS in a ratio of 1:200 for 30 minutes in ice. After the cells were rinsed with 5% FBS in PBS, they were fixed for 20 minutes with 2% paraformaldehyde dissolved in PBS with 5% of FBS. The samples were rinsed with PBS and were incubated in 1% FBS in PBS to block nonspecific binding sites for 20 minutes. The solution of secondary antibody anti-mouse F(ab′)2 fragments of IgG (H+L) conjugated with Alexa Fluor 488 (Molecular Probes, Thermo Fisher Scientific) was diluted 1:400 in 1% FBS in PBS. This solution was added to the sample for 2 hours in the dark. After being rinsed with PBS, the cell nuclei were stained with Hoechst #33342, which penetrates through the nonpermeabilized cell membrane. Images were taken using a Leica TCS SPE DM2500 upright confocal microscope, magnification 40×/1.15 NA oil.

Real-time polymerase chain reaction (PCR)

Real-time PCR was performed to investigate the relative mRNA expression of ECM proteins, collagen I and Fn, in the dermal fibroblasts. The cells were harvested on days 4 and 7 of cultivation on the modified PLA membrane. The total RNA was isolated using the Total RNA Purification

Micro Kit (35300; Norgen Biotek, Thorold, ON, Canada), according to the manufacturer's protocol. The cells were rinsed with PBS and the membrane was placed into a 1.5 mL tube filled with RNA lysis solution enriched with mercaptoethanol (1%).

Reverse transcription was performed using the Omniscript Reverse Transcription Kit (205113; Qiagen, Hilden, Germany) and random hexamers (New England Biolabs, Inc, Ipswich, MA, USA) and was carried out according to the manufacturer's protocol.

The mRNA level was quantified using 5×HOT FIRE-Pol Probe qPCR Mix Plus (ROX) (08-36-00001; Solis BioDyne, Tartu, Estonia) and by TaqMan Gene Expression Assays (4331182; Thermo Fisher Scientific), labeled with FAM reporter dye specific to human collagen I COL1A1 (Hs00164004_m1) or specific to human Fn FN1 (Hs01549976_m1) as a target gene, and beta (β)-actin ACTB (Hs01060665_g1) as a reference gene. The experiments were performed in duplicate. The final reaction volume was 20 μL of solution. The mRNA expression level was determined using the Viia™ 7 Real-time PCR System (Applied Biosystems™; Thermo Fisher Scientific) in a 96-well optical reaction plate. The amplification conditions consisted of uracil-DNA glycosylase incubation at 50°C for 2 minutes and initial DNA polymerase enzyme activation at 95°C for 10 minutes, followed by 40 cycles of denaturation at 95°C for 15 seconds and annealing/extension at 60°C for 1 minute.

Two independent samples were used for each experimental group and time interval. The experiment was performed five times. Expression values were obtained from Ct numbers. The relative gene expression was calculated as $2^{-\Delta Ct}$.

Statistics

The data were presented as mean ± either standard deviation or standard error of the mean. Statistical significance was evaluated using analysis of variance with the Tukey post hoc test for pairwise comparison. Values of $p \leq 0.05$ were considered as significant.

Results

The morphology and the mechanical properties of two different types of fibrin nanocoatings on a PLA membrane

The fibers of the PLA membrane were randomly oriented and mostly straight. The diameter of the fibers ranged from tens of nanometer to >1 μm. The average fiber diameter was >300 nm, as we had measured in our earlier studies.[12,13]

In accordance with the protocol for fibrin preparation, fibrin either covered only individual fibers in the PLA membrane (Figure 1, F1) or covered individual fibers and in addition formed a fine homogeneous nanofibrous mesh on the surface of the membrane (Figure 1, F2). In our previous study, fibrin did not form a homogeneous mesh on the whole surface of the membrane.[12] Fn (Figure 2, red) was adsorbed especially on top of the fibrin mesh (Figure 2, green) and formed an additional nanofibrous mesh (Figure 1, F2+Fn). Fn was also adsorbed on the fibrin of the F1 nanocoating (Figure 1, F1+Fn); however, it was hardly detectable by immunofluorescence microscopy. The stability of the fibrin nanocoatings on the PLA membrane was proved in our previous study.[12] The morphology of the fibrin nanocoating without seeded cells remained almost unchanged after 7 days in the cell cultivation conditions, while it was progressively degraded on the membranes with cells.

Furthermore, the way in which the fibrin nanocoating had been prepared had a minor effect on the mechanical properties of the PLA membrane. Mechanical puncture testing returned very similar results for all three groups (Table 1). The null hypothesis was rejected only for x_{Fmax}, as this parameter decreased significantly for the F1 nanocoating compared to pristine (p-value=0.025). By contrast, the other parameters did not differ (p-value for k=0.599, F_{max}=0.376 and W=0.417); however, there was an evident trend toward increasing resistance against mechanical loading for the F2 nanocoating.

Cell adhesion, spreading, and metabolic activity

The washout step of the remaining unreacted thrombin during the preparation of the fibrin nanocoatings was determined as the crucial point for the formation of a nanofibrous homogeneous mesh on the surface of the membrane (F2 nanocoating), and also for the fibrin nanocoating covering individual fibers of the membrane (F1 nanocoating). Different behavior of human dermal fibroblasts was observed on these two different types of fibrin nanocoating. The number of adhered fibroblasts on the F1 nanocoating was lower, and the cells remained in their typical spindle-like shape (Figure 1, F1). However, the number of adhered fibroblasts on the F2 nanocoating was higher, and the cells tended to adopt a polygon-like shape (Figure 1, F2). As was mentioned above, Fn formed a secondary nanofibrous mesh (Figure 2, red) on the surface of the initially developed fibrin mesh (Figure 2, green) and enhanced the cell adhesion on both types of fibrin nanocoating (Figure 1, F1/F2+Fn). It was observed that fibroblasts (Figure 2, blue and magenta) adhered preferentially on top of Fn mesh (Figure 2, red). Moreover, the shape of the
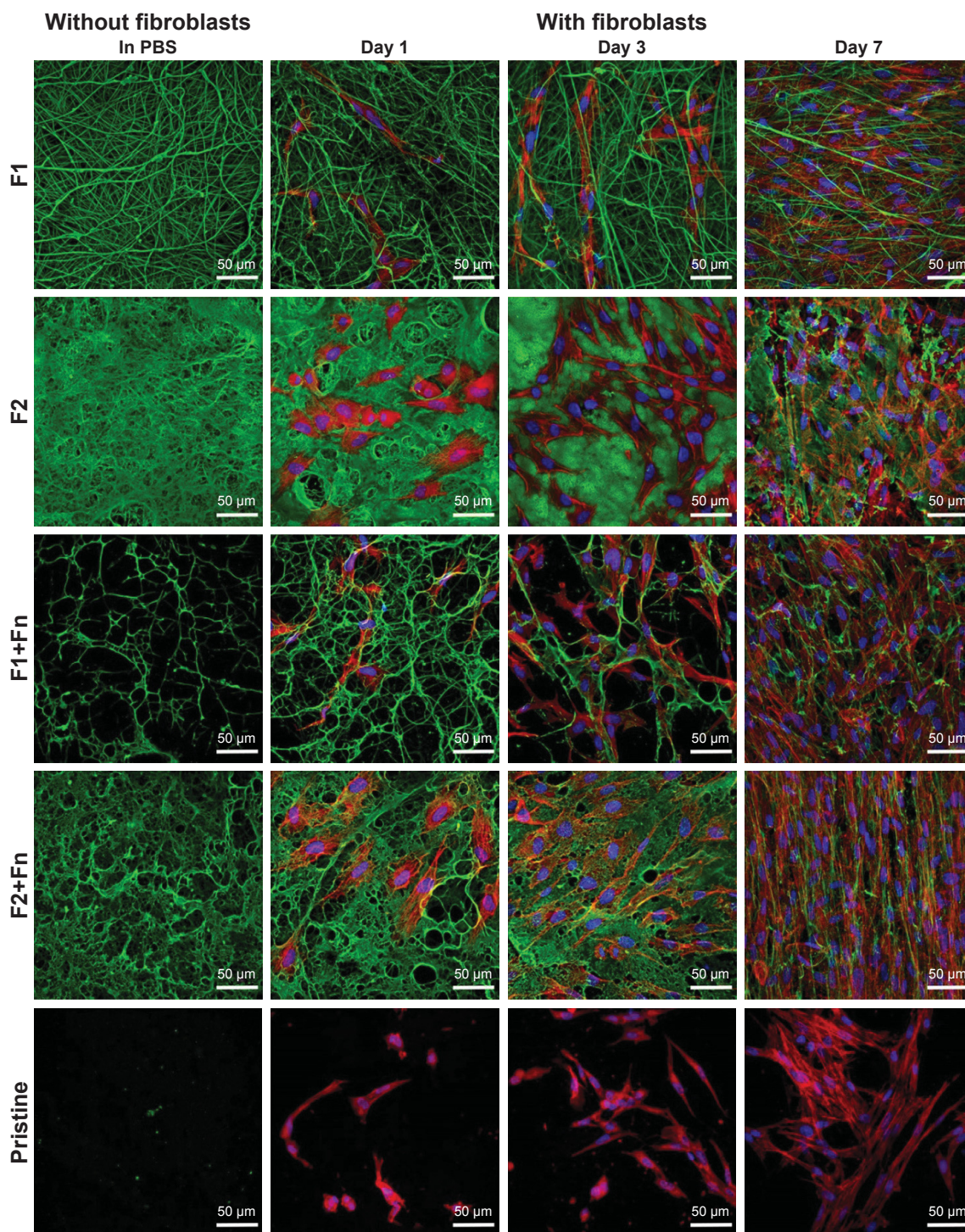
Figure 1 Immunofluorescence staining of two different types of fibrin nanocoatings on polylactic acid membrane (column 1, in PBS) and the shape of human dermal fibroblasts on the fibrin nanocoatings (columns 2–4) on days 1, 3, and 7 after cell seeding. The membrane with the fibrin nanocoating covering only individual fibers (F1), with fibrin covering individual fibers and forming a mesh on the surface of the membrane (F2), and Fn adsorbed on fibrin (+Fn). A noncoated membrane (pristine) was used as a control sample. Fibrin and Fn nanocoatings were stained with primary and secondary antibodies (Alexa 488 – green). The cells were stained with phalloidin–tetramethylrhodamine (actin cytoskeleton – red) and with Hoechst #33258 (cell nuclei – blue). Leica TCS SPE DM2500 confocal microscope, magnification 40×/1.15 numerical aperture oil.
Abbreviation: Fn, fibronectin.

adhered fibroblasts mimicked well the morphology of the Fn mesh (Figure 2B and Figure 1, F2+Fn).

The enhancing effect of the fibrin mesh (F2) and of the Fn mesh (F2+Fn) on cell growth was evident mainly in the later cell cultivation intervals (Figure 1). On day 3 after cell seeding, several cell mitoses were observed on membranes with F2 and F2+Fn nanocoatings, but the cells remained mostly in their polygon-like shape (Figure 1). On membranes

Table 1 Mechanical puncture testing of wet membranes

		Pristine	F1	F2
k	N/mm	0.494±0.17	0.486±0.11	0.598±0.28
x_{Fmax}	mm	3.344±0.10*	3.042±0.23*	3.282±0.12
F_{max}	N	1.234±0.42	1.116±0.18	1.554±0.79
W	J	4.609±1.69	3.558±0.56	4.883±2.50

Notes: The values are stated as mean ± SD. k represents the stiffness of the membrane, F_{max} is the detected maximum force, x_{Fmax} is the membrane extension at the maximum force, and W is the work necessary to completely tear the membrane. F1 – the membrane with fibrin covering only individual fibers. F2 – the membrane with fibrin covering individual fibers and forming a mesh on the surface of the membrane. A pristine noncoated membrane was used as a control material. Each group contained six independent samples and p-value returned by one-way analysis-of-variance test for k=0.025, x_{Fmax}=0.599, F_{max}=0.376, and W=0.417. *A significant difference was found between the pristine and F1 groups by the post hoc Tukey's honest significant difference test.

with F1 and F1+Fn nanocoatings, the cells proliferated less, but their spindle-like shape enabled them to migrate into the fibrin-coated PLA membrane (Figure 1). On day 7 after cell seeding, the fine fibrin (F2) and Fn meshes (F2+Fn) were almost degraded, and the fibroblasts penetrated into the deeper layers of the PLA membrane. After 1 week, the Fn mesh on the membranes with F1+Fn and F2+Fn nanocoatings was completely replaced by the extracellular Fn produced by the fibroblasts (Figure 1). On the noncoated membranes, which were used as a control material, the fibroblasts were mostly round and were not strongly adhered, in all three cultivation intervals (Figure 1, pristine).

The cell mitochondrial activity (measured by an MTS assay) was used as an indirect method for estimating the cell proliferation. The metabolic activity of human dermal fibroblasts was measured on days 1, 3, and 7 after cell seeding (Figure 3). In all intervals, it was detected that the fibroblast mitochondrial activity was significantly higher on the fibrin-coated membranes than on the pristine (noncoated) membranes, which is in accordance with our previous works.[12,13] The most apparent differences between the
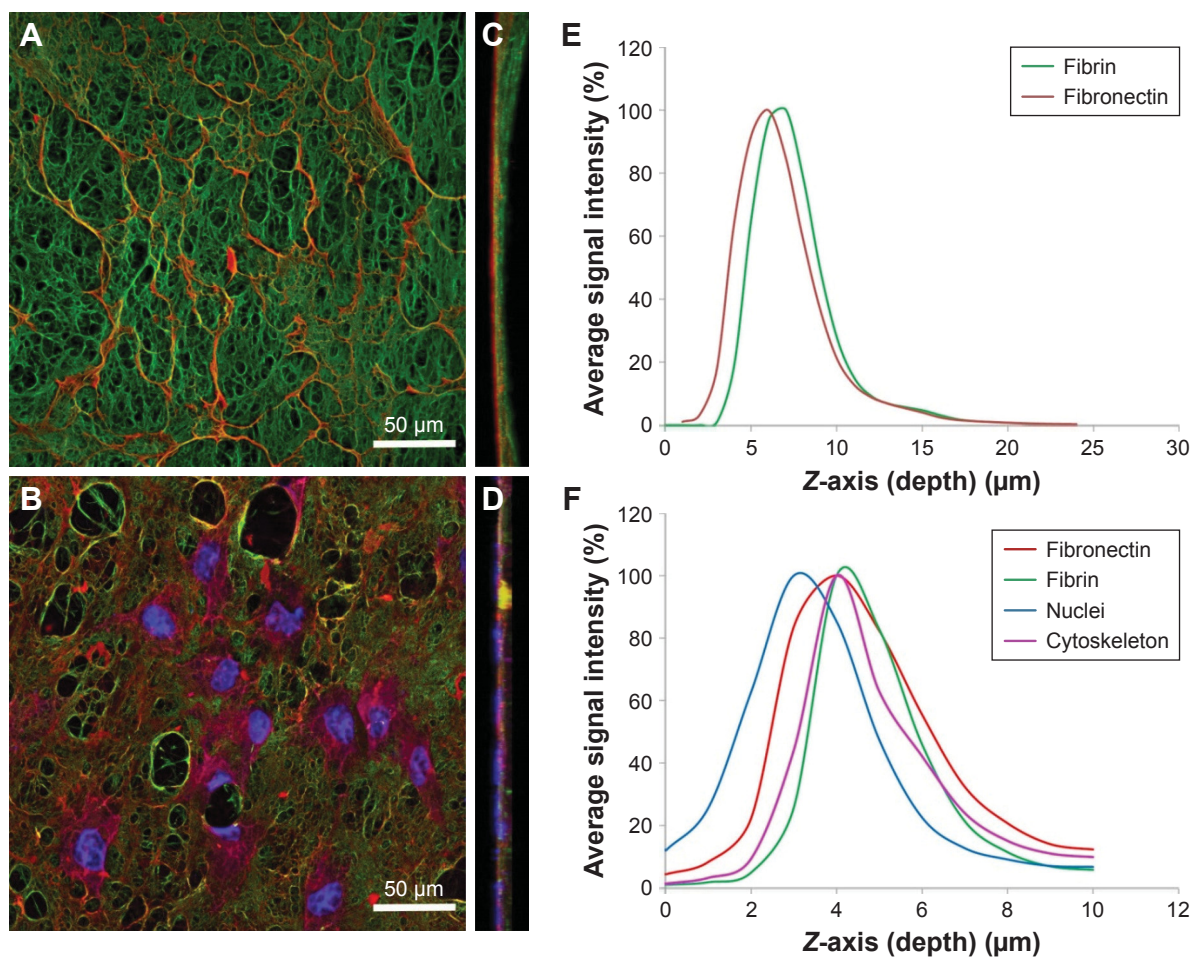

Figure 2 The signal intensity profiles of immunofluorescence stained fibrin mesh (F2 nanocoating) with attached fibronectin, without (**A**) or with (**B**) human dermal fibroblasts on day 1 after cell seeding. Fibrin and fibronectin were stained with primary and secondary antibodies (fibrin – Alexa 488 – green and fibronectin – Alexa 633 – red). The cells were stained with phalloidin–tetramethylrhodamine (actin cytoskeleton – magenta) and with Hoechst #33258 (cell nuclei – blue). Maximum intensity projection – front view (**A**, **B**) and side view (**C**, **D**). The function plots (**E**, **F**) represent the average image plane intensity in a given color channel versus the z-axis (depth) of a confocal z-stack image. Leica TCS SPE DM2500 confocal microscope, magnification 40×/1.15 NA oil, and Leica TCS SP8, objective HCX PL APO, magnification 40×/1.25–0.75 NA Oil CS.
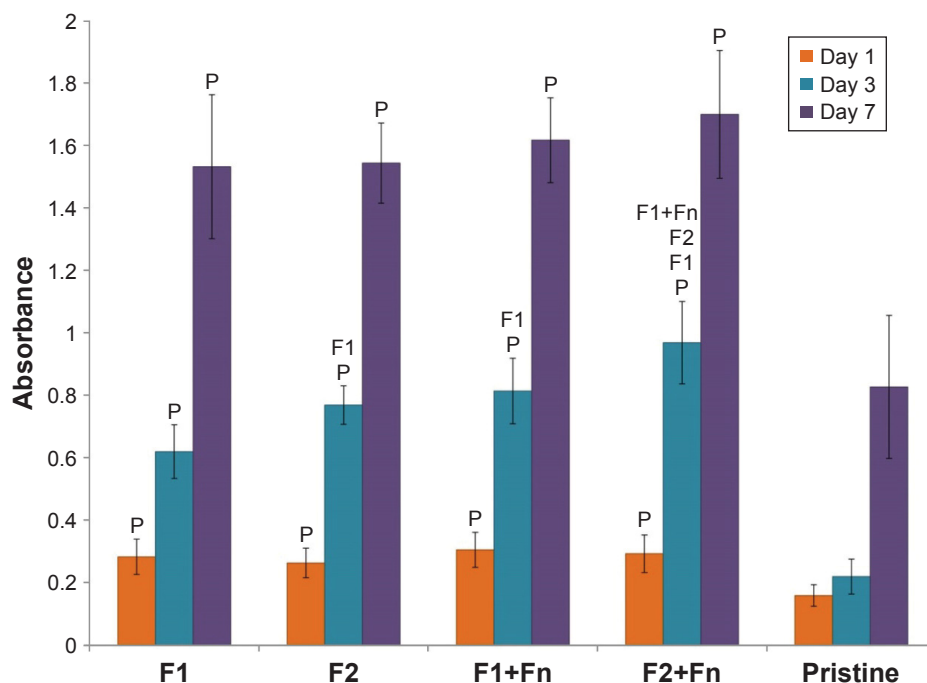**Abbreviation:** NA, numerical aperture.

Figure 3 Mitochondrial activity of human dermal fibroblasts measured by MTS assay on days 1, 3, and 7 after cell seeding on a polylactic acid membrane. The membrane with fibrin covering only individual fibers (F1), with fibrin covering individual fibers and forming a mesh on the surface of the membrane (F2), and Fn adsorbed on fibrin (+Fn). A noncoated membrane (pristine) was used as a control sample. Arithmetic mean ± SD from nine measurements made on three independent samples for each experimental group and time interval. The experiment was performed three times. Statistical significance ($p \leq 0.05$) evaluated using analysis of variance with Tukey's method is displayed above each experimental group, indicated by the abbreviation of the group or by P representing pristine.
Abbreviation: Fn, fibronectin.

types of fibrin nanocoatings of the cells were observed on day 3 after cell seeding. The cell mitochondrial activity was significantly higher on samples with a fibrin mesh (F2 and F2+Fn) than on samples with F1 and F1+Fn nanocoatings (Figure 3). Fn attached to the fibrin significantly increased the cell mitochondrial activity (Figure 3, F1+Fn, F2+Fn). The significantly highest fibroblast mitochondrial activity was measured on the F2 nanocoating with an Fn mesh (Figure 3, F2+Fn). On days 1 and 7 after cell seeding, the cell mitochondrial activity was almost the same on all types of fibrin nanocoatings (Figure 3).

ECM synthesis by human dermal fibroblasts

The results of the relative mRNA expression from real-time PCR showed that the structure and the morphology of the fibrin nanocoatings also had a crucial impact on the expression of ECM proteins in the cells growing on these nanocoatings. The mRNA expression was measured in two cell culture intervals (on days 4 and 7 after cell seeding). On the basis of the previous studies, AA was added to the cell culture medium in order to enhance the expression and the formation of collagen I fibers.[12] The mRNA expression of collagen I and Fn was significantly higher on F2 nanocoatings

than on F1 nanocoatings (Figure 4A and B). Fn attached to the fibrin mesh (F2+Fn) did not significantly influence the ECM expression (Figure 4A and B). However, Fn attached to F1 nanocoatings (F1+Fn) significantly increased the collagen I mRNA expression in both intervals (Figure 4A). On day 7, the collagen I expression on F1 nanocoatings with Fn (F1+Fn) was almost the same as the expression on the F2 nanocoatings (F2 and F2+Fn; Figure 4A). However, these differences were not observed in the expression of Fn mRNA (Figure 4B). The relative expression of collagen I was significantly higher on both types of fibrin nanocoatings than on the noncoated (pristine) PLA membranes (Figure 4A). The relative expression of Fn in the cells on F1 nanocoatings (F1 and F1+Fn) was almost the same as the relative expression on the pristine membranes. This pattern was observed in both cell culture intervals (Figure 4B).

All these results correlate with the immunofluorescence microscopy images in which the formation of collagen I and Fn fibers was visualized (Figures 5 and 6). Higher production of extracellular collagen I and Fn fibers was detected on PLA membranes with an F2 nanocoating than with an F1 nanocoating (Figures 5 and 6), which is in accordance with the measurements of relative mRNA expressions (Figure 4).
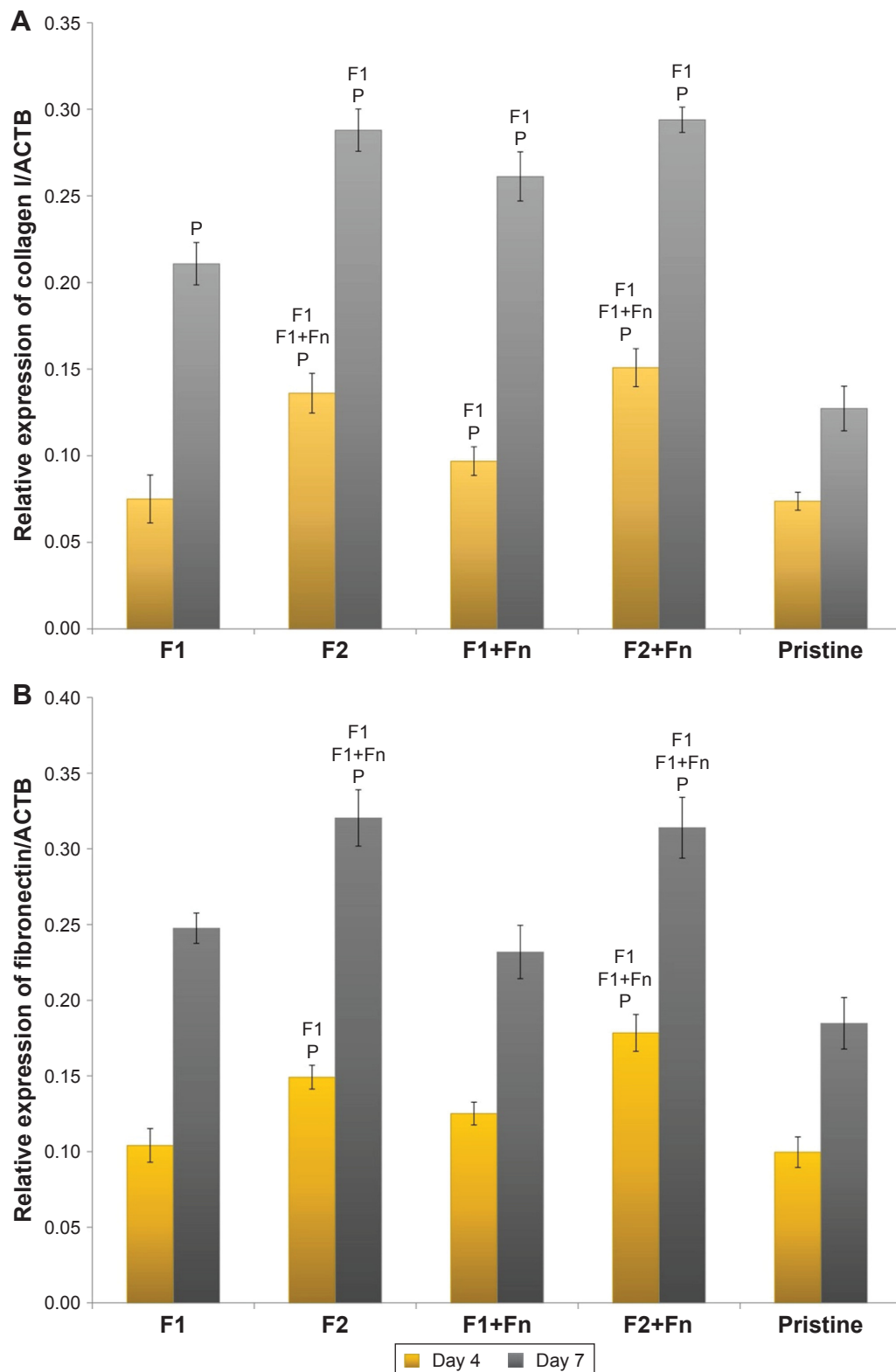
Figure 4 Relative expression of collagen I (**A**) and Fn (**B**) measured by real-time polymerase chain reaction in human dermal fibroblasts on days 4 and 7 after cell seeding on polylactic acid membranes with a fibrin structure. The membrane with fibrin covering individual fibers (F1), with fibrin covering individual fibers and forming a mesh on the membrane surface (F2), and Fn adsorbed on fibrin (+Fn). A noncoated membrane (pristine) was used as a control sample. ACTB was used as a reference gene. The arithmetic mean ± SD was calculated for each experimental group and time interval from 10 measurements made in five independent experiments. Statistical significance ($p \leq 0.05$) evaluated using analysis of variance with Tukey's method is displayed above each experimental group, indicated by the abbreviation of the group or by P representing pristine.
Abbreviation: Fn, fibronectin.
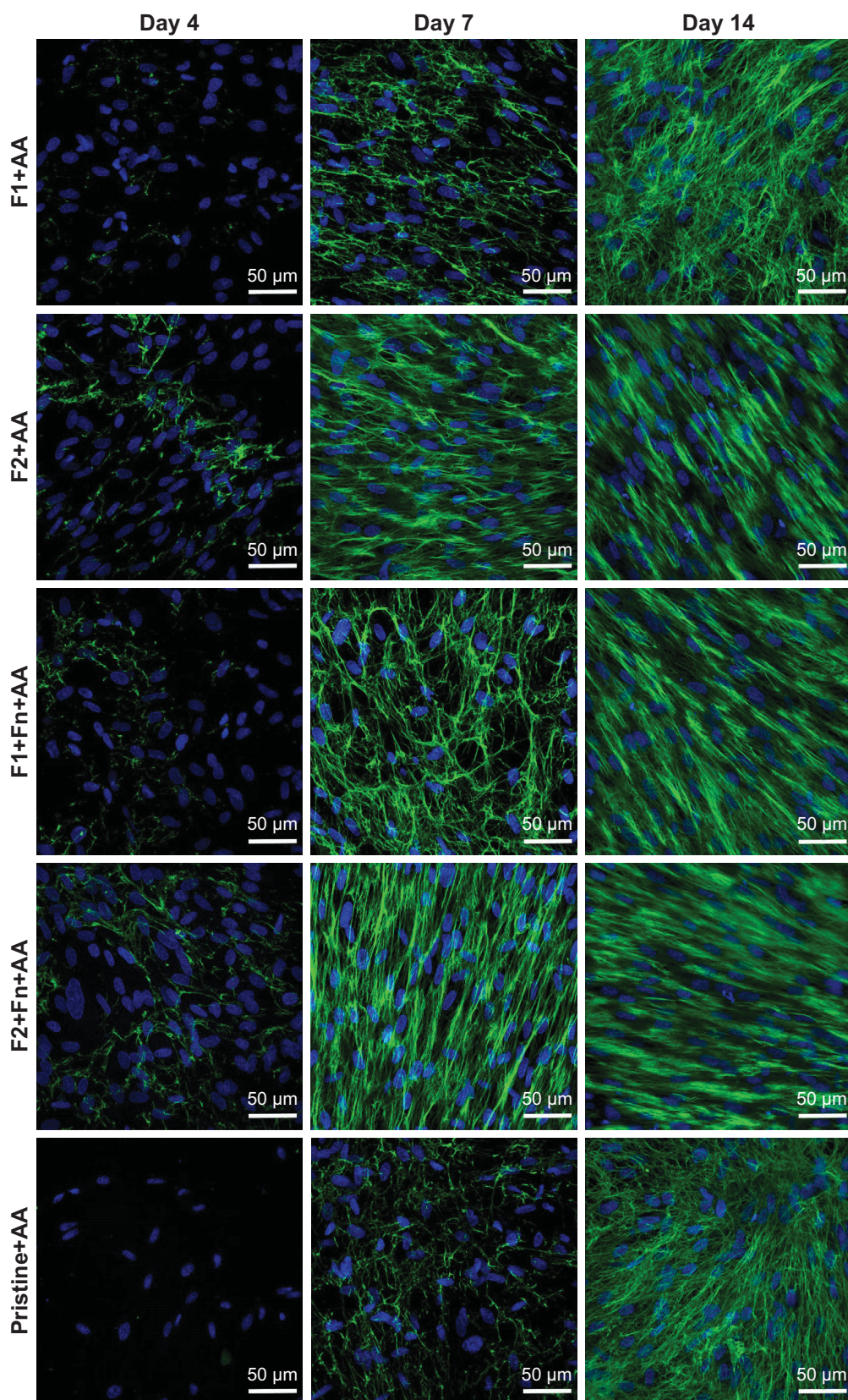
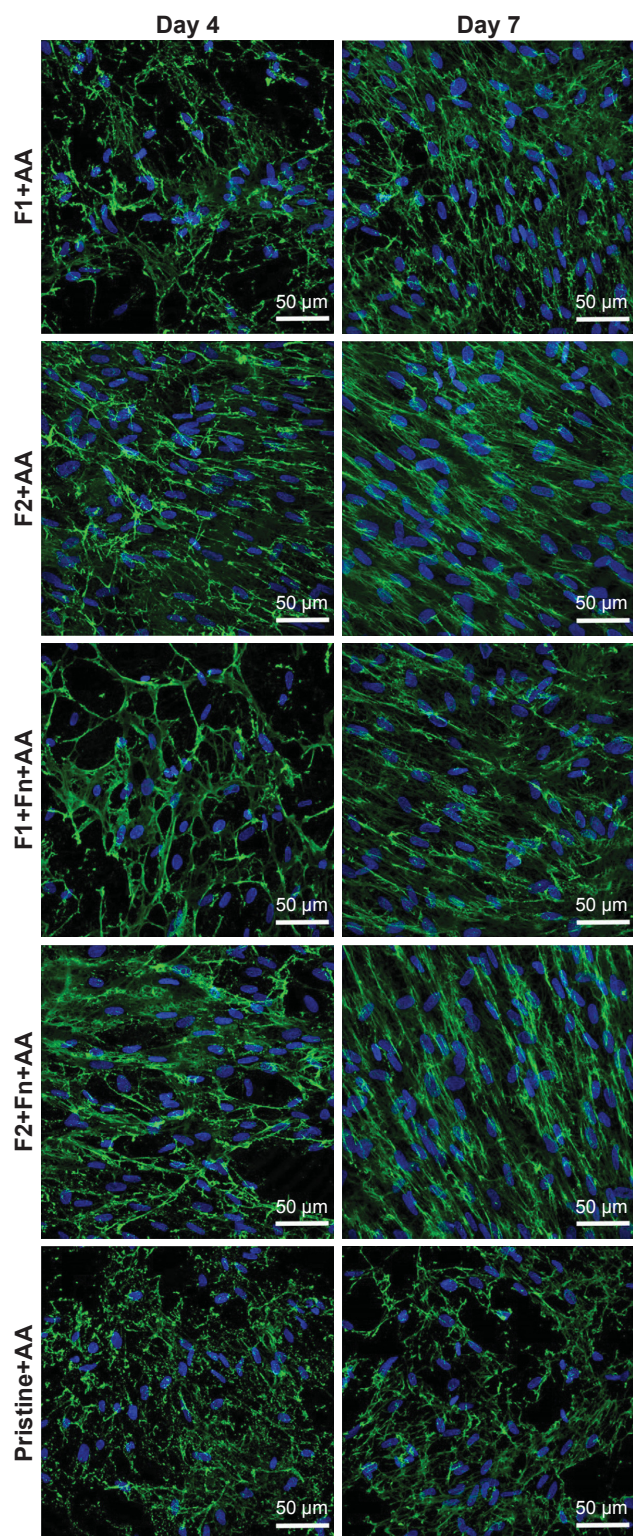**Figure 5** Immunofluorescence staining of extracellular collagen I fibers (green) produced by human dermal fibroblasts on polylactic acid membranes with two different types of fibrin nanocoatings on days 7, 10, and 14 after seeding. The membrane with fibrin covering individual fibers (F1), with fibrin covering individual fibers and forming a mesh on the membrane surface (F2), and Fn adsorbed on fibrin (+Fn). A noncoated membrane (pristine) was used as a control sample. The cells were cultivated in the standard cell culture medium with AA. Cell nuclei stained with Hoechst #33342 (blue). Leica TCS SPE DM2500 confocal microscope, magnification 40×/1.15 numerical aperture oil.

Abbreviations: AA, 2-phospho-L-ascorbic acid trisodium salt; Fn, fibronectin.

Figure 6 Immunofluorescence staining of extracellular Fn fibers (green) produced by human dermal fibroblasts on polylactic acid membranes with two different types of fibrin nanocoatings on days 4 and 7 after seeding. The membrane with fibrin covering individual fibers (F1), with fibrin covering individual fibers and forming a mesh on the membrane surface (F2), and Fn adsorbed on fibrin (+Fn). A noncoated membrane (pristine) was used as a control sample. The cells were cultivated in the standard cell culture medium with AA. Cell nuclei stained with Hoechst #33342 (blue). Leica TCS SPE DM2500 confocal microscope, magnification 40×/1.15 NA oil.
Abbreviations: AA, 2-phospho-L-ascorbic acid trisodium salt; Fn, fibronectin; NA, numerical aperture.

Discussion

The chemical and physical properties of the substrate for cell seeding are crucial for successful cell adhesion and growth. Many recent studies have discussed the influence of substrate properties (ie, surface wettability, electrical charge and conductivity, surface roughness and topography, substrate rigidity, and deformability) on the cell behavior and the colonization of a material with cells.[16,20] Successful colonization of materials with desirable cell behavior, that is, cell adhesion, proliferation, migration, differentiation, and production of specific markers by cells as in a natural environment, is critical for the development of tissue substitutes. Skin substitutes are mostly fabricated from substrates based on natural biopolymers occurring in skin (mainly collagen) or during wound healing (fibrin).[21] These proteins are favorable for cells because they support a desirable cell behavior.[2] However, a protein scaffold in the form of a gel, a glue, or a sealant is mostly fragile, highly elastic, and deformable. These matrices are not stable, and they degrade quickly. Moreover, these material properties may lead to a collapse of the substrate under the traction forces of the adhering cells.[22] Therefore, sufficient stability of the matrices could be achieved by depositing the biomolecules on an appropriate stronger carrier, for example, made of biodegradable polyesters such as PLA. This combined scaffold can provide stable mechanical support with appropriate properties for cell adhesion and growth. In our studies, we focus on the fabrication of PLA nanofibrous membranes coated with fibrin.

In this study, we prepared fibrin nanocoatings with different structures. The first nanocoating (F1) only covered the individual fibers in the membrane. The second nanocoating (F2) covered the individual fibers and, in addition, it formed a fine homogeneous nanofibrous mesh on surface of the membrane and filled the pores between the fibers. The different morphology and structure of F1 and F2 nanocoatings can be explained by the different mode of preparation for the two types of nanocoating. While the preparation of the F1 nanocoating included washing out the unbound thrombin with Tris buffer, the F2 nanocoating was prepared without washing out the thrombin. To the best of our knowledge, this phenomenon has not previously been described. These different modes of preparation probably controlled the amount of adsorbed thrombin on the membrane and the amount of subsequently bound fibrinogen to the active thrombin sites. In other words, the concentration of thrombin and fibrinogen adsorbed on the membrane could influence the formation of the fibrin coating. Previously published studies have revealed that the concentration of thrombin and fibrinogen had an

impact on the formation of the fibrin network. A higher concentration of thrombin (above 1 U/mL) induced the formation of thin fibrin fibers, while a lower concentration of thrombin (under 0.001 U/mL) induced the formation of thick fibrin fibers.[23,24] In our study, we used a highly concentrated thrombin (2.5 U/mL) solution, and we observed the formation of thin fibrin fibers, mainly in the case of the fibrin mesh (F2 nanocoating). The concentration of fibrinogen in solution during the adsorption influences the density, the orientation, and the accessibility of the individual fibrinogen domains of the surface-bound fibrinogen. At low fibrinogen surface density (under 20 µg/mL), the majority of the molecules appear to be adsorbed side-on (lying on the surface). At high fibrinogen density (above 100 µg/mL), the molecules are adsorbed end-on (standing on the surface). The experimental data suggest that the distal ends of the (adsorbed) fibrinogen molecules (containing polymerization sites) are oriented anti-parallel to each other, proving an off-axis location of the distal-end domains.[25] Fibrinogen adsorbed from the initial lowly concentrated solution promoted the formation of a surface-attached fibrin network better than fibrinogen adsorbed from the highly concentrated solution. In our study, we prepared stable fibrin by initial adsorption of fibrinogen from a lowly concentrated solution (10 µg/mL), and then by incubation of the thrombin-activated surface with a highly concentrated fibrinogen solution (200 µg/mL). Riedel et al had previously shown that combining a lowly concentrated fibrinogen solution in the first step and a highly concentrated fibrinogen solution in the second step led to the formation of a well-developed fibrin network. The fibrin network grows on the surface because of the catalytic action of the surface-bound thrombin on the ambient fibrinogen solution.[18] In the case of the F2 nanocoating, due to the thrombin non-washing-out step, the concentration of thrombin adsorbed on the membrane was probably higher than in the case of the F1 nanocoating. This high concentration of thrombin may have enabled fibrinogen to bind in a greater amount in the second preparation step, leading to the formation of a fibrin mesh on the membrane. Moreover, Albala reported that fibrin sealants with high concentrations of fibrinogen tend to produce stronger clots.[4] As was revealed by the membrane puncture testing performed in our study, the F2 nanocoating improves the mechanical properties of PLA membranes only slightly, while there was also quite high variability within the treated group. There was even less membrane extension with the F1 coating at maximum force, than with the pure PLA membrane (Table 1). In general, scaffolds fabricated from fibrin are usually mechanically weak, not self-supporting,

and require reinforcement with mechanically more resistant natural or synthetic polymers, for example, hyaluronic acid,[26] polyvinyl alcohol,[27] or PLA.[28]

In this study, we have proved that fibrin deposited on PLA membranes strongly improves the cell adhesion, proliferation, and synthesis of ECM proteins (collagen I and Fn). This confirms the results from our previous works.[12,13] As we have discussed, fibrin enabled cell adhesion by binding a specific fibrin molecule site by an adhesion receptor, mainly integrins of group β_1. Fibrin also further enhanced cell adhesion by attaching other cell adhesion-mediating proteins (eg, Fn, vitronectin, or collagen) from the serum supplement of the cell culture medium.[1,12]

This study has revealed the different behavior of dermal fibroblasts depending on the differences in the morphology of the fibrin nanocoating covering the membrane. The results showed that the F2 nanocoating (fibrin mesh) provided better support than the F1 nanocoating for the adhesion and proliferation of dermal fibroblasts. In addition, the shape of the adhered cells differed with the type of fibrin nanocoating. While the cells on the F1 nanocoating remained in a spindle-like shape, a polygon-like shape was typical for the cells cultivated on the F2 nanocoating. The spindle-like shape of fibroblasts seems to be more physiologic in the 3-D environment of natural skin dermis.[29] However, a 2-D substrate may provide better support for the initial cell adhesion that results in homogeneous cell growth. Cells cultivated on flat substrates, for example, on PS culture dishes, mostly show faster initial adhesion and spreading than cells cultivated in 3-D matrices. However, 2-D substrates mostly do not enable the specific behavior of cells as in the natural 3-D system, mainly their migration and differentiation.[30] The fine nanofibrous fibrin mesh of the F2 nanocoating resembled a 2-D surface, but its nanostructure mimicked the natural ECM, enabling faster and more successful adhesion of cells through adhesion receptors.[17] The additional fibrin mesh in the F2 nanocoating filled the void spaces among the PLA fibers, and thus provided the cells with a larger area to adhere to. On this surface, the cells did not need to bridge the void spaces among the PLA fibers, and could utilize the entire lower part of their cytoplasmic membrane for adhesion through the cell adhesion receptors. This resulted in stronger specific mechanical and biochemical signals delivered to the cells. Moreover, the surface with the F2 coating could accommodate a higher number of cells. A similar improvement in cell behavior was observed in human osteoblast-like cells in cultures on PLGA and PLA nanofibers reinforced with diamond or hydroxyapatite nanoparticles. This led to reduction

in the size of the void spaces among the nanofibers.[31,32] In addition, fibroblasts are able to reorganize a nanostructured fibrin mesh, and this facilitates cell migration and synthesis of their own ECM proteins.[33]

The Fn attached to the fibrin nanocoating further improved the attachment of the cells and their subsequent proliferation. We showed a similar effect in our previous study.[13] Fn is known as a major adhesive protein with the RGD amino acid sequences bound by cells through adhesive receptors.[34] The cells adhering to the fine nanofibrous Fn mesh formed secondarily on the F2 nanocoating followed the morphology of the mesh (Figure 2B). This observation suggests that F2+Fn nanocoating is the most similar to the natural environment.

On day 3 after cell seeding, we observed differences in the proliferation of dermal fibroblasts, depending on the type of nanocoating. The cell mitochondrial activity, which is also considered as an indirect indicator of cell proliferation, was higher on the F2 nanocoating than on the F1 nanocoating. Moreover, the Fn attached to the fibrin nanocoating led to improved cell proliferation. The highest cell metabolic activity was observed on the F2+Fn nanocoating. The fibrin mesh combined with the Fn mesh probably provided the best substrate for initial attachment of the fibroblasts, and this led to faster cell proliferation. We observed no differences in cell proliferation between samples on days 1 and 7 after cell seeding. After seeding, the cells concentrate physiologically on their attachment to the substrate, and they do not proliferate (lag phase). In later cell cultivation intervals (1 week), the cells reorganized and degraded the fine fibrin or the Fn mesh, and replaced it by their own ECM, mainly by collagen I and Fn. However, the samples with the F1 nanocoating mostly remained in non-reorganized form after 1 week of cell cultivation. From this point of view, the type of fibrin nanocoating did not affect the cell proliferation in later cell cultivation intervals. However, the mitochondrial activity of the cells was still significantly higher on the fibrin-coated membranes than on the noncoated membranes.

The morphology of the fibrin nanocoating also has a significant impact on the synthesis of ECM proteins – collagen I and Fn. In our previous studies, we reported a positive effect of fibrin on the synthesis of collagen I and Fn.[12,13] The present study has shown that the F2 nanocoating significantly increased the relative expression of collagen I and Fn and the formation of extracellular fibers of proteins on the material surface, whereas the F1 nanocoating showed mostly a similar effect to that of noncoated membranes. This pattern was especially observed on day 4 after cell seeding.

The fibroblasts contract physiologically and remodel the fibrin matrix formed after a skin injury, and finally replace it with their own synthesized ECM.[6] If we compare F1 and F2 nanocoatings, it seems that the fine nanofibrous fibrin mesh of the F2 nanocoating was formed into a more physiologic structure, which enabled the fibroblasts to remodel it and replace it with their own ECM. Nevertheless, the relative expression of collagen I on the F1 nanocoating was enhanced by attaching Fn to the fibrin. It was shown that Fn is important for the production by fibroblasts of mature collagen fibrils and other extracellular proteins.[35,36] Moreover, the Fn formed an additional nanofibrous mesh on top of the F1 nanocoating. As was mentioned above, the fine nanostructure seems to better mimic the natural ECM matrix. This can improve the healing process, and enable the fibroblasts to synthesize their own ECM in in vitro conditions.

Conclusion

The morphology of the fibrin nanocoating on PLA membranes can regulate the mechanical properties of the membrane and the behavior of dermal fibroblasts. A fine homogeneous fibrin mesh provides more support than fibrin coating of individual fibers for the adhesion, spreading, and proliferation of cells. The expression of ECM proteins was also enhanced by the fibrin mesh, and the highest ECM synthesis was stimulated on PLA membranes coated with a fibrin mesh with secondarily attached Fn. It can be concluded that fibrin nanocoating, especially in the form of a nanostructured homogeneous mesh, significantly accelerated the natural behavior of the cells. A homogeneous fibrin mesh can, therefore, be considered as a suitable coating for synthetic materials for subsequent application in skin tissue engineering.

Acknowledgments

Disclosure

The authors report no conflicts of interest in this work.

References

1. Laurens N, Koolwijk P, de Maat MP. Fibrin structure and wound healing. *J Thromb Haemost*. 2006;4(5):932–939.

2. Tracy LE, Minasian RA, Caterson EJ. Extracellular matrix and dermal fibroblast function in the healing wound. *Adv Wound Care (New Rochelle)*. 2016;5(3):119–136.

3. Gailit J, Clarke C, Newman D, Tonnesen MG, Mosesson MW, Clark RA. Human fibroblasts bind directly to fibrinogen at RGD sites through integrin alpha(v)beta3. *Exp Cell Res*. 1997;232(1):118–126.

4. Albala DM. Fibrin sealants in clinical practice. *Cardiovasc Surg*. 2003; 11(Suppl 1):5–11.

5. Gugerell A, Pasteiner W, Nurnberger S, et al. Thrombin as important factor for cutaneous wound healing: comparison of fibrin biomatrices in vitro and in a rat excisional wound healing model. *Wound Repair Regen*. 2014;22(6):740–748.

6. Tuan TL, Song A, Chang S, Younai S, Nimni ME. In vitro fibroplasia: matrix contraction, cell growth, and collagen production of fibroblasts cultured in fibrin gels. *Exp Cell Res*. 1996;223(1):127–134.

7. Mazzone L, Pontiggia L, Reichmann E, Ochsenbein-Kolble N, Moehrlen U, Meuli M. Experimental tissue engineering of fetal skin. *Pediatr Surg Int*. 2014;30(12):1241–1247.

8. Zeng RX, He JY, Zhang YL, Liu XX, Zhang Y, Tang Q. Experimental study on repairing skin defect by tissue-engineered skin substitute compositely constructed by adipose-derived stem cells and fibrin gel. *Eur Rev Med Pharmacol Sci*. 2017;21(3 Suppl):1–5.

9. Han CM, Zhang LP, Sun JZ, Shi HF, Zhou J, Gao CY. Application of collagen-chitosan/fibrin glue asymmetric scaffolds in skin tissue engineering. *J Zhejiang Univ Sci B*. 2010;11(7):524–530.

10. Han HH, Jun D, Moon SH, Kang IS, Kim MC. Fixation of split-thickness skin graft using fast-clotting fibrin glue containing undiluted high-concentration thrombin or sutures: a comparison study. *Springerplus*. 2016;5(1):1902.

11. Gorodetsky R, Clark RA, An J, et al. Fibrin microbeads (FMB) as biodegradable carriers for culturing cells and for accelerating wound healing. *J Invest Dermatol*. 1999;112(6):866–872.

12. Bacakova M, Musilkova J, Riedel T, et al. The potential applications of fibrin-coated electrospun polylactide nanofibers in skin tissue engineering. *Int J Nanomedicine*. 2016;11:771–789.

13. Bacakova M, Pajorova J, Stranska D, et al. Protein nanocoatings on synthetic polymeric nanofibrous membranes designed as carriers for skin cells. *Int J Nanomedicine*. 2017;12:1143–1160.

14. Murad S, Grove D, Lindberg KA, Reynolds G, Sivarajah A, Pinnell SR. Regulation of collagen synthesis by ascorbic acid. *Proc Natl Acad Sci U S A*. 1981;78(5):2879–2882.

15. Park HJ, Ock SM, Kim HJ, et al. Vitamin C attenuates ERK signalling to inhibit the regulation of collagen production by LL-37 in human dermal fibroblasts. *Exp Dermatol*. 2010;19(8):E258–E264.

16. Bacakova L, Filova E, Parizek M, Ruml T, Svorcik V. Modulation of cell adhesion, proliferation and differentiation on materials designed for body implants. *Biotechnol Adv*. 2011;29(6):739–767.

17. Sun L, Stout DA, Webster TJ. The nano-effect: improving the long-term prognosis for musculoskeletal implants. *J Long Term Eff Med Implants*. 2012;22(3):195–209.

18. Riedel T, Brynda E, Dyr JE, Houska M. Controlled preparation of thin fibrin films immobilized at solid surfaces. *J Biomed Mater Res A*. 2009;88(2):437–447.

19. Schindelin J, Arganda-Carreras I, Frise E, et al. Fiji: an open-source platform for biological-image analysis. *Nat Methods*. 2012;9(7):676–682.

20. Bacakova L, Svorcik V. Cell colonization control by physical and chemical modification of materials. In: Kimura D, editor. *Cell Growth Processes: New Research*. New York: Nova Science Publishers, Inc.; 2008:5–56.

21. Vig K, Chaudhari A, Tripathi S, et al. Advances in skin regeneration using tissue engineering. *Int J Mol Sci*. 2017;18(4):789.

22. Engler A, Bacakova L, Newman C, Hategan A, Griffin M, Discher D. Substrate compliance versus ligand density in cell on gel responses. *Biophys J*. 2004;86(1 Pt 1):617–628.

23. Carr ME Jr, Hermans J. Size and density of fibrin fibers from turbidity. *Macromolecules*. 1978;11(1):46–50.

24. Wolberg AS. Thrombin generation and fibrin clot structure. *Blood Rev*. 2007;21(3):131–142.

25. Dyr JE, Tichý I, Jiroušková M, et al. Molecular arrangement of adsorbed fibrinogen molecules characterized by specific monoclonal antibodies and a surface plasmon resonance sensor. *Sens Actuat B Chem*. 1998; 51(1):268–272.

26. Lee F, Kurisawa M. Formation and stability of interpenetrating polymer network hydrogels consisting of fibrin and hyaluronic acid for tissue engineering. *Acta Biomater*. 2013;9(2):5143–5152.

27. Bidault L, Deneufchatel M, Vancaeyzeele C, Fichet O, Larreta-Garde V. Self-supported fibrin-polyvinyl alcohol interpenetrating polymer networks: an easily handled and rehydratable biomaterial. *Biomacromolecules*. 2013;14(11):3870–3879.

28. Law JX, Musa F, Ruszymah BH, El Haj AJ, Yang Y. A comparative study of skin cell activities in collagen and fibrin constructs. *Med Eng Phys*. 2016;38(9):854–861.

29. Fernandez-Madrid F, Noonan S, Riddle J. The "spindle-shaped" body in fibroblasts: intracellular collagen fibrils. *J Anat*. 1981;132(Pt 2): 157–166.

30. Duval K, Grover H, Han LH, et al. Modeling physiological events in 2D vs. 3D cell culture. *Physiology (Bethesda)*. 2017;32(4):266–277.

31. Parizek M, Douglas TE, Novotna K, et al. Nanofibrous poly(lactide-co-glycolide) membranes loaded with diamond nanoparticles as promising substrates for bone tissue engineering. *Int J Nanomedicine*. 2012;7:1931–1951.

32. Novotna K, Zajdlova M, Suchy T, et al. Polylactide nanofibers with hydroxyapatite as growth substrates for osteoblast-like cells. *J Biomed Mater Res A*. 2014;102(11):3918–3930.

33. Mazlyzam AL, Aminuddin BS, Fuzina NH, et al. Reconstruction of living bilayer human skin equivalent utilizing human fibrin as a scaffold. *Burns*. 2007;33(3):355–363.

34. Ruoslahti E, Pierschbacher MD. New perspectives in cell adhesion: RGD and integrins. *Science*. 1987;238(4826):491–497.

35. Sottile J, Hocking DC. Fibronectin polymerization regulates the composition and stability of extracellular matrix fibrils and cell-matrix adhesions. *Mol Biol Cell*. 2002;13(10):3546–3559.

36. Sethi KK, Yannas IV, Mudera V, Eastwood M, McFarland C, Brown RA. Evidence for sequential utilization of fibronectin, vitronectin, and collagen during fibroblast-mediated collagen contraction. *Wound Repair Regen*. 2002;10(6):397–408.

ORIGINAL RESEARCH

A two-layer skin construct consisting of a collagen hydrogel reinforced by a fibrin-coated polylactide nanofibrous membrane

Marketa Bacakova[1,*]
Julia Pajorova[1,2,*]
Antonin Broz[1]
Daniel Hadraba[1,3]
Frantisek Lopot[3]
Anna Zavadakova[4]
Lucie Vistejnova[4]
Milan Beno[5]
Ivan Kostic[6]
Vera Jencova[7]
Lucie Bacakova[1]

[1]Department of Biomaterials and Tissue Engineering, Institute of Physiology of the Czech Academy of Sciences, Prague, Czech Republic; [2]2nd Faculty of Medicine, Charles University, Prague, Czech Republic; [3]Department of Anatomy and Biomechanics, Faculty of Physical Education and Sport, Charles University, Prague, Czech Republic; [4]Biomedical Center, Medical Faculty in Pilsen, Charles University, Pilsen, Czech Republic; [5]Institute of Experimental Endocrinology, Biomedical Research Center of the Slovak Academy of Sciences, Bratislava, Slovak Republic; [6]Institute of Informatics, Slovak Academy of Sciences, Bratislava, Slovak Republic; [7]Department of Chemistry, Technical University of Liberec, Liberec, Czech Republic

*These authors contributed equally to this work

Correspondence: Marketa Bacakova
Institute of Physiology of the Czech Academy of Sciences, Videnska 1083, Prague 4, 14220, Czech Republic
Tel +42 029 644 3765
Email marketa.bacakova@fgu.cas.cz

Background: Repairs to deep skin wounds continue to be a difficult issue in clinical practice. A promising approach is to fabricate full-thickness skin substitutes with functions closely similar to those of the natural tissue. For many years, a three-dimensional (3D) collagen hydrogel has been considered to provide a physiological 3D environment for co-cultivation of skin fibroblasts and keratinocytes. This collagen hydrogel is frequently used for fabricating tissue-engineered skin analogues with fibroblasts embedded inside the hydrogel and keratinocytes cultivated on its surface. Despite its unique biological properties, the collagen hydrogel has insufficient stiffness, with a tendency to collapse under the traction forces generated by the embedded cells.

Methods: The aim of our study was to develop a two-layer skin construct consisting of a collagen hydrogel reinforced by a nanofibrous poly-L-lactide (PLLA) membrane pre-seeded with fibroblasts. The attractiveness of the membrane for dermal fibroblasts was enhanced by coating it with a thin nanofibrous fibrin mesh.

Results: The fibrin mesh promoted the adhesion, proliferation and migration of the fibroblasts upwards into the collagen hydrogel. Moreover, the fibroblasts spontaneously migrating into the collagen hydrogel showed a lower tendency to contract and shrink the hydrogel by their traction forces. The surface of the collagen was seeded with human dermal keratinocytes. The keratinocytes were able to form a basal layer of highly mitotically-active cells, and a suprabasal layer.

Conclusion: The two-layer skin construct based on collagen hydrogel with spontaneously immigrated fibroblasts and reinforced by a fibrin-coated nanofibrous membrane seems to be promising for the construction of full-thickness skin substitute.

Keywords: full-thickness skin substitutes, collagen hydrogel, fibroblast and keratinocyte co-cultivation, fibrin, nanostructure

Introduction

The skin is the organ of the human body that is most exposed to external agents. It provides a natural barrier between the surrounding environment and the human internal organs. From the tissue engineering point of view, the most important feature of the skin is its ability to self-remodel and regenerate, and to replace the tissue that is continuously being lost. Anatomically, the skin tissue can be divided into three layers: epidermis, with its main cellular type of keratinocytes; dermis, consisting mainly of fibroblasts; and hypodermis, which is rich in adipose cells.[1] For many years, tissue engineers have been trying to construct under in vitro

conditions an appropriate full-thickness skin equivalent that contains all three layers of the skin. However, there are still many limitations.

Two-dimensional (2D) flat materials are commonly used for cell cultivation, but these materials can induce an apical-basal polarity, which can restrict the adhesion and the migration of the cells in the x-y axis, leading to non-physiological behavior of the skin cells, eg fibroblasts.[2,3] A more complex three-dimensional (3D) microenvironment is therefore necessary for a non-prescribed polarity of the fibroblasts, and also for their spreading and migration in all three dimensions.[2] Novel 3D biomaterials aim to mimic the physiological environment of natural extracellular matrix (ECM), and thus to ensure better conditions for cell adhesion, spreading, proliferation, migration, matrix protein synthesis, and differentiation.[2,4]

Synthetic materials made of polylactide (PLA) or polycaprolactone (PCL) are commonly processed into fibrous scaffolds by conventional electrospinning, followed by cell seeding.[5,6] Although the synthetic scaffolds are non-toxic and mimic the mechanical and morphological properties of native tissues, they often do not provide sufficient support for cell adhesion and proliferation. The synthetic materials are therefore often modified with biomolecules in order to improve their attractiveness for cells, and thereby to accelerate the healing process.[7] For example, in our previous studies, nanofibrous PLA membranes were modified with fibrin, a key protein occurring during wound healing, in order to enhance the adhesion and growth of human dermal fibroblasts.[8,9] Moreover, we found out that two morphologically different structures of fibrin coatings had a significant influence on the cell behavior.[10] In addition, other studies have shown that collagen-containing composites or collagen-coated nanofibers are more attractive for cells than pure synthetic scaffolds, due to their greater biocompatibility and biodegradability.[9,11,12] Fu et al[13] (2016) found that collagen-coated PCL nanofibers increased the proliferation of skin fibroblasts. Fibrinogen-coated nanofibers decreased the growth of fibroblasts, but they supported the migration and the expression in these cells of α-smooth muscle actin, which is a typical marker for fibroblast differentiation into myofibroblasts. It was also found that the PCL/collagen nanofibrous membrane alone did not stimulate keratinocyte migration, while further coating of this membrane with an ultrafine fibrous collagen network significantly increased the cell motility.[14] Mahjour et al[15] used a layer-by-layer method to construct PCL/collagen nanofibers with

fibroblasts and keratinocytes, and applied this construct to full-thickness wounds on nude mice. Native collagen in any form therefore increases fibroblast chemotaxis, angiogenesis and keratinocyte migration.

The most recent studies have shown that fibroblast behavior is more physiological if the fibroblasts are entrapped in a 3D structure of hydrogels.[16,17] The hydrogels are able to self-assemble from a liquid monomeric phase to a polymeric mesh network under a certain temperature, pH, and enzymatic activity.[18,19] The hydrogels are covalently or non-covalently cross-linked, which enables the encapsulation of living cells.[20] Various nature-derived hydrogels for wound healing and regeneration applications have been described in earlier studies. These hydrogels were derived mainly from collagen,[21] fibrin,[16] alginate-gelatin,[22] hyaluronan-chitosan or chitosan-gelatin,[23,24] which are molecules similar to the macromolecular-based components of the body. However, one of the most discussed tasks in tissue engineering is the correlation between the stiffness of a hydrogel and the kinetics of cell adhesion and migration, which is related to the degradation and the remodeling time of the material.[25,26] The degradation time and the remodeling time should be in balance, and both are highly dependent on the behavior of the encapsulated cells. When the cells are entrapped in hydrogels, the surrounding environment changes their gene expression pattern and stimulates biosynthesis of their own ECM molecules, which results in degradation and remodeling of the hydrogels.[4,27] Various matrix metalloproteases (MMP-1, MMP-2, MMP-8, MMP-13 and MMP-14) are involved in the degradation processes and in the migration of the cells in the hydrogels.[17] In addition to the degradation, the cells can also synthesize their own molecules of ECM, and in this way they can remodel the hydrogels.[22,28] The morphology of fibroblasts in 3D collagen hydrogels varies from bipolar to dendritic in shape, depending on the stiffness and the tension of the hydrogels. Jiang and Grinnell[29] and Grinnell[30] also described the mechanical interactions between the collagen hydrogel and the fibroblasts. Entanglement of the fibroblasts into the surrounding matrix moves their forces to the hydrogel, and this results in contraction or compaction of the hydrogels.[29,30] In order to develop a large-size clinically applicable transplant, Braziulis et al[21] used plastic compression for a collagen type I hydrogel to increase the stability and to improve the mechanical properties of the material.[21] Another way to improve the mechanical properties of the hydrogels is to reinforce them with the use of biodegradable synthetic scaffolds, eg poly(lactic-co-glycolide) (PLGA) nanofibrous membranes or knitted meshes.[23,31]

In this study, we prepared a two-layer cell construct consisting of a poly-L-lactide (PLLA) nanofibrous membrane coated with a thin nanofibrous fibrin mesh and seeded with human dermal fibroblasts. After the attachment and the initial growth of the fibroblasts, a collagen hydrogel was formed on the fibroblast-seeded membrane. Finally, human epidermal keratinocytes were seeded on top of the collagen hydrogel. We hypothesized that the 3D-structured collagen hydrogel would enable the fibroblasts to migrate into the hydrogel from the membrane, and the collagen hydrogel with naturally immigrated fibroblasts would therefore simulate the skin dermis. The top of the collagen gel with a layer of adhering and growing keratinocytes would simulate the skin epidermis. The biodegradable PLLA nanofibrous membrane would serve as a substrate for the initial attachment and growth of fibroblasts, and as a mechanical support for a soft collagen hydrogel with skin cells. Coating the membrane with a thin nanostructured fibrin mesh was expected to enhance fibroblast adhesion and proliferation, leading to accelerated fibroblast migration into the collagen hydrogel. We supposed that spontaneous migration of the fibroblasts from the membrane into the collagen hydrogel could lower the tendency of these cells to contract and to shrink the gel by their traction forces, which occurs when fibroblasts are directly embedded into the collagen hydrogel during the gelling process.[17,32,33] The aims of this study were to evaluate the ability of human dermal fibroblasts to migrate into the collagen hydrogel from the nanofibrous membrane, to compare the behavior and the migration of the fibroblast from a non-coated membrane and from a fibrin mesh-coated membrane, and to evaluate the behavior of human epidermal keratinocytes adhering on the collagen hydrogel surface.

Materials and methods
Preparation of nanofibrous PLLA membranes

A nanofibrous PLLA membrane was prepared by the electrospinning process. PLLA with a molecular weight of 45,000–55,000 Da (Polyscitech, Akina Inc., Lafayette, IN, USA) was dissolved in a solvent system composed of a mixture of chloroform and ethanol in a ratio of 9:1 (v/v, Penta s.r.o., Prague, Czech Republic) to a final polymer concentration of 10 wt%. The polymer solution was then used for the electrospinning process.

Nanofibrous membranes were prepared using Nanospider NS 1WS500U (Elmarco s.r.o., Liberec, Czech Republic). The resulting fibers 940±340 nm in diameter were collected on a spunbond layer at a distance of 190 mm from the electrospinning string. The collector rolled at a rate of 10 mm/minute. The applied voltage was 40 kV for the string and 10 kV for the collector. The process was carried out at an ambient temperature of 25°C and at relative humidity of 30%.

Cell harvesting and cultivation

The two-layer construct consisted of human neonatal dermal fibroblasts and human epidermal keratinocytes. The human neonatal dermal fibroblasts were purchased from Lonza (Basel, Switzerland, Cat. No. CC-2509) and were cultivated in Dulbecco's Modified Eagle's Medium (DMEM; Sigma-Aldrich Co., St Louis, MO, USA) with 10% of fetal bovine serum (FBS; Sebak GmbH, Aidenbach, Germany) and 40 µg/mL of gentamicin (LEK, Ljubljana, Slovenia). The human epidermal keratinocytes were harvested from the skin of a young adult donor with approval of the local ethics committee (Ethics committee, Medical Faculty of Charles University, approval number EK-VP/15/0/2017) and after confirmed written informed consent provided by the donor that is in compliance with the Declaration of Helsinki. The skin graft was digested in 0.25% trypsin solution (Sigma-Aldrich Co.) for 1 hour at 37°C. After that, the epidermis was separated from the dermis. The epidermis was inserted in a drop of the cultivation medium. After a while, the cells were spontaneously released from the epidermis graft, and they were collected and seeded on mitomycin-inactivated 3T3 mouse embryonic fibroblasts adhered on the bottom of a cultivation flask. The 3T3 mouse embryonic fibroblasts were purchased from Sigma-Aldrich Co. (Cat. No. 93061524-1VL). The keratinocytes were cultivated in a mixture of the cell cultivation DMEM medium and Ham's Nutrient Mixture F12 medium (DMEM/F 12, Sigma-Aldrich Co.) in a ratio of 3:1. The mixture was supplemented with 10% of FBS (Sebak GmbH, Germany), 10 ng/mL epidermal growth factor (EGF, Sigma-Aldrich Co.), 10 µg/mL insulin (Sigma-Aldrich Co.), 0.4 µg/mL hydrocortisone (Sigma-Aldrich Co.), 10^{-10} M cholera toxin (Sigma-Aldrich Co.), 1000 U/mL of streptomycin and 0.1 mg/mL of penicillin (Sigma-Aldrich Co.).

The fibroblasts and keratinocytes were cultivated in an incubator at 37°C with a humidified atmosphere saturated with 5% of CO_2 in the air.

Preparation of the two-layer skin construct

A two-layer cell construct was composed of a PLLA nanofibrous membrane pre-seeded with human dermal fibroblasts, a collagen hydrogel and human dermal keratinocytes (Figure 1). The membrane samples were fixed in Cell Crown inserts (Scaffdex Ltd., Tampere, Finland) fitting into 24-well cell culture plates (TPP, Trasadingen, Switzerland) and seeded with human dermal fibroblasts. The fibroblasts were seeded on the membrane at a density of 30,000 cells, and were cultivated in DMEM supplemented with 10% of FBS (Sebak GmbH, Germany) and 40 µg/mL of gentamicin (LEK, Slovenia). To enhance the adhesion and proliferation of the fibroblasts, the PLLA membrane was coated with a thin nanofibrous fibrin mesh before cell seeding. After 3 days of fibroblast cultivation, the collagen hydrogel was prepared on the fibroblast-seeded membrane, and the fibroblasts started to migrate into the hydrogel. The ability of the fibroblasts to migrate into a collagen hydrogel from a non-coated membrane and from a fibrin-coated PLLA membrane was compared in four time intervals (on days 1, 3, 7 and 14 after collagen preparation, ie on days 4, 6, 10 and 17 after cell seeding). The preparation of the fibrin mesh and the collagen hydrogel is described in detail below in the following sections.

The construct consisting of the nanofibrous fibrin-coated PLLA membrane was then selected for seeding with keratinocytes on top of the collagen hydrogel (Figure 1). The keratinocytes were seeded at a density of 60,000 cells after 4 days of collagen hydrogel preparation (resp. of fibroblast migration). After the keratinocytes had been seeded, the medium was replaced by DMEM/F12 with supplements, as mentioned above. After 2 days of keratinocyte cultivation, the culture medium was further supplemented with 2-phospho-L-ascorbic acid trisodium salt (AA) at a concentration of 50 µg/mL, in order to stimulate the cells to synthesize ECM proteins. The medium was changed every 2 days.

Preparation of the fibrin mesh on the nanofibrous membrane

The fibrin mesh on the membrane was prepared according to our previously published work.[10] The fibrin was formed by activation of water-soluble human fibrinogen (341576; EMD Millipore, Billerica, MA, USA) with human thrombin (T6884; Sigma-Aldrich Co.).[34] Briefly, the fibrinogen in a concentration of 10 µg/mL, diluted in TRIS buffer (consisting of 50 mM TRIS-HCl, 100 nM NaCl and 2.5 mM $CaCl_2$), was adsorbed on the membrane for 1 hour. After rinsing with TRIS buffer, the adsorbed fibrinogen was activated with thrombin (2.5 U/mL in TRIS buffer) for 15 minutes. The thrombin-activated surface was directly treated without TRIS rinsing with a
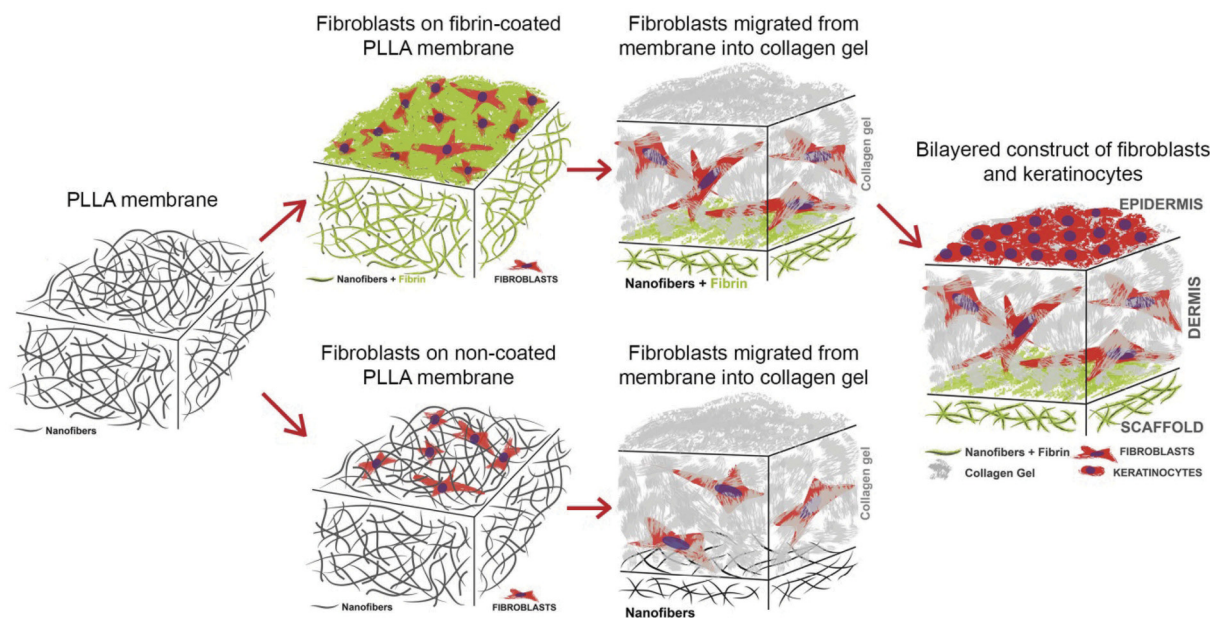

Figure 1 Scheme of the preparation of the constructs for evaluating the migration of the fibroblasts, consisting of a non-coated membrane or a fibrin-coated PLLA nanofibrous membrane seeded with human dermal fibroblasts and covered with a collagen hydrogel. The construct with the fibrin-coated PLLA nanofibrous membrane was then selected for seeding with keratinocytes and for preparing a bilayered construct simulating the dermis and the epidermis of the natural skin.
Abbreviation: PLLA, poly-L-lactide.

solution of 200 µg/mL of fibrinogen in a TRIS buffer and 0.5 U/mL of antithrombin III (Chromogenix, Milano, Italy) in deionized water for 1 hour to form a stable thin fibrin mesh. The antithrombin III blocked the unreacted thrombin remaining on the membrane in order to prevent the formation of a 3D fibrin gel.

Preparation of the collagen hydrogel on a nanofibrous membrane pre-seeded with fibroblasts

The type I collagen used for preparing the hydrogel matrix for the migration of the fibroblasts was isolated from rat tails. The tendons were removed from the rat tails, and were digested in 0.1 M acetic acid for 48 hours. The collagen digested in acetic acid was ultracentrifuged at the maximum speed (approx. 46,000 x g) for 1 hour in order to remove the tissue debris. The supernatant containing the collagen was neutralized with 0.1 M sodium hydroxide and was centrifuged at 1,500 x g for 10 minutes. The supernatant was removed and the collagen pellet was lyophilized. The lyophilized collagen I was dissolved in 0.02 M acetic acid to a concentration of 5 mg/mL and was stored as a stock solution.

The collagen hydrogel was prepared on day 3 after seeding of the fibroblasts. For 1 mL of 3 mg/mL collagen suspension 600 µL of collagen stock solution (5 mg/mL), 390 µL of DMEM (supplemented with 10% FBS and 40 µg/mL of gentamicin) and 10 µL of sodium bicarbonate (Sigma-Aldrich Co.) were mixed, and a total volume of 400 µL was applied on the fibroblast-seeded membrane and was left to polymerize for 20 minutes at 37°C, in a humidified atmosphere with 5% of CO_2 in the air, to reach pH around 7.4. The change in pH from acidic to neutral and 37°C caused the collagen to polymerize into a gel. After collagen polymerization, the 1.5 mL of DMEM (supplemented with 10% FBS and 40 µg/mL of gentamicin) was carefully added to the samples.

Collagen hydrogels unconfined compression test

The collagen hydrogel disks reinforced by a PLLA membrane without cells were prepared under the same conditions as the samples with cells (37°C, a humidified atmosphere with 5% of CO_2, pH~7.4). Thicker hydrogel disks were required for the unconfined compression test. The hydrogel disks were approximately 3 mm in thickness for the compression test, and approximately 0.5 mm in

thickness for seeding the cells. The 840 µL of collagen stock solution (5 mg/mL) was diluted in 546 µL of DMEM (supplemented with 10% FBS and 40 µg/mL of gentamicin) and 14 µL of sodium bicarbonate (Sigma-Aldrich Co.). The total volume of 1400 µL of collagen solution (3 mg/mL) was applied on the PLLA membrane without cells. The prepared unconfined samples were 12.6 mm in diameter, and the compression test was performed on six parallel samples. The fresh samples in PBS were placed between two stainless steel cylinders at 21°C. The cylinder was attached to the Kistler 9203 force sensor (1000 Hz, sensitivity 0.001 N, range±10N, Kistler, Switzerland) and moved in quasi-static mode at 2 mm/minute (stepper motor PD28-3-1021, Trinamic, Hamburg, Germany). The initial length l_0 was the length at detecting positive force (height F≠0 =1.82±0.27 mm).

The force and the position data were recalculated into the stress-stain curve reflecting l_0, ø and A_0, respectively. The mechanical properties of the composite material were characterized by the Young's moduli in the linear parts of the stress-strain curves. The data were acquired by the Dewetron data acquisition system (Dewetron, Grambach, Austria) and were analyzed in Matlab 2017a (Mathworks, USA).

Morphology of the fibrin mesh and the collagen hydrogel on the nanofibrous membrane

The morphology of the fibrin mesh and the collagen hydrogel prepared on a nanofibrous membrane was studied by scanning electron microscopy (SEM). The morphology of the fibrin mesh degraded by cells while they were being cultivated on the fibrin-coated membrane was further observed by fluorescence confocal microscopy.

For SEM, the nanofibrous membrane with fibrin was fixed with a 1% solution of osmium tetroxide, and the collagen hydrogel was fixed with 4% paraformaldehyde in PIPES buffer (pH~7) (Sigma-Aldrich Co.). The samples were dehydrated in the standard gradient (20–40 minutes in each of 30%, 50%, 70%, 96%, and 100% ethanol solutions). Samples from absolute alcohol were incubated in the following series of drying solutions: 1:1 ethanol/acetone, 100% acetone, 1:1 acetone/hexamethyl-disilazane, 100% hexamethyldisilazane, with each step taking 20–40 minutes. Air drying of the sample for a period of 24 hours was followed by coating with gold-palladium. The surface morphology and the topography of the fibers were observed using a high-resolution

scanning electron microscope with a Quanta FEG 250 field emission cathode (FEI, USA). High-vacuum mode, acceleration voltage 10 kV and secondary electrons mode using an Everhart-Thornley detector (ETD) were used for imaging.

The morphology of the fibrin mesh was evaluated by immunofluorescence staining performed on freshly prepared cell-free samples and on samples cultivated with cells in various time intervals. The samples were treated with a solution of 1% bovine serum albumin and 0.1% Tween 20 in a phosphate-buffered saline (PBS, all Sigma-Aldrich Co.) for 20 minutes at room temperature, in order to block non-specific binding sites. Then the samples were incubated with a primary antibody against human fibrinogen (A0080; polyclonal rabbit antibody, Dako Denmark A/S, Glostrup, Denmark) diluted in the blocking solution (1% albumin and 0.1% Tween 20 in PBS) in a ratio of 1:200 for 1 hour at 37°C. After that, the samples were rinsed with PBS and were incubated with a secondary antibody, ie goat anti-rabbit F(ab')2 fragments of IgG (H + L), conjugated with Alexa Fluor® 488 (A11070; Molecular Probes (Thermo Fisher Scientific), Eugene, OR, USA) diluted in the blocking solution in a ratio of 1:400 for 1 hour at room temperature in the dark. The samples were scanned on a Leica TCS SPE DM2500 upright confocal microscope, objective 40x/1.15 NA oil.

Visualization of the cell morphology and migration in the two-layer construct

The morphology of the dermal fibroblasts adhered on the nanofibrous membrane and migrated into the collagen hydrogel was studied by staining the filamentous actin (F-actin) cytoskeleton and the cell nucleus. The spreading and the morphology of keratinocytes were evaluated by the same staining, and, in addition, by staining the intermediate filaments containing keratin 14.

Before staining, the cells were fixed with 4% paraformaldehyde, and the cell membrane was permeabilized with 0.1% Triton X-100 (Sigma-Aldrich Co.) diluted in PBS for 30 minutes at room temperature. Then the samples were treated in a solution of 1% bovine serum albumin and 0.1% Tween 20 in PBS (all Sigma-Aldrich Co.) to block non-specific binding sites. Subsequently, the F-actin was stained with phalloidin conjugated with tetramethylrhodamine isothiocynate (TRITC) fluorescent

dye (5 µg/mL, diluted in PBS, Sigma-Aldrich Co.), and the cell nucleus was stained with Hoechst #33258 (5 µg/ml diluted in PBS, Sigma-Aldrich Co.) for 1 hour at room temperature in the dark. The keratin 14 of the keratinocytes was stained by incubating the samples with primary antibody to human cytokeratin 14 (ab7800, monoclonal mouse antibody, clone LL002, Abcam, Cambridge, United Kingdom) diluted in a blocking solution (1% albumin and 0.1% Tween 20 in PBS) in a ratio of 1:200 for 1 hour at 37°C. The samples were rinsed with PBS, and were then incubated with a secondary antibody, ie goat anti-mouse F(ab')2 fragments of IgG (H + L), conjugated with Alexa Fluor® 488 (A11017; Molecular Probes) diluted in the blocking solution in a ratio of 1:400 for 1 hour at room temperature in the dark. The samples for evaluating fibroblast migration into the collagen hydrogel were scanned on a Leica TCS SPE DM2500 upright confocal microscope, objective 40x/1.15 NA oil and 20x/20x/0.75 IMM CORR CS2; FWD 0.66, zoom 2x. The maximal depth of fibroblast migration into the collagen hydrogel from the non-coated or fibrin-coated membranes was measured during scanning on three parallel samples. Statistical significance was evaluated using nonparametric Kruskal-Wallis One Way Analysis of Variance on Ranks, Dunn's Method, statistical significance ($p \leq 0.05$). Samples of the whole two-layer construct were scanned on a Dragonfly 503 (Andor, Belfast, NI, UK) spinning disk confocal microscope with a Zyla 4.2 PLUS sCMOS camera, objective HC PL APO 20x/0.75 IMM CORR CS2; Free Working Distance =0.66 mm.

Cell mitochondrial activity

The proliferation and the viability of the human dermal fibroblasts that adhered on the membrane and that migrated into the collagen hydrogel were determined by the activity of cell mitochondrial enzymes, using the Cell Titer 96® AQueous One Solution Cell Proliferation Assay (MTS, Promega Corporation, Madison, WI, USA). The metabolic activity was determined on days 1, 3, 7, and 14 after the collagen hydrogel was prepared.

The collagen hydrogel with immigrated fibroblasts was carefully removed from the membrane, and both parts of the sample were moved into fresh cell culture wells to avoid the influence of cells adhered to the bottom of the well. The metabolic activity of the cells was separately determined in the hydrogel and on the membrane beneath the hydrogel. The non-coated

membranes and the fibrin-coated membranes without collagen hydrogel seeded with fibroblasts were used as control samples to observe any difference in the metabolic activity of the cells adhered on the two types of membranes. The assay was performed according to the manufacturer's protocol. The amount of formazan dye produced by the cells after 2 hours of incubation was quantified by measuring the absorbance. The absorbance was measured with wavelength 490 nm and with reference wavelength 700 nm, using a VersaMax ELISA Microplate Reader spectrophotometer (Molecular Devices Corporation, Sunnyvale, CA, USA).

Four parallel samples were used for each experimental group and time interval. The experiment was performed twice. The data was presented as the mean ± standard deviation (from eight measurements). Statistical significance was evaluated using parametric analysis of variance (ANOVA), with the Tukey post hoc test for pairwise comparison. Values of $p \leq 0.05$ were considered as significant.

An evaluation of the morphology of the collagen hydrogel and its shrinkage by migrating fibroblasts

The shrinkage of the collagen gel due to migrating fibroblasts was evaluated visually, and the diameter of the collagen hydrogel circle was measured in four time intervals of cell migration, ie on days 1, 3, 7, and 14 after the hydrogel was prepared. The diameter of the hydrogel circle was measured on the gel contour marked with several points at the edge of the hydrogel (see below). The freshly prepared collagen samples and the samples incubated without cells for 14 days under cell cultivation conditions were used as controls. Four parallel samples were used for each experimental group and time interval. The diameter of the hydrogel was presented as the mean ± standard deviation.

Results

Morphology of the fibrin mesh and the collagen hydrogel on the nanofibrous membrane

The PLLA membrane consisted of randomly-oriented fibers. The diameter of the fibers varied in a large range, from tens of nanometers to micrometers. The average diameter of the fiber was 940 nm ±340 nm (Figure 2A and B).

The fibrin covered the fibers of the membrane, and it also formed a thin homogeneous nanofibrous mesh on the surface of the membrane and among its fibers. The diameter of the fibers of the fibrin mesh ranged from tens of nanometers to approx. 100 nm (Figure 2C and D).

The nanofibers were formed during the collagen gelling process. They were randomly-oriented in the bulk with a diameter in tens of nanometers. The average diameter of the nanofibers was 47±7.6 nm (Figure 2E and F).

Collagen hydrogels unconfined compression test

The stress strain curves representing the collagen hydrogel disks displayed a linear response up to 21.29±4.36%

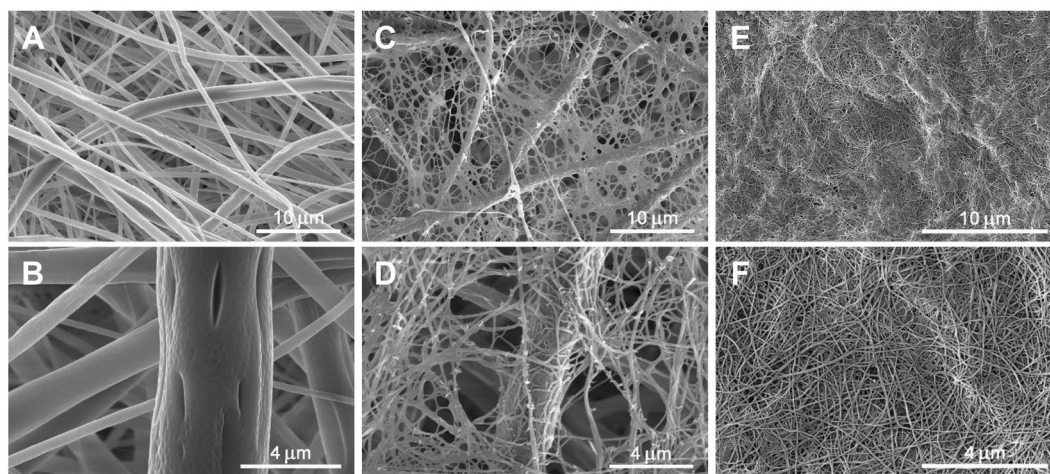**Figure 2** Morphology of a non-modified PLLA membrane (**A** – magnification 10,000×, **B** – magnification 30,000×), a fibrin mesh on a PLLA membrane (**C** – magnification 10,000×, **D** – magnification 25,000×) and a collagen hydrogel (**E** – magnification 15 000×, **F** – magnification 37,587×. Scanning electron microscopy (Quanta FEG 250 high-resolution scanning electron microscope).
Abbreviation: PLLA, poly-L-lactide.

deformation at unconfined compression. The Young's modulus was 3.0±1.4 kPa in this region. The next linear region was detected from approximately 56.69±9.91% deformation, where the Young's modulus was 89.4±13.2 kPa at unconfined compression; however, structural changes occurred in the sample disks in this region.

Migration of dermal fibroblasts into the collagen hydrogel from fibrin-coated vs non-coated membranes

We prepared a construct consisting of a pristine, ie non-coated, PLLA nanofibrous membrane or consisting of a membrane coated with a thin nanofibrous fibrin mesh, human dermal fibroblasts and the collagen I hydrogel. The collagen hydrogel was prepared on the fibroblast-seeded membrane after 3 days of cell cultivation. We compared the ability of fibroblasts to migrate into the collagen hydrogel from a non-coated membrane and from a fibrin-coated PLLA membrane in four time

intervals (on days 1, 3, 7, and 14 after collagen preparation, ie on days 4, 6, 10, and 17 after cell seeding).

The cell proliferation and viability were determined by measuring the activity of cell mitochondrial enzymes (ie cell metabolic activity). We separately determined the metabolic activity of the fibroblasts migrating in the collagen hydrogel and the fibroblasts adhered on the membrane beneath the hydrogel. Moreover, the metabolic activity of the fibroblasts adhered on the control membranes (non-coated and fibrin-coated membranes) without the collagen hydrogel was evaluated in order to see the effect of the fibrin mesh on fibroblast proliferation. There was greater metabolic activity of the cells proliferating on the control fibrin-coated membrane (without collagen) than on the control non-coated membrane (without collagen) (Figure 3, the first pair of columns). We observed these differences in all cultivation time intervals, with statistical significance on day 1. Similarly, the fibrin mesh also increased the fibroblast proliferation on the membrane beneath the collagen (Figure 3, the second pair of columns), with statistical significance on days 1, 3 and 7 after the collagen
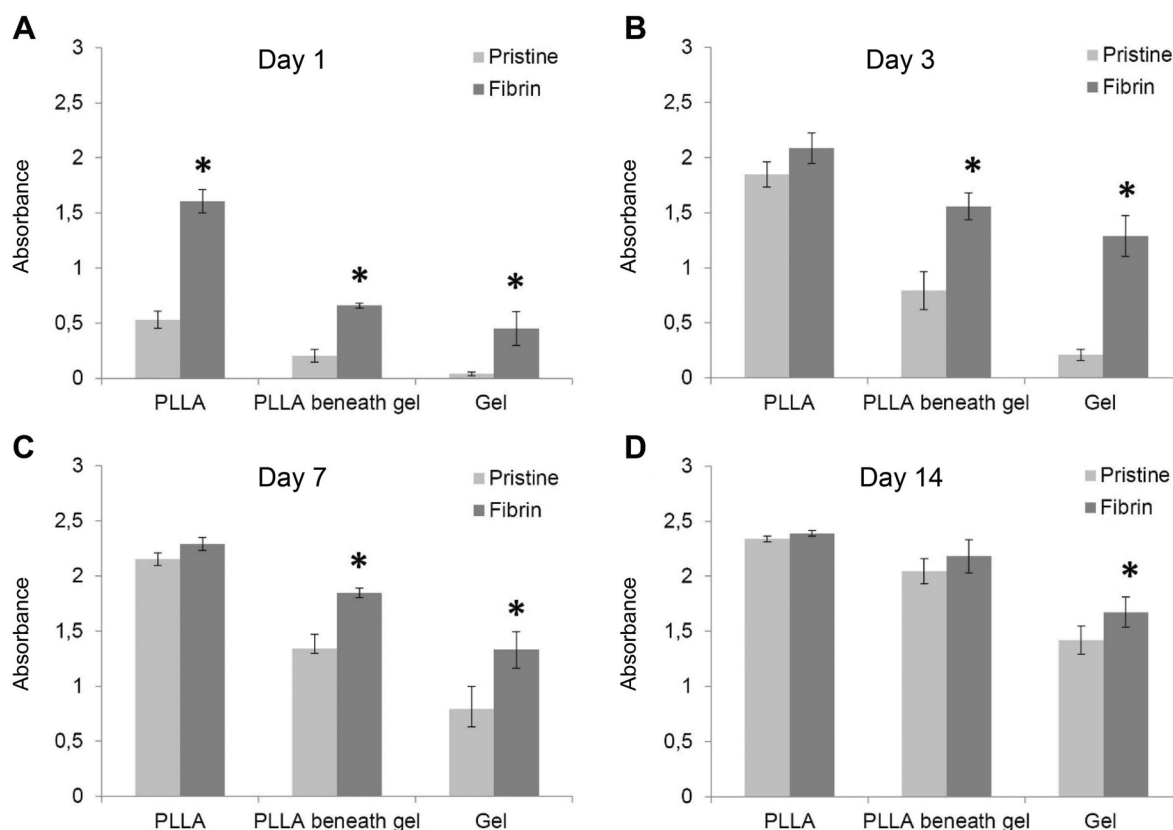

Figure 3 Mitochondrial activity of human dermal fibroblasts migrated into the collagen hydrogel from the non-coated PLLA membrane (Pristine) or from the fibrin-coated (Fibrin) PLLA membrane on day 1 (**A**), day 3 (**B**), day 7 (**C**) and day 14 (**D**) after preparation of the collagen. Cell mitochondrial activity on the control membrane without the hydrogel (PLLA, first pair of columns), separately on the membrane beneath the hydrogel (PLLA beneath gel, second pair of columns) and in the hydrogel (Gel, third pair of columns). Arithmetic mean ± SD from 8 measurements, ANOVA, Student-Newman-Keuls method, statistical significance (p≤0.05): * compared with a non-coated membrane (Pristine).
Abbreviation: PLLA, poly-L-lactide.

hydrogel was prepared (Figure 3A–C). The metabolic activity of the cells migrated into the collagen hydrogel from the fibrin-coated membrane was significantly higher than the activity of the cells migrated into the hydrogel from the non-coated membrane in all time intervals (Figure 3, third pair of columns).

The results for cell mitochondrial activity were confirmed by visualization of the cells migrating from the membrane into the collagen hydrogel using immunofluorescent confocal microscopy. The cells migrating into the collagen hydrogel and the cells adhering on the membrane beneath the hydrogel were separately visualized in various time intervals of cell migration (Figure 4). In addition, the fibroblasts adhered on the control membranes (non-coated and fibrin-coated membranes) without the collagen hydrogel were observed (Figure 5). Before the preparation of the collagen hydrogel on the membrane after the 3rd day of cell cultivation, the cells were almost in a confluent layer on the fibrin-coated membrane, while on the non-coated membrane, the cells had reached a lower population density (Figure 5, Day 0). On day 1 of cell migration, the cells started to migrate into the collagen hydrogel only from the fibrin-coated membrane. On the non-coated membrane, the cells remained attached to the membrane or to the bottom of the hydrogel (Figure 4, Day 1). In other words, the cells adhering and proliferating on the fibrin-coated membrane started to migrate 1 day after the hydrogel had been prepared, while the cells on the non-coated membrane started migrating later. The supporting influence of the fibrin mesh on the attachment of cells to the membrane and on their proliferation led to a higher number of cells migrating into the collagen hydrogel in all time intervals (Figure 4, the 1st and 2nd rows). In addition, the cells migrated deeper into the hydrogel from the fibrin-coated membrane than from the non-coated membrane, and this difference reached statistical significance on day 3. The depth of the cell migration increased significantly from the 3rd day to the 7th day (Figure 6). On day 14, the cells migrated throughout the collagen hydrogel, and they formed a confluent layer on top of the hydrogel, mainly in the case of the fibrin-coated membrane (Figure 4, 1st and 2nd row).
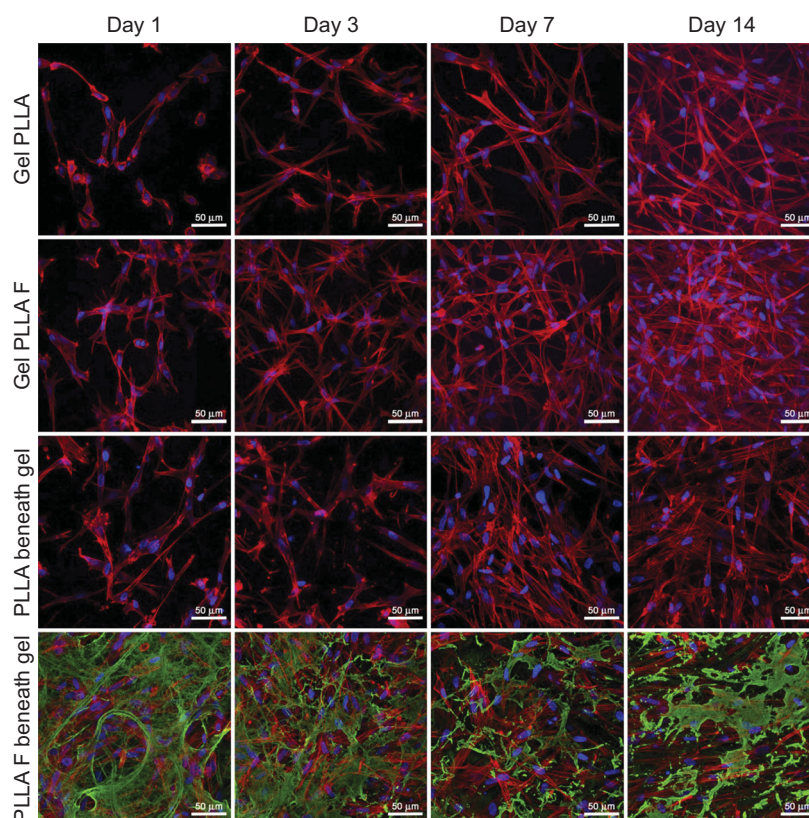

Figure 4 Human dermal fibroblasts in the collagen hydrogel migrated from a non-coated membrane (Gel PLLA) and from a fibrin-coated membrane (Gel PLLA F) for 1, 3, 7, and 14 days, or human dermal fibroblasts proliferated on the non-coated membrane (PLLA beneath gel) or on the fibrin-coated membrane (PLLA F beneath gel) beneath the collagen hydrogel for 4, 7, 10, and 17 days. The fibrin was stained by immunofluorescence (Alexa 488, green). The cells were stained with phalloidin-TRITC (red; F-actin cytoskeleton) and with Hoechst #33,258 (blue; cell nuclei). Leica TCS SPE DM2500 confocal microscope, 20x/0.75 IMM CORR CS2 zoom 2x or obj. 40x/1.15 NA oil, maximal intensity projection images.
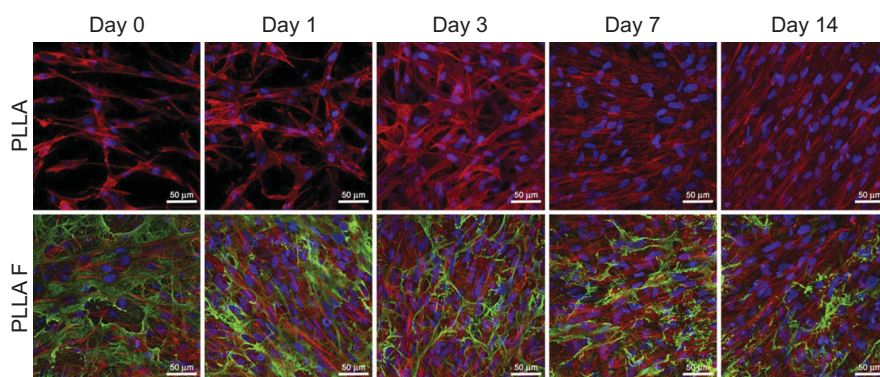**Abbreviation:** PLLA, poly-L-lactide.

Figure 5 Human dermal fibroblasts on the control non-coated membrane (PLLA) and on the fibrin-coated membranes (PLLA F) without the collagen gel. The cells on the membranes on the 3rd day after they were seeded and before collagen hydrogel preparation (Day 0), and cultivated for 1, 3, 7, and 14 additional days (ie 4, 7, 10,and 17 days in total). The fibrin was stained by immunofluorescence (Alexa 488, green). The cells were stained with phalloidin-TRITC (red; F-actin cytoskeleton) and with Hoechst #33258 (blue; cell nuclei). Leica TCS SPE DM2500 confocal microscope, objective 40x/1.15 NA oil, maximal intensity projection images.
Abbreviation: PLLA, poly-L-lactide.

The cells that remained adhering on the membrane beneath the collagen hydrogel were able to divide and proliferate, and their population increased in time (Figure 4, the 3rd and 4th rows). If we compare the cell behavior on the membranes beneath the collagen hydrogel (Figure 4, the 3rd and 4th rows) and on the control membranes (without collagen, Figure 5), the number of adherent cells was significantly higher on the control membranes in all time intervals. On the control fibrin-coated membrane, the cells gradually

degraded and reorganized the fibrin mesh. On day 14, the fibrin mesh was almost degraded, and only residues of it remained on the membrane (Figure 5, 2nd row), while the fibrin coating on the membrane beneath the hydrogel was only slightly altered by the cells (Figure 4, 4th row).

The collagen hydrogel was not considerably contracted and shrunk by the fibroblasts migrating in the collagen over a period of 14 days (Figure 7). The fresh collagen hydrogel prepared on the fibroblast-seeded
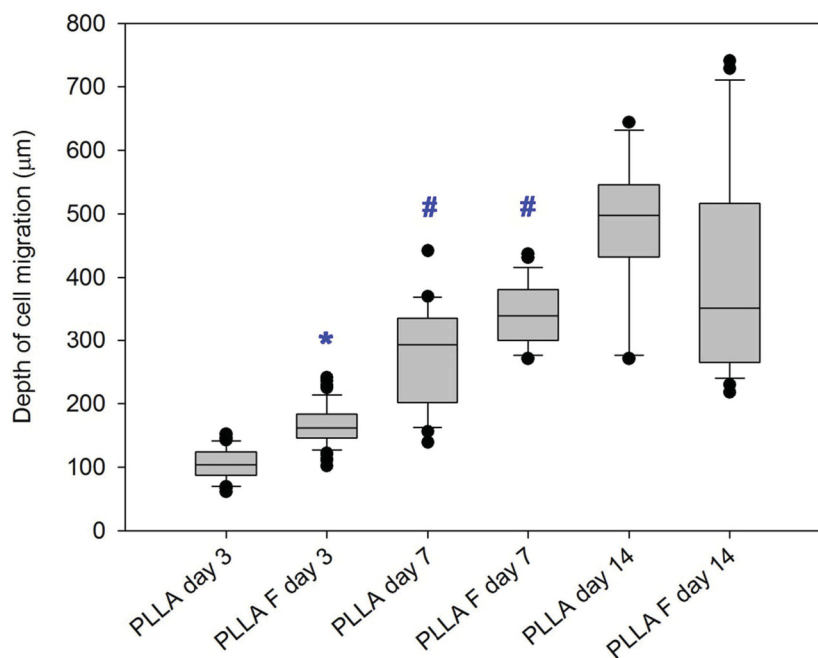

Figure 6 Depth of migration of human dermal fibroblasts into the collagen hydrogel from the non-coated PLLA membrane (PLLA) or from the fibrin-coated PLLA membrane (PLLA + F) on days 3, 7, and 14 of cell migration. Nonparametric Kruskal-Wallis One Way Analysis of Variance on Ranks, Dunn's Method, statistical significance ($p \le 0.05$): *in comparison with the non-coated membrane (PLLA), # in comparison with day 3.
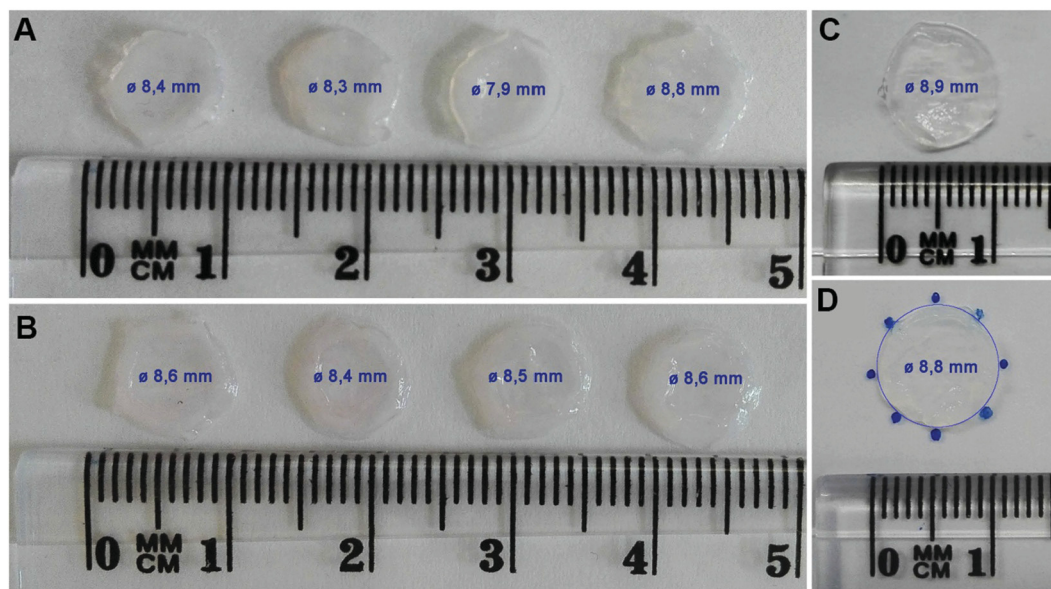
Figure 7 The morphology of the collagen hydrogel with embedded human dermal fibroblasts migrated from the non-coated membrane (**A**) and from the fibrin-coated membrane (**B**) for 14 days. The control collagen hydrogel without cells incubated at 37°C, 5% CO_2 for 14 days (**C**). The measurement principle for hydrogel shrinkage (**D**): the diameter of the hydrogel circle was measured on the gel contour marked with several points. The value of the diameter (Ø) of each hydrogel is displayed inside the hydrogel image, and is presented as mean ± standard deviation.

membrane was approximately 8.9 mm in diameter. After 14 days of cell migration, the diameter of the hydrogel reached 8.4±0.3 mm (presented as a mean ± standard deviation). In addition, there was no obvious difference between the remodeling of the collagen hydrogel by the cells migrating from the non-coated membrane (hydrogel diameter was 8.3±0.4 mm) and from the fibrin-coated membrane (hydrogel diameter was 8.5±0.1 mm).

Creating the two-layer construct consisting of dermal fibroblasts and keratinocytes

A two-layer construct was prepared using a PLLA nanofibrous membrane coated with a thin nanofibrous fibrin mesh and seeded with human dermal fibroblasts. The collagen hydrogel prepared after 3 days of fibroblast seeding allowed the fibroblasts to migrate inside the gel. The human dermal keratinocytes were seeded on top of the collagen hydrogel after 4 days of fibroblast migration.

Before the keratinocytes were seeded, the fibroblasts were allowed to immigrate into the collagen hydrogel (Figure 8A and B). Inside the hydrogel, the cells were spread, and showed a spindle-like morphology with well-developed F-actin microfilaments (Figures 8 and 9), as we also showed in the previous section in Figure 4. After the collagen hydrogel had been

seeded with keratinocytes, the fibroblasts continued proliferating inside the hydrogel and migrating through the hydrogel from the bottom to the top (Figure 9). The keratinocytes were able to attach to the collagen hydrogel, and to divide and proliferate throughout the experiment, ie for 14 days. The number of proliferating keratinocytes increased with cultivation time. The cells had already reached a confluent layer on the whole surface of the collagen hydrogel 7 days after keratinocyte seeding (Figure 9C and D). The keratinocytes had well-developed filaments containing cytokeratin 14 (Figure 9). Video S1 shows the keratinocytes and fibroblasts in the collagen hydrogel in individual horizontal sections from the top to the bottom of the collagen hydrogel. On the hydrogel surface, the keratinocytes formed a suprabasal layer of large cells frequently without cell nuclei and a confluent basal layer of small cells that were still dividing and proliferating. The layer of keratinocytes does not allow the fibroblasts to migrate throughout the whole volume of the collagen hydrogel, thus the fibroblasts remained inside the hydrogel without migrating to the surface (Figure 9). If the keratinocytes were not seeded on the collagen hydrogel, the fibroblasts migrated through the whole thickness of the gel and formed a confluent layer on top of the hydrogel (Figure 8E–H).

Figure 10 and Video S2 show the entire two-layer construct after 14 days of keratinocyte cultivation. The bottom of the skin construct is composed of a nanofibrous membrane with a confluent layer of proliferating fibroblasts (red) and with
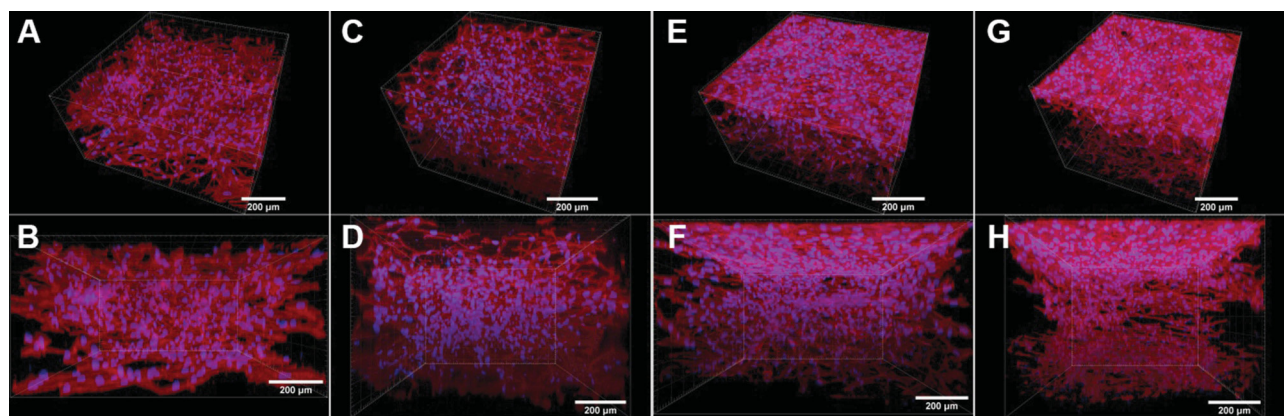
Figure 8 Human dermal fibroblasts in the collagen hydrogel migrated from the fibrin-coated PLLA membrane, without the hydrogel being seeded with keratinocytes (control samples). The fibroblasts migrated from the membrane into the collagen hydrogel for 4 days (**A** and **B**), 6 days (**C** and **D**), 11 days (**E** and **F**), and 18 days (**G** and **H**). The fibroblasts were stained with phalloidin–TRITC for the cell F-actin cytoskeleton (red), and with Hoechst #33258 for the cell nuclei (blue). Dragonfly 503 spinning disk confocal microscope with a Zyla 4.2 PLUS sCMOS camera, objective HC PL APO 20x/0.75 IMM CORR CS2.
Abbreviation: PLLA, poly-L-lactide.

residues of the fibrin mesh (green) degraded by the fibroblasts. The fibroblasts are homogeneously immigrated inside the collagen hydrogel, and the keratinocytes are adhered in the confluent layer on top of the collagen hydrogel (green).

Adding keratinocytes into the construct did not significantly promote shrinkage of the collagen hydrogel. There was a similar slight alteration in the morphology and in the contraction of the collagen hydrogel during cell cultivation when only fibroblasts were seeded into the construct, see our comments in the previous section, and Figure 7.

Discussion

Many previous studies have shown that the 3D microenvironment of hydrogels provides better physiological conditions than 2D flat substrates for cell spreading, proliferation, migration and differentiation.[35] The cells embedded in the hydrogels, especially fibroblasts and other mesenchymal cells, tend to be more spread, with a typical spindle-like morphology, and they form a network with cell contacts in all three dimensions.[16,17] On
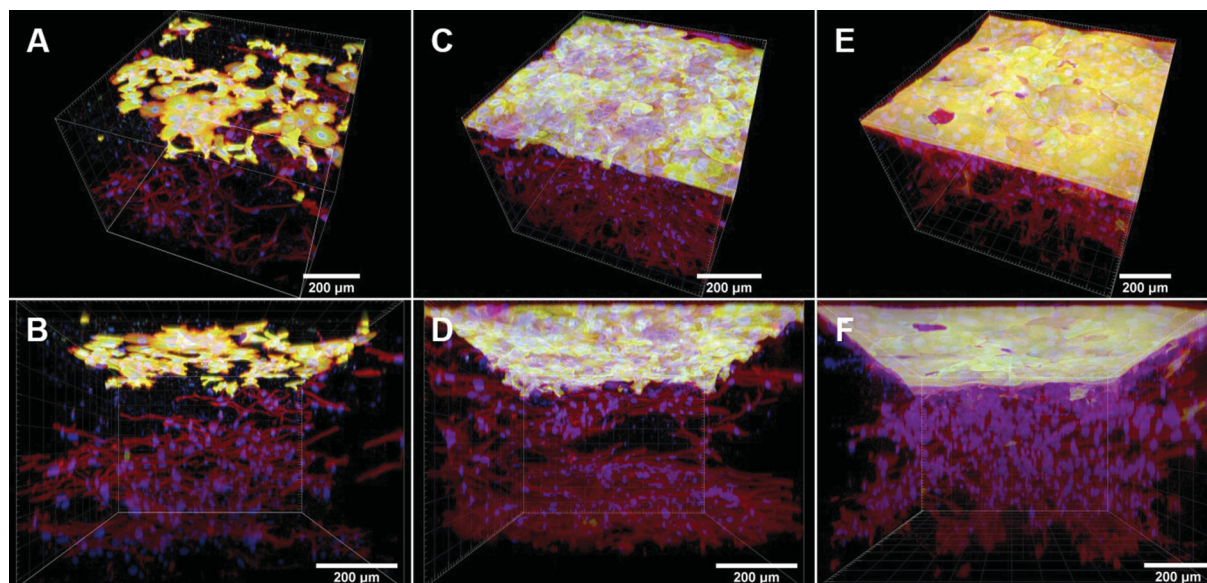

Figure 9 Human dermal fibroblasts in the collagen hydrogel migrated from the fibrin-coated PLLA membrane, and human dermal keratinocytes seeded on top of the hydrogel on day 4 of fibroblast migration. The fibroblasts migrated from the membrane into the collagen hydrogel for a period of 6 days (**A** and **B**), 11 days (**C** and **D**) and 18 days (**E** and **F**). The keratinocytes were cultivated for 2 days (**A** and **B**), 7 days (**C** and **D**) and 14 days (**E** and **F**). Both cell types were stained with phalloidin–TRITC for the cell F-actin cytoskeleton (red), and with Hoechst #33258 for the cell nuclei (blue). The cytokeratin 14 in the keratinocytes was stained by immunofluorescence (Alexa 488, green). Dragonfly 503 spinning disk confocal microscope with a Zyla 4.2 PLUS sCMOS camera, objective HC PL APO 20x/0.75 IMM CORR CS2.
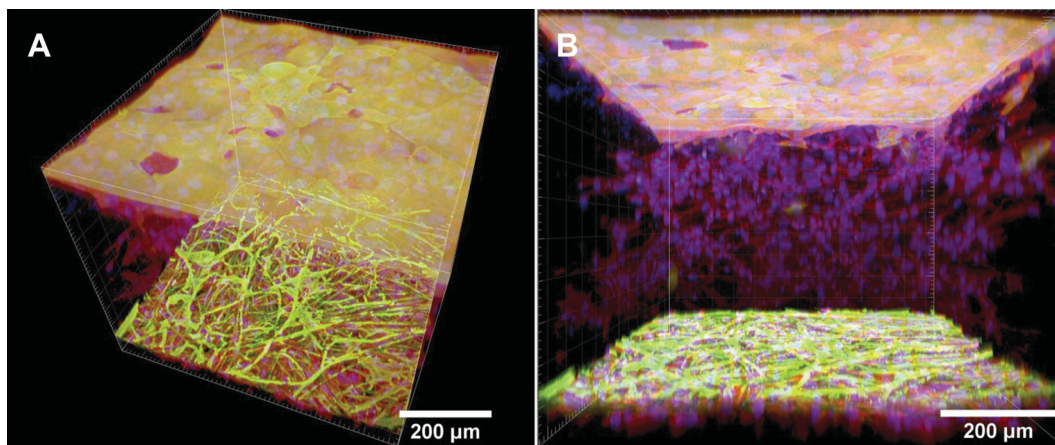**Abbreviation:** PLLA, poly-L-lactide.

Figure 10 The two-layer construct of skin cells composed of the fibrin-coated PLLA membrane seeded with human dermal fibroblasts, the collagen hydrogel with fibroblasts migrating inside the gel, and the keratinocyte layer on top of the hydrogel. Top-side view of the construct (**A**), and side-view of the construct (**B**). The fibroblasts migrated from the membrane into the collagen hydrogel for a period of 18 days. Keratinocytes proliferated on the hydrogel for 14 days. The PLLA membrane with fibroblasts and the collagen hydrogel with immigrated fibroblasts and keratinocytes on the top of hydrogel were stained separately. Both cell types were stained with phalloidin – TRITC for the cell F-actin cytoskeleton (red), and with Hoechst #33258 for the cell nuclei (blue). The cytokeratin 14 in the keratinocytes and the fibrin mesh on the nanofibrous membrane (at the bottom) were stained by immunofluorescence (Alexa 488, green). Dragonfly 503 spinning disk confocal microscope with a Zyla 4.2 PLUS sCMOS camera, objective HC PL APO 20x/0.75 IMM CORR CS2.

the other hand, keratinocytes with their apical-basal polarity prefer a 2D structured surface of the hydrogels. Fujisaki et al[36] and many other researchers have observed that collagen hydrogels, mainly collagen IV and collagen I, support the adhesion, proliferation and stratification of keratinocytes.[17,36,37] In addition, the biosynthesis of ECM molecules by fibroblasts and keratinocytes is enhanced by the physiological conditions of the hydrogels, which is important for hydrogel remodeling and for separating the two cell types by forming the basement membrane.[28,38,39] Although the encapsulated fibroblasts are separated from the keratinocytes growing on the surface, their communication continues to be mediated by the cytokines and growth factors released from the cells in a paracrine manner, or by cell-hydrogel mechanosensation.[40–43] The paracrine-based relationship of the cells can be regulated by changing the permeability and the structural properties of the cell-encapsulating substances. For example, Chiu et al[44] modulated the permeability of fibrin constructs by varying the concentration of fibrinogen and thrombin.[44] Bader et al[45] changed the keratinocyte-fibroblast paracrine communication by gelatin-based semi-interpenetrating networks.[45] Moreno-Arotzena et al[46] characterized the collagen hydrogel as a biomaterial with a higher void ratio and higher permeability than the fibrin hydrogel.[46] One of the current approaches to the construction of full-thickness skin substitutes therefore involves embedding dermal fibroblasts into 3D

hydrogels and cultivating epidermal keratinocytes on the surface of hydrogels. Although these 3D co-culture systems have been used for many years for in vitro studies of epithelial-mesenchymal interactions,[47] for keratinocyte differentiation,[36] for the dynamics of the basement membrane[38] and for many other applications, there are many limitations on clinical applications that still need to be overcome.

Although hydrogels have excellent biocompatibility and biodegradability properties for wound healing applications, they are not mechanically stable and their structure tends to be contracted under the traction forces of the embedded cells.[27,48] The Young's modulus of collagen hydrogels oscillates around units of kPa, depending on temperature, pH, duration of neutralization and many other conditions during polymerization.[49,50] In order to keep the cells alive during polymerization of the collagen hydrogels, the conditions have to be physiological for the cells, eg 37 °C, pH~7.4. However, it has previously been observed that the collagen hydrogels formed under physiological conditions are less stiff than those polymerized at basic pH.[49,51] However, the stiffness of hydrogel fibers plays an important role in cell behavior. Greater stiffness of the fibers suppressed cell adhesion, spreading, proliferation and migration into the hydrogel, due to a lower ability of the cells to transfer their traction forces to the hydrogel fibers.[25,52]

Many approaches leading to improved hydrogel stability and improved mechanical properties have therefore recently been studied. Braziulis et al[21] used plastic

compression for a collagen type I hydrogel. Similarly, Kim et al[53] induced structural and mechanical changes to the fibrin-collagen matrix by compressing it. Lotz et al[48] reduced the fibroblast-mediated contraction of the collagen hydrogel by cross-linking it with succinimidyl glutarate polyethylene glycol. Another way to improve the mechanical properties of hydrogels is to reinforce them by means of biodegradable synthetic scaffolds.[22] For example, Franco et al[23] combined PCL/PLGA membranes with chitosan-gelatin hydrogels in an optimal ratio to achieve appropriate biocompatibility and mechanical properties for creating a two-layer construct of fibroblasts and keratinocytes. Hartmann-Fritsch et al[31] incorporated nanofibrous PLGA membranes or knitted meshes into a bovine collagen I hydrogel with embedded fibroblasts and keratinocytes seeded on the surface. These authors obtained optimal stability of tissue-engineered full-thickness skin analogues by using a knitted mesh, where the epidermal part was well-stratified and the dermal part was revascularized in in vivo experiments. In the present study, we stabilized the collagen hydrogel by underlaying it with a nanofibrous fibrin-coated synthetic biodegradable PLLA membrane, pre-seeded with skin fibroblasts. Our results are in accordance with the recent studies which have shown that the Young's modulus of collagen hydrogels formed in physiological conditions varied around units of kPa.[49,51,52] The collagen hydrogel disks returned to their original state when compressed at low strain (up to 21%). As the scaffolds had a composite character, the mechanical response depended not only on the mechanical properties of the collagen hydrogel but also on the nanofibrous PLLA membrane. The results indicated that collagen hydrogel and PLLA membrane form a serial mechanical connection at compression in which the PLLA membrane start dominating at higher strains (over 56%). In addition, at higher strains, the collagen hydrogel undergoes structural changes. Pre-seeding the membrane with fibroblasts allowed the fibroblasts later to migrate into the collagen hydrogel without significant contraction of the hydrogel. The stability of the collagen hydrogel can be explained by the optimal ratio between the degradation processes and the remodeling processes mediated by the fibroblasts. During collagen polymerization, the fibroblasts adhering on the membrane were already in their proliferating phase, and they might not generate the strong traction forces that they generate while they are spreading. Moreover, after collagen polymerization, the cells could start migrating into the hydrogel by degrading it with matrix

metalloproteases, and by synthesizing their own ECM proteins.[16,17] In other words, we suppose that the traction forces generated by fibroblasts migrating from the PLLA membrane might be weaker than those generated by fibroblasts directly embedded into the collagen hydrogel. Direct embedding of the fibroblasts into the hydrogel during polymerization can be followed by cell spreading and by generating the intensive cell traction forces that are transmitted into the collagen fibrils. However, fibroblasts migrating from the membrane gradually degrade and remodel the collagen, which enables them to migrate spontaneously into the hydrogel, and leaves the collagen hydrogel relatively unchanged.

In order to increase the attractiveness of the PLLA membrane for the adhesion, spreading and proliferation of the fibroblasts pre-seeded on the membrane, we coated the membrane with a homogeneous nanofibrous fibrin mesh. In our previous study,[10] we showed that a nanostructured fibrin mesh apparently enhanced fibroblast adhesion, proliferation and biosynthesis of ECM proteins, mainly collagen I and fibronectin. In this study, we have additionally found that the fibrin mesh significantly increased the migration of fibroblasts into the collagen hydrogel in comparison with the non-modified PLLA membrane. Similar results were obtained by Fu et al[13] in experiments with fibrinogen-coated PCL nanofibers. They reported that coating PCL membranes with fibrinogen accelerated the migration of fibroblasts and stimulated their differentiation to myofibroblasts in a transforming growth factor (TGF)-β1 rich microenvironment.[13] In addition, due to the greater adhesion and proliferation of the cells caused by the fibrin mesh, a higher number of cells might migrate into collagen hydrogel. In contrast to our previous work,[8] we observed that the fibrin mesh under the collagen gel was not degraded, even on day 14 after fibroblast seeding. This may have been caused by focusing the fibroblasts on migrating and on remodeling the 3D collagen hydrogel, rather than focusing on the degradation and remodeling of the fibrin mesh, which was described in detail in our previous studies.[8–10]

In order to create a two-layer cellular skin construct, the collagen hydrogel enriched by spontaneously immigrated fibroblasts was seeded with primary dermal keratinocytes. A monolayer of adhered keratinocytes, with well-developed F-actin and basal cytokeratin 14 filaments, was formed on the whole surface of the collagen hydrogel after 7 days. The cells were able to divide for 14 days of cultivation, and they formed the basal layer with

highly mitotically active cells and a suprabasal layer with large cells frequently without cell nuclei. Our results correlated with other similar studies focused on the cultivation of keratinocytes on a collagen gel,[21,28,31,54] or on other forms of collagen substrates.[9,36,55] The previous studies also reported that a PCL/collagen nanofibrous membrane alone did not stimulate keratinocyte migration, while subsequently coating a membrane composed of an ultrafine fibrous collagen network significantly increased the cell motility.[14] Our results and other studies have proved that native collagen in the form of a hydrogel provides a physiological 3D microenvironment for the optimal co-cultivation of fibroblasts and keratinocytes. Furthermore, the high void ratio and the high permeability of collagen hydrogels enable paracrine communication between cells.[46]

Conclusion

We have prepared a two-layer skin construct of fibroblasts and keratinocytes composed of a nanofibrous fibrin-coated PLLA membrane pre-seeded with human dermal fibroblasts, a collagen hydrogel and keratinocytes. The results have shown that the fibroblasts were able to migrate from the membrane upwards into the collagen hydrogel. The PLLA membrane underlying the collagen hydrogel reinforced the whole skin construct, and served as a substrate for the initial attachment, growth and subsequent spontaneous migration of fibroblasts. Moreover, coating the membrane with a nanofibrous fibrin mesh further considerably enhanced the migration of the fibroblasts into the hydrogel. The fibroblasts did not mediate a significant contraction of the collagen hydrogel during their migration, such as has been repeatedly observed when fibroblasts are directly embedded into a collagen hydrogel during the gelling process. The keratinocytes seeded on top of the collagen formed a homogeneous basal layer of proliferating cells. This two-layer skin construct based on a collagen hydrogel with spontaneously immigrated fibroblasts and reinforced by a fibrin-coated nanofibrous membrane seems to be promising for the treatment of extensive full-thickness skin wounds.

Acknowledgments

Disclosure

References

1. Gunter CI, Bader A, Machens H. Regenerative Therapies. In: Steinhoff G, editor. *Regenerative Medicine - from Protocol to Patient*. 3 ed. Netherlands: Springer International Publishing; 2016:367–386.
2. Duval K, Grover H, Han LH, et al. Modeling physiological events in 2D vs. 3D cell culture. *Physiology (Bethesda)*. 2017;32(4):266–277. doi:10.1152/physiol.00036.2016
3. Ihalainen TO, Aires L, Herzog FA, Schwartlander R, Moeller J, Vogel V. Differential basal-to-apical accessibility of lamin A/C epitopes in the nuclear lamina regulated by changes in cytoskeletal tension. *Nat Mater*. 2015;14(12):1252–1261. doi:10.1038/nmat4389
4. Ahearne M. Introduction to cell-hydrogel mechanosensing. *Interface Focus*. 2014;4(2):20130038. doi:10.1098/rsfs.2013.0038
5. Yari A, Teimourian S, Amidi F, et al. The role of biodegradable engineered random polycaprolactone nanofiber scaffolds seeded with nestin-positive hair follicle stem cells for tissue engineering. *Adv Biomed Res*. 2016;5:22. doi:10.4103/2277-9175.175911
6. Hejazian LB, Esmaeilzade B, Moghanni Ghoroghi F, et al. The role of biodegradable engineered nanofiber scaffolds seeded with hair follicle stem cells for tissue engineering. *Iran Biomed J*. 2012;16(4):193–201.
7. Chen S, Liu B, Carlson MA, Gombart AF, Reilly DA, Xie J. Recent advances in electrospun nanofibers for wound healing. *Nanomedicine (Lond)*. 2017;12(11):1335–1352. doi:10.2217/nnm-2017-0017
8. Bacakova M, Musilkova J, Riedel T, et al. The potential applications of fibrin-coated electrospun polylactide nanofibers in skin tissue engineering. *Int J Nanomedicine*. 2016;11:771–789. doi:10.2147/IJN.S99317
9. Bacakova M, Pajorova J, Stranska D, et al. Protein nanocoatings on synthetic polymeric nanofibrous membranes designed as carriers for skin cells. *Int J Nanomedicine*. 2017;12:1143–1160. doi:10.2147/IJN.S121299

10. Pajorova J, Bacakova M, Musilkova J, et al. Morphology of a fibrin nanocoating influences dermal fibroblast behavior. *Int J Nanomedicine*. 2018;13:3367–3380. doi:10.2147/IJN.S162644

11. Zhou T, Wang N, Xue Y, et al. Electrospun tilapia collagen nanofibers accelerating wound healing via inducing keratinocytes proliferation and differentiation. *Colloids Surf B Biointerfaces*. 2016;143:415–422. doi:10.1016/j.colsurfb.2016.03.052

12. Lai HJ, Kuan CH, Wu HC, et al. Tailored design of electrospun composite nanofibers with staged release of multiple angiogenic growth factors for chronic wound healing. *Acta Biomater*. 2014;10 (10):4156–4166. doi:10.1016/j.actbio.2014.05.001

13. Fu X, Xu M, Jia C, et al. Differential regulation of skin fibroblasts for their TGF-β1-dependent wound healing activities by biomimetic nanofibers. *J Mater Chem B*. 2016;4(31):5246–5255. doi:10.1039/C6TB00882H

14. Fu X, Xu M, Liu J, Qi Y, Li S, Wang H. Regulation of migratory activity of human keratinocytes by topography of multiscale collagen-containing nanofibrous matrices. *Biomaterials*. 2014;35 (5):1496–1506. doi:10.1016/j.biomaterials.2013.11.013

15. Mahjour SB, Fu X, Yang X, Fong J, Sefat F, Wang H. Rapid creation of skin substitutes from human skin cells and biomimetic nanofibers for acute full-thickness wound repair. *Burns*. 2015;41(8):1764–1774. doi:10.1016/j.burns.2015.06.011

16. Miron-Mendoza M, Lin X, Ma L, Ririe P, Petroll WM. Individual versus collective fibroblast spreading and migration: regulation by matrix composition in 3D culture. *Exp Eye Res*. 2012;99:36–44.

17. Sriram G, Bigliardi PL, Bigliardi-Qi M. in vitro. *Eur J Cell Biol*. 2015;94(11):483–512. doi:10.1016/j.ejcb.2015.08.001

18. Chaudhari AA, Vig K, Baganizi DR, et al. Future prospects for scaffolding methods and biomaterials in skin tissue engineering: a review. *Int J Mol Sci*. 2016;17(12):1974. doi:10.3390/ijms17121974

19. Shang J, Theato P. Smart composite hydrogel with pH-, ionic strength- and temperature-induced actuation. *Soft Matter*. 2018. doi:10.1039/C8SM01728J

20. Jhon MS, Andrade JD. Water and hydrogels. *J Biomed Mater Res*. 1973;7(6):509–522. doi:10.1002/jbm.820070604

21. Braziulis E, Diezi M, Biedermann T, et al. Modified plastic compression of collagen hydrogels provides an ideal matrix for clinically applicable skin substitutes. *Tissue Eng Part C Methods*. 2012;18 (6):464–474. doi:10.1089/ten.TEC.2011.0561

22. Lee S, Kim HS, Yoo HS. Electrospun nanofibrils embedded hydrogel composites for cell cultivation in a biomimetic environment. *RSC Adv*. 2017;7(85):54246–54253. doi:10.1039/C7RA08595H

23. Franco RA, Nguyen TH, Lee BT. Preparation and characterization of electrospun PCL/PLGA membranes and chitosan/gelatin hydrogels for skin bioengineering applications. *J Mater Sci Mater Med*. 2011;22 (10):2207–2218. doi:10.1007/s10856-011-4402-8

24. Huang J, Ren J, Chen G, et al. Tunable sequential drug delivery system based on chitosan/hyaluronic acid hydrogels and PLGA microspheres for management of non-healing infected wounds. *Mater Sci Eng C Mater Biol Appl*. 2018;89:213–222. doi:10.1016/j. msec.2018.04.009

25. Nam K, Sakai Y, Hashimoto Y, Kimura T, Kishida A. Fabrication of a heterostructural fibrillated collagen matrix for the regeneration of soft tissue function. *Soft Matter*. 2012;8(2):472–480. doi:10.1039/ C1SM06543B

26. Branco Da Cunha C, Klumpers DD, Li WA, et al. Influence of the stiffness of three-dimensional alginate/collagen-I interpenetrating networks on fibroblast biology. *Biomaterials*. 2014;35(32):8927–8936. doi:10.1016/j.biomaterials.2014.06.047

27. Polio SR, Smith ML. Patterned hydrogels for simplified measurement of cell traction forces. *Methods Cell Biol*. 2014;121:17–31. doi:10.1016/B978-0-12-800281-0.00002-6

28. El Ghalbzouri A, Commandeur S, Rietveld MH, Mulder AA, Willemze R. Replacement of animal-derived collagen matrix by human fibroblast-derived dermal matrix for human skin equivalent products. *Biomaterials*. 2009;30(1):71–78. doi:10.1016/j.biomaterials.2008.09.002

29. Jiang H, Grinnell F. Cell-matrix entanglement and mechanical anchorage of fibroblasts in three-dimensional collagen matrices. *Mol Biol Cell*. 2005;16(11):5070–5076.

30. Grinnell F. Fibroblast biology in three-dimensional collagen matrices. *Trends Cell Biol*. 2003;13(5):264–269.

31. Hartmann-Fritsch F, Biedermann T, Braziulis E, et al. Collagen hydrogels strengthened by biodegradable meshes are a basis for dermo-epidermal skin grafts intended to reconstitute human skin in a one-step surgical intervention. *J Tissue Eng Regen Med*. 2016;10 (1):81–91. doi:10.1002/term.1665

32. Delvoye P, Wiliquet P, Leveque JL, Nusgens BV, Lapiere CM. Measurement of mechanical forces generated by skin fibroblasts embedded in a three-dimensional collagen gel. *J Invest Dermatol*. 1991;97(5):898–902.

33. Legant WR, Miller JS, Blakely BL, Cohen DM, Genin GM, Chen CS. Measurement of mechanical tractions exerted by cells in three-dimensional matrices. *Nat Methods*. 2010;7(12):969–971. doi:10.1038/nmeth.1531

34. Riedel T, Brynda E, Dyr JE, Houska M. Controlled preparation of thin fibrin films immobilized at solid surfaces. *J Biomed Mater Res A*. 2009;88(2):437–447. doi:10.1002/jbm.a.31755

35. Arnette C, Koetsier JL, Hoover P, Getsios S, Green KJ. In vitro model of the epidermis: connecting protein function to 3D structure. *Methods Enzymol*. 2016;569:287–308. doi:10.1016/bs.mie.2015. 07.015

36. Fujisaki H, Adachi E, Hattori S. Keratinocyte differentiation and proliferation are regulated by adhesion to the three-dimensional meshwork structure of type IV collagen. *Connect Tissue Res*. 2008;49(6):426–436. doi:10.1080/03008200802324998

37. Klar AS, Michalak K, Bottcher-Haberzeth S, Reichmann E, Meuli M, Biedermann T. The expression pattern of keratin 24 in tissue-engineered dermo-epidermal human skin substitutes in an in vivo model. *Pediatr Surg Int*. 2018;34(2):237–244. doi:10.1007/s00383-017-4198-9

38. Marionnet C, Pierrard C, Vioux-Chagnoleau C, Sok J, Asselineau D, Bernerd F. Interactions between fibroblasts and keratinocytes in morphogenesis of dermal epidermal junction in a model of reconstructed skin. *J Invest Dermatol*. 2006;126(5):971–979. doi:10.1038/sj.jid.5700230

39. Breitkreutz D, Koxholt I, Thiemann K, Nischt R. Skin basement membrane: the foundation of epidermal integrity–BM functions and diverse roles of bridging molecules nidogen and perlecan. *Biomed Res Int*. 2013;2013:179784. doi:10.1155/2013/179784

40. Tuan TL, Keller LC, Sun D, Nimni ME, Cheung D. Dermal fibroblasts activate keratinocyte outgrowth on collagen gels. *J Cell Sci*. 1994;107(Pt 8):2285–2289.

41. Wojtowicz AM, Oliveira S, Carlson MW, Zawadzka A, Rousseau CF, Baksh D. The importance of both fibroblasts and keratinocytes in a bilayered living cellular construct used in wound healing. *Wound Repair Regen*. 2014;22(2):246–255. doi:10.1111/wrr.12154

42. Doyle AD, Yamada KM. Mechanosensing via cell-matrix adhesions in 3D microenvironments. *Exp Cell Res*. 2016;343(1):60–66. doi:10.1016/j.yexcr.2015.10.033

43. Stunova A, Vistejnova L. Dermal fibroblasts-A heterogeneous population with regulatory function in wound healing. *Cytokine Growth Factor Rev*. 2018;39:137–150. doi:10.1016/j.cytogfr.2018.01.003

44. Chiu CL, Hecht V, Duong H, Wu B, Tawil B. Permeability of three-dimensional fibrin constructs corresponds to fibrinogen and thrombin concentrations. *Biores Open Access*. 2012;1(1):34–40. doi:10.1089/ biores.2012.0211

45. Bader RA, Kao WJ. Modulation of the keratinocyte-fibroblast paracrine relationship with gelatin-based semi-interpenetrating networks containing bioactive factors for wound repair. *J Biomater Sci Polym Ed*. 2009;20(7–8):1005–1030. doi:10.1163/156856209X444402

46. Moreno-Arotzena O, Meier JG, Del Amo C, Garcia-Aznar JM. Characterization of fibrin and collagen gels for engineering wound healing models. *Materials (Basel)*. 2015;8(4):1636–1651. doi:10.3390/ma8041636

47. Maas-Szabowski N, Shimotoyodome A, Fusenig NE. Keratinocyte growth regulation in fibroblast cocultures via a double paracrine mechanism. *J Cell Sci*. 1999;112(Pt 12):1843–1853.

48. Lotz C, Schmid FF, Oechsle E, Monaghan MG, Walles H, Groeber-Becker F. Cross-linked collagen hydrogel matrix resisting contraction to facilitate full-thickness skin equivalents. *ACS Appl Mater Interfaces*. 2017;9(24):20417–20425. doi:10.1021/acsami.7b04017

49. Achilli M, Mantovani D. Tailoring mechanical properties of collagen-based scaffolds for vascular tissue engineering: the effects of pH, temperature and ionic strength on gelation. *Polymers*. 2010;2:4. doi:10.3390/polym2040664

50. Lopez-Garcia MD, Beebe DJ, Crone WC. Mechanical interactions of mouse mammary gland cells with collagen in a three-dimensional construct. *Ann Biomed Eng*. 2010;38(8):2485–2498. doi:10.1007/s10439-010-0015-5

51. Antoine EE, Vlachos PP, Rylander MN. Tunable collagen I hydrogels for engineered physiological tissue micro-environments. *PLoS One*. 2015;10:3. doi:10.1371/journal.pone.0122500

52. Xie J, Bao M, Bruekers SMC, Huck WTS. Collagen gels with different fibrillar microarchitectures elicit different cellular responses. *ACS Appl Mater Interfaces*. 2017;9(23):19630–19637. doi:10.1021/acsami.7b03883

53. Kim OV, Litvinov RI, Chen J, Chen DZ, Weisel JW, Alber MS. Compression-induced structural and mechanical changes of fibrin-collagen composites. *Matrix Biol*. 2017;60–61:141–156. doi:10.1016/j.matbio.2016.10.007

54. Stark H-J, Szabowski A, Fusenig NE, Maas-Szabowski N. Organotypic cocultures as skin equivalents: a complex and sophisticated in vitro system. *Biol Proced Online*. 2004;6:55–60. doi:10.1251/bpo72

55. Benny P, Badowski C, Lane EB, Raghunath M. Making more matrix: enhancing the deposition of dermal-epidermal junction components in vitro and accelerating organotypic skin culture development, using macromolecular crowding. *Tissue Eng Part A*. 2015;21(1–2):183–192. doi:10.1089/ten.TEA.2013.0784

Supplementary materials

Video S1 The horizontal sections through the collagen hydrogel with keratinocytes adhered on the hydrogel surface and fibroblasts homogeneously immigrated inside the collagen hydrogel. The fibroblasts migrated from the membrane into the collagen hydrogel for a period of 11 days. Keratinocytes proliferated on the hydrogel for 7 days. Both cell types were stained with phalloidin–TRITC for the cell F-actin cytoskeleton (red), and with Hoechst #33258 for the cell nuclei (blue). The cytokeratin 14 in the keratinocytes was stained by immunofluorescence (Alexa 488, green). Dragonfly 503 spinning disk confocal microscope with a Zyla 4.2 PLUS sCMOS camera, objective HC PL APO 20x/0.75 IMM CORR CS2.

Video S2 This video shows the two-layer construct of skin cells, depicted in Figure 10, in dynamic mode. The construct was composed of the fibrin-coated PLLA membrane seeded with human dermal fibroblasts, the collagen hydrogel with fibroblasts migrating inside the gel, and the keratinocyte layer on top of hydrogel. The fibroblasts migrated from the membrane into the collagen hydrogel for a period of 18 days. Keratinocytes proliferated on the hydrogel for 14 days. The PLLA membrane with fibroblasts and the collagen hydrogel with immigrated fibroblasts and keratinocytes on the top of hydrogel were stained separately. Both cell types were stained with phalloidin – TRITC for the cell F-actin cytoskeleton (red), and with Hoechst #33258 for the cell nuclei (blue). The cytokeratin 14 in the keratinocytes and the fibrin mesh on the nanofibrous membrane (at the bottom) were stained by immunofluorescence (Alexa 488, green). Dragonfly 503 spinning disk confocal microscope with a Zyla 4.2 PLUS sCMOS camera, objective HC PL APO 20x/0.75 IMM CORR CS2.

Research Article

The Influence of Negative Pressure and of the Harvesting Site on the Characteristics of Human Adipose Tissue-Derived Stromal Cells from Lipoaspirates

Martina Travnickova [1,2] **Julia Pajorova,**[1,2] **Jana Zarubova** [1] **Nikola Krocilova,**[1] **Martin Molitor,**[3] **and Lucie Bacakova**[1]

[1]*Department of Biomaterials and Tissue Engineering, Institute of Physiology of the Czech Academy of Sciences, Videnska 1083, 142 20 Prague 4, Czech Republic*
[2]*Second Faculty of Medicine, Charles University, V Uvalu 84, 150 06 Prague 5, Czech Republic*
[3]*Department of Plastic Surgery, Hospital Na Bulovce and First Faculty of Medicine, Charles University, Budinova 67/2, 180 81 Prague 8, Czech Republic*

Correspondence should be addressed to Martina Travnickova; martina.travnickova@fgu.cas.cz

Background. Adipose tissue-derived stromal cells (ADSCs) have great potential for cell-based therapies, including tissue engineering. However, various factors can influence the characteristics of isolated ADSCs. *Methods.* We studied the influence of the harvesting site, i.e., inner thigh ($n = 3$), outer thigh ($n = 7$), and abdomen ($n = 9$), and of negative pressure, i.e., low (-200 mmHg) and high (-700 mmHg), on the characteristics of isolated ADSCs. We counted initial yields of attached cells after isolation. In subsequent passage, we studied the number, viability, diameter, doubling time, mitochondrial activity, and CD surface markers of isolated ADSCs. *Results.* We revealed higher initial cell yields from the outer thigh region than from the abdomen region. Negative pressure did not influence the cell yields from the outer thigh region, whereas the yields from the abdomen region were higher under high negative pressure than under low negative pressure. In the subsequent passage, in general, no significant relationship was identified between the different negative pressure and ADSC characteristics. No significant difference was observed in the characteristics of thigh ADSCs and abdomen ADSCs. Only on day 1, the diameter was significantly bigger in outer thigh ADSCs than in abdomen ADSCs. Moreover, we noted a tendency of thigh ADSCs (i.e., inner thigh+outer thigh) to reach a higher cell number on day 7. *Discussion.* The harvesting site and negative pressure can potentially influence initial cell yields from lipoaspirates. However, for subsequent *in vitro* culturing and for use in tissue engineering, it seems that the harvesting site and the level of negative pressure do not have a crucial or limiting effect on basic ADSC characteristics.

1. Background

Stem cells of various origin are fundamental elements for cell-based therapies in regenerative medicine, particularly for tissue engineering. Nowadays, tissue engineering tends to use stem cells that (1) are pluripotent or multipotent, (2) can be routinely harvested in large quantities, and (3) are surrounded by fewer ethical issues than other types. Mesenchymal stromal cells (MSCs) are multipotent plastic-adherent

fibroblast-like cells. They can be harvested predominantly from adult organs and tissues, i.e., bone marrow, peripheral blood, adipose tissue, skin, skeletal muscle, dental pulp, brain, and endometrium [1]. Not only adult tissues but also extrafoetal tissues, such as placenta, umbilical cord tissue, amniotic membrane, and amniotic fluid can also serve as sources of MSCs. The characteristics and the differentiation of bone marrow-derived stromal cells (BMSCs) have been widely studied, as they were the first MSCs to be described.

BMSCs provide favourable differentiation characteristics. However, the BMSC harvesting procedure is uncomfortable for donors and adipose tissue-derived stromal cells (ADSCs) provide similar yields of isolated cells, together with greater subsequent proliferation capacity [2]. In recent years, ADSCs have become an ideal target for tissue engineering and cell-based therapies. A relatively easy harvesting procedure and the multipotent characteristics of ADSCs make these stromal cells suitable for various uses [3]. The possibility of autologous application in cell-based therapies can be a further advantage of ADSCs.

The methods for isolating ADSCs from adipose tissue can be divided into enzymatic and nonenzymatic approaches [4, 5]. Until now, enzymatic digestion using collagenase has been the most widely performed procedure. However, newer alternative nonenzymatic techniques (e.g., vibration and centrifuging) can also be applied, especially for clinical purposes [6]. After enzymatic digestion and centrifugation, three separated parts are obtained, namely, the upper oily part containing adipocytes, the middle part consisting of digested tissue, and the reddish stromal vascular fraction (SVF) pellet at the bottom [7]. The SVF part is a mixture of distinct cell types consisting of ADSCs and variably also of pericytes, preadipocytes, endothelial precursor cells, endothelial cells, macrophages, smooth muscle cells, fibroblasts, and lymphocytes [5].

A large number and range of studies focused on obtaining ADSCs have been published. The studies have investigated various fat-harvesting procedures, cell isolation procedures, and donor factors. All these factors can influence the viability, the yields, and the subsequent proliferation and differentiation of the isolated cells. Tumescent liposuction is used as one of the easiest procedures for harvesting adipose tissue. The negative pressure (vacuum) that is used during the liposuction procedure is an important factor that influences the quality and the amount of harvested tissue. Lee et al. studied the effect of different negative pressures (i.e., -381 mmHg and -635 mmHg) on fat grafting [8]. In their *in vivo* study, no significant differences in the weight or in the histology of the fat grafts were observed; moreover, higher negative pressure did not affect the viability of the fat grafts [8]. Similarly, in a study by Charles-de-Sá et al., no significant differences, either in the viability of the adipocytes or in the number of MSCs, were found in adipose tissue obtained under various negative pressures [9]. However, other studies have reported a significant influence of negative pressure on cell characteristics. Mojallal et al. measured greater cell yields in adipose tissue harvested under a lower negative pressure (-350 mmHg) than under a higher negative pressure (-700 mmHg) [10]. Similarly, Chen et al. reported more than 2-fold higher cell numbers in SVF isolated from adipose tissue harvested under a lower negative pressure (-225 mmHg $\pm$ 37 mmHg) than under a higher negative pressure (-410 mmHg $\pm$ 37 mmHg) [11]. They also reported faster cell growth and higher secretion of some growth factors in cells obtained under lower negative pressure in the initial passages [11].

The harvesting site of the superficial adipose tissue seems to be another important donor factor potentially influencing the viability and the proliferation of the isolated cells. Jurgens et al. compared the numbers of cells isolated from the abdomen area and from the hip/thigh area. They found a significantly higher frequency of ADSCs in SVF isolates derived from the abdomen area, but no significant differences were found in the absolute numbers of nucleated cells [12]. However, the osteogenic and chondrogenic differentiation capacity of the ADSCs was not affected by the harvesting site [12]. Padoin et al. observed higher cell yields from the lower abdomen and from the inner thigh than from other liposuction areas (i.e., upper abdomen, flank, trochanteric area, and knee) [13]. Differences in the viability and in the amount of SVF and in the numbers of ADSCs after culturing, were also studied by Tsekouras and coworkers. In their study, the SVF from the outer thigh exhibited higher cell numbers [14]. This tendency also continued in subsequent cell culturing, where the outer and inner thigh samples both showed higher numbers of ADSCs than the abdomen, waist, or inner knee samples. Other studies reported no statistically significant differences in the volumes of fat grafts [15, 16] or in adipocyte viability [17] according to the donor sites.

Not only the negative pressure during liposuction and in the donor harvesting site but also different harvesting procedures [18] and other individual donor factors have been found to influence the viability, proliferation, and differentiation characteristics of ADSCs. Further factors include body mass index (BMI), age, gender, intercurrent diseases, such as diabetes mellitus, and also radiotherapy and drug treatment [19].

There is a need to investigate and confirm the best harvesting conditions for ADSCs, which could help to bring them into routine use in clinical practice. Until now, studies have not been uniform and have been focused predominantly on different cell types (adipocytes, preadipocytes, total SVF). The potential differences in the characteristics of ADSCs seem to be nonnegligible and need to be further clarified for future use in tissue engineering. The objective of our study was to investigate the influence of negative pressure during liposuction and also of the donor site on the yields of initially attached cells and on subsequent cell proliferation, achieved cell numbers, cell viability, diameter, and phenotypic markers of isolated ADSCs when cultured in *in vitro* conditions.

2. Materials and Methods

2.1. Group of Donors and Liposuction Procedure. A comparative study was performed on samples of subcutaneous adipose tissue from 15 healthy donors after informed consent at Hospital Na Bulovce in Prague. The group of females ($n = 14$) and one male ($n = 1$) underwent tumescent liposuction, whereby adipose tissue from the inner thigh ($n = 3$), from the outer thigh ($n = 7$), and from the abdomen ($n = 9$) was harvested. Harvesting was conducted in compliance with the tenets of the Declaration of Helsinki on experiments involving human tissues and under ethical approval issued by the Ethics Committee of Hospital Na Bulovce in Prague (August 21, 2014). The liposuctions were performed under sterile conditions, using tumescence. The tumescent solution
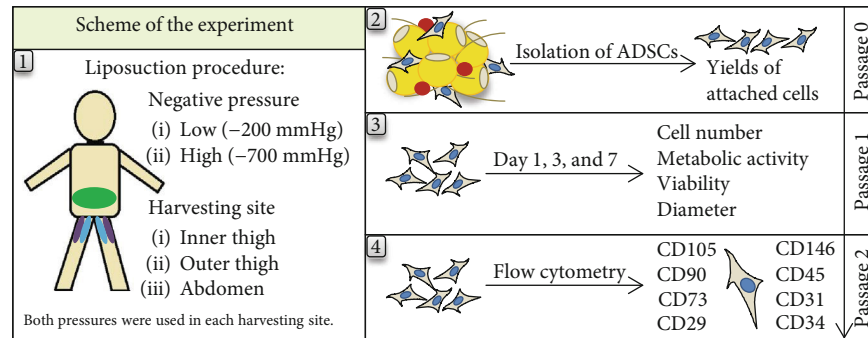
SCHEME 1: Scheme of the experiment. Sites in the abdomen, the inner thigh, and the outer thigh where liposuction at low negative pressure (-200 mmHg) and at high negative pressure (-700 mmHg) was performed. After the cell isolation, the initial yields of attached cells were counted. In subsequent passages, the number, viability, diameter, doubling time, mitochondrial activity (all in passage 1), and CD surface markers (passage 2) of isolated ADSCs were evaluated.

contained a 1000 mL of physiological solution with adrenaline (1 : 200,000) 1 mL and bicarbonate 8.4% 20 mL. In order to protect the harvested stromal cells from possible toxicity, no local anaesthetics were used. We used a liposuction machine (MEDELA dominant) that enabled continuous negative pressure to be set, and we utilized negative pressure of -200 mmHg and -700 mmHg. Superficial fat tissue was harvested using a Coleman Style blunt cannula with 4 holes and an inner diameter of 3 mm. Both low negative pressure (i.e., -200 mmHg) and high negative pressure (i.e., -700 mmHg) were used during liposuction in selected harvesting sites for each donor. Specifically, in the abdominal region, low pressure was used on one side of the abdomen, while high pressure was applied on the opposite side of the abdomen. Similarly, in the outer and inner thigh regions, low pressure was applied on one leg and the high pressure was applied on the contralateral leg (Scheme 1). A different cannula and vacuum suction container was used for low and high pressure harvesting to prevent contamination of low pressure harvesting material with high pressure harvesting material and vice versa. The age range of the donors was 26–53 years (mean age 37.8 ± 7.8 years) and the BMI range was $19.60 - 36.17$ kg/m^2 (mean BMI 25.44 ± 4.37 kg/m^2) (Table 1). The donors did not suffer from diabetes or from hypertension, and they were not tobacco users.

2.2. Isolation of ADSCs.

The isolation procedure was performed in fresh lipoaspirates (within 2 hours after the liposuction procedure) according to the isolation protocol by Estes et al. [7]. However, we made some slight modifications, as described in our previous study [20]. In brief, the lipoaspirates were washed several times with phosphate-buffered saline (PBS; Sigma-Aldrich). Then, the lipoaspirate was digested, using PBS containing 1% (wt/vol) bovine serum albumin (BSA; Sigma-Aldrich) and type I collagenase 0.1% (wt/vol) (Worthington) for 1 hour at a temperature of 37°C. After the digestion procedure, the tissue was centrifuged, and the upper and middle layers were aspirated. The obtained SVF was washed three times. A filter with pores 100 μm in size (Cell Strainer, BD Falcon) was additionally used to filter the cell suspension of SVF right before seeding

TABLE 1: Donors included in our study. The group of females ($n = 14$) and one male ($n = 1$; abdomen site) underwent tumescent liposuction, in which adipose tissue was harvested from the inner thigh ($n = 3$), from the outer thigh ($n = 7$), and from the abdomen ($n = 9$). In each harvesting site, the lipoaspirate was obtained both under low and under high negative pressure.

Donor site	Age (years)	BMI (kg/m^2)	No. of samples
Inner thigh	42.0 ± 4.6	27.70 ± 7.40	3
Outer thigh	35.4 ± 7.8	23.56 ± 2.45	7
Abdomen	38.3 ± 8.6	25.06 ± 4.08	9
Together	37.8 ± 7.8	25.44 ± 4.37	19 samples from 15 donors

into culture flasks (75 cm^2, TPP, Switzerland) in a density of 0.16 mL of original lipoaspirate/cm^2. The isolated cells were cultured in Dulbecco's modified Eagle medium (DMEM; Gibco), supplemented with 10% (vol/vol) foetal bovine serum (FBS; Gibco), gentamicin (40 μg/mL; LEK), and recombinant human fibroblast growth factor basic (FGF2; 10 ng/mL; GenScript). The primary cells, referred to as "passage 0," were cultured until they reached 70%–80% confluence. Then, the cells were passaged.

For the experiments that followed (Scheme 1), the cells isolated from the lipoaspirate harvested under low negative pressure (i.e., -200 mmHg) are referred to as "low," and the cells isolated from the lipoaspirate harvested under high negative pressure (i.e., -700 mmHg) are referred to as "high." The compared groups of cells are referred to as low inner thigh (low I thigh), high inner thigh (high I thigh), low outer thigh (low O thigh), high outer thigh (high O thigh), low abdomen, and high abdomen.

2.3. Yields of Initially Attached Cells.

For the primary culture of isolated cells, as mentioned above, the seeding density was 0.16 mL of original lipoaspirate/cm^2. On day 1 after isolation and seeding (passage 0), the culture medium was changed with the fresh medium, and the unattached cells were washed away. Then, the cell yields per 1 mL of lipoaspirate were counted from the number of attached cells, because only these cells are relevant for potential use in tissue engineering.

Microphotographs of 4 to 6 randomly chosen microscopic fields for each sample were taken by phase-contrast microscope and were analysed by manual cell counting. Then, the number of attached cells was compared depending on different negative pressure or on the harvesting site.

2.4. Cell Number, Viability, Diameter, and Doubling Time. The cells from each donor, harvested under low and high negative pressure within the corresponding areas in the abdomen or in the thigh, were cultured and then analysed. The isolated cells in passage 1 were seeded into 12-well tissue culture polystyrene plates (TPP, Switzerland; well diameter 2.1 cm) in a density of 14,000 cells/cm^2 (i.e., 50,000 cells/well) and were cultivated in DMEM+10% (vol/vol) FBS+10 ng/mL FGF2 for 7 days. The volume of the cell culture medium was 3 mL/well. The cells were cultivated in a humidified air atmosphere with 5% CO$_2$ at a temperature of 37°C. On days 1, 3, and 7, the cells were washed with PBS and were then detached by incubation with Trypsin-EDTA Solution (Sigma-Aldrich) for 4 minutes at 37°C. The effect of the Trypsin-EDTA solution was subsequently inhibited by adding a medium with FBS, and the cells were resuspended. The number, the viability, and the diameter of the detached cells in each well were measured using a Vi-CELL XR Cell Viability Analyzer (Beckman Coulter). In this analyser, the cell viability is evaluated by a trypan blue exclusion test. From 5 to 8 independent samples for each experimental group of a donor in each time interval were analysed. The cell population doubling time (DT) was calculated from the ADSC numbers, according to the following equation: $DT = t \times \ln{(2)}/(\ln{(N)} - \ln{(N_0)})$, where t represents the duration of culture, N represents the number of cells on day 3, and N_0 represents the number of cells on day 1.

2.5. Cell Mitochondrial Activity. The activity of mitochondrial enzymes is generally measured in order to estimate the cell proliferation activity. The isolated cells in passage 1 were seeded into 24-well tissue culture polystyrene plates (TPP, Switzerland; well diameter 1.5 cm) in a density of 14,000 cells/cm^2 (i.e., 25,000 cells/well) and were cultivated in DMEM+10% FBS+10 ng/mL FGF2 for 7 days. The volume of cell culture medium was 1.5 mL/well. On days 3 and 7, a CellTiter 96® Aqueous One Solution Cell Proliferation Assay (MTS; Promega Corporation) was performed according to the manufacturer's protocol. In brief, the principle of the MTS assay is based on a colorimetric change of the yellow tetrazolium salt to brown formazan. This change is brought about by the activity of mitochondrial enzymes. The absorbance was measured at a wavelength of 490 nm, using a VersaMax ELISA microplate reader (Molecular Devices LLC). From 5 to 6 independent samples were measured for each experimental group in each time interval.

2.6. Flow Cytometry. In passage 2, the cells were characterised by flow cytometry, using antibodies against specific surface CD markers. An evaluation was made of the percentage of cells in the population that contained standard markers of ADSCs, i.e., CD105 (also referred to as endoglin, a membrane glycoprotein which is part of the TGF-β receptor com-

plex), CD90 (Thy-1, a thymocyte antigen belonging to the immunoglobulin superfamily), and CD73 (ecto-5′-nucleotidase, a glycosylphosphatidylinositol-anchored membrane protein). Other evaluated markers included CD29 (integrin β_1, a component of receptors for collagen and fibronectin), CD146 (a melanoma cell adhesion molecule, a receptor for laminin), CD31 (also referred to as platelet-endothelial cell adhesion molecule-1, PECAM-1), and hematopoietic cell markers CD34 and CD45 [3]. In brief, the cells were washed with PBS and were incubated with Trypsin-EDTA for 4 minutes at 37°C. Subsequently, the medium with FBS was added and the cells were centrifuged (5 min, 300 g). The supernatant was aspired off, and the cells were resuspended in PBS with 0.5% (wt/vol) BSA (Sigma-Aldrich). The cells were equally divided into aliquots (i.e., 250,000 cells/aliquot). FITC-, Alexa488-, Alexa647-, or PE-conjugated monoclonal antibodies, i.e., against CD105, CD45 (Exbio Praha), CD90 (BD Biosciences), CD73, CD146, CD31 (BioLegend), CD29 and CD34 (Invitrogen), were added separately into aliquots. The aliquots were incubated with the antibodies for 30 minutes at 4°C in dark conditions. Next, the stained cells were washed three times with PBS with 0.5% (wt/vol) BSA and were analysed with the Accuri C6 Flow Cytometer System (BD Biosciences). In each aliquot, 20,000 events were recorded for each CD surface marker.

2.7. Microscopy Techniques. Phase-contrast microscopy was used to visualise the process of attachment, spreading, and growth in native ADSCs after isolation (passage 0). The immunofluorescence staining of CD surface markers was performed on native adhering ADSCs (passage 2) using PE-CD90 (BD Science) and Alexa488-CD29 (Invitrogen) antibodies. Cell nuclei in native cells were counterstained with Hoechst 33342 (Sigma-Aldrich) for 30 minutes at room temperature in the dark. Olympus microscope IX71 (objective magnification 10x or 20x) was used to take representative images.

2.8. Statistical Analysis. First, to evaluate the significance of different negative pressures, the observed data (i.e., initial cell yields, later cell numbers, and mitochondrial activity) were presented as the ratio of low-pressure cells to high-pressure cells for each donor. The Mann-Whitney Rank Sum test was used to test the equality of the medians of the ratios on different days of the experiment. Second, an unpaired two-sample t-test (for parametric data) or a Mann-Whitney Rank Sum test (for nonparametric data) was used to test the significance of the differences between the outer thigh area and the abdomen area. The inner thigh region was not statistically compared with other harvesting sites due to a relatively small group of samples (i.e., from only 3 patients). All the measured data were tested for normality according to the Kolmogorov-Smirnov test. Data which showed a Gaussian distribution are expressed as mean ± SD. However, due to the small sample size and the wide dispersion among the donors, some of the data did not show a Gaussian distribution. The nonparametric data are expressed as the median and the interquartile range (IQ range). The statistical analysis was performed using SigmaStat Software (Systat Software

Inc., USA); $p < 0.001$ (for flow cytometry) or $p < 0.05$ (for all other methods) was considered statistically significant. The plots were generated in R (programming language).

3. Results

3.1. Growth of Cells after Isolation and Cell Yields. In passage 0, we observed slight differences in the range of cell adhesion and growth among the cells harvested from various donors. However, the cells from all donors usually reached 70% or 80% confluence by day 10. Figure 1 shows representative images of the process of adhesion and growth in ADSCs after isolation from the same patient. On day 1 after isolation, the number of attached cells per 1 mL of lipoaspirate was counted in each sample. The ratio of attached low-pressure cells to attached high-pressure cells for each donor showed a median level near to 1.0 for the outer thigh region, which means a similar number of attached cells for both pressures (Figure 2(a)). However, the median level of this ratio (0.79) was significantly lower for the abdomen region (Figure 2(a)) which indicates higher cell yields from high-pressure lipoaspirates from this harvesting site. We observed a significantly 2-fold or 3-fold higher number of attached cells from the outer thigh region than from the abdomen region (Figure 2(b)). The inner thigh region was not statistically compared with other harvesting sites due to the relatively small group of samples.

3.2. Cell Number. The number of cells obtained from the corresponding areas of the abdomen or the thigh under low negative pressure and under high negative pressure for the same donor was measured on days 1, 3, and 7. The ratio of the number of low-pressure cells to the number of high-pressure cells on a specific day of the culture from each donor showed median levels near to 1.0 in cells from the inner thigh, outer thigh, and abdomen areas (Figure 3). There were no statistical differences in cell numbers between the outer thigh and abdomen areas on days 1 and 3 (Figure 4). When the groups of cells from the inner thigh and the outer thigh were evaluated together, we observed higher cell number in thigh ADSCs than in abdomen ADSCs ($p = 0.048$) on day 7 (Figure 4).

3.3. Doubling Time. The doubling time was calculated between days 1 and 3 (i.e., 48 hours of cell culture). There were similar median values in all sample groups, from 24.99 hours (low abdomen) to 28.65 hours (high inner thigh) (Figure 5). No significant differences were observed between the sample groups.

3.4. Viability and Diameter. No significant differences were found in the viability of the cells, measured by the trypan blue exclusion test, on day 1 (from 88.0% for low abdomen to 93.6% for low outer thigh), on day 3 (from 93.5% for high abdomen to 96.6% for high outer thigh), and on day 7 (from 90.3% for high inner thigh to 95.9% for high outer thigh) (Table 2). We observed significantly larger diameter of outer thigh ADSCs than of abdomen ADSCs ($p = 0.038$) on day 1. However, no significant differences in diameter were observed on day 3 and on day 7 (Table 3).

3.5. Cell Mitochondrial Activity. The activity of mitochondrial enzymes in ADSCs, considered as an indirect indicator of cell proliferation activity, was measured on days 3 and 7 after seeding. The ratio of the mitochondrial activity of the low-pressure cells to the mitochondrial activity of the high-pressure cells on a specific day of the culture from each donor revealed median levels near to 1.0 in cells from the inner thigh, outer thigh, and abdomen areas, and no significant differences were observed between the low-pressure cells and the high-pressure cells (Figure 6). Similarly, there were no significant differences in the mitochondrial activity of cells from different donor sites on day 3 (Table 4). On day 7, we observed a tendency toward lower mitochondrial activity of inner thigh ADSCs than of other harvesting sites; however, no statistical analysis was performed due to the relatively small sample size.

3.6. Flow Cytometry. The percentage of cells positive for typical markers of mesenchymal stromal cells, i.e., CD105, CD90, CD73, and CD29, was very high in ADSCs obtained from all tested sources. No significant differences were found in the presence of these markers in cells obtained from lipoaspirates taken at different negative pressures and from different harvesting sites (Table 5). However, slightly lower and more variable values were obtained in abdomen-derived ADSCs. Representative images of CD90 and CD29 immunostaining are shown in Figure 7(b). We also observed variability in the percentage of CD146+ cells among the donors (from 3.9% in low inner thigh and low outer thigh to 10.9% in low abdomen) (Figure 7(a)). This variability was slightly higher in ADSCs from the abdomen area and was not dependent on negative pressure. The percentage of cells bearing hematopoietic and endothelial cell markers, namely, CD45, CD34, and CD31, was very low and showed no significant differences between cells obtained at different negative pressures and from different donor sites (Table 5).

4. Discussion

A set of experiments was performed to reveal the influence of negative pressure and harvesting site on the characteristics of isolated ADSCs from a number of donors. For future use in tissue engineering, we were mainly interested in significant differences in the basic adhesion and growth characteristics of ADSCs in passages 1 and 2 after isolation. Our study provided an opportunity to compare isolated cells from the same topographic area that had been harvested under low negative pressure and under high negative pressure from each donor. In passage 0, we observed slight differences in the rate of attachment and spreading and in the growth of the ADSCs of the donors after the cells had been isolated. These initial interdonor differences may have been caused by differences in ADSC frequency in the obtained SVF cells. Varying frequencies of ADSCs, determined by a colony-forming unit assay and/or by a limiting dilution assay, have been found in the adipose tissue harvested from various donor sites [12] or when different harvesting procedures are used [21]. Specifically, Jurgens et al. observed significantly higher frequency of ADSCs isolated from adipose tissue harvested
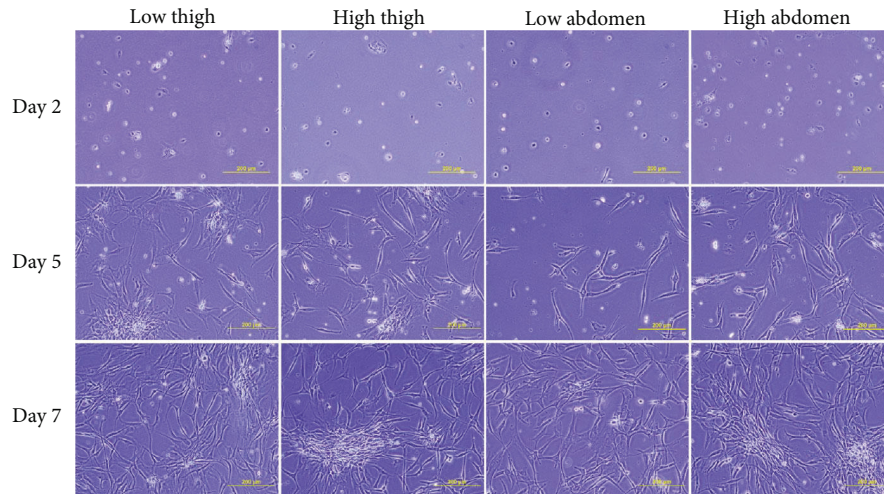
FIGURE 1: The process of attachment, spreading, and growth in ADSCs from the same patient on days 2, 5, and 7 after isolation. The ADSCs were isolated from the inner thigh area and from the abdomen area, under low negative pressure (-200 mmHg) and under high negative pressure (-700 mmHg). Passage 0. Scale bar 200 μm. Representative images are shown.
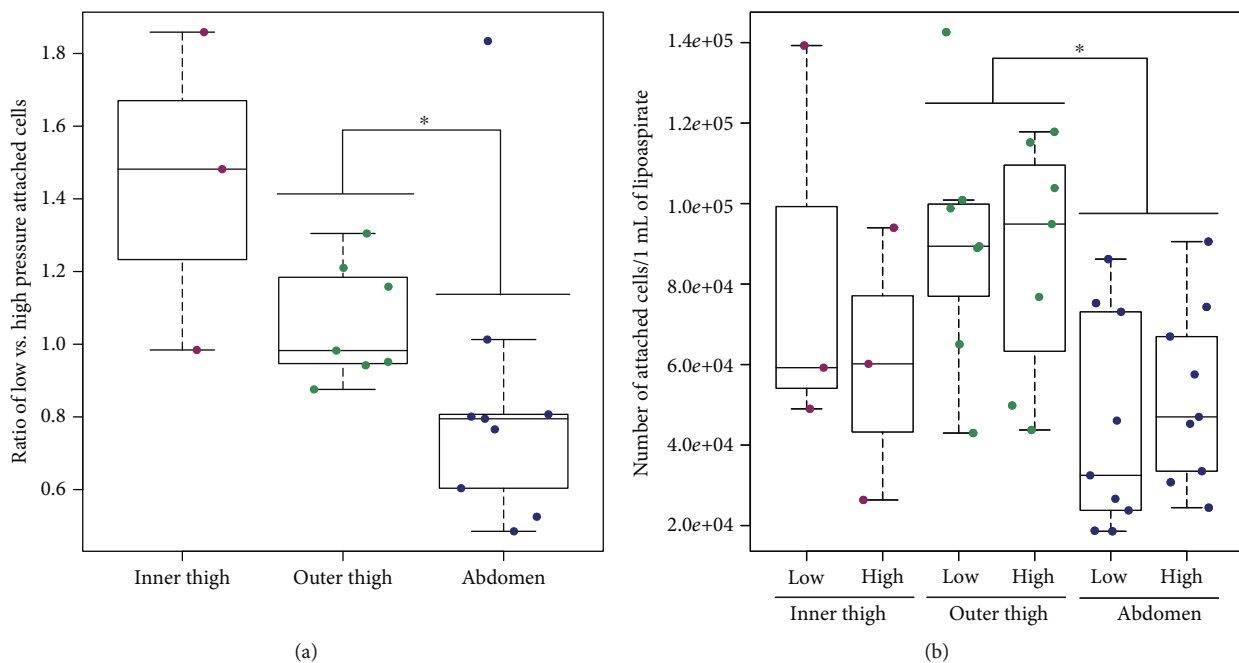

(a)

(b)

FIGURE 2: Cell yields counted from the number of initially attached cells. (a) The ratio of the number of low-pressure cells to the number of high-pressure cells for each donor on day 1 after isolation; passage 0. $p < 0.05$ (*) is for harvesting area (outer thigh vs. abdomen) significance testing. (b) The number of attached cells per 1 mL of lipoaspirate; passage 0. $p < 0.05$ (*) is for harvesting area significance testing (outer thigh vs. abdomen). The inner thigh region was not statistically compared to the outer thigh and abdomen regions due to the relatively small sample size.

from the abdomen region than from the hip/thigh region [12]. Oedayrajsingh-Varma et al. observed a significantly higher frequency of ADSCs isolated from adipose tissue obtained by resection and tumescent liposuction than from tissue obtained by ultrasound-assisted liposuction [21]. In those studies, the absolute number of nucleated cells in the harvested adipose tissue and the number of viable cells in the stromal vascular fraction were not affected by the anatomical site or by the type of surgical procedure. However,

in other studies, the anatomical site did have an influence on the total SVF and on the ADSC yields. Iyyanki et al. observed significantly higher total SVF yields from the abdominal harvesting site than from the flank and axilla harvesting sites; however, the ADSC yields did not differ significantly [18]. In a study by Fraser et al., the abdomen-adipocyte yield was 1.7-fold higher than the hip-adipocyte yield, and the adipocyte yields displayed large donor-to-donor variabilities [22]. However, neither the nucleated cell
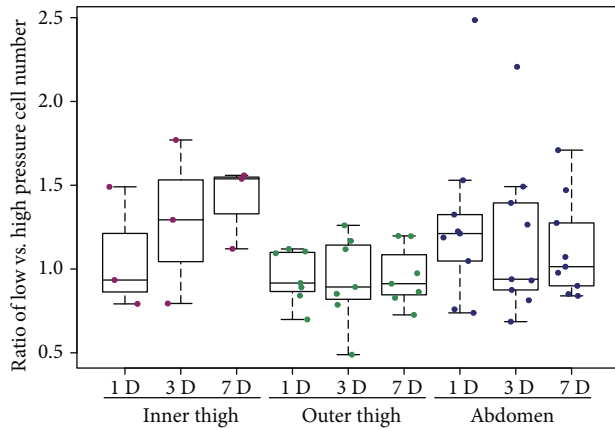
FIGURE 3: The influence of negative pressure on the number of ADSCs. The ratio of the number of low-pressure cells to the number of high-pressure cells for each donor. The measurements were performed on ADSCs from the inner thigh ($n = 3$) area, from the outer thigh ($n = 7$) area, and from the abdomen ($n = 9$) area on day 1 (1D), day 3 (3D), and day 7 (7D); passage 2. No significant differences among the groups were observed.

yields nor the preadipocyte yields differed significantly [22]. A large range of ADSC yields among donors was also observed, and no statistical differences were found between the abdomen, the thigh, and the mammary areas [21]. By contrast, our study showed a potential influence of harvesting site, as we observed a higher number of attached cells per 1 mL of lipoaspirate for the outer thigh area than for the abdomen area on day 1 after isolation in *in vitro* culture. Different results concerning the influence of harvesting site on cell yields might be obtained because of the differences in the target cell populations being studied in different papers. For plastic surgery purposes, the cell yields of all nucleated cells, adipocytes, preadipocytes, and SVF are also a subject of interest. However, tissue engineering focuses more on the yields of adherent ADSCs that can be further proliferated and/or differentiated.

The total number of harvested cells can also be influenced by the level of negative pressure used during the liposuction procedure. In a study by Mojallal et al., a lower negative pressure (-350 mmHg) during liposuction resulted in higher SVF yields than a higher negative pressure (-700 mmHg) [10]. Similarly, in a more recent study by Cheriyan et al., higher counts and higher viability of adipocytes were found in lipoaspirates obtained at a lower negative pressure (-250 mmHg) than at a higher negative pressure (-760 mmHg) [23]. However, each of these studies was performed on three patients only. In our study, the number of attached cells after the isolation was similar for low- and high-pressure cells from the outer thigh region, whereas the abdomen region was characterised by initial higher cell yields of attached cells for high pressure.

Although the initial SVF yields, adipocyte yields, and ADSC frequency in lipoaspirates can vary, later differences during *in vitro* ADSC culturing were of particular interest to us. Our study was focused on the number, the mitochondrial activity, and the viability of the ADSCs in subsequent passaging. We observed similar cell numbers and mitochondrial activity independently of low- and high-negative pressure for a specific region. This means that the subsequent proliferation of ADSCs was not affected by the negative pressure used during the liposuction procedure. Chen et al. observed initial higher proliferation activity (assessed by Cell Counting Kit-8) in lower negative pressure SVF cells than in higher negative pressure SVF cells from the abdominal area in passages 1 and 2 [11]. However, these significant differences did not appear in passage 3 [11]. Similarly, our results could also provide support for the theory that the differences in proliferation activity between low-pressure cells and high-pressure cells become less noticeable after passaging during *in vitro* cultivation. Interestingly, other researchers have reported that different apparatuses and different levels of negative pressure during liposuction do not influence the percentage and the viability of adipocytes and isolated mesenchymal stromal cells [9]. The discrepancies among the comparative studies may also have arisen because different cell populations were being studied. That is, negative pressure techniques may have a bigger effect on adipocytes, due to their bigger size, while they may have only a minimal effect on smaller cells, including progenitor cells [22]. It is therefore necessary to consider carefully which types of cells from adipose tissue are to be harvested and used. In our study, the outer thigh ADSCs were bigger in diameter in the cell suspension on day 1 after seeding than the abdomen ADSCs. However, the cells were of similar diameters on days 3 and 7.

The function and the representation of cell types in adipose tissue vary among the topographic regions. Preadipocytes and ADSCs obtained from subcutaneous, mesenteric, omental, or intrathoracic fat depots display distinct expression profiles and differentiation capacity [24, 25]. Subcutaneous fat depots are easier to obtain than other fat depots. Although the morphology of subcutaneous and visceral fat did not differ significantly, the harvested subcutaneous ADSCs displayed significantly higher cell numbers, a shorter doubling time, and higher CD146 expression than for visceral ADSCs in later passages [26]. Moreover, within the subcutaneous depots, superficial depots seem to have better stemness and multipotency characteristics of the cells than deep subcutaneous depots [27]. Until now, the harvesting site of fat depots has usually been selected on the basis of actual need or choice. However, the particular anatomic source of adipose tissue harvesting can play a role in further reconstructive surgery and cell-based therapies. The cells from different fat depots express different homeobox (Hox) genes. This supports the idea that they are of different embryonic origin, and so the donor and the host adipose tissue sites need to be carefully matched [28]. Kouidhi et al. compared the gene expression of human knee ADSCs with chin ADSCs [29]. They found more enhanced expression of Pax3 (i.e., a neural crest marker) in chin ADSCs than in knee ADSCs, whereas the expression of most of the Hox genes that are typical for the mesodermal environment was higher in knee ADSCs than in chin ADSCs. In later passages, chin ADSCs also displayed higher self-renewal potential [29]. In our study, we obtained similar numbers and similar viability of ADSCs from the inner thigh area, the outer thigh area, and
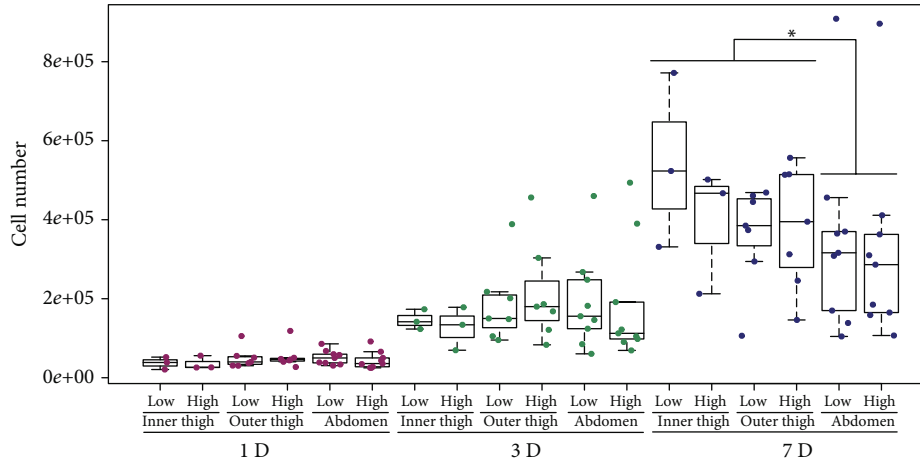
FIGURE 4: The number of ADSCs. The ADSCs were harvested under low pressure and under high pressure from the inner thigh area, the outer thigh area, and the abdomen area. Days 1, 3, and 7; passage 2. On day 7, the thigh ADSCs (i.e., inner thigh+outer thigh) reached significantly higher ($p = 0.048$) cell numbers than the abdomen ADSCs. $p < 0.05$ (*) is for harvesting area significance testing.
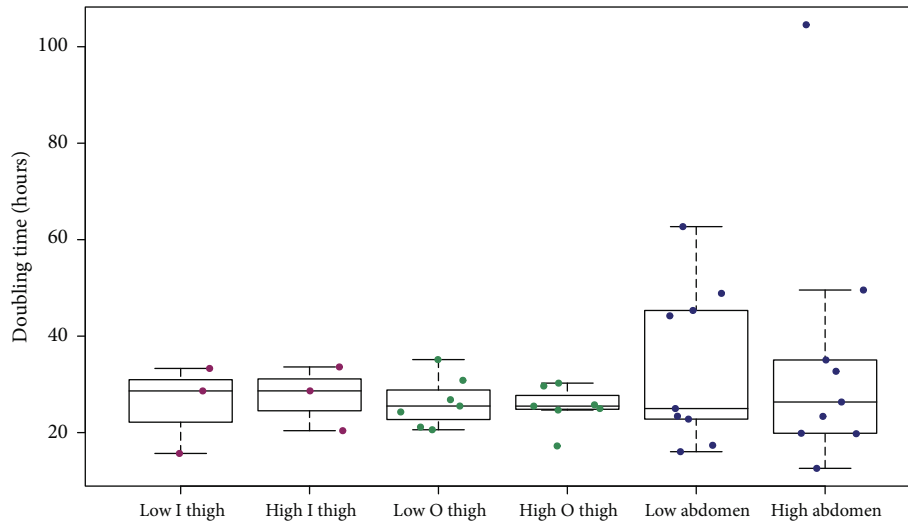

FIGURE 5: Population doubling time. Population doubling time of low-pressure ADSCs and high-pressure ADSCs from the inner thigh ($n = 3$) area, from the outer thigh ($n = 7$) area, and from the abdomen ($n = 9$) area. No significant differences were observed among the groups investigated here.

TABLE 2: The viability of ADSCs. The viability of ADSCs harvested under low pressure and under high pressure from the inner thigh area, from the outer thigh area, and from the abdomen area on days 1, 3, and 7 in passage 2. No significant difference was observed between the outer thigh and the abdomen harvesting sites. The inner thigh region was not statistically compared to the outer thigh and abdomen regions due to the relatively small sample size.

| Group of cells | Viability of ADSCs (%) | | | | | |
| | Day 1 | | Day 3 | | Day 7 | |
	Median	IQ range	Median	IQ range	Median	IQ range
Low I thigh	91.7	90.5-94.6	96.2	93.1-96.5	93.2	92.7-95.8
High I thigh	91.9	89.9-93.2	94.8	92.7-95.3	90.3	88.6-94.6
Low O thigh	93.6	84.8-95.8	93.8	91.2-96.5	95.2	89.4-96.9
High O thigh	93.5	80.7-94.5	96.6	94.3-97.3	95.9	95.6-97.0
Low abdomen	88.0	87.5-90.0	94.6	90.8-95.3	94.8	91.7-97.1
High abdomen	92.4	90.3-93.7	93.5	92.4-95.0	95.2	93.2-97.0

TABLE 3: The diameter of ADSCs. The diameter of ADSCs was measured using the Vi-CELL XR Cell Counter on days 1, 3, and 7; $p < 0.05$ (*) is for harvesting area significance testing (i.e., outer thigh and abdomen). The inner thigh region was not statistically compared to the outer thigh and abdomen regions due to the relatively small sample size.

Group of cells	Diameter of ADSCs (microns)		
	Day 1 Mean ± SD	Day 3 Mean ± SD	Day 7 Mean ± SD
Low I thigh	16.76 ± 0.74	14.67 ± 0.13	12.55 ± 0.38
High I thigh	15.73 ± 0.39	14.92 ± 0.26	12.91 ± 1.18
Low O thigh	16.32 ± 0.82	14.71 ± 1.46	12.97 ± 0.49
High O thigh	17.04 ± 0.80	14.52 ± 1.10	13.77 ± 0.68
Low abdomen	15.67 ± 1.33	14.52 ± 1.48	13.39 ± 0.87
High abdomen	15.70 ± 1.27	14.93 ± 1.43	13.86 ± 1.10

TABLE 4: The cell mitochondrial activity of ADSCs. The cell mitochondrial activity of ADSCs measured on days 3 and 7. No significant difference was observed between the outer thigh and the abdomen harvesting sites. The inner thigh region was not statistically compared to the outer thigh and abdomen regions due to the relatively small sample size.

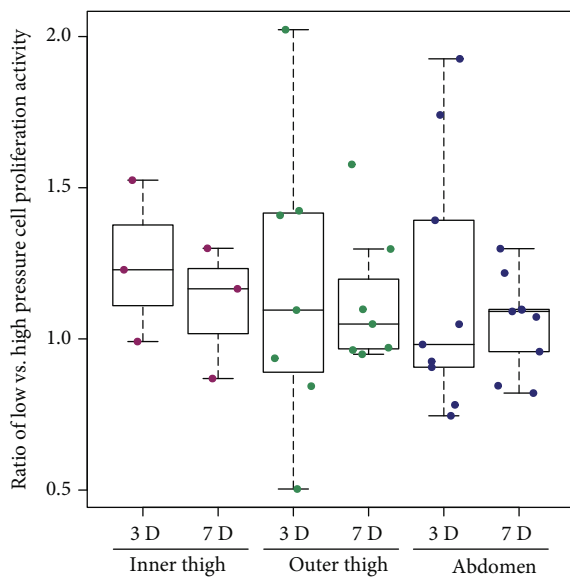| Group of cells	Cell mitochondrial activity (absorbance)	
	Day 3 Mean ± SD	Day 7 Mean ± SD
Low I thigh	0.38 ± 0.25	0.41 ± 0.22
High I thigh	0.34 ± 0.29	0.41 ± 0.31
Low O thigh	0.53 ± 0.17	0.69 ± 0.14
High O thigh	0.52 ± 0.24	0.62 ± 0.10
Low abdomen	0.51 ± 0.25	0.71 ± 0.29
High abdomen	0.47 ± 0.24	0.69 ± 0.29

FIGURE 6: The influence of negative pressure on the mitochondrial activity of ADSCs. The ratio of the mitochondrial activity of low-pressure cells to the mitochondrial activity of high-pressure cells obtained for each donor. The measurements were performed on ADSCs from the inner thigh ($n = 3$) area, from the outer thigh ($n = 7$) area, and from the abdomen ($n = 9$) area on day 3 (3D) and on day 7 (7D). No significant differences among the observed groups were observed.

the abdomen area on days 1 and 3. Thus, our results are in accordance with studies by other researchers, in which similar growth kinetics were found in ADSCs from the abdomen area and from the hip/thigh area [12, 30]. However, with similar cell numbers on days 1 and 3, we observed a tendency of thigh ADSCs (inner thigh+outer thigh) to reach higher values than abdomen ADSCs on day 7 ($p = 0.048$). It therefore seems that there may be a significant difference in later cell numbers between the harvesting sites for most of the patients included in our study, though we observed large variation among the donors. Interestingly, we also observed a tendency toward lower mitochondrial activity of inner thigh

ADSCs than of outer thigh ADSCs and abdomen ADSCs on day 7. These results may correspond with the slightly higher cell numbers of inner thigh ADSCs on day 7, when the cells have already reached confluence and have reduced their proliferation activity. However, the smaller number of inner thigh ADSC samples than in the case of other groups (i.e., outer thigh ADSCs and abdomen ADSC) may also have affected the results. The harvesting site can also influence the colony-forming unit (CFU) in isolated ADSCs. Fraser et al. observed that the CFU was higher in hip ADSCs than in abdomen ADSCs [22]. This finding could be in accordance with a higher proliferation rate of hip/thigh ADSCs in later time intervals of the culture [22].

During our experiments, we observed a nonparametric distribution of the donors' data. The interdonor variabilities that were not dependent on the harvesting site or on negative pressure may have been caused by other donor factors. Age and BMI are other factors known to play a considerable role in SVF and ADSC yields and characteristics [19]. However, research findings regarding the influence of age and BMI on ADSC yields are often contradictory [31–33]. For example, in the study by de Girolamo et al., the cellular yield of ADSCs was significantly greater from older patients than from younger patients [31], while in the study by Faustini et al., the patient's age seemed not to influence the cell yield [32]. Significant donor-to-donor variability has also been reported in multilineage differentiation capacity, self-renewal capacity, and immunomodulatory cytokine secretion [34]. Although some of these variabilities can be explained by a medical history of breast cancer and subsequent treatment, there were also significant differences among donors who had not been diagnosed with cancer [34]. Atherosclerosis is another donor factor which can alter the secretome and reduce the immunomodulatory capacity of ADSCs due to impaired mitochondrial functions [35]. In addition, the ADSCs isolated from patients with renovascular disease exhibited a higher level of DNA damage and lower migratory capacity than ADSCs from healthy donors [36]. In another study, ADSCs isolated from patients suffering

TABLE 5: The percentage of CD surface markers in ADSCs. The percentage of CD105-, CD90-, CD73-, CD29-, CD146-, CD45-, CD31-, and CD34-positive ADSCs. No significant difference was observed between the outer thigh and the abdomen harvesting sites. The inner thigh region was not statistically compared to the outer thigh and abdomen regions due to the relatively small sample size.

Group of cells	CD markers (% positive cells)							
	CD105		CD90		CD73		CD29	
	Median	IQ range	Median	IQ range	Median	IQ range	Median	IQ range
Low I thigh	99.9	99.2-99.9	99.5	99.5-99.7	99.9	99.8-100	99.8	99.2-100
High I thigh	99.9	94.1-99.9	99.6	99.3-99.8	99.9	99.9-100	99.8	99.8-100
Low O thigh	99.9	98.3-100	99.6	99.2-99.9	100	99.9-100	99.8	99.8-100
High O thigh	99.9	96.2-99.9	99.6	99.2-99.9	100	99.9-100	99.9	99.8-100
Low abdomen	99.5	82.3-99.9	99.4	97.5-99.8	99.8	99.6-99.9	99.6	90.5-99.8
High abdomen	98.9	89.1-99.8	99.5	97.3-99.8	99.8	99.6-99.9	99.6	95.1-99.8

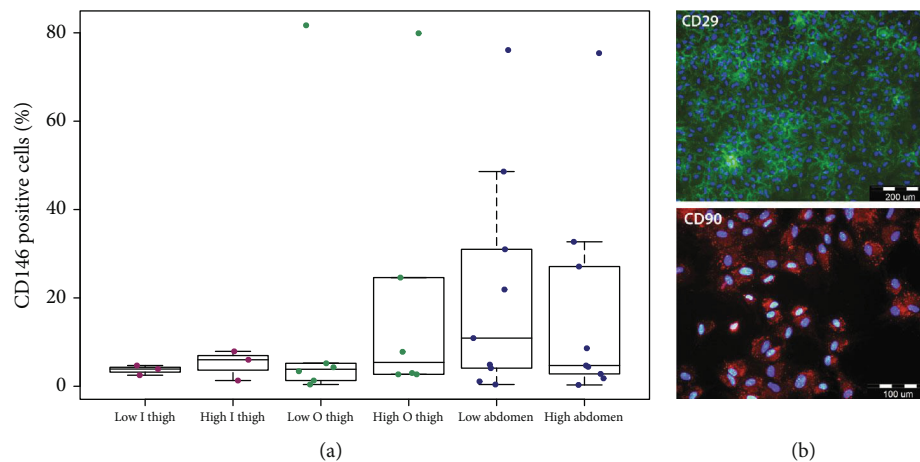| Group of cells	CD markers (% positive cells)							
	CD146		CD45		CD31		CD34	
	Median	IQ range	Median	IQ range	Median	IQ range	Median	IQ range
Low I thigh	3.9	2.9-4.5	4.3	3.9-4.7	0.5	0.3-1.0	0.4	0.3-0.7
High I thigh	6.0	2.5-7.4	3.3	2.9-4.0	0.8	0.4-1.0	0.8	0.4-1.7
Low O thigh	3.9	1.3-5.2	1.8	1.5-6.9	0.5	0.2-0.7	1.1	0.4-6.3
High O thigh	5.4	2.7-24.6	1.8	1.1-12.6	0.6	0.1-2.4	0.9	0.3-6.1
Low abdomen	10.9	3.4-35.4	5.2	4.5-7.5	0.3	0.2-0.5	1.0	0.5-1.6
High abdomen	4.7	2.6-28.5	4.1	3.1-5.4	0.4	0.2-1.0	0.9	0.5-1.7

FIGURE 7: (a) The percentage of CD146-positive cells in each group of cells. No significant differences among the harvesting sites were observed. (b) The immunofluorescence staining of CD29 and CD90 in ADSCs. Cell nuclei are counterstained with Hoechst 33342. Olympus microscope IX71. Scale bar 200 μm (CD29) and 100 μm (CD90).

from scleroderma, an autoimmune connective tissue disease, showed a lower proliferation rate and lower migration capacity than in the control ADSCs from healthy donors [37].

Many papers have reported on various donor-to-donor factors that have a potential impact on the characteristics of mesenchymal stromal cells. In addition, it seems that there are many cell-to-cell variations within the same donor. This cell-to-cell heterogeneity can be manifested both *in vitro* and *in vivo* by interclonal functional and molecular variation, e.g., variable differentiation capacity, existing fast-growing and slow-growing clones, and other differences in proteome and transcriptome [38]. The percentage of various clones in MSCs develops and changes during cell passaging. Even

within a single MSC clone, there is a growing body of evidence that the intraclonal heterogeneity alters cell behaviour and characteristics [38].

In most of the donors, we proved a high level of positivity of the isolated cells for CD105, CD90, CD73, and CD29 (>80% in ADSCs) and a low level of positivity or absence of CD45, CD31, and CD33 (≤2% in ADSCs), according to the guidelines for characterizing ADSCs [39]. We observed no significant differences in the presence of CD markers depending on negative pressure or on harvesting site. Our results are in accordance with those reported by other researchers, who have found no differences in CD markers in SVF harvested from different sites [12, 14, 30]. In another

study, the presence of pericytes, progenitor endothelial cells, preadipocyte cells, and mesenchymal cells in SVF was not influenced by different negative pressures [9]. In addition, in the study by Chen et al., where higher negative pressure had a negative influence on yields, on growth, and on the secretion of growth factors, no differences in CD markers were found [11]. Interestingly, we observed variability in the presence of CD146 among the donors. The presence of CD146$^+$ cells in subcutaneous depots was also not negligible in a study by Lee et al. [26]. CD146 positivity can be a sign of pericytes. Pericytes are cells in contact with small vessels in the adipose tissue, and they are also present in the harvested SVF [40]. The origin of the pericyte is not the only possible explanation. For a review of other theories explaining the presence of CD146, see [41]. In MSCs, high expression of CD146 is associated with a commitment towards vascular smooth muscle cell lineage [42]. This commitment could be interesting for vascular tissue engineering, when differentiating ADSCs towards vascular smooth muscle cells is required. CD146$^+$ cells in combination with human umbilical vein endothelial cells (HUVECs) were also reported to support the formation and the elongation of capillary-like tubular structures [26]. Lee et al. also observed greater proliferation of CD146$^+$ cells than of CD146$^-$ cells; however, the percentage of CD146$^+$ cells in an ADSC culture decreased with subsequent subculturing [26]. It seems that the CD146 expression among ADSCs is relatively heterogeneous and could play an important role in potential specific tissue engineering applications. The presence of other hematopoietic and endothelial cell markers (e.g., CD34, CD45, and CD31) can influence future therapies using SVF or ADSCs. The optimal ratio of ADSCs and hematopoietic stem cell progenitors in isolated SVF defined by specific CD surface markers seems to be the key for successful stem cell therapies [43].

4.1. Limitation. The first limitation of our study is the relatively small sample size, with uneven numbers of samples from each donor site (i.e., inner thigh ($n = 3$), outer thigh ($n = 7$), and abdomen ($n = 9$)). Due to the smallest sample size of inner thigh ADSCs, we did not make a statistical comparison between this group of cells and outer thigh ADSCs or abdomen ADSCs. A greater number of donors would be desirable. However, we assume that for ADSC characterization under *in vitro* culture conditions and for later tissue engineering purposes, the sample size is sufficient.

The second limitation of the study is that it was primarily focused on negative pressure and on the harvesting site and not on other patient factors, such as age, gender, or BMI; these other characteristics were therefore not completely uniform among the donors. Nevertheless, the studied groups showed similar age and BMI parameters with normal data distribution.

The third limitation of the study is that it was focused on the later use of ADSCs in tissue engineering. Therefore, we characterized only the fraction of isolated ADSCs that adhered to the plastic culture flasks. The yields of ADSCs were counted after they had adhered to the flasks, and their characteristics (cell proliferation, flow cytometry analysis of surface markers) were studied in subsequent passages. No

other cell types (i.e., adipocytes or all nucleated cells) were analysed in this study with respect to their yields or their viability. The conclusions concerning the influence of negative pressure and harvesting site therefore refer only to plastic-adherent ADSCs.

To characterize the ADSCs in *in vitro* culture conditions, we chose passage 1 and passage 2 depending on specific analyses. These passages were the same for all analysed ADSCs. However, the growth dynamics of the cells is known to vary from passage to passage, and this variability can also be specific in each isolated ADSC population.

5. Conclusion

In our study, we observed a significantly higher number of initially attached cells per 1 mL of lipoaspirate for the outer thigh region than for the abdomen region on day 1 after isolation. Different negative pressure was not the key determinant factor for cell yields of the outer thigh region, whereas high negative pressure had a positive influence on the cell yields of the abdomen region. However, for the subsequent culturing, no significant relationship was identified between the characteristics of isolated ADSCs and the level of negative pressure used during liposuction. In addition, the harvesting site influenced the ADSCs only mildly in some parameters on specific days of the culture (i.e., diameter on day 1). In general, no significant influence of the harvesting site was observed on the cell number, mitochondrial activity, viability, diameter, or on the presence of CD markers. These thigh ADSCs reached a higher cell number than for abdomen ADSCs on day 7 only in cases where cells from the inner thigh and outer thigh areas were evaluated together. However, we observed donor-to-donor variability in initial adhesion, in absolute cell numbers, and in the expression of some CD markers. Thus, our results could suggest that donor-to-donor differences may be affected not only by the harvesting site and by negative pressure but also by other factors. For subsequent *in vitro* culturing and use in tissue engineering, it seems that the harvesting site and the level of negative pressure do not have a crucial or limiting effect on basic ADSC characteristics. Nevertheless, it is necessary to make a thorough investigation of the area from which ADSCs are to be harvested and the specific liposuction procedure that is to be used, with reference to the purpose for which the adipose tissue is being harvested.

Abbreviations

ADSC: Adipose tissue-derived stromal cell
BMSC: Bone marrow mesenchymal stromal cell
BMI: Body mass index
BSA: Bovine serum albumin
DMEM: Dulbecco's modified Eagle medium
DT: Doubling time
FBS: Foetal bovine serum
FGF2: Fibroblast growth factor basic
IQ range: Interquartile range
MSC: Mesenchymal stromal cell
SVF: Stromal vascular fraction.

Data Availability

Data can be requested from the corresponding author on reasonable request.

Ethical Approval

The study was approved by the Ethics Committee of Hospital Na Bulovce in Prague (August 21, 2014). No animals were used in this study.

Consent

All participants in the study gave informed written consent.

Conflicts of Interest

The authors declare that they have no conflict of interest.

Acknowledgments

References

[1] L. A. Marquez-Curtis, A. Janowska-Wieczorek, L. E. McGann, and J. A. Elliott, "Mesenchymal stromal cells derived from various tissues: biological, clinical and cryopreservation aspects," *Cryobiology*, vol. 71, no. 2, pp. 181–197, 2015.

[2] S. Kern, H. Eichler, J. Stoeve, H. Klüter, and K. Bieback, "Comparative analysis of mesenchymal stem cells from bone marrow, umbilical cord blood, or adipose tissue," *Stem Cells*, vol. 24, no. 5, pp. 1294–1301, 2006.

[3] L. Bacakova, J. Zarubova, M. Travnickova et al., "Stem cells: their source, potency and use in regenerative therapies with focus on adipose-derived stem cells - a review," *Biotechnology Advances*, vol. 36, no. 4, pp. 1111–1126, 2018.

[4] F. Simonacci, N. Bertozzi, and E. Raposio, "Off-label use of adipose-derived stem cells," *Annals of Medicine and Surgery*, vol. 24, pp. 44–51, 2017.

[5] P. Bora and A. S. Majumdar, "Adipose tissue-derived stromal vascular fraction in regenerative medicine: a brief review on biology and translation," *Stem Cell Research & Therapy*, vol. 8, no. 1, p. 145, 2017.

[6] E. Raposio, F. Simonacci, and R. E. Perrotta, "Adipose-derived stem cells: comparison between two methods of isolation for clinical applications," *Annals of Medicine and Surgery*, vol. 20, pp. 87–91, 2017.

[7] B. T. Estes, B. O. Diekman, J. M. Gimble, and F. Guilak, "Isolation of adipose-derived stem cells and their induction to a chondrogenic phenotype," *Nature Protocols*, vol. 5, no. 7, pp. 1294–1311, 2010.

[8] J. H. Lee, J. C. Kirkham, M. C. McCormack, A. M. Nicholls, M. A. Randolph, and W. G. Austen Jr., "The effect of pressure and shear on autologous fat grafting," *Plastic and Reconstructive Surgery*, vol. 131, no. 5, pp. 1125–1136, 2013.

[9] L. Charles-de-Sá, N. F. Gontijo de Amorim, D. Dantas et al., "Influence of negative pressure on the viability of adipocytes and mesenchymal stem cell, considering the device method used to harvest fat tissue," *Aesthetic Surgery Journal*, vol. 35, no. 3, pp. 334–344, 2015.

[10] A. Mojallal, C. Auxenfans, C. Lequeux, F. Braye, and O. Damour, "Influence of negative pressure when harvesting adipose tissue on cell yield of the stromal-vascular fraction," *Bio-medical Materials and Engineering*, vol. 18, no. 4-5, pp. 193–197, 2008.

[11] Y. W. Chen, J. R. Wang, X. Liao et al., "Effect of suction pressures on cell yield and functionality of the adipose- derived stromal vascular fraction," *Journal of Plastic, Reconstructive & Aesthetic Surgery*, vol. 70, no. 2, pp. 257–266, 2017.

[12] W. J. F. M. Jurgens, M. J. Oedayrajsingh-Varma, M. N. Helder et al., "Effect of tissue-harvesting site on yield of stem cells derived from adipose tissue: implications for cell-based therapies," *Cell and Tissue Research*, vol. 332, no. 3, pp. 415–426, 2008.

[13] A. V. Padoin, J. Braga-Silva, P. Martins et al., "Sources of processed lipoaspirate cells: influence of donor site on cell concentration," *Plastic and Reconstructive Surgery*, vol. 122, no. 2, pp. 614–618, 2008.

[14] A. Tsekouras, D. Mantas, D. I. Tsilimigras, D. Moris, M. Kontos, and G. C. Zografos, "Comparison of the viability and yield of adipose-derived stem cells (ASCs) from different donor areas," *In Vivo*, vol. 31, no. 6, pp. 1229–1234, 2017.

[15] A. A. Lim, K. Fan, K. A. Allam et al., "Autologous fat transplantation in the craniofacial patient: the UCLA experience," *The Journal of Craniofacial Surgery*, vol. 23, no. 4, pp. 1061–1066, 2012.

[16] K. Small, M. Choi, O. Petruolo, C. Lee, and N. Karp, "Is there an ideal donor site of fat for secondary breast reconstruction?," *Aesthetic Surgery Journal*, vol. 34, no. 4, pp. 545–550, 2014.

[17] R. J. Rohrich, E. S. Sorokin, and S. A. Brown, "In search of improved fat transfer viability: a quantitative analysis of the role of centrifugation and harvest site," *Plastic and Reconstructive Surgery*, vol. 113, no. 1, pp. 391–395, 2004.

[18] T. Iyyanki, J. Hubenak, J. Liu, E. I. Chang, E. K. Beahm, and Q. Zhang, "Harvesting technique affects adipose-derived stem cell yield," *Aesthetic Surgery Journal*, vol. 35, no. 4, pp. 467–476, 2015.

[19] J. Varghese, M. Griffin, A. Mosahebi, and P. Butler, "Systematic review of patient factors affecting adipose stem cell viability and function: implications for regenerative therapy," *Stem Cell Research & Therapy*, vol. 8, no. 1, pp. 1–15, 2017.

[20] A. Przekora, M. Vandrovcova, M. Travnickova et al., "Evaluation of the potential of chitosan/β-1,3-glucan/hydroxyapatite material as a scaffold for living bone graft production in vitro by comparison of ADSC and BMDSC behaviour on its surface," *Biomedical Materials*, vol. 12, no. 1, article 015030, 2017.

[21] M. J. Oedayrajsingh-Varma, S. M. van Ham, M. Knippenberg et al., "Adipose tissue-derived mesenchymal stem cell yield and growth characteristics are affected by the tissue-harvesting procedure," *Cytotherapy*, vol. 8, no. 2, pp. 166–177, 2006.

[22] J. K. Fraser, I. Wulur, Z. Alfonso, M. Zhu, and E. S. Wheeler, "Differences in stem and progenitor cell yield in different subcutaneous adipose tissue depots," *Cytotherapy*, vol. 9, no. 5, pp. 459–467, 2007.

[23] T. Cheriyan, H. K. Kao, X. Qiao, and L. Guo, "Low harvest pressure enhances autologous fat graft viability," *Plastic and Reconstructive Surgery*, vol. 133, no. 6, pp. 1365–1368, 2014.

[24] T. Tchkonia, M. Lenburg, T. Thomou et al., "Identification of depot-specific human fat cell progenitors through distinct expression profiles and developmental gene patterns," *American Journal of Physiology-Endocrinology and Metabolism*, vol. 292, no. 1, pp. E298–E307, 2007.

[25] V. Russo, C. Yu, P. Belliveau, A. Hamilton, and L. E. Flynn, "Comparison of human adipose-derived stem cells isolated from subcutaneous, omental, and intrathoracic adipose tissue depots for regenerative applications," *Stem Cells Translational Medicine*, vol. 3, no. 2, pp. 206–217, 2014.

[26] N. E. Lee, S. J. Kim, S. J. Yang et al., "Comparative characterization of mesenchymal stromal cells from multiple abdominal adipose tissues and enrichment of angiogenic ability via CD146 molecule," *Cytotherapy*, vol. 19, no. 2, pp. 170–180, 2017.

[27] G. Di Taranto, C. Cicione, G. Visconti et al., "Qualitative and quantitative differences of adipose-derived stromal cells from superficial and deep subcutaneous lipoaspirates: a matter of fat," *Cytotherapy*, vol. 17, no. 8, pp. 1076–1089, 2015.

[28] C. Dani, R. Foissac, A. Ladoux, and B. Chignon-Sicard, "Autologous fat grafts: can we match the donor fat site and the host environment for better postoperative outcomes and safety?," *Current Surgery Reports*, vol. 5, no. 7, p. 14, 2017.

[29] M. Kouidhi, P. Villageois, C. M. Mounier et al., "Characterization of human knee and chin adipose-derived stromal cells," *Stem Cells International*, vol. 2015, Article ID 592090, 11 pages, 2015.

[30] K. A. Iwen, A. C. Priewe, M. Winnefeld et al., "Gluteal and abdominal subcutaneous adipose tissue depots as stroma cell source: gluteal cells display increased adipogenic and osteogenic differentiation potentials," *Experimental Dermatology*, vol. 23, no. 6, pp. 395–400, 2014.

[31] L. de Girolamo, S. Lopa, E. Arrigoni, M. F. Sartori, F. W. Baruffaldi Preis, and A. T. Brini, "Human adipose-derived stem cells isolated from young and elderly women: their differentiation potential and scaffold interaction during in vitro osteoblastic differentiation," *Cytotherapy*, vol. 11, no. 6, pp. 793–803, 2009.

[32] M. Faustini, M. Bucco, T. Chlapanidas et al., "Nonexpanded mesenchymal stem cells for regenerative medicine: yield in stromal vascular fraction from adipose tissues," *Tissue Engineering Part C: Methods*, vol. 16, no. 6, pp. 1515–1521, 2010.

[33] H. J. Yang, K. J. Kim, M. K. Kim et al., "The stem cell potential and multipotency of human adipose tissue-derived stem cells vary by cell donor and are different from those of other types of stem cells," *Cells, Tissues, Organs*, vol. 199, no. 5-6, pp. 373–383, 2014.

[34] A. M. Parsons, D. M. Ciombor, P. Y. Liu, and E. M. Darling, "Regenerative potential and inflammation-induced secretion profile of human adipose-derived stromal vascular cells are influenced by donor variability and prior breast cancer diagnosis," *Stem Cell Reviews*, vol. 14, no. 4, pp. 546–557, 2018.

[35] O. Kizilay Mancini, M. Lora, A. Cuillerier et al., "Mitochondrial oxidative stress reduces the immunopotency of mesenchymal stromal cells in adults with coronary artery disease," *Circulation Research*, vol. 122, no. 2, pp. 255–266, 2018.

[36] A. Saad, X. Y. Zhu, S. Herrmann et al., "Adipose-derived mesenchymal stem cells from patients with atherosclerotic renovascular disease have increased DNA damage and reduced angiogenesis that can be modified by hypoxia," *Stem Cell Research & Therapy*, vol. 7, no. 1, p. 128, 2016.

[37] M. Griffin, C. M. Ryan, O. Pathan, D. Abraham, C. P. Denton, and P. E. M. Butler, "Characteristics of human adipose derived stem cells in scleroderma in comparison to sex and age matched normal controls: implications for regenerative medicine," *Stem Cell Research & Therapy*, vol. 8, p. 23, 2017.

[38] C. M. McLeod and R. L. Mauck, "On the origin and impact of mesenchymal stem cell heterogeneity: new insights and emerging tools for single cell analysis," *European Cells and Materials*, vol. 34, pp. 217–231, 2017.

[39] P. Bourin, B. A. Bunnell, L. Casteilla et al., "Stromal cells from the adipose tissue-derived stromal vascular fraction and culture expanded adipose tissue-derived stromal/stem cells: a joint statement of the International Federation for Adipose Therapeutics and Science (IFATS) and the International Society for Cellular Therapy (ISCT)," *Cytotherapy*, vol. 15, no. 6, pp. 641–648, 2013.

[40] L. Zimmerlin, V. S. Donnenberg, M. E. Pfeifer et al., "Stromal vascular progenitors in adult human adipose tissue," *Cytometry: Part A*, vol. 77, no. 1, pp. 22–30, 2010.

[41] A. Bajek, N. Gurtowska, J. Olkowska, L. Kazmierski, M. Maj, and T. Drewa, "Adipose-derived stem cells as a tool in cell-based therapies," *Archivum Immunologiae et Therapiae Experimentalis*, vol. 64, no. 6, pp. 443–454, 2016.

[42] N. Espagnolle, F. Guilloton, F. Deschaseaux, M. Gadelorge, L. Sensébé, and P. Bourin, "CD146 expression on mesenchymal stem cells is associated with their vascular smooth muscle commitment," *Journal of Cellular and Molecular Medicine*, vol. 18, no. 1, pp. 104–114, 2014.

[43] M. O. Kilinc, A. Santidrian, I. Minev et al., "The ratio of ADSCs to HSC-progenitors in adipose tissue derived SVF may provide the key to predict the outcome of stem-cell therapy," *Clinical and Translational Medicine*, vol. 7, no. 1, p. 5, 2018.

Research review paper

Stem cells: their source, potency and use in regenerative therapies with focus on adipose-derived stem cells – a review

Lucie Bacakova[a,*], Jana Zarubova[a], Martina Travnickova[a], Jana Musilkova[a], Julia Pajorova[a], Petr Slepicka[b], Nikola Slepickova Kasalkova[b], Vaclav Svorcik[b], Zdenka Kolska[c], Hooman Motarjemi[d], Martin Molitor[d]

[a] Department of Biomaterials and Tissue Engineering, Institute of Physiology of the Czech Academy of Sciences, Videnska 1083, 14220 Prague, 4-Krc, Czech Republic
[b] Department of Solid State Engineering, University of Chemistry and Technology Prague, Technicka 5, 166 28 Prague, 6-Dejvice, Czech Republic
[c] Faculty of Science, J.E. Purkyne University, Ceske mladeze 8, 400 96 Usti nad Labem, Czech Republic
[d] Clinic of Plastic Surgery, Faculty Hospital Na Bulovce, Budinova 67/2, 180 81 Prague, 8-Liben, Czech Republic

ARTICLE INFO

ABSTRACT

Stem cells can be defined as units of biological organization that are responsible for the development and the regeneration of organ and tissue systems. They are able to renew their populations and to differentiate into multiple cell lineages. Therefore, these cells have great potential in advanced tissue engineering and cell therapies. When seeded on synthetic or nature-derived scaffolds in vitro, stem cells can be differentiated towards the desired phenotype by an appropriate composition, by an appropriate architecture, and by appropriate physicochemical and mechanical properties of the scaffolds, particularly if the scaffold properties are combined with a suitable composition of cell culture media, and with suitable mechanical, electrical or magnetic stimulation. For cell therapy, stem cells can be injected directly into damaged tissues and organs in vivo. Since the regenerative effect of stem cells is based mainly on the autocrine production of growth factors, immunomodulators and other bioactive molecules stored in extracellular vesicles, these structures can be isolated and used instead of cells for a novel therapeutic approach called "stem cell-based cell-free therapy". There are four main sources of stem cells, i.e. embryonic tissues, fetal tissues, adult tissues and differentiated somatic cells after they have been genetically reprogrammed, which are referred to as induced pluripotent stem cells (iPSCs). Although adult stem cells have lower potency than the other three stem cell types, i.e. they are capable of differentiating into only a limited quantity of specific cell types, these cells are able to overcome the ethical and legal issues accompanying the application of embryonic and fetal stem cells and the mutational effects associated with iPSCs. Moreover, adult stem cells can be used in autogenous form. These cells are present in practically all tissues in the organism. However, adipose tissue seems to be the most advantageous tissue from which to isolate them, because of its abundancy, its subcutaneous location, and the need for less invasive techniques. Adipose tissue-derived stem cells (ASCs) are therefore considered highly promising in present-day regenerative medicine.

1. Introduction

The need to replace or regenerate damaged tissues is ever-increasing, due to age-related and other degenerative diseases, tumors, trauma and congenital defects. The first choice in regenerative therapy is to reconstruct damaged tissues using differentiated cells obtained by biopsy, expanded in vitro and seeded on appropriate scaffolds, made of artificial and/or natural materials. Differentiated cells have the correct phenotype for a given application, and perform desired biological functions, e.g. they produce the extracellular matrix (ECM) in correct organization, secrete specific signaling molecules, and interact properly with neighboring cells and tissues. However, the usage of differentiated cells in tissue engineering applications is often limited by low quantity of the harvested cells and by their low proliferation potential while they are expanding in vitro. This is particularly true in aged and polymorbid patients, who especially need regenerative therapies (for a review, see Ikada, 2006; Shekkeris et al., 2012). Although some organs, e.g. the liver, have a high regenerative capacity in vivo, the cultivation and expansion of cells from these organs may be complicated in vitro (for a review, see Atala, 2005).

Advanced regenerative therapies are therefore concentrated on stem cells, which can be used (1) for direct application to damaged sites, i.e.

for cell therapy, or (2) for tissue engineering, using appropriate scaffolds as carriers for these cells. The application of stem cells is considered to be more advantageous than the use of differentiated cells, because stem cells can be obtained more easily and in larger quantities, have a much higher proliferation capacity, withstand more passages, undergo senescence later, can be differentiated into a wide range of desired cell phenotypes, and also support the vascularization of scaffolds (for a review, see Shekkeris et al., 2012; Zhang et al., 2012; Mizuno et al., 2013).

Stem cells can be defined as units of organization of biological systems that are responsible for the regeneration and development of organs and tissues. These cells can also be considered as units of evolution via natural selection. Stem cells are undifferentiated cells with clonogenic potential that are capable of self-renewal and differentiation into multiple cell lineages (Weissman, 2000; Weissman, 2015; Dulak et al., 2015). In tissue engineering in vitro, this differentiation can be induced by growing the cells on scaffolds with an appropriate composition, architecture, physicochemical and mechanical properties. For example, coating the growth supports with laminin and vitronectin enhanced the differentiation of murine cardiovascular progenitor cells (i.e., cells obtained by differentiation of stem cells from mouse embryos) towards endothelial cells, while coating with fibronectin supported differentiation towards vascular smooth muscle cells (Gluck et al., 2014). The three-dimensional architecture of nanofibrous scaffolds fabricated from poly(ε-caprolactone), i.e. PCL, stimulated the differentiation of mesenchymal stem cells (MSCs), obtained from the bone marrow of miniature pigs, into osteoblasts more successfully than 2D nanofibrous PCL scaffolds (Rampichova et al., 2013). Chondrogenic differentiation of stem cells obtained from the adipose tissue of rats (ASCs) was controlled by the hydrophilicity of PCL scaffolds, adjusted by blending PCL with a triblock copolymer of PCL-polytetrahydrofuran-PCL (Vaikkath et al., 2016). In chitosan-based scaffolds, the osteogenic differentiation of ASCs was negatively correlated with the scaffold porosity, i.e. it was the highest at the lowest porosity of 10% (Ardeshirylajimi et al., 2018).

The stiffness of the scaffolds has also been shown to be an important regulator of stem cell differentiation. On very soft collagen-coated polyacrylamide gels (elastic modulus from 0.1 to 1.0 kPa), having mechanical characteristics similar to those of brain tissue, MSCs derived from the bone marrow differentiated towards neurons. On stiffer gels (elastic modulus from 8 to 17 kPa), mimicking the muscle tissue, the cells became myogenic, and on the stiffest matrices (elastic modulus from 25 to 40 kPa), the cells differentiated towards osteoblasts (Engler et al., 2006; for a review, see Bacakova et al., 2011). Similar results were also achieved with human umbilical cord stem cells cultivated on collagen-coated polyacrylamide gels of varied stiffness (Witkowska-Zimny et al., 2012). The substrate stiffness was also decisive for the differentiation of ASCs towards adipocytes or osteoblasts. On polydimethylsiloxane substrates, softer matrices supported adipogenic cell differentiation, while the stiffer matrices were beneficial for osteogenic cell differentiation, associated with a higher expression of the Ras homolog family member A (RhoA), Rho associated coiled coil containing protein kinase 2 (ROCK-1/-2), and proteins involved in the Wnt/β-catenin signaling pathway (Zhang et al., 2018a). In crosslinked hyaluronan hydrogel substrates, the matrix stiffness also markedly influenced the chondrogenic potential of ASCs (Teong et al., 2018).

Another important factor is a suitable composition of the cell cultivation media, especially the presence of specific growth factors and other biomolecules in this media. For example, differentiation of stem cells towards endothelial cells requires the supplementation of vascular endothelial growth factor (VEGF) (Colazzo et al., 2014; for a review, see Dan et al., 2015). Vascular smooth muscle cell differentiation was stimulated by the presence of transforming growth factor-β (TGF-β) (Park et al., 2013a; for a review, see Dan et al., 2015), neurogenic differentiation was stimulated by the presence of forskolin and valproic acid (New et al., 2015), and osteogenic cell differentiation by the presence of

β-glycerol phosphate, ascorbic acid, dexamethasone (Juhasova et al., 2011; Tirkkonen et al., 2013) and dihydroxyvitamin D_3 (Olivares-Navarrete et al., 2012; Logovskaya et al., 2013).

The third important factor promoting the differentiation of stem cells in vitro towards a desired phenotype is mechanical stimulation, mimicking the load to which the cells are exposed under physiological conditions in vivo. For example, the differentiation of stem cells towards endothelial cell phenotype is stimulated by laminar shear stress (Fischer et al., 2009; Colazzo et al., 2014; for a review, see Dan et al., 2015), differentiation towards smooth muscle cell phenotype is stimulated by uniaxial cyclic strain (Lee et al., 2007; Park et al., 2012), differentiation towards osteoblasts by vibrational stress (Prè et al., 2011) and towards keratinocytes by pressure stress (Kobayashi et al., 2014) or by uniaxial strain (Powell et al., 2010).

The effects of mechanical stimulation can be substituted, at least partly, by electrical stimulation or stimulation by a magnetic field, which has been used e.g. for differentiation of stem cells towards neuronal cells (Jaatinen et al., 2015; Ma et al., 2016), cardiomyocytes (Bekhite et al., 2013; Llucià-Valldeperas et al., 2015), skeletal myocytes (Birk et al., 2014; Wan et al., 2016), endothelial cells (Sauer et al., 2005), osteoblasts (Ross et al., 2015; Petecchia et al., 2015; Arjmand et al., 2018), chondrocytes (Mardani et al., 2016) and tendon cells (Gonçalves et al., 2016). In addition to these factors, which tend to be of a physiological character, the differentiation of stem cells can also be programmed by genetic manipulations. For example, ASCs transfected by (sex determining region Y)-box 2 (Sox2) gene and cultured in a neurogenic cell culture medium differentiated into neuron-like cells, which expressed markers of neurogenic cell differentiation, e.g. genes encoding microtubule-associated protein 2 (MAP2) and Tuj1 (class III beta-tubulin) at mRNA and protein level (Qin et al., 2015).

In order to achieve a high level of stem cell differentiation towards a desired phenotype, all the factors mentioned above have been applied in various combinations, usually at least two of these factors consecutively (Ferroni et al., 2016) or, more frequently, at the same time (Park et al., 2012; Birk et al., 2014; Colazzo et al., 2014; Zhang et al., 2018a).

When stem cells are injected directly into damaged tissues and organs in vivo, their regenerative effects are based mainly on the autocrine production of a wide spectrum of bioactive molecules, e.g. growth factors, cytokines, chemokines, antiapoptotic factors and immunomodulators in the form of proteins of small RNA species (Maumus et al., 2013; Gallina et al., 2015; Kuo et al., 2016). The bioactive molecules synthesized in stem cells are stored in extracellular vesicles, which can be collected from the media conditioned by stem cells and administered systemically or locally into damaged tissues. This approach is referred to as stem cell-based cell-free therapy (Kupcova Skalnikova, 2013; Baglio et al., 2015; Konala et al., 2016; Marote et al., 2016; Prochazka et al., 2016).

The first, more general part of this review is focused on the sources from which stem cells can be obtained, and on the potency of stem cells from different sources, i.e., on their capability to differentiate into specific cell types. The second, more specialized part of the review is concentrated on ASCs, i.e. their cultivation, expansion, characterization, differentiation and use in tissue engineering and in cell therapies, including the shared experience of the members of the authorial team.

2. Sources and potency of stem cells

For purposes of tissue engineering and cell therapies, stem cells are usually obtained from four basic sources. The main sources are (1) embryonic tissue, (2) fetal tissues, such as fetus, placenta (i.e., amnion and chorion), amniotic fluid and umbilical cord (Wharton jelly, blood), (3) specific locations in the adult organism, e.g. fat, bone marrow, skeletal muscle, skin or blood (for more details, see below), and (4) differentiated somatic cells after they have been genetically reprogrammed, i.e., iPSCs (Table 1).

Table 1
Sources and potency of stem cells for regenerative therapies

Stem cells	Source		Potency	Reference
Embryonic	Morula		Totipotent	Kucia et al., 2007; Can, 2008
	Blastocyst		Pluripotent	Weissman, 2000; Weissman, 2015; Kucia et al., 2007; Jean et al., 2013; Dulak et al., 2015
Fetal	Fetus		Multipotent Pluripotent	Chen et al., 2011; Jiao et al., 2012; Kerr et al., 2008; Hua et al., 2009
	Extrafetal tissues	Placenta (amnion, chorion)	Multipotent, pluripotent	Bryzek et al., 2013; Jaramillo-Ferrada et al., 2012
		Amniotic fluid	Multipotent, pluripotent	Da Sacco et al., 2011
		Wharton jelly in the umbilical cord	Multipotent, pluripotent	Van Pham et al., 2016
		Umbilical cord blood	Multipotent	Jaing, 2014; Witkowska-Zimny et al., 2012; Kargozar et al., 2018
Adult	Bone marrow mesenchymal stem cells		Multipotent, pluripotent Multipotent, oligopotent, bipotent and unipotent	Jaramillo-Ferrada et al., 2012; Zuba-Surma et al., 2011; Visvader and Clevers, 2016; Zou et al., 2016; Zhang et al., 2012; Ding et al., 2011
	Other tissues and organs (adipose tissue, skin, skeletal muscle, heart, liver, neural tissue, blood, etc.)			
Induced	Somatic differentiated cells		Pluripotent	Takahashi et al., 2007; Yu et al., 2007; Tan et al., 2014; Rony et al., 2015; Singh et al., 2015

As is indicated in Table 1, these groups of stem cells are of different potency, i.e. capability of gene activation, and they therefore vary in the number of cell types towards which they can differentiate. Only embryonic stem cells derived from morula are totipotent, i.e. capable of differentiating into all types of cells present in the organism, including placental cells (Kucia et al., 2007; Can, 2008). Embryonic stem cells derived from blastocyst, i.e. a later stage of embryonic development, are pluripotent, i.e. they can create any tissue in the body except the placenta. Embryonic stem cells are identified by expressing the stage-specific embryonic antigen (SSEA), and transcription factors Nanog (named by Dr. Ian Chambers after a celtic legend "Tir na nOg", i.e. Land of Eternal Youth) and octamer-binding transcription factor-4 (Oct-4) (Weissman, 2000; Kucia et al., 2007; Jean et al., 2013; Dulak et al., 2015). Cells derived directly from fetus are usually multipotent, i.e. able to differentiate only to a limited number of specialized cell types (Chen et al., 2011; Jiao et al., 2012), although certain locations with pluripotent cells have also been reported, e.g. testis (Kerr et al., 2008) and lung (Hua et al., 2009). However, pluripotent cells can typically be obtained from extrafetal tissues, particularly amnion, amniotic fluid, chorion and umbilical cord. Cells derived from amnion and chorion expressed SSEA-3 and SSEA-4 antigens, specific tissue-restricted antigens, namely TRA- 1-60 and TRA- 1-81 (Bryzek et al., 2013), and also Oct-4, Sox2, Nanog, Lin28 (i.e., gene encoding Lin-28 homolog A protein) and Krueppel-like factor 4 (Klf4) (Jaramillo-Ferrada et al., 2012) which are markers of pluripotency. Markers of pluripotency were also found in cells from amniotic fluid (Da Sacco et al., 2011) and in Wharton jelly (Van Pham et al., 2016), while cells from umbilical blood were rather multipotent (Jaing, 2014).

Somatic cells reprogrammed genetically are a further source of pluripotent stem cells. They are referred to as induced pluripotent stem cells (iPSCs). The iPSCs have typically been created by ectopic expression of four transcription factors, which was forced by viral vectors. These transcription factors included c-Myc (cellular homolog of the retroviral v-myc oncogene), Klf4, Sox2 and Oct3/4 (Takahashi et al., 2007) or Sox2, Oct4, Lin28 and Nanog (Yu et al., 2007). In order to eliminate the risk of mutation and potential tumorigenicity through viral integration, alternative non-viral reprogramming factors (i.e., not carrying aberrant genetic information) have been tested. These factors include various cocktails of transcription factors, and various small-size chemical molecules acting as inhibitors of specific signaling or epigenetic regulators, such as valproic acid or sodium butyrate (i.e. inhibitors of histone deacetylase), parnate (inhibitor of histone demethylase), CHiR99021, i.e., an inhibitor of glycogen synthase kinase 3 (GSK-3), or forskolin and D4476 (i.e., chemical "substitutes" for Oct4). Even widely-used dietary supplements, such as vitamin C and other antioxidants, have been found to improve the genomic and epigenomic

characteristics of iPSCs, when introduced into reprogramming media (Rony et al., 2015; Singh et al., 2015). Nevertheless, the small chemical molecules can also have adverse effects on cells and on developing tissues, e.g. valproic acid, known to cause serious abnormalities in embryo and fetus development. Other approaches to the creation of iPSCs were therefore developed, such as treatment of cells with small non-coding RNA molecules, referred to as microRNA (i.e., miRNA), which play important roles in RNA silencing and post-transcriptional control of the gene expression (Singh et al., 2015). Other possible methods include nuclear transfer, i.e. transfer of the nucleus of somatic cells into an oocyte, or even parthenogenesis of oocytes (Atala, 2005; Kastenberg and Odorico, 2008; for a review, see Tan et al., 2014).

3. Reasons for applying adult stem cells in regenerative therapies

Adult stem cells (Table. 1) are located in practically all organs and tissues of the adult organism, e.g. skin, brain, heart, blood vessels, skeletal muscle, intestine, liver, kidneys, reproductive organs, adipose tissue and bone marrow (for a review, see Ding et al., 2011; Zhang et al., 2012; Zou et al., 2016; Visvader and Clevers, 2016; Varghese et al., 2017), and they are also in body fluids, such as blood (including menstrual blood; Ding et al., 2011) and urine (Schosserer et al., 2015). Like stem cells obtained from extrafetal tissues, adult stem cells can overcome the mutational and other adverse effects associated with iPSCs. They are also not affected by the ethical and legal issues accompanying the use of stem cells obtained from human oocytes, embryos and fetus (Mizuno, 2013; Nae et al., 2013; Tan et al., 2014). Moreover, adult stem cells can be isolated and applied in autologous form. In addition, stem cells derived from extrafetal tissues can be isolated after the birth of an individual and stored for potential future use, if this individual needs a regenerative therapy later in life. However, even in well-developed countries, this approach is not currently used due to its relatively high cost, limited storage capacities, potential loss of cell viability with time of storage, etc. These cells are therefore more suitable for allogenous applications, i.e. as donor cells. However, although the immunogenicity of stem cells (except that of iPSCs), is generally considered to be low (Ong and Sugii, 2013; Patel et al., 2013), a potential immune reaction against an allogeneic implant, and therefore the need for immunosuppressive therapy, cannot be excluded. Therefore, from this point of view, adult stem cells can be considered as the most advantageous stem cell type for the purposes of cell therapy and tissue engineering.

Adult stem cells are usually multipotent (for a review, see Zhang et al., 2012; Zou et al., 2016), though cells expressing markers of pluripotency are also found among them, e.g. in bone marrow (Jaramillo-Ferrada et al., 2012), where they are referred to as very

small embryonic-like stem cells (VSELs; Zuba-Surma et al., 2011). However, some adult stem cells are oligopotent, bipotent or even unipotent, e.g. basal cells in the epidermis, spermatogonial stem cells and satellite cells in skeletal muscles (Visvader and Clevers, 2016). Some cells with limited potency are also referred to as progenitor cells. The difference between typical stem cells and progenitor cells lies not only in the potency of the cells, but also in the limited number of divisions of progenitor cells and the higher level of differentiation of these cells towards a specific cell type. Examples of progenitor cells include endothelial progenitor cells (EPCs), which are promising for endothelialization of blood vessel replacements *in vitro* (Melchiorri et al., 2016) and particularly for spontaneous endothelialization of these replacements after they have been implanted *in vivo*. This is also referred to as "self-endothelialization" or "*in situ* endothelialization". The capture of EPCs from the blood stream, and the further growth and differentiation of EPCs into mature endothelial cells can be achieved by functionalization of vascular grafts with various biologically active molecules or particles, such as oligopeptidic ligands for adhesion molecules of the integrin superfamily on EPCs (RGD, REDV or YIGSR), growth factors (VEGF or fibroblast growth factor-2, FGF-2), antibodies against specific molecules present on EPCs (CD 31, CD 133), nucleic acid aptamers and peptide aptamers, and magnetic particles (for a review, see Avci-Adali, 2013; Pang et al., 2015). Other examples of progenitor cells are pancreatic progenitor cells, which are promising for the treatment of type-1 diabetes mellitus (Tremblay et al., 2016), and periosteal progenitor cells, which are able to differentiate into osteoblasts or chondroblasts (Huang et al., 2014). In some cells, the boundary between stem cells and progenitor cells has not been clearly established. These cells have therefore been referred to as stem/progenitor cells, e.g. neural stem/progenitor cells, which are promising for the treatment of Alzheimer's disease (Tincer et al., 2016), and spinal cord injury (Tashiro et al., 2016), and as liver stem/progenitor cells, which are important for liver tissue regeneration (Liu et al., 2016).

4. Adipose tissue-derived stem cells

Among adult stem cells, adipose stem cells (ASCs) seem to be the most advantageous for use in cell therapies and in tissue engineering. The reason is that adipose tissue is available in relatively high quantity in many patients, and due to its subcutaneous localization, it is relatively easily accessible without significant donor site morbidity (Tobita et al., 2011; Mizuno et al., 2013). In comparison with other types of tissues in the human organism, ASCs in the adipose tissue are abundant, so they can be isolated in large quantities. It has been reported that 500 times more stem cells can be obtained from adipose tissue than from equal amounts of bone marrow (for a review, see Zhang et al., 2012; Mizuno et al., 2013; Ong and Sugii, 2013).

In comparison with bone marrow mesenchymal stem cells (BMMSCs), ASCs can be relatively easily harvested in higher quantities, and with less discomfort and less damage to the donor site (Frölich et al., 2014; Varghese et al., 2017). ASCs have also been reported to undergo senescence later than BMMSCs (Kokai et al., 2014; Ding et al., 2013), and have a higher proliferation capacity than BMMSCs (Barba et al., 2013). ASCs are also more active in autocrine production of some growth factors and immunomodulators than other types of stem cells. For example, ASCs expressed higher levels of mRNA for vascular endothelial growth factor-D (VEGF-D), insulin-like growth factor-1 (IGF-1) and interleukin-8 (IL-8) than other mesenchymal stem cell populations, such as BMMSCs, dermal papilla cells and dermal sheath cells (Hsiao et al., 2012). ASCs were more efficient in treating spinal cord injury in rats than BMMSCs. This was attributed to greater migration and proliferation activity of ASCs and more secretion of VEGF, brain-derived neurotrophic factor (BDNF) and hepatocyte growth factor (HGF) in these cells (Zhou et al., 2013) The secretion of immunomodulators, such as interleukin-6 (IL-6) and TGF-β1, was also higher in ASCs than in BMMSCs for equal cell numbers (Melief et al.,

2013). However, as it was shown in our earlier study (Przekora et al., 2017) and in studies by other authors (Kargozar et al., 2018), ASCs were less active in osteogenic cell differentiation than BMMSCs.

Although ASCs were discovered relatively recently, in 2002 (for a review, see Nae et al., 2013), they have been widely clinically applied in human patients, particularly for reconstructive, corrective, aesthetic and cosmetic purposes. These applications have included so-called cell-assisted lipotransfer (CAL) for tissue augmentation, when autologous ASCs were implanted together with an autologous fat graft in order to enhance its survival and to reduce its postoperative atrophy or resorption. This technique has been used e.g. for cosmetic breast enhancement and for facial contouring. In the form of local injections, ASCs have been applied for rejuvenation of skin and for healing wounds caused by radiation therapy (for a review, see Hanson et al., 2010; Tobita et al., 2011; Nae et al., 2013; Kokai et al., 2014). ASCs were successfully used in the treatment of Parry-Romberg syndrome, which is characterized by progressive atrophy of the right hemiface (Sterodimas et al., 2010). Due to their immunomodulatory and immunosuppressive effects, ASCs have been clinically tested and used in treatments for inflammatory and autoimmune disorders, such as graft *versus* host reaction, Crohn's disease, and even multiple sclerosis, by intravenous infusion of stem cells (Locke et al., 2009; Frölich et al., 2014; Kokai et al., 2014). In treatment of patients with refractory Perineal Crohn's Disease, good results were obtained by combined therapy with ASCs, platelet-rich plasma and endorectal flaps (Wainstein et al., 2018). The treatment of multiple sclerosis was also improved in experiments in rats *in vivo* by the co-transplantation of ASCs and human cells secreting neurotrophic factor (Razavi et al., 2018).

Another important clinical application of ASCs has been in the repair of bone tissue, namely maxilla, where ASCs have been implanted together with β-tricalcium phosphate incorporated with human recombinant bone morphogenetic protein-2 (BMP-2), and in repairing a calvarial defect using ASCs with fibrin glue in a 7-year-old girl with a severe head injury (for a review, see Kokai et al., 2014). ASCs have also been used in treating patients with critical limb ischemia, e.g. during diabetes. Multiple intramuscular injections of autologous ASCs into ischemic legs have improved their revascularization and the healing of wounds on these legs (Lee et al., 2012; Bura et al., 2014). Therefore, the ASCs could be used instead of BMMSCs, which have been relatively widely applied for treating the diabetic foot (Vojtassák et al., 2006). Infusion of ASCs pre-differentiated towards neuronal phenotype, together with hematopoietic bone marrow stem cells, was clinically used for treating a patient with post-traumatic brachial plexus injury (Thakkar et al., 2014) and patients with paraplegia after traumatic spinal cord injury (Thakkar et al., 2016).

In recent studies performed on laboratory animals, administration of ASCs generally improved the treatment of various disorders and injuries, such as pulmonary arterial hypertension in rats (Luo et al., 2018) and injury of the optic nerve in rats (Li et al., 2018). ASCs prevented the scaring of vocal folds in rats (Morisaki et al., 2018), and together with platelet-rich plasma, these cells enhanced the neovascularization and survival of fat grafts in mice (Xiong et al., 2018). Studies performed *in vitro* showed that medium conditioned by ASCs protected cells from death induced by cisplatin used for treatment of the head and neck squamous cell carcinoma (HNSCC) (Chiu et al., 2018). When ASCs were directly added to cultures of HNSCC cell lines, they did not increase the number of HNSCC cells. Similarly in experiments performed on mice *in vivo*, addition of ASCs to xenografts prepared from HNSCC cells did not increase tumor growth (Danan et al., 2018).

In spite of all these encouraging results, the use of ASCs and other mesenchymal stem cells in cancer therapy still remains controversial, i.e. associated with the risk of supportive effects of these cells on tumor growth and metastatic potential, mediated by production of a wide spectrum of growth factors, cytokines, immune suppressors and other bioactive molecules by stem cells. These cells can also stimulate epithelial-mesenchymal transition involved in the onset and progression of

tumor diseases (Mohr and Zwacka, 2018). In addition, some disappointing results were obtained during 15-years of clinical application of stem cells (including ASCs) for treatment of cardiac diseases. These negative results can be attributed to the source and the type of stem cells, heterogeneity of stem cell populations, cell isolation procedure, and aging and senescence of stem cells, positively correlated with the patient age and the time of cell cultivation (for a review, see Nigro et al., 2018).

ASCs are cells of mesodermal origin which reside perivascularly within white adipose tissue. These cells are a physiological source for adipogenesis and expansion of the adipose tissue, which is needed during an increased intake of energy by an organism (for a review, see Ong and Sugii, 2013). Apart from adipogenesis, ASCs can be stimulated under *in vitro* conditions to differentiate into many other mesodermal cell types, e.g. osteoblasts (Logovskaya et al., 2013; Tirkkonen et al., 2013; Catalano et al., 2017; Kargozar et al., 2018), articular and tracheal chondrocytes (Mardani et al., 2016; Forget et al., 2016; Batioglu-Karaaltin et al., 2015), nucleus pulposus-like cells (Zhou et al., 2018), cardiomyocytes (Carvalho et al., 2013; Safaeijavan et al., 2014), skeletal myocytes (Forcales, 2015), vascular and visceral smooth muscle cells (Wang et al., 2010; Park et al., 2012; Marra et al., 2011), endothelial cells (Fischer et al., 2009; Marino et al., 2012; Bekhite et al., 2014), and dermal fibroblasts (Sivan et al., 2016). In addition, ASCs are capable of transdifferentiation towards cells of ectodermal origin, such as keratinocytes (Chavez-Munoz et al., 2013; Sivan et al., 2014; Ravichandran et al., 2013, Owczarczyk-Saczonek et al., 2017), neurons (Chudickova et al., 2015; Jaatinen et al., 2015; New et al., 2015; Marei et al., 2018), Schwann cells (De Luca et al., 2015), retinal pigment epithelial cells (Alonso-Alonso and Srivastava, 2015), corneal epithelial cells (Harkin et al., 2015), and towards cells of endodermal origin, such as hepatocytes (Taléns-Visconti et al., 2006; Guo et al., 2017) and pancreatic islet cells (Thakkar et al., 2015). ASCs were also used for construction of bioengineered lungs in a dynamic bioreactor on scaffolds prepared by decellularization of non-transplantable lungs (Farré et al., 2018).

However, the transdifferentiation of ASCs towards ectodermal and endodermal cells is generally more difficult and often incomplete. It usually requires combinations of several of the inductive factors mentioned in the Introduction, such as special composition of cell culture media, appropriate scaffolds, mechanical or electromagnetic stimulation, and also genetic reprogramming (Chudickova et al., 2015; Han et al., 2015; Qin et al., 2015). Moreover, the differentiation of ASCs towards some mesodermal cell types can also be difficult, namely towards corneal endothelial cells (Harkin et al., 2015) and vascular endothelial cells (Fischer et al., 2009; Bekhite et al., 2014). The reasons could be lack of VEGF receptors on ASCs (for a review, see Dan et al., 2015), methylation of CD31 and CD144 promoters (Boquest et al., 2007), diabetes mellitus (Policha et al., 2014), and also polarization of endothelial cells. These cells show apical-basal polarity, i.e. functional specialization of their luminal and basolateral membranes (Roberts and Sandra, 1993; Pelton et al., 2014), and planar polarity, which is important for endothelial cell movement, proliferation, angiogenesis and response to shear stress (Ju et al., 2010; McCue et al., 2006), while ASCs belong to the category of mesenchymal cells, i.e. mesodermal cells which lack polarity. For this reason, the differentiation of ASCs into mesenchymal cells, such as adipocytes, osteoblasts, fibroblasts or muscle cells, is considered to be relatively easy.

In addition to direct differentiation into specific cell types, ASCs can support the differentiation and phenotypic maturation of various cell types indirectly, i.e. in a paracrine manner. In a study by Mead et al. (2014), PCR array determined the gene expression of 84 growth factors and their receptors. In a study by Otero-Ortega et al. (2015), proteomic analysis of ASC secretome identified 2416 proteins. In a study by Kalinina et al. (2015), more than 600 secreted proteins were detected in culture media conditioned by ASCs. Finally, in a study by Riis et al. (2016), mass spectrometry analysis indicated the presence of 3228

molecules in the ASC proteome, 98 molecules in the peptidome, and 342 molecules in the secretome. The molecules secreted by ASCs included growth factors, such as platelet-derived growth factor (PDGF)-AA and PDGF-AB/BB, nerve growth factor (NGF), neurotrophin-3 (NT-3), brain-derived neurotrophic factor (BDNF), glial cell line-derived neurotrophic factor (GDNF), (Salgado et al., 2010; Hsiao et al., 2012; Mead et al., 2014), keratinocyte growth factor (KGF; Alexaki et al., 2012; Owczarczyk-Saczonek et al., 2017), TGF-β, hepatoma-derived growth factor, connective tissue growth factor (CTGF) (Kapur and Katz, 2013; Otero-Ortega et al., 2015), hepatocyte growth factor (HGF; Kilroy et al., 2007; Salgado et al., 2010; Kapur and Katz, 2013), VEGF (Chung et al., 2015; An et al., 2015; Thamm et al., 2015), insulin-like growth factor-1 (IGF-1; Hsiao et al., 2012; An et al., 2015), FGF-1 and FGF-2 (Bhang et al., 2009; Hsiao et al., 2012; Kapur and Katz, 2013). Other molecules secreted by ASCs include ECM molecules, e.g. collagen, fibronectin, tenascin, osteonectin (Kapur and Katz, 2013; Frazier et al., 2013), matrix metalloproteases, which prevent fibrosis of damaged tissue (Kapur and Katz, 2013; Kalinina et al., 2015; Thamm et al., 2015), hematopoietic factors, such as colony-stimulating factors for macrophages (M-CSF), granulocytes and monocytes (GM-CSF), and IL-7 (Kilroy et al., 2007; Owczarczyk-Saczonek et al., 2017), and immunomodulatory factors, particularly IL-10, which acts as an anti-inflammatory factor (Kapur and Katz, 2013). Infusion of ASCs in mice with experimental colitis decreased the level of proinflammatory cytokines, namely tumor necrosis factor-α (TNF-α), specific interleukins, i.e. IL-1β, IL-6 and IL-12, and interferon-γ (Kapur and Katz, 2013). A culture medium conditioned by ASCs considerably restricted the inflammatory activation of microglia induced by bacterial lipopolysaccharide, manifested by cytokine secretion, expression of CD68, migration and proliferation of microglia, and this effect was mediated by modulation of sphingosine kinase/S1P signaling (Marfia et al., 2016). On the other hand, ASCs were also found to secrete proinflammatory cytokines, such as interleukins 6, 8, and 11, TNF-α (Kilroy et al., 2007; Salgado et al., 2010; An et al., 2015). Paracrine secretion of the mentioned factors in ASCs can be further modulated by hypoxia (Frazier et al., 2013; Kapur and Katz, 2013; Park et al., 2013b; Bekhite et al., 2014; An et al., 2015; Kalinina et al., 2015; Riis et al., 2016). In addition, the factors secreted by ASCs modulate the secretome in target cells, e.g. in keratinocytes (Kapur and Katz, 2013) or in glial cells (Marconi et al., 2013).

In spite of some negative results mentioned above, the direct differentiation of ASCs towards desired cell types, and also their indirect regenerative effects mediated by paracrine secretion, still hold great promise for the treatment of serious disorders, such as cardiovascular disorders (Fischer et al., 2009; He et al., 2010; Carvalho et al., 2013; Policha et al., 2014), metabolic disorders, particularly diabetes mellitus (Thakkar et al., 2015), neurological disorders, such as Huntington's disease, Parkinson's disease, Alzheimer's disease and amyotrophic lateral sclerosis (Marconi et al., 2013; Chang et al., 2014; Forostyak et al., 2016), damage to the brain (Tajiri et al., 2014), to the spinal cord (Thakkar et al., 2016) and to the peripheral nerves (de Luca et al., 2015; Thakkar et al., 2014), ischemia of the brain (Tian et al., 2012) and damage to other tissues, e.g. those affected by systemic sclerosis (Guillaume-Jugnot et al., 2016) or by osteoarthritis (Mardani et al., 2016; Succar et al., 2016). They are also promising for wound healing (Chavez-Munoz et al., 2013; Sivan et al., 2014; Sivan et al., 2016; Ravichandran et al., 2013; Thamm et al., 2015) and treatment of skin diseases, e.g. alopecia and vitiligo (Owczarczyk-Saczonek et al., 2017).

5. Our experience with ASCs

In our experiments, ASCs were isolated from lipoaspirates obtained by liposuction from the abdominal region of patients (women, age 40-43 years) at negative pressure -700 mmHg. The ASCs were harvested by a method described by Estes et al. (2010), with slight modifications reported in our earlier study (Przekora et al., 2017). In order to wash
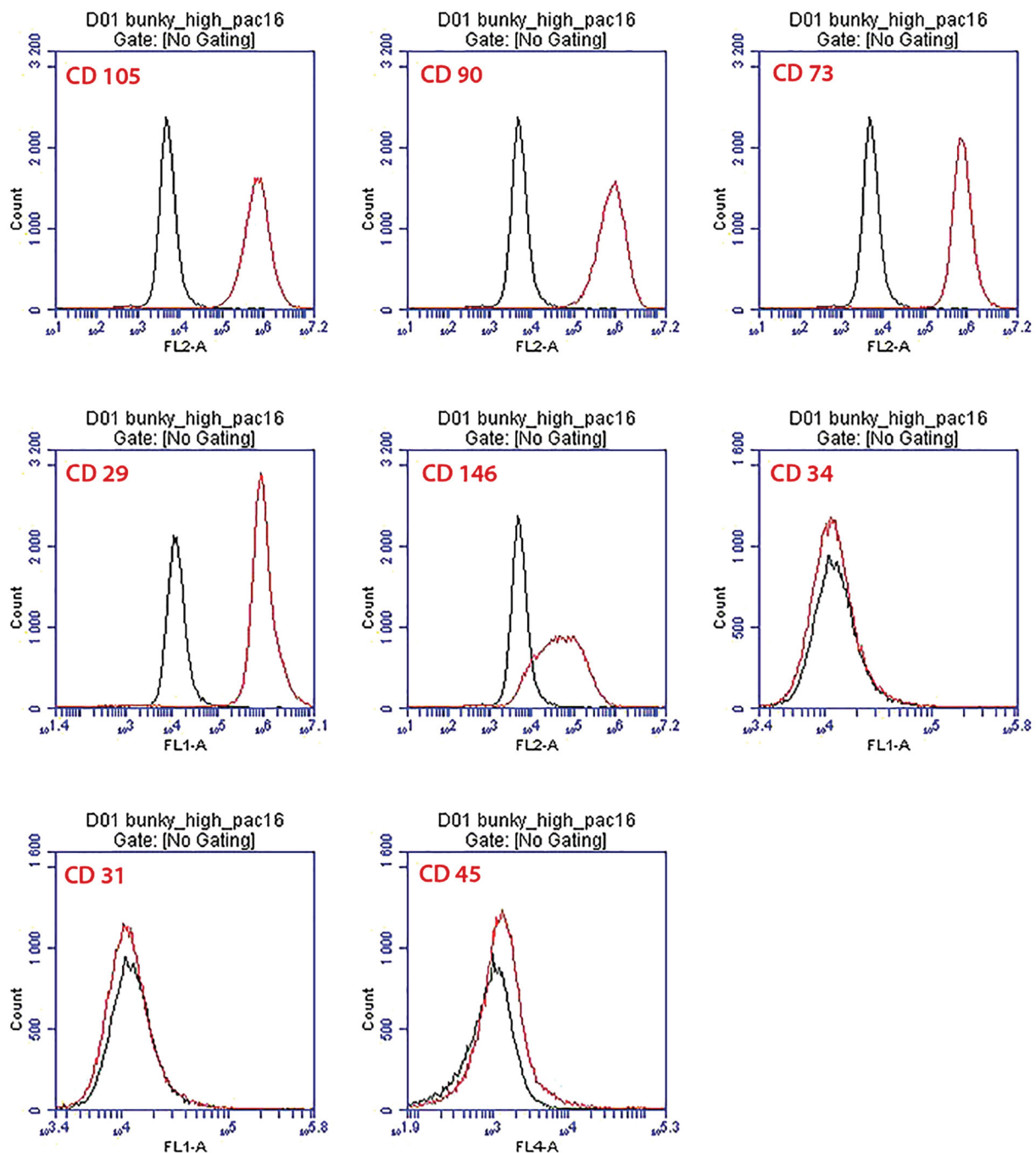
Fig. 1. CD markers on ASCs revealed by flow cytometry. Black curves: control cells without fluorescence-labelled antibodies; red curves: cells stained with fluorescence-labelled antibodies against specific CD markers. Percentage of positivity: CD 105 - 99.7%, CD 90 - 99.7%, CD 73 - 99.7%, CD 29 - 99.5%, CD 146 - 66.9%, CD 34 - 0.1%, CD 31 - 0.0%, CD 45 - 3.0%. Cells in passage 2, BD AccuriTM C6 plus flow cytometer.

out the blood, the lipoaspirate was rinsed several times in phosphate-buffered saline (PBS), digested by 0.1% type I collagenase in PBS for 1 hour at 37 °C, and centrifuged. The vascular-stromal fraction was washed several times, and was finally filtered using a filter with pores 100 μm in diameter (Cell Strainer) purchased from BD Falcon, USA). The cells were seeded into tissue culture polystyrene flasks (75 cm^2, purchased from TPP, Trasadingen, Switzerland) at a density of 0.16 ml of the original lipoaspirate per cm^2. The cells were cultivated at 37 °C in Dulbecco's modified Eagle's Minimum Essential Medium (DMEM) supplemented with 10% of fetal bovine serum (FBS), 40 μg/ml of gentamicin and 5 ng/ml of FGF-2 in a humidified air atmosphere with 5% of CO_2. After approximately 80% of confluence was reached, the cells were passaged using a solution of trypsin and

ethylenediaminetetraacetic acid (EDTA) in PBS for 5 min. at 37 °C. In passage 2, the cells were characterized by flow cytometry using antibodies against specific cluster of differentiation (CD) markers (Fig. 1).

Flow cytometry revealed the presence of standard surface markers of ASCs, namely CD 105 (endoglin), CD 90 (immunoglobulin Thy-1), CD 73 (ecto-5'-nucleotidase), and also CD 29 (fibronectin receptor) and CD 146 (melanoma cell adhesion molecule, receptor for laminin). However, the ASCs were negative or almost negative for CD 31 (also referred to as platelet-endothelial cell adhesion molecule-1, PECAM-1), for CD 34 (an antigen of hematopoietic progenitor cells), and for CD 45 (protein tyrosine phosphatase receptor type C, a marker of hematopoietic cells). The presence or absence of these markers was also found in earlier studies performed on ASCs by other researchers (for a review,
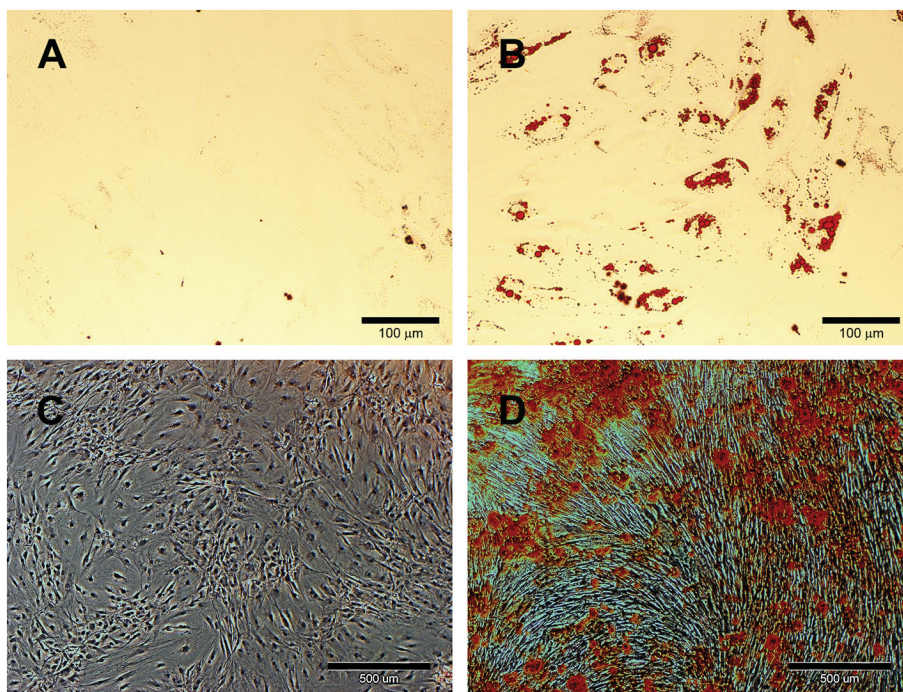
Fig. 2. Adipogenic (A, B) and osteogenic (C, D) differentiation of ASCs (passage 3 and 4) induced by specific culture media. A, B: ASCs were grown for 9 days in a standard medium (A) or in an adipogenic medium (B), and were then incubated with Oil Red O, which stains lipids. C, D: ASCs were grown for 14 days in a standard medium (C) or in an osteogenic medium (D), and were then incubated with Alizarin Red S, which stains the mineral deposits. Olympus IX 71 microscope, DP 70 digital camera. Scale bar is 100 μm (A, B) or 500 μm (C, D).

see Tobita et al., 2011; Zhang et al., 2012; Baer et al., 2013; Barba et al., 2013; Mizuno, 2013; Nae et al., 2013; Ong and Sugii, 2013; Kokai et al., 2014; Camilleri et al., 2016; Owczarczyk-Saczonek et al., 2017; Varghese et al., 2017). However, in some studies, ASCs were found to be positive for CD 34, although this antigen is not currently present in ASCs. This antigen has been reported in non-passaged ASCs or in ASCs in low passages, and disappeared with repeated passaging (for a review, see Baer, 2014).

The identity of the ASCs was further evaluated by their ability to differentiate into adipocytes. As a medium supporting adipogenic cell differentiation, DMEM medium (with 10% of FBS) supplemented with dexamethasone (1 mM), indomethacin (60 mM), 3-isobutyl-1-methyl-xanthine (0.5 mM, hydrocortisone (0.5 mM) and insulin (10 mg/ml), was applied (Naderi et al., 2014; for a review, see Zhang et al., 2012). Adipogenic cell differentiation was evaluated by staining the cells with Oil Red O, which stains lipids. This staining revealed that in the adipogenic culture medium, the cells developed multiple lipid-containing droplets inside the cells, while in the control conventional DMEM medium without adipogenic supplements, the number of these droplets was minimal (Fig. 2). Adipogenic differentiation of ASCs and adipose tissue engineering is highly important for plastic and reconstructive surgery of soft tissue defects induced by trauma, congenital abnormalities or surgical resection, as mentioned above, such as facial contouring, breast augmentation, healing of chronic wounds, e.g. wounds caused by radiation (for a review, see Sterodimas et al., 2010; Hanson et al., 2010; Tobita et al., 2011; Nae et al., 2013; Kokai et al., 2014; Naderi et al., 2014; Zhan et al., 2016).

Secondly, we attempted to differentiate ASCs towards osteoblastic phenotype. As has been mentioned above, ASCs are mesenchymal cells, i.e. mesodermal cells which lack polarity. Differentiation of ASCs into osteoblasts, which also lack polarity, is therefore considered to be relatively easy. After reaching subconfluence, the cells were exposed to an osteogenic medium, i.e. DMEM with FBS (10 %) and gentamicin (40 μg/ml), further supplemented with 10^{-8} M dexamethasone (393 ng/ml), 10 mM β-glycerolphosphate (2.16 mg/ml), 2 mM L-glutamine (292 μg/ml), 10^{-6} M dihydroxyvitamin D_3 (385 ng/ml) and ascorbic acid (50 μg/ml) (Zhang et al., 2012; Logovskaya et al., 2013; Tirkkonen et al., 2013; Ferroni et al., 2016) for 14 days. Then, the mineralization of the matrix deposited by the ASCs, which is a marker

of their differentiation towards the osteogenic phenotype, was assessed by staining with Alizarin Red S, which visualizes calcium deposits (Prè et al., 2011; Ferroni et al., 2016). It was clearly seen that the ASCs cultured in the osteogenic medium formed large calcium-containing deposits, while the control cells cultured in standard DMEM with 10% of FBS did not form these deposits (Fig. 2). The ASCs cultured in the osteogenic medium in our studies also increased their content of type I collagen, alkaline phosphatase (ALP) and osteocalcin, which are considered as early, medium-term and late markers of osteogenic cell differentiation, respectively, as estimated by measuring the intensity of the fluorescence of these molecules after they have been immunofluorescence stained (Krocilova et al., 2015). However, in our recent study on human ASCs cultured on composite chitosan/glucan/hydroxyapatite scaffolds, the production of osteocalcin, a marker of fully differentiated osteoblasts, was lower in ASCs than in human BMMSCs, although the production of Runx2 and of type I collagen, i.e., early indicators of cell differentiation towards the osteogenic phenotype, were comparable in both cell types (Przekora et al., 2017).

Other molecules supporting osteogenic cell differentiation include bone morphogenic protein-2 (Levi et al., 2011), simvastatin (Zhang et al., 2018b) or whey protein (Douglas et al., 2018). These molecules can be incorporated into the scaffolds (Levi et al., 2011; Zhang et al., 2018b) or added into the cell culture media (Douglas et al., 2018). The osteogenic differentiation of ASCs cultured in presence of osteogenic molecules can be further enhanced by electromagnetic stimulation (Ferroni et al., 2016), by acoustic stimulation using extracorporeal shockwaves (ESWs; Catalano et al., 2017) or by mechanical stimulation, such as vibrational stress (Prè et al., 2011).

In the third set of experiments, we attempted to differentiate ASCs towards vascular smooth muscle cells (VSMC) for potential reconstruction of the *tunica media* in vascular replacements. For this purpose, fibrin layers were developed on flexible silicon substrates by a method described earlier (Riedel et al., 2009; Filova et al., 2014). Fibrin is a provisional ECM molecule, playing a key role in the regeneration of damaged tissues. Fibrin was expected to improve the suitability of silicon, which is a rather bioinert material, for the attachment, spreading and proliferation of cells. The silicon substrates were seeded with ASCs in DMEM with FBS (10%) and gentamicin (40 μg/ml). After 2 days of static cultivation (necessary for proper attachment and spreading of the
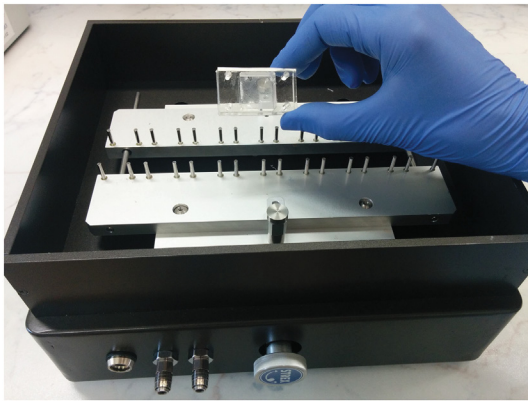
Fig. 3. The STREX dynamic cultivation system (B Bridge International, Ltd., USA) with flexible silicon chambers for coating with various biomaterials and cell seeding.

cells), the cells were exposed to uniaxial stretching in the STREX dynamic cultivation system (B Bridge International, Ltd, USA; Fig. 3).

The ASCs reacted to dynamic cultivation under uniaxial stretching in the STREX system by changing their orientation and by a change in the intensity of the fluorescence of α-smooth muscle actin (α-SMA), a contractile protein and a marker of early differentiation towards VSMC, and also vinculin, which is a protein of focal adhesions, associated with integrin adhesion molecules and taking part in the adhesion of cells to either artificial or nature-derived materials. After 1 day of stretching at

a frequency of 0.5 Hz and at an amplitude of 5%, immunofluorescence staining of vinculin revealed that the cells became oriented in parallel and perpendicular to the direction of stretching, while the control cells cultivated under static conditions became randomly oriented on the cultivation substrate (Fig. 4 A, B). The cells sustained their parallel orientation during stretching, and after 3 days of stretching at a frequency 0.5 Hz and at an amplitude of 5%, they were still oriented in parallel. (Fig. 4 C, D). In addition, the intensity of the immuno-fluorescence of α-SMA in the cells (Fig. 4 E, F) increased with increasing time of stretching (the cells were first stretched at a frequency of 0.5 Hz for 1 day, and then at a frequency of 1 Hz for 3 days or 6 days). Therefore, the combination of soft flexible material with appropriate stretching of ASCs can induce differentiation of these cells towards the VSMC phenotype. Similar results, i.e. enhanced expression of α-SMA and myosin heavy chain (MHC) were obtained in strain-stimulated human ASCs cultured on elastic nanofibrous scaffolds (Park et al., 2012). However, in a study by Lee et al. (2007), uniaxial cyclic strain alone (amplitude 10%, frequency of 1 Hz for 7 days) decreased the expression of α-SMA and h_1-calponin, i.e. another early marker of VSMC differentiation. These markers increased only after the addition of TGF-β_1 into the cultivation media (Lee et al., 2007). Other factors supporting the differentiation of ASCs towards VSMC phenotype were angiotensin II (Kim et al., 2008a), bradykinin (Kim et al., 2008b), thromboxane A_2 (Kim et al., 2009), sphingosine 1-phosphate (Nincheri et al., 2009), bone morphogenetic protein-4 (BMP-4; Wang et al., 2010), retinoic acid (Park et al., 2012) and epidermal growth factor (EGF; Lachaud et al., 2014).
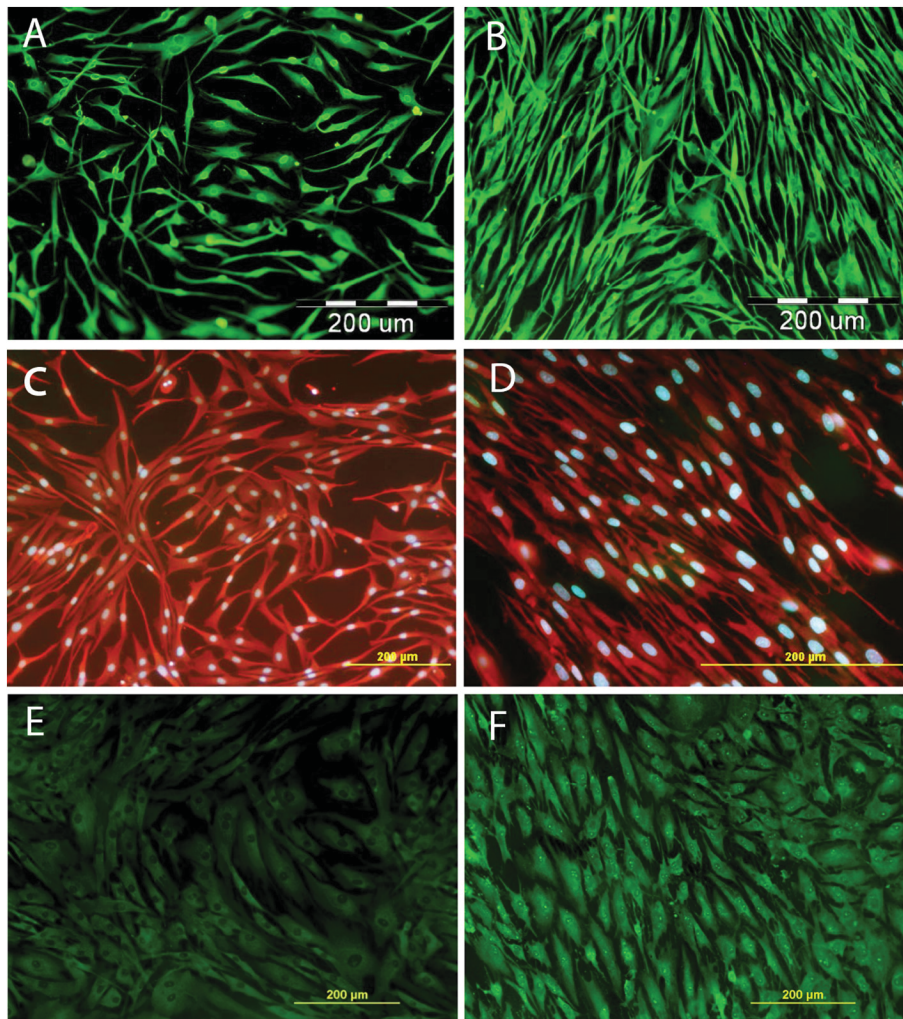

Fig. 4. ASCs cultured in the STREX dynamic cultivation system. A, B: Immunofluorescence staining of vinculin in the control static 1-day-culture (A) or under stretching at a frequency of 0.5 Hz and at an amplitude of 5% for 1 day (B). C, D: Orientation of the cells after 3-day cultivation in control static cultures (C) or under stretching at a frequency of 0.5 Hz and at an amplitude of 5% for 3 days (D). The cells were visualized with Texas Red™ C_2 Maleimide (which stains proteins of the cell membranes and cytoplasm; red fluorescence) and Hoechst #33258 (which stains the DNA of the cell nuclei; blue fluorescence). E, F: Immunofluorescence of α-SMA in cells cultured at the stretching frequency of 0.5 Hz for 1 day and then at 1 Hz for 3 days (E) or for 6 days (F). Olympus IX 71 (A, B) and Olympus IX 50 (C, D, E, F) microscopes, DP 70 digital camera, obj. 10x, with the exception of D, where obj. 20x was used. Scale bar 200 μm.
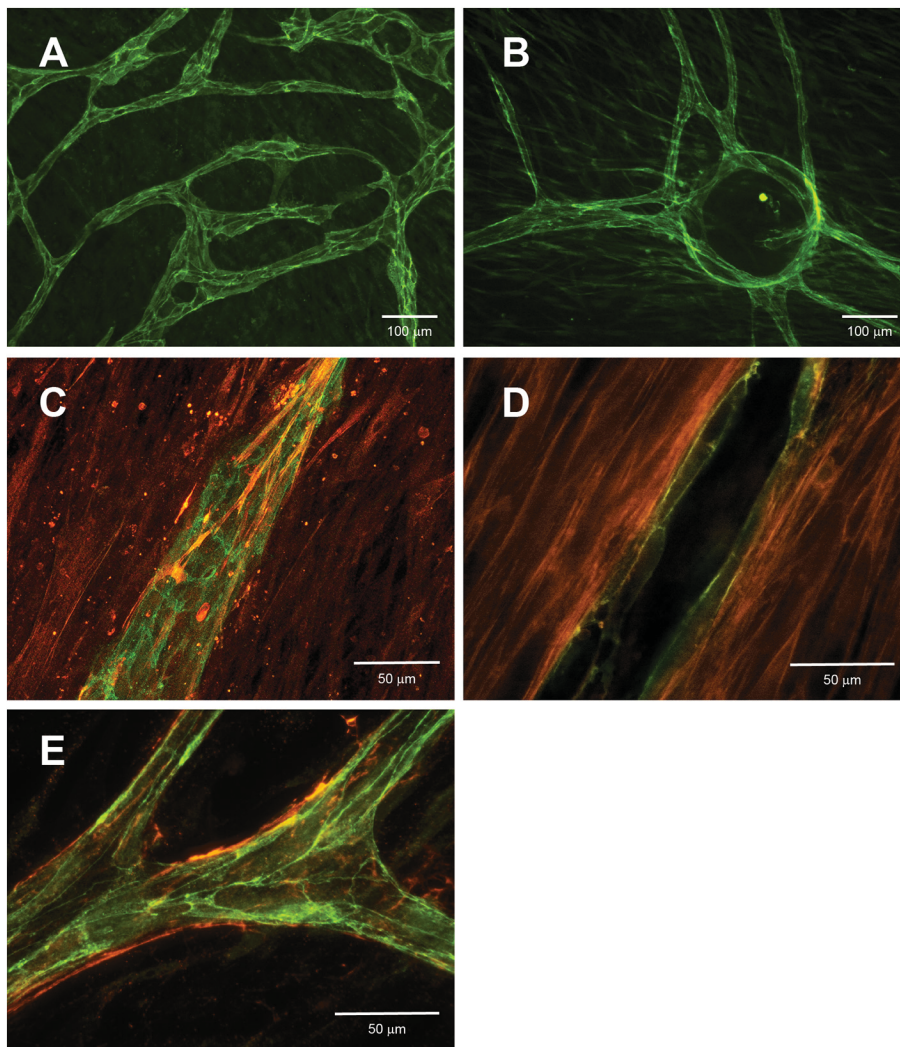
Fig. 5. Fig. 5. Formation of tubular structures in a co-culture of HUVECs and ASCs. A, B: blood vessel formation by vasculogenesis (A) and by angiogenesis (B). HUVECs are stained against VE-cadherin, i.e. an adhesion molecule taking part in cell-cell adhesion and a marker of endothelial cell layer continuity (green fluorescence). C: ASCs stabilizing a newly formed blood vessel and differentiating towards VSMCs or pericytes positive for α-SMA (red fluorescence). D: vascular lumen surrounded by HUVECs positive for VE-cadherin (green) and differentiating ASCs positive for α-SMA (red). E: Basal lamina formation. Type IV collagen, a component of the basal lamina, is stained in red; VE-cadherin in HUVECs is stained in green. Nikon Ti-E inverted fluorescence microscope with a CARV II confocal scanner. Objective Nikon CFI Plan Fluor 20X, DIC, 20x/0.5 NA, WD = 2.1 mm, scale bar 100 μm (A, B). Objective Nikon CFI S Fluor 40X Oil, DIC, 40x/1.3 NA, WD = 0.22 mm, scale bar 50 μm (C–E).

As has been mentioned above, the differentiation of ASCs towards vascular endothelial cells is relatively difficult. However, these cells can support the vascularization of damaged tissues and their regeneration *in vivo* (Bhang et al., 2009; Lee et al., 2012; Bura et al., 2014; for a review, see Salgado et al., 2010), or vascularization of tissue-engineered replacements of these tissues *in vitro* (Sánchez-Muñoz et al., 2015; Chung et al., 2016; Shishatskaya et al., 2016; for a review, see Pill et al., 2015). In our fourth set of experiments, ASCs were co-cultured with human umbilical vein endothelial cells (HUVECs) in the EGM-2 medium (Lonza, Cat. No. CC-3162), containing EGF, VEGF, IGF-1, FGF-β, FBS (final concentration 2%) and antibiotics. Endothelial cells in the co-culture with ASCs self-assembled into vascular sprouts that became interconnected into a vascular network. This organoid culture system enabled us to study both vasculogenesis and angiogenesis. To simulate vasculogenesis, i.e. the formation of blood vessels *de novo*, HUVECs were seeded in a suspension into the ASC culture. Angiogenesis, i.e. sprouting newly-formed blood vessels from pre-existing blood vessels, was simulated using a bead assay. For this purpose, Cytodex 3 microcarrier beads (GE Healthcare Life Sciences, Cat. No. 17048501) were coated with HUVECs and were then added to the culture of ASCs. In this way, endothelial sprouting took place from one point, i.e. from the bead, which in this setting simulated the parental blood vessel. After 7 days in culture, ASCs that were in close contact with capillaries stained positively for α-SMA, an important marker of cell differentiation towards VSMCs or towards pericytes (Merfeld-Clauss et al., 2010), stabilizing the vessel wall (Fig. 5). This organoid system enables a study to be made of extracellular matrix deposition, and also vascular lumen formation.

Similar results were achieved in a study byRohringer et al. (2014), in which the proximity of ASCs and vascular endothelial cells in co-cultures in fibrin gels stimulated the formation of a vascular network. ASCs in fibrin-based or matrix-free co-culture systems expressed markers of pericytes, e.g. α-SMA (Merfeld-Clauss et al., 2010) and neural/glial antigen 2 (NG-2;Natesan et al., 2011; Rohringer et al., 2014), and provided a layer of mural cells necessary for stabilizing the newly-formed blood vessels (He et al., 2010). After transplantation of ASCs into ischemic hind limbs of mice *in vivo*, most of the transplanted ASCs were localized as adjacent to the microvessels (Bhang et al., 2009). The differentiation of ASCs toward pericytes and their tubulogenic activity can occur without growth factor stimulation (Natesan et al., 2011), but differentiation has also been attributed to the secretion of VEGF-A and VEGF-D and other angiogenic factors by ASCs (Bhang et al., 2009; Hsiao et al., 2012). Similar behavior was also observed in ASCs in direct contact with neurons. ASCs in co-cultures with dorsal root ganglia neurons differentiated towards Schwann cells and improved the regeneration of these neurons (de Luca *et al.*, 2015).

In our fifth set of experiments, we concentrated on the potential use of ASCs for skin tissue engineering. These cells can be directly differentiated towards keratinocytes. However, this is difficult, due to the need for transdifferentiation of mesodermal cells to ectodermal cells and polarization of keratinocytes (Chavez-Munoz et al., 2013; Ravichandran et al., 2013; Sivan et al., 2014). ASCs can also be
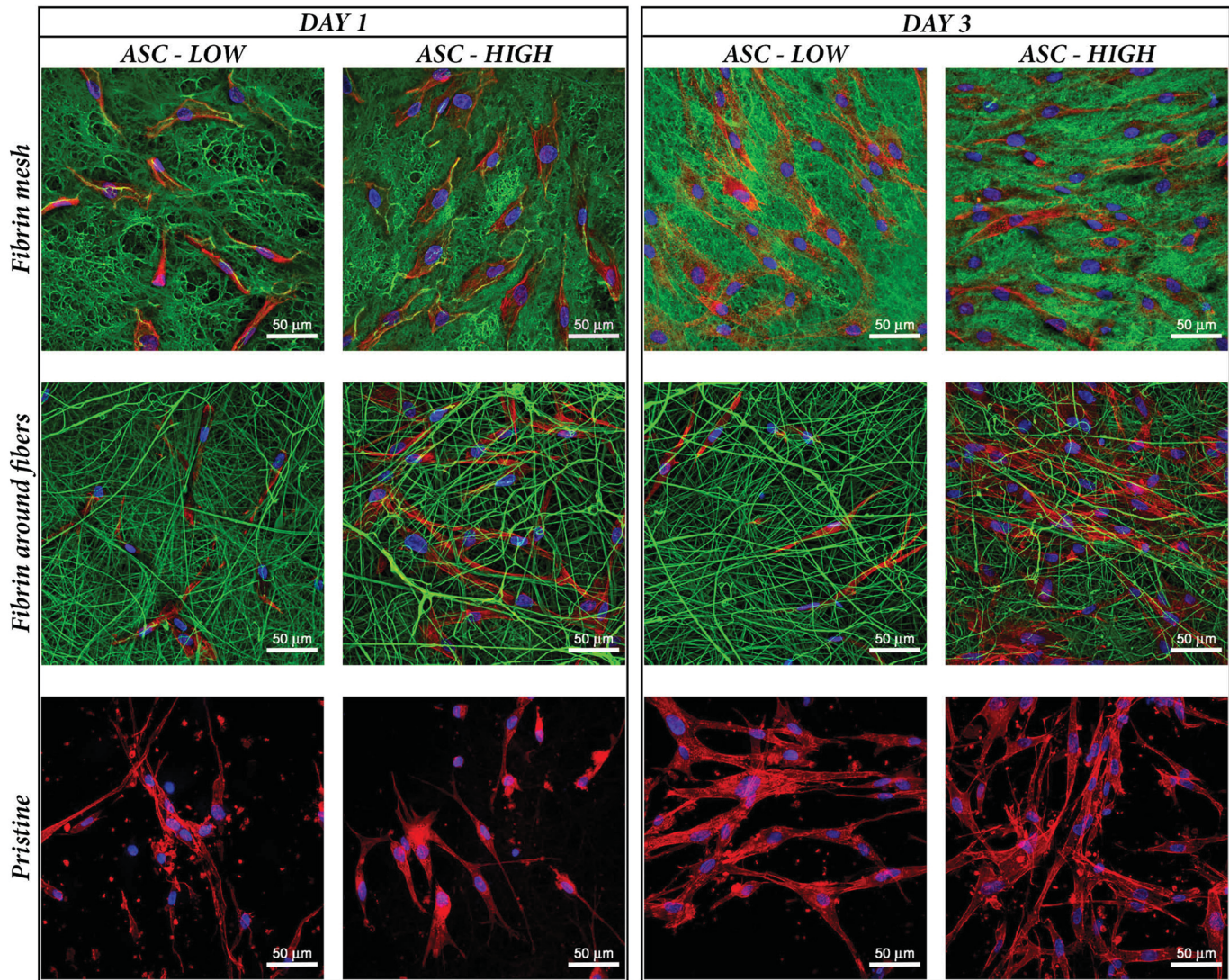
Fig. 6. Adhesion and proliferation of ASCs isolated from lipoaspirates obtained by liposuction at a lower negative pressure (−200 mmHg, ASC-LOW) or at higher negative pressure (−700 mmHg; ASC-HIGH) in 1-day-old and 3-days-old cultures on nanofibrous PLLA meshes modified with fibrin prepared according protocol 1 (a fine homogeneous fibrin mesh on the membrane surface + coating of the individual fibers in the membrane with fibrin; upper row), according to protocol 2 (only coating of the individual fibers in the membrane with fibrin; middle row) and a non-modified PLLA membrane (pristine; lower row). Fibrin was visualized by immunofluorescence staining using a secondary antibody conjugated with Alexa Fluor 488 (green fluorescence). The F-actin in the cells was stained with phalloidin conjugated with TRITC (red fluorescence), and the cell nuclei were stained with Hoechst #33258 (blue fluorescence). Confocal microscope Leica TCS SPE DM2500, obj. 40x/1.15 NA oil. Scale bar 50 μm.
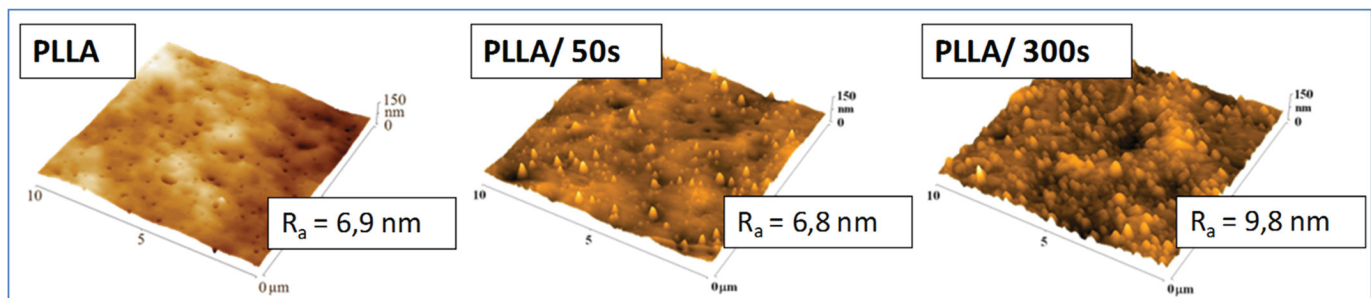

Fig. 7. AFM morphology of pristine PLLA and PLLA modified with argon plasma at 3W and exposure time of 50 and 300 s. R_a values represent the arithmetic roughness of the sample.

differentiated towards dermal fibroblasts, another important cell type in tissue-engineered skin constructs (Sivan et al., 2016; Shishatskaya et al., 2016). Another option is to use ASCs as feeder cells instead of currently-used fibroblasts, particularly xenogeneic mouse 3T3 fibroblasts, in order to promote phenotypic maturation of keratinocytes (Trottier et al., 2008; Monfort et al., 2013; Gutiérrez-Rivera and Izeta,

2015) and vascularization of skin constructs (Sánchez-Muñoz et al., 2015; Chung et al., 2016; Shishatskaya et al., 2016). In our experiments, ASCs were isolated from lipoaspirates obtained by liposuction from the abdominal region of patients at higher or lower negative pressure, i.e. at −700 mmHg, or at −200 mmHg, respectively. The cells were cultured on nanofibrous membranes made of poly(L-lactide)
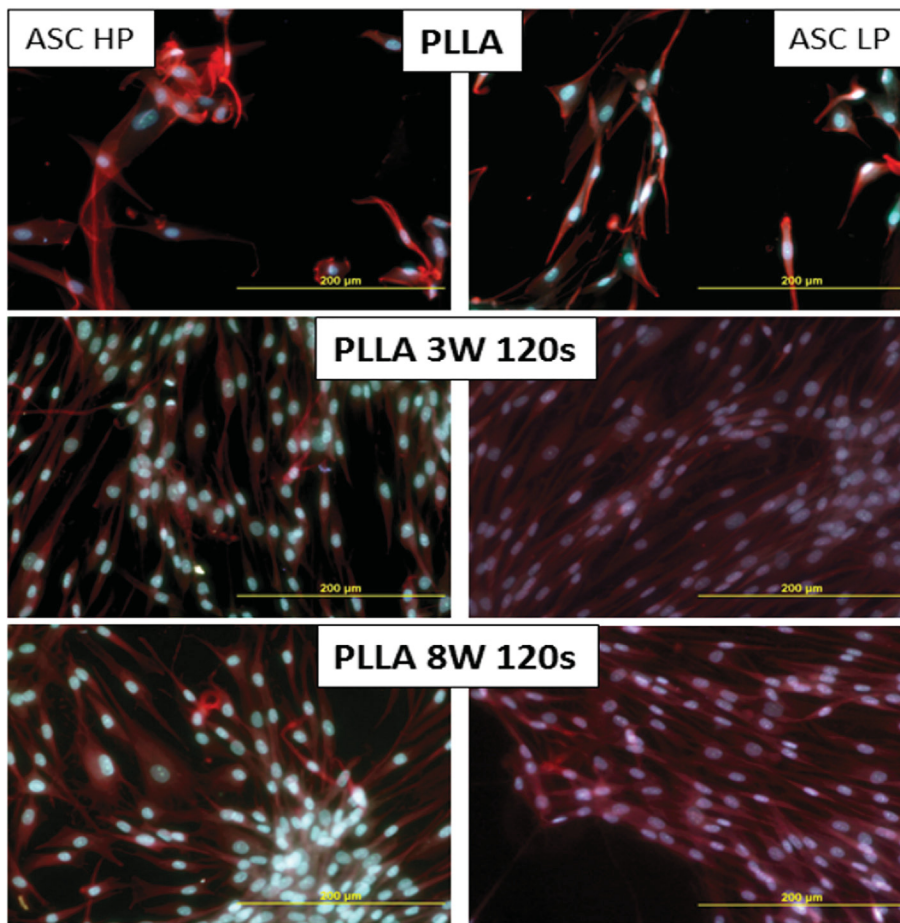
Fig. 8. Images of stem cells isolated from lipoaspirates (acquired at higher negative pressure - ASC HP, or at lower negative pressure - ASC LP) cultured for 7 days on PLLA and on PLLA modified with argon plasma (exposure time 120 s at 3 or 8 W). The proteins of the cell membrane & cytoplasm were stained using Texas Red^{TM} C$_2$ Maleimide, and the DNA in the cell nuclei was stained using Hoechst #33258. Olympus IX 50 microscope, digital DP 70 camera, obj. 20x, scale bar 200 μm.

(PLLA) in DMEM with 10% of FBS, 40 μg/ml of gentamicin and 5 ng/ml of FGF-2. To improve cell adhesion and growth, the membranes were modified with fibrin according to two different protocols. In the first protocol, fibrin formed a fine homogeneous nanofibrous fibrin mesh on the surface of the PLLA membrane, and at the same time, it surrounded each individual fiber of the membrane. In the second protocol, fibrin surrounded only the individual fibers of the membrane. The cell adhesion, growth and morphology were then evaluated in two time intervals, i.e., on days 1 and 3 after seeding. We found that the numbers of ASCs obtained at higher negative pressure (ASC-high) on the control non-modified membrane and on both types of fibrin-modified membranes were higher than the number of ASCs obtained at lower negative pressure (ASC-low). At the same time, both ASC-high and ASC-low adhered better and proliferated faster on PLLA membranes modified with fibrin than on the control non-modified membranes. Membranes modified according the first protocol, i.e. with a fine fibrin mesh covering the PLLA membrane and fibrin embedding the individual fibers, provided a more suitable substrate for the attachment, spreading and proliferation of both ASC-high and ASC-low than the membranes modified according the second protocol, where only the individual fibers were surrounded with fibrin (Fig. 6). The membranes modified according the first protocol also provided better support for cell migration inside the membranes, which was more apparent in ASC-high. Thus, abdominal ASCs isolated from lipoaspirates obtained at a higher negative pressure (−700 mmHg) seem to be more advantageous for application in skin tissue engineering. Also in our earlier study, abdominal ASC-high proliferated more quickly than ASC-low, although their osteogenic differentiation, estimated by the intensity of the fluorescence of type I collagen, ALP and osteocalcin, was lower than in ASC-low (Krocilova et al., 2015). Other factors that can influence the

yield, adhesion, growth, differentiation, viability and senescence of ASCs are various patient factors, such as age, body mass index, gender, menopausal status, donor site, and also intercurrent diseases, such as diabetes mellitus, infection with human immunodeficiency virus, and cancer with its therapies, including radiotherapy, chemotherapy and tamoxifen usage (for a review, see Choudhery et al., 2014; Owczarczyk-Saczonek et al., 2017; Varghese et al., 2017).

In studies on cell-material interaction, it is generally accepted that the adhesion, growth, viability, differentiation and other functions of cells, including ASCs, are strongly influenced by the physicochemical characteristics of the substrate surface, particularly its chemical composition, wettability, electrical charge and conductivity, morphology, roughness and topography. These properties can be advantageously modulated by various physical or chemical techniques, such as irradiation with ions, ultraviolet light, laser, and particularly by plasma treatment (for a review, see Bacakova et al., 2011; Slepicka et al., 2015). These techniques activate the polymers for further grafting with biologically-active chemical functional groups, molecules and nanoparticles (for a review, see Slepicka et al., 2015). In our last set of experiments, PLLA foils were treated with argon plasma (power 3 or 8W, exposure time 50, 120 or 300 s) and were characterized by several methods, such as reflection goniometry, electrokinetic analysis, X-ray photoelectron spectroscopy (XPS) and atomic force microscopy (AFM). Reflection goniometry revealed that the wettability of the samples increased immediately after plasma treatment, but decreased in aged samples, and this decrease was positively correlated with the power of the plasma, and particularly with the time of exposure to the plasma. Nevertheless, the water drop contact angle, which is a measure of the wettability of the material surface, still remained in the range favorable for the adhesion and proliferation of cells (approx. from 56° to 75°;

Slepickova Kasalkova et al., 2017). It has been revealed that the cell adhesion, migration and proliferation reached optimum values on surfaces with moderate wettability (for a review, see Bacakova et al., 2011), and also with a suitable surface charge determined by electrokinetic analysis (Kolska et al., 2014). XPS revealed a decreased content of oxygen in the superficial layer of the modified PLLA (which correlates well with decreased wettability of the polymer) but an increase in the content of nitrogen, which is most probably caused by the reaction of the plasma-activated PLLA surface with air. Finally, AFM revealed an increase in the amount of crystallites and in nanoscale surface roughness with exposure time (Fig. 7). The changes in the physicochemical properties of the material surface induced by plasma treatment in general had positive effects on the growth of ASCs isolated from lipoaspirates obtained by liposuction at low or high negative pressure (ASC LP and ASC HP, respectively). In 7-day-old cultures, the cell population density was markedly higher on plasma-treated PLLA than on untreated PLLA (Fig. 8). After exposure time of 120 s, the cells were more homogeneously distributed on samples treated with plasma treated at 3 W power, whereas on samples treated at 8 W, the cells formed clusters or did not cover the entire surface of the sample. A more homogeneous distribution was found in ASC LP, which also grew in a more orderly manner and in a uniform direction (Slepickova Kasalkova et al., 2017).

6. Conclusion

Stem cells, defined as organization units of biological systems that are responsible for both the development and the regeneration of organs and tissues, are an indispensable tool in advanced tissue engineering and cell therapies. There are four main sources of these cells, namely embryonic tissue, fetal tissues (i.e., directly the fetus or extrafetal tissues), adult tissues (e.g. fat, bone marrow, blood, skin or skeletal muscle), and differentiated somatic cells after they have been genetically reprogrammed, i.e., induced pluripotent stem cells (iPSCs). On the one hand, embryonic stem cells, fetal stem cells and iPSCs have a higher potency to differentiate towards numerous cell phenotypes than adult stem cells, i.e., they are totipotent or pluripotent, while adult stem cells are only multipotent, i.e. able to differentiate to only a limited number of cell types. On the other hand, adult stem cells are able to overcome the ethical and legal issues accompanying the use of human oocytes, embryos and fetus as sources of stem cells, and also the mutational and other adverse effects associated with iPSCs. Last but not least, adult stem cells can be obtained and applied in autologous form. For tissue engineering, adult stem cells can be seeded on synthetic or nature-derived scaffolds and differentiated towards a desired phenotype by combinations of appropriate composition, architecture, mechanical properties and physicochemical properties of the scaffolds, appropriate composition of the cell culture media, and appropriate mechanical and/or electromagnetic stimulation. For cell therapies, stem cells can be directly applied to damaged tissues, or they can be used in the form of extracellular vesicles, containing bioactive molecules produced by these cells in an autocrine manner, particularly growth factors and immunomodulatory molecules. Among adult stem cells, adipose tissue stem cells seem to be the most promising cell types, because they can be accessed relatively easily and non-invasively, and are available in considerable quantities.

Acknowledgements

References

Alexaki, V.I., Simantiraki, D., Panayiotopoulou, M., Rasouli, O., Venihaki, M., Castana, O., Alexakis, D., Kampa, M., Stathopoulos, E.N., Castanas, E., 2012. Adipose tissue-derived mesenchymal cells support skin reepithelialization through secretion of KGF-1 and PDGF-BB: comparison with dermal fibroblasts. Cell Transplant. 21, 2441–2454.

Alonso-Alonso, M.L., Srivastava, G.K., 2015. Current focus of stem cell application in retinal repair. World J. Stem Cells. 7, 641–648.

An, H.Y., Shin, H.S., Choi, J.S., Kim, H.J., Lim, J.Y., Kim, Y.M., 2015. Adipose mesenchymal stem cell secretome modulated in hypoxia for remodeling of radiation-induced salivary gland damage. PLoS One 10, e0141862.

Ardeshirylajimi, A., Delgoshaie, M., Mirzaei, S., Khojasteh, A., 2018. Different porosities of chitosan can influence the osteogenic differentiation potential of stem cells. J. Cell. Biochem. 119, 625–633.

Arjmand, M., Ardeshirylajimi, A., Maghsoudi, H., Azadian, E., 2018. Osteogenic differentiation potential of mesenchymal stem cells cultured on nanofibrous scaffold improved in the presence of pulsed electromagnetic field. J. Cell. Physiol. 233, 1061–1070.

Atala, A., 2005. Tissue engineering, stem cells and cloning: current concepts and changing trends. Expert. Opin. Biol. Ther. 5, 879–892.

Avci-Adali, M., Stoll, H., Wilhelm, N., Perle, N., Schlensak, C., Wendel, H.P., 2013. In vivo tissue engineering: mimicry of homing factors for self-endothelialization of blood-contacting materials. Pathobiology 80, 176–181.

Bacakova, L., Filova, E., Parizek, M., Ruml, T., Svorcik, V., 2011. Modulation of cell adhesion, proliferation and differentiation on materials designed for body implants. Biotechnol. Adv. 29, 739–767.

Baer, P.C., 2014. Adipose-derived mesenchymal stromal/stem cells: An update on their phenotype in vivo and in vitro. World J. Stem Cells. 6, 256–265.

Baer, P.C., Kuçi, S., Krause, M., Kuçi, Z., Zielen, S., Geiger, H., Bader, P., Schubert, R., 2013. Comprehensive phenotypic characterization of human adipose-derived stromal/stem cells and their subsets by a high throughput technology. Stem Cells Dev. 22, 330–339.

Baglio, S.R., Rooijers, K., Koppers-Lalic, D., Verweij, F.J., Pérez Lanzón, M., Zini, N., Naaijkens, B., Perut, F., Niessen, H.W., Baldini, N., Pegtel, D.M., 2015. Human bone marrow- and adipose-mesenchymal stem cells secrete exosomes enriched in distinctive miRNA and tRNA species. Stem Cell Res Ther 6, 127.

Barba, M., Cicione, C., Bernardini, C., Michetti, F., Lattanzi, W., 2013. Adipose-derived mesenchymal cells for bone regeneration: state of the art. Biomed. Res. Int. 416391.

Batioglu-Karaaltin, A., Karaaltin, M.V., Ovali, E., Yigit, O., Kongur, M., Inan, O., Bozkurt, E., Cansiz, H., 2015. In vivo tissue-engineered allogenic trachea transplantation in rabbits: a preliminary report. Stem Cell Rev. 11, 347–356.

Bekhite, M.M., Figulla, H.R., Sauer, H., Wartenberg, M., 2013. Static magnetic fields increase cardiomyocyte differentiation of Flk-1+ cells derived from mouse embryonic stem cells via Ca2+ influx and ROS production. Int. J. Cardiol. 167, 798–808.

Bekhite, M.M., Finkensieper, A., Rebhan, J., Huse, S., Schultze-Mosgau, S., Figulla, H.R., Sauer, H., Wartenberg, M., 2014. Hypoxia, leptin, and vascular endothelial growth factor stimulate vascular endothelial cell differentiation of human adipose tissue-derived stem cells. Stem Cells Dev. 23, 333–351.

Bhang, S.H., Cho, S.W., Lim, J.M., Kang, J.M., Lee, T.J., Yang, H.S., Song, Y.S., Park, M.H., Kim, H.S., Yoo, K.J., Jang, Y., Langer, R., Anderson, D.G., Kim, B.S., 2009. Locally delivered growth factor enhances the angiogenic efficacy of adipose-derived stromal cells transplanted to ischemic limbs. Stem Cells 27, 1976–1986.

Birk, R., Sommer, U., Faber, A., Aderhold, C., Schulz, J.D., Hörmann, K., Goessler, U.R., Stern-Straeter, J., 2014. Evaluation of the effect of static magnetic fields combined with human hepatocyte growth factor on human satellite cell cultures. Mol. Med. Rep. 9, 2328–2334.

Boquest, A.C., Noer, A., Sørensen, A.L., Vekterud, K., Collas, P., 2007. CpG methylation profiles of endothelial cell-specific gene promoter regions in adipose tissue stem cells suggest limited differentiation potential toward the endothelial cell lineage. Stem Cells 25, 852–861.

Bryzek, A., Czekaj, P., Plewka, D., Komarska, H., Tomsia, M., Lesiak, M., Sieroń, A.L., Sikora, J., Kopaczka, K., 2013. Expression and co-expression of surface markers of pluripotency on human amniotic cells cultured in different growth media. Ginekol. Pol. 84, 1012–1024.

Bura, A., Planat-Benard, V., Bourin, P., Silvestre, J.S., Gross, F., Grolleau, J.L., Saint-Lebese, B., Peyrafitte, J.A., Fleury, S., Gadelorge, M., Taurand, M., Dupuis-Coronas, S., Leobon, B., Casteilla, L., 2014. Phase I trial: the use of autologous cultured adipose-derived stroma/stem cells to treat patients with non-revascularizable critical limb ischemia. Cytotherapy 16, 245–257.

Camilleri, E.T., Gustafson, M.P., Dudakovic, A., Riester, S.M., Garces, C.G., Paradise, C.R., Takai, H., Karperien, M., Cool, S., Sampen, H.J., Larson, A.N., Qu, W., Smith, J., Dietz, A.B., van Wijnen, A.J., 2016. Identification and validation of multiple cell surface markers of clinical-grade adipose-derived mesenchymal stromal cells as novel release criteria for good manufacturing practice-compliant production. Stem Cell Res Ther 7, 107.

Can, A., 2008. A concise review on the classification and nomenclature of stem cells. Turk. J. Haematol. 25, 57–59.

Carvalho, P.H., Daibert, A.P., Monteiro, B.S., Okano, B.S., Carvalho, J.L., Cunha, D.N., Favarato, L.S., Pereira, V.G., Augusto, L.E., Del Carlo, R.J., 2013. Differentiation of adipose tissue-derived mesenchymal stem cells into cardiomyocytes. Arq. Bras. Cardiol. 100, 82–89.

Catalano, M.G., Marano, F., Rinella, L., de Girolamo, L., Bosco, O., Fortunati, N., Berta, L., Frairia, R., 2017. Extracorporeal shockwaves (ESWs) enhance the osteogenic medium-induced differentiation of adipose-derived stem cells into osteoblast-like cells. J. Tissue Eng. Regen. Med. 11, 390–399.

Chang, K.A., Lee, J.H., Suh, Y.H., 2014. Therapeutic potential of human adipose-derived stem cells in neurological disorders. J. Pharmacol. Sci. 126, 293–301.

Chavez-Munoz, C., Nguyen, K.T., Xu, W., Hong, S.J., Mustoe, T.A., Galiano, R.D., 2013. Transdifferentiation of adipose-derived stem cells into keratinocyte-like cells: engineering a stratified epidermis. PLoS One 8, e80587.

Chen, P.M., Yen, M.L., Liu, K.J., Sytwu, H.K., Yen, B.L., 2011. Immunomodulatory properties of human adult and fetal multipotent mesenchymal stem cells. J. Biomed. Sci. 18, 49.

Chiu, Y.J., Yang, J.S., Hsu, H.S., Tsai, C.H., Ma, H., 2018. Adipose-derived stem cell conditioned medium attenuates cisplatin-triggered apoptosis in tongue squamous cell carcinoma. Oncol. Rep. 39, 651–658.

Choudhery, M.S., Badowski, M., Muise, A., Pierce, J., Harris, D.T., 2014. Donor age negatively impacts adipose tissue-derived mesenchymal stem cell expansion and differentiation. J. Transl. Med. 12, 8.

Chudickova, M., Bruza, P., Zajicova, A., Trosan, P., Svobodova, L., Javorkova, E., Kubinova, S., Holan, V., 2015. Targeted neural differentiation of murine mesenchymal stem cells by a protocol simulating the inflammatory site of neural injury. J. Tissue Eng. Regen. Med. http://dx.doi.org/10.1002/term.2059.

Chung, E., Rytlewski, J.A., Merchant, A.G., Dhada, K.S., Lewis, E.W., Suggs, L.J., 2015. Fibrin-based 3D matrices induce angiogenic behavior of adipose-derived stem cells. Acta Biomater. 17, 78–88.

Chung, E., Rybalko, V.Y., Hsieh, P.L., Leal, S.L., Samano, M.A., Willauer, A.N., Stowers, R.S., Natesan, S., Zamora, D.O., Christy, R.J., Suggs, L.J., 2016. Fibrin-based stem cell containing scaffold improves the dynamics of burn wound healing. Wound Repair Regen. 24, 810–819.

Colazzo, F., Alrashed, F., Saratchandra, P., Carubelli, I., Chester, A.H., Yacoub, M.H., Taylor, P.M., Somers, P., 2014. Shear stress and VEGF enhance endothelial differentiation of human adipose-derived stem cells. Growth Factors 32, 139–149.

Da Sacco, S., De Filippo, R.E., Perin, L., 2011. Amniotic fluid as a source of pluripotent and multipotent stem cells for organ regeneration. Curr. Opin. Organ Transplant. 16, 101–105.

Dan, P., Velot, É., Decot, V., Menu, P., 2015. The role of mechanical stimuli in the vascular differentiation of mesenchymal stem cells. J. Cell Sci. 128, 2415–2422.

Danan, D., Lehman, C.E., Mendez, R.E., Langford, B., Koors, P.D., Dougherty, M.I., Peirce, S.M., Gioeli, D.G., Jameson, M.J., 2018. Effect of adipose-derived stem cells on head and neck squamous cell carcinoma. Otolaryngol. Head Neck Surg. 194599817750361.

De Luca, A.C., Faroni, A., Reid, A.J., 2015. Dorsal root ganglia neurons and differentiated adipose-derived stem cells: an in vitro co-culture model to study peripheral nerve regeneration. J. Vis. Exp.(96).

Ding, D.C., Shyu, W.C., Lin, S.Z., 2011. Mesenchymal stem cells. Cell Transplant. 20, 5–14.

Ding, D.C., Chou, H.L., Hung, W.T., Liu, H.W., Chu, T.Y., 2013. Human adipose-derived stem cells cultured in keratinocyte serum free medium: Donor's age does not affect the proliferation and differentiation capacities. J. Biomed. Sci. 20, 59.

Douglas, T.E.L., Vandrovcova, M., Krocilova, N., Keppler, J.K., Zarubova, J., Skirtach, A.G., Bacakova, L., 2018. Application of whey protein isolate in bone regeneration: Effects on growth and osteogenic differentiation of bone-forming cells. J. Dairy Sci. 101, 28–36.

Dulak, J., Szade, K., Szade, A., Nowak, W., Józkowicz, A., 2015. Adult stem cells: hopes and hypes of regenerative medicine. Acta Biochim. Pol. 62, 329–337.

Engler, A.J., Sen, S., Sweeney, H.L., Discher, D.E., 2006. Matrix elasticity directs stem cell lineage specification. Cell 126, 677–689.

Estes, B.T., Diekman, B.O., Gimble, J.M., Guilak, F., 2010. Isolation of adipose-derived stem cells and their induction to a chondrogenic phenotype. Nat. Protoc. 5, 1294–1311.

Farré, R., Otero, J., Almendros, I., Navajas, D., 2018. Bioengineered lungs: A challenge and an opportunity. Arch. Bronconeumol. 54, 31–38.

Ferroni, L., Tocco, I., De Pieri, A., Menarin, M., Fermi, E., Piattelli, A., Gardin, C., Zavan, B., 2016. Pulsed magnetic therapy increases osteogenic differentiation of mesenchymal stem cells only if they are pre-committed. Life Sci. 152, 44–51.

Filova, E., Brynda, E., Riedel, T., Chlupac, J., Vandrovcova, M., Svindrych, Z., Lisa, V., Houska, M., Pirk, J., Bacakova, L., 2014. Improved adhesion and differentiation of endothelial cells on surface-attached fibrin structures containing extracellular matrix proteins. J. Biomed. Mater. Res. A 102, 698–712.

Fischer, L.J., McIlhenny, S., Tulenko, T., Golesorkhi, N., Zhang, P., Larson, R., Lombardi, J., Shapiro, I., DiMuzio, P.J., 2009. Endothelial differentiation of adipose-derived stem cells: effects of endothelial cell growth supplement and shear force. J. Surg. Res. 152, 157–166.

Forcales, S.V., 2015. Potential of adipose-derived stem cells in muscular regenerative therapies. Front. Aging Neurosci. 7, 123.

Forget, J., Awaja, F., Gugutkov, D., Gustavsson, J., Gallego Ferrer, G., Coelho-Sampaio, T., Hochman-Mendez, C., Salmeron-Sánchez, M., Altankov, G., 2016. Differentiation of human mesenchymal stem cells toward quality cartilage using fibrinogen-based nanofibers. Macromol. Biosci. 16, 1348–1359.

Forostyak, O., Forostyak, S., Kortus, S., Sykova, E., Verkhratsky, A., Dayanithi, G., 2016. Physiology of Ca(2+) signalling in stem cells of different origins and differentiation stages. Cell Calcium 59, 57–66.

Frazier, T.P., Gimble, J.M., Kheterpal, I., Rowan, B.G., 2013. Impact of low oxygen on the secretome of human adipose-derived stromal/stem cell primary cultures. Biochimie 95, 2286–2296.

Frölich, K., Hagen, R., Kleinsasser, N., 2014. Adipose-derived stromal cells (ASC) - basics and therapeutic approaches in otorhinolaryngology. Laryngorhinootologie. 93, 369–380.

Gallina, C., Turinetto, V., Giachino, C., 2015. A new paradigm in cardiac regeneration: The mesenchymal stem cell secretome. Stem Cells Int. 2015, 765846.

Gluck, J.M., Delman, C., Chyu, J., MacLellan, W.R., Shemin, R.J., Heydarkhan-Hagvall, S., 2014. Microenvironment influences vascular differentiation of murine cardiovascular progenitor cells. J Biomed Mater Res B Appl Biomater 102, 1730–1739 R.

Gonçalves, A.I., Rodrigues, M.T., Carvalho, P.P., Bañobre-López, M., Paz, E., Freitas, P., Gomes, M.E., 2016. Exploring the potential of starch/polycaprolactone aligned magnetic responsive scaffolds for tendon regeneration. Adv. Health Mater. 5, 213–222.

Guillaume-Jugnot, P., Daumas, A., Magalon, J., Sautereau, N., Veran, J., Magalon, G., Sabatier, F., Granel, B., 2016. State of the art. Autologous fat graft and adipose tissue-derived stromal vascular fraction injection for hand therapy in systemic sclerosis patients. Curr. Res. Transl. Med. 64, 35–42.

Guo, D.L., Wang, Z.G., Xiong, L.K., Pan, L.Y., Zhu, Q., Yuan, Y.F., Liu, Z.S., 2017. Hepatogenic differentiation from human adipose-derived stem cells and application for mouse acute liver injury. Artif. Cells Nanomed. Biotechnol. 45, 224–232.

Gutiérrez-Rivera, A., Izeta, A., 2015. Does fat get you skinny? Exp. Dermatol. 24, 740–741.

Han, S.M., Coh, Y.R., Ahn, J.O., Jang, G., Yum, S.Y., Kang, S.K., Lee, H.W., Youn, H.Y., 2015. Enhanced hepatogenic transdifferentiation of human adipose tissue mesenchymal stem cells by gene engineering with Oct4 and Sox2. PLoS One 10, e0108874.

Hanson, S.E., Gutowski, K.A., Hematti, P., 2010. Clinical applications of mesenchymal stem cells in soft tissue augmentation. Aesthet. Surg. J. 30, 838–842.

Harkin, D.G., Foyn, L., Bray, L.J., Sutherland, A.J., Li, F.J., Cronin, B.G., 2015. Concise reviews: can mesenchymal stromal cells differentiate into corneal cells? A systematic review of published data. Stem Cells 33, 785–791.

He, W., Nieponice, A., Soletti, L., Hong, Y., Gharaibeh, B., Crisan, M., Usas, A., Peault, B., Huard, J., Wagner, W.R., Vorp, D.A., 2010. Pericyte-based human tissue engineered vascular grafts. Biomaterials 31, 8235–8244.

Hsiao, S.T., Asgari, A., Lokmic, Z., Sinclair, R., Dusting, G.J., Lim, S.Y., Dilley, R.J., 2012. Comparative analysis of paracrine factor expression in human adult mesenchymal stem cells derived from bone marrow, adipose, and dermal tissue. Stem Cells Dev. 21, 2189–2203.

Hua, J., Yu, H., Dong, W., Yang, C., Gao, Z., Lei, A., Sun, Y., Pan, S., Wu, Y., Dou, Z., 2009. Characterization of mesenchymal stem cells (MSCs) from human fetal lung: potential differentiation of germ cells. Tissue Cell 41, 448–455.

Huang, C., Xue, M., Chen, H., Jiao, J., Herschman, H.R., O'Keefe, R.J., Zhang, X., 2014. The spatiotemporal role of COX-2 in osteogenic and chondrogenic differentiation of periosteum-derived mesenchymal progenitors in fracture repair. PLoS One 9, e100079.

Ikada, Y., 2006. Challenges in tissue engineering. J. R. Soc. Interface 3, 589–601.

Jaatinen, L., Salemi, S., Miettinen, S., Hyttinen, J., Eberli, D., 2015. The combination of electric current and copper promotes neuronal differentiation of adipose-derived stem cells. Ann. Biomed. Eng. 43, 1014–1023.

Jaing, T.H., 2014. Umbilical cord blood: a trustworthy source of multipotent stem cells for regenerative medicine. Cell Transplant. 23, 493–496.

Jaramillo-Ferrada, P.A., Wolvetang, E.J., Cooper-White, J.J., 2012. Differential mesengenic potential and expression of stem cell-fate modulators in mesenchymal stromal cells from human-term placenta and bone marrow. J. Cell. Physiol. 227, 3234–3242.

Jean, C., Aubel, P., Soleihavoup, C., Bouhallier, F., Voisin, S., Lavial, F., Pain, B., 2013. Pluripotent genes in avian stem cells. Develop. Growth Differ. 55, 41–51.

Jiao, F., Wang, J., Dong, Z.L., Wu, M.J., Zhao, T.B., Li, D.D., Wang, X., 2012. Human mesenchymal stem cells derived from limb bud can differentiate into all three embryonic germ layers lineages. Cell Rep. 14, 324–333.

Ju, R., Cirone, P., Lin, S., Griesbach, H., Slusarski, D.C., Crews, C.M., 2010. Activation of the planar cell polarity form in DAAM1 leads to inhibition of endothelial cell proliferation, migration, and angiogenesis. Proc. Natl. Acad. Sci. U. S. A. 107, 6906–6911.

Juhasova, J., Juhas, S., Klima, J., Strnadel, J., Holubova, M., Motlik, J., 2011. Osteogenic differentiation of miniature pig mesenchymal stem cells in 2D and 3D environment. Physiol. Res. 60, 559–5571.

Kalinina, N., Kharlampieva, D., Loguinova, M., Butenko, I., Pobeguts, O., Efimenko, A., Ageeva, L., Sharonov, G., Ischenko, D., Alekseev, D., Grigorieva, O., Sysoeva, V., Rubina, K., Lazarev, V., Govorun, V., 2015. Characterization of secretomes provides evidence for adipose-derived mesenchymal stromal cells subtypes. Stem Cell Res Ther 6, 221.

Kapur, S.K., Katz, A.J., 2013. Review of the adipose derived stem cell secretome. Biochimie 95, 2222–2228.

Kargozar, S., Mozafari, M., Hashemian, S., Brouki Milan, P., Hamzehlou, S., Soleimani, M., Joghataei, M.T., Gholipourmalekabadi, M., Korourian, A., Mousavizadeh, K., Seifalian, A.M., 2018. Osteogenic potential of stem cells-seeded bioactive nanocomposite scaffolds: A comparative study between human mesenchymal stem cells derived from bone, umbilical cord Wharton's jelly, and adipose tissue. J Biomed Mater Res B Appl Biomater 106, 61–72.

Kastenberg, Z.J., Odorico, J.S., 2008. Alternative sources of pluripotency: science, ethics, and stem cells. Transplant. Rev. (Orlando). 22, 215–222.

Kerr, C.L., Hill, C.M., Blumenthal, P.D., Gearhart, J.D., 2008. Expression of pluripotent stem cell markers in the human fetal testis. Stem Cells 26, 412–421.

Kilroy, G.E., Foster, S.J., Wu, X., Ruiz, J., Sherwood, S., Heifetz, A., Ludlow, J.W., Stricker, D.M., Potiny, S., Green, P., Halvorsen, Y.D., Cheatham, B., Storms, R.W., Gimble, J.M., 2007. Cytokine profile of human adipose-derived stem cells: expression of angiogenic, hematopoietic, and pro-inflammatory factors. J. Cell. Physiol. 212, 702–709.

Kim, Y.M., Jeon, E.S., Kim, M.R., Jho, S.K., Ryu, S.W., Kim, J.H., 2008a. Angiotensin II-induced differentiation of adipose tissue-derived mesenchymal stem cells to smooth muscle-like cells. Int. J. Biochem. Cell Biol. 40, 2482–2491.

Kim, Y.M., Jeon, E.S., Kim, M.R., Lee, J.S., Kim, J.H., 2008b. Bradykinin-induced expression of alpha-smooth muscle actin in human mesenchymal stem cells. Cell.

Signal. 20, 1882–1889.

Kim, M.R., Jeon, E.S., Kim, Y.M., Lee, J.S., Kim, J.H., 2009. Thromboxane a(2) induces differentiation of human mesenchymal stem cells to smooth muscle-like cells. Stem Cells 27, 191–199.

Kobayashi, Y., Sanno, Y., Sakai, A., Sawabu, Y., Tsutsumi, M., Goto, M., Kitahata, H., Nakata, S., Kumamoto, J., Denda, M., Nagayama, M., 2014. Mathematical modeling of calcium waves induced by mechanical stimulation in keratinocytes. PLoS One 9, e92650.

Kokai, L.E., Marra, K., Rubin, J.P., 2014. Adipose stem cells: biology and clinical applications for tissue repair and regeneration. Transl. Res. 163, 399–408.

Kolska, Z., Reznickova, A., Nagyova, M., Slepickova, Kasalkova N., Sajdl, P., Slepicka, P., Svorcik, V., 2014. Plasma activated polymers grafted with cysteamine improving surfaces cytocompatibility. Polym. Degrad. Stab. 101, 1–9.

Konala, V.B., Mamidi, M.K., Bhonde, R., Das, A.K., Pochampally, R., Pal, R., 2016. The current landscape of the mesenchymal stromal cell secretome: A new paradigm for cell-free regeneration. Cytotherapy 18, 13–24.

Krocilova, N., Bacakova, L., Parizek, M., Havlikova, J., Motarjemi, H., Molitor, M., Gabor, R., Marvan, J., 2015. Growth of human adipose-derived stem cells on Ti-6Al-4V alloy with various surface modifications. In: Proceedings of NANOCON 2015, 7th International Conference on Nanomaterials - Research & Application, 14.–16.10 2015, pp. 466–471 978-80-87294-53-6. (Brno, Czech Republic).

Kucia, M., Wu, W., Ratajczak, M.Z., 2007. Bone marrow-derived very small embryonic-like stem cells: their developmental origin and biological significance. Dev. Dyn. 236, 3309–3320.

Kuo, Y.R., Wang, C.T., Cheng, J.T., Kao, G.S., Chiang, Y.C., Wang, C.J., 2016. Adipose-derived stem cells accelerate diabetic wound healing through the induction of autocrine and paracrine effects. Cell Transplant. 25, 71–81.

Kupcova Skalnikova, H., 2013. Proteomic techniques for characterisation of mesenchymal stem cell secretome. Biochimie 95, 2196–2221.

Lachaud, C.C., López-Beas, J., Soria, B., Hmadcha, A., 2014. EGF-induced adipose tissue mesothelial cells undergo functional vascular smooth muscle differentiation. Cell Death Dis. 5, e1304.

Lee, W.C., Maul, T.M., Vorp, D.A., Rubin, J.P., Marra, K.G., 2007. Effects of uniaxial cyclic strain on adipose-derived stem cell morphology, proliferation, and differentiation. Biomech. Model. Mechanobiol. 6, 265–273.

Lee, H.C., An, S.G., Lee, H.W., Park, J.S., Cha, K.S., Hong, T.J., Park, J.H., Lee, S.Y., Kim, S.P., Kim, Y.D., Chung, S.W., Bae, Y.C., Shin, Y.B., Kim, J.I., Jung, J.S., 2012. Safety and effect of adipose tissue-derived stem cell implantation in patients with critical limb ischemia: a pilot study. Circ. J. 76, 1750–1760.

Levi, B., Hyun, J.S., Nelson, E.R., Li, S., Montoro, D.T., Wan, D.C., Jia, F.J., Glotzbach, J.C., James, A.W., Lee, M., Huang, M., Quarto, N., Gurtner, G.C., Wu, J.C., Longaker, M.T., 2011. Nonintegrating knockdown and customized scaffold design enhances human adipose-derived stem cells in skeletal repair. Stem Cells 29, 2018–2029.

Li, X., Zhao, S., Wang, L., 2018. Therapeutic effect of adipose derived stem cell transplantation on optic nerve injury in rats. Mol. Med. Rep. 17, 2529–2534.

Liu, W.H., Ren, L.N., Wang, T., Navarro-Alvarez, N., Tang, L.J., 2016. The involving roles of intrahepatic and extrahepatic stem/progenitor cells (SPCs) to liver regeneration. Int. J. Biol. Sci. 12, 954–963.

Llucià-Valldeperas, A., Sanchez, B., Soler-Botija, C., Gálvez-Montón, C., Prat-Vidal, C., Roura, S.I., Rosell-Ferrer, J., Bragos, R., Bayes-Genis, A., 2015. Electrical stimulation of cardiac adipose tissue-derived progenitor cells modulates cell phenotype and genetic machinery. J. Tissue Eng. Regen. Med. 9, E76–83.

Locke, M., Windsor, J., Dunbar, P.R., 2009. Human adipose-derived stem cells: isolation, characterization and applications in surgery. ANZ J. Surg. 79, 235–244.

Logovskaya, L.V., Bukharova, T.B., Volkov, A.V., Vikhrova, E.B., Makhnach, O.V., Goldshtein, D.V., 2013. Induction of osteogenic differentiation of multipotent mesenchymal stromal cells from human adipose tissue. Bull. Exp. Biol. Med. 155, 145–150.

Luo, L., Zheng, W., Lian, G., Chen, H., Li, L., Xu, C., Xie, L., 2018. Combination treatment of adipose-derived stem cells and adiponectin attenuates pulmonary arterial hypertension in rats by inhibiting pulmonary arterial smooth muscle cell proliferation and regulating the AMPK/BMP/Smad pathway. Int. J. Mol. Med. 41, 51–60.

Ma, Q., Chen, C., Deng, P., Zhu, G., Lin, M., Zhang, L., Xu, S., He, M., Lu, Y., Duan, W., Pi, H., Cao, Z., Pei, L., Li, M., Liu, C., Zhang, Y., Zhong, M., Zhou, Z., Yu, Z., 2016. Extremely low-frequency electromagnetic fields promote in vitro neuronal differentiation and neurite outgrowth of embryonic neural stem cells via up-regulating TRPC1. PLoS One 11, e0150923.

Marconi, S., Bonaconsa, M., Scambi, I., Squintani, G.M., Rui, W., Turano, E., Ungaro, D., D'Agostino, S., Barbieri, F., Angiari, S., Farinazzo, A., Constantin, G., Del Carro, U., Bonetti, B., Mariotti, R., 2013. Systemic treatment with adipose-derived mesenchymal stem cells ameliorates clinical and pathological features in the amyotrophic lateral sclerosis murine model. Neuroscience 248, 333–343.

Mardani, M., Roshankhah, S., Hashemibeni, B., Salahshoor, M., Naghsh, E., Esfandiari, E., 2016. Induction of chondrogenic differentiation of human adipose-derived stem cells by low frequency electric field. Adv. Biomed. Res. 5, 97.

Marei, H.E.S., El-Gamal, A., Althani, A., Afifi, N., Abd-Elmaksoud, A., Farag, A., Cenciarelli, C., Thomas, C., Anwarul, H., 2018. Cholinergic and dopaminergic neuronal differentiation of human adipose tissue derived mesenchymal stem cells. J. Cell. Physiol. 233, 936–945.

Marfia, G., Navone, S.E., Hadi, L.A., Paroni, M., Berno, V., Beretta, M., Gualtierotti, R., Ingegnoli, F., Levi, V., Miozzo, M., Geginat, J., Fassina, L., Rampini, P., Tremolada, C., Riboni, L., Campanella, R., 2016. The adipose mesenchymal stem cell secretome inhibits inflammatory responses of microglia: evidence for an involvement of sphingosine-1-phosphate signalling. Stem Cells Dev. 25, 1095–1107.

Marino, G., Rosso, F., Ferdinando, P., Grimaldi, A., de Biasio, G., Cafiero, G., Barbarisi, M., Barbarisi, A., 2012. Growth and endothelial differentiation of adipose stem cells on polycaprolactone. J. Biomed. Mater. Res. A 100, 543–548.

Marote, A., Teixeira, F.G., Mendes-Pinheiro, B., Salgado, A.J., 2016. MSCs-Derived Exosomes: cell-secreted nanovesicles with regenerative potential. Front. Pharmacol. 7, 231.

Marra, K.G., Brayfield, C.A., Rubin, J.P., 2011. Adipose stem cell differentiation into smooth muscle cells. Methods Mol. Biol. 702, 261–268.

Maumus, M., Jorgensen, C., Noël, D., 2013. Mesenchymal stem cells in regenerative medicine applied to rheumatic diseases: role of secretome and exosomes. Biochimie 95, 2229–2234.

McCue, S., Dajnowiec, D., Xu, F., Zhang, M., Jackson, M.R., Langille, B.L., 2006. Shear stress regulates forward and reverse planar cell polarity of vascular endothelium in vivo and in vitro. Circ. Res. 98, 939–946.

Mead, B., Logan, A., Berry, M., Leadbeater, W., Scheven, B.A., 2014. Paracrine-mediated neuroprotection and neuritogenesis of axotomised retinal ganglion cells by human dental pulp stem cells: comparison with human bone marrow and adipose-derived mesenchymal stem cells. PLoS One 9, e109305.

Melchiorri, A.J., Bracaglia, L.G., Kimerer, L.K., Hibino, N., Fisher, J.P., 2016. In Vitro endothelialization of biodegradable vascular grafts via endothelial progenitor cell seeding and maturation in a tubular perfusion system bioreactor. Tissue Eng. Part C Methods. 22, 663–670.

Melief, S.M., Zwaginga, J.J., Fibbe, W.E., Roelofs, H., 2013. Adipose tissue-derived multipotent stromal cells have a higher immunomodulatory capacity than their bone marrow-derived counterparts. Stem Cells Transl. Med. 2, 455–463.

Merfeld-Clauss, S., Gollahalli, N., March, K.L., Traktuev, D.O., 2010. Adipose tissue progenitor cells directly interact with endothelial cells to induce vascular network formation. Tissue Eng. Part A. 16, 2953–2966.

Mizuno, H., 2013. Adipose-derived stem cells for regenerative medicine in the field of plastic and reconstructive surgery. J. Oral Biosciences. 55, 132–136.

Mohr, A., Zwacka, R., 2018. The future of mesenchymal stem cell-based therapeutic approaches for cancer - From cells to ghosts. Cancer Lett. 414, 239–249.

Monfort, A., Soriano-Navarro, M., García-Verdugo, J.M., Izeta, A., 2013. Production of human tissue-engineered skin trilayer on a plasma-based hypodermis. J. Tissue Eng. Regen. Med. 7, 479–490.

Morisaki, T., Kishimoto, Y., Tateya, I., Kawai, Y., Suzuki, R., Tsuji, T., Hiwatashi, N., Nakamura, T., Omori, K., Kitano, H., Takeuchi, H., Hirano, S., 2018. Adipose-derived mesenchymal stromal cells prevented rat vocal fold scarring. Laryngoscope 128, E33–E40.

Naderi, N., Wilde, C., Haque, T., Francis, W., Seifalian, A.M., Thornton, C.A., Xia, Z., Whitaker, I.S., 2014. Adipogenic differentiation of adipose-derived stem cells in 3-dimensional spheroid cultures (microtissue): implications for the reconstructive surgeon. J. Plast. Reconstr. Aesthet. Surg. 67, 1726–1734.

Nae, S., Bordeianu, I., Stăncioiu, A.T., Antohi, N., 2013. Human adipose-derived stem cells: definition, isolation, tissue-engineering applications. Romanian J. Morphol. Embryol. 54, 919–924.

Natesan, S., Zhang, G., Baer, D.G., Walters, T.J., Christy, R.J., Suggs, L.J., 2011. A bilayer construct controls adipose-derived stem cell differentiation into endothelial cells and pericytes without growth factor stimulation. Tissue Eng. Part A. 17, 941–953.

New, S.E., Alvarez-Gonzalez, C., Vagaska, B., Gomez, S.G., Bulstrode, N.W., Madrigal, A., Ferretti, P., 2015. A matter of identity - Phenotype and differentiation potential of human somatic stem cells. Stem Cell Res. 15, 1–13.

Nigro, P., Bassetti, B., Cavallotti, L., Catto, V., Carbucicchio, C., Pompilio, G., 2018. Cell therapy for heart disease after 15 years: Unmet expectations. Pharmacol. Res. 127, 77–91.

Nincheri, P., Luciani, P., Squecco, R., Donati, C., Bernacchioni, C., Borgognoni, L., Luciani, G., Benvenuti, S., Francini, F., Bruni, P., 2009. Sphingosine 1-phosphate induces differentiation of adipose tissue-derived mesenchymal stem cells towards smooth muscle cells. Cell. Mol. Life Sci. 66, 1741–1754.

Olivares-Navarrete, R., Sutha, K., Hyzy, S.L., Hutton, D.L., Schwartz, Z., McDevitt, T., Boyan, B.D., 2012. Osteogenic differentiation of stem cells alters vitamin D receptor expression. Stem Cells Dev. 21, 1726–1735.

Ong, W.K., Sugii, S., 2013. Adipose-derived stem cells: fatty potentials for therapy. Int. J. Biochem. Cell Biol. 45, 1083–1086.

Otero-Ortega, L., Gutiérrez-Fernández, M., Ramos-Cejudo, J., Rodríguez-Frutos, B., Fuentes, B., Sobrino, T., Hernanz, T.N., Campos, F., López, J.A., Cerdán, S., Vázquez, J., Díez-Tejedor, E., 2015. White matter injury restoration after stem cell administration in subcortical ischemic stroke. Stem Cell Res Ther 6, 121.

Owczarczyk-Saczonek, A., Wociór, A., Placek, W., Maksymowicz, W., Wojtkiewicz, J., 2017. The use of adipose-derived stem cells in selected skin diseases (vitiligo, alopecia, and nonhealing wounds). Stem Cells Int. 2017, 4740709.

Pang, J.H., Farhatnia, Y., Godarzi, F., Tan Rajadas, J., Cousins, B.G., Seifalian, A.M., 2015. In situ endothelialization: Bioengineering considerations to translation. Small 11, 6248–6264.

Park, I.S., Kim, S.H., Heo, D.N., Jung, Y., Kwon, I.K., Rhie, J.W., Kim, S.H., 2012. Synergistic effect of biochemical factors and strain on the smooth muscle cell differentiation of adipose-derived stem cells on an elastic nanofibrous scaffold. J. Biomater. Sci. Polym. Ed. 23, 1579–1593.

Park, W.S., Heo, S.C., Jeon, E.S., Hong Da, H., Son, Y.K., Ko, J.H., Kim, H.K., Lee, S.Y., Kim, J.H., Han, J., 2013a. Functional expression of smooth muscle-specific ion channels in TGF-β(1)-treated human adipose-derived mesenchymal stem cells. Am. J. Physiol. Cell. Physiol. 305, C377–C391.

Park, I.S., Kim, S.H., Jung, Y., Rhie, J.W., Kim, S.H., 2013b. Endothelial differentiation and vasculogenesis induced by three-dimensional adipose-derived stem cells. Anat. Rec. (Hoboken). 296, 168–177.

Patel, D.M., Shah, J., Srivastava, A.S., 2013. Therapeutic potential of mesenchymal stem cells in regenerative medicine. Stem Cells Int. 2013, 496218.

Pelton, J.C., Wright, C.E., Leitges, M., Bautch, V.L., 2014. Multiple endothelial cells

constitute the tip of developing blood vessels and polarize to promote lumen formation. Development 141, 4121–4126.

Petecchia, L., Sbrana, F., Utzeri, R., Vercellino, M., Usai, C.L., Visai, L., Vassalli, M., Gavazzo, P., 2015. Electro-magnetic field promotes osteogenic differentiation of BM-hMSCs through a selective action on Ca(2 +)-related mechanisms. Sci. Rep. 5, 13856.

Pill, K., Hofmann, S., Redl, H., Holnthoner, W., 2015. Vascularization mediated by mesenchymal stem cells from bone marrow and adipose tissue: a comparison. Cell. Regen. (Lond). 4, 8.

Policha, A., Zhang, P., Chang, L., Lamb, K., Tulenko, T., DiMuzio, P., 2014. Endothelial differentiation of diabetic adipose-derived stem cells. J. Surg. Res. 192, 656–663.

Powell, H.M., McFarland, K.L., Butler, D.L., Supp, D.M., 2010. Boyce ST. Uniaxial strain regulates morphogenesis, gene expression, and tissue strength in engineered skin. Tissue Eng. Part A. 16, 1083–1092.

Prè, D., Ceccarelli, G., Gastaldi, G., Asti, A., Saino, E., Visai, L., Benazzo, F., Cusella De Angelis, M.G., Magenes, G., 2011. The differentiation of human adipose-derived stem cells (hASCs) into osteoblasts is promoted by low amplitude, high frequency vibration treatment. Bone 49, 295–303.

Prochazka, V., Jurcikova, J., Lassak, O., Vitkova, K., Pavliska, L., Porubova, L., Buszman, P.P., Krauze, A., Fernandez, C., Jaluvka, F., Spackova, I., Lochman, I., Jana, D., Merfeld-Clauss, S., March, K.L., Traktuev, D.O., Johnstone, B.H., 2016. Therapeutic potential of adipose-derived therapeutic factor concentrate for treating critical limb ischemia. Cell Transplant. 25, 1623–1633.

Przekora, A., Vandrovcova, M., Travnickova, M., Pajorova, J., Molitor, M., Ginalska, G., Bacakova, L., 2017. Evaluation of the potential of chitosan/β-1,3-glucan/HA material as scaffold for living bone graft production in vitro by comparison of ADSC and BMDSC behaviour on its surface. Biomed. Mater. 12, 015030.

Qin, Y., Zhou, C., Wang, N., Yang, H., Gao, W., 2015. Conversion of adipose tissue-derived mesenchymal stem cells to neural stem cell-like cells by a single transcription factor, Sox2. Cell Rep. 17, 221–226.

Rampichova, M., Chvojka, J., Buzgo, M., Prosecka, E., Mikes, P., Vyslouzilova, L., Tvrdik, D., Kochova, P., Gregor, T., Lukas, D., Amler, E., 2013. Elastic three-dimensional poly (ε-caprolactone) nanofibre scaffold enhances migration, proliferation and osteogenic differentiation of mesenchymal stem cells. Cell Prolif. 46, 23–37.

Ravichandran, R., Venugopal, J.R., Sundarrajan, S., Mukherjee, S., Forsythe, J., Ramakrishna, S., 2013. Click chemistry approach for fabricating PVA/gelatin nanofibers for the differentiation of ADSCs to keratinocytes. J. Mater. Sci. Mater. Med. 24, 2863–2871.

Razavi, S., Ghasemi, N., Mardani, M., Salehi, H., 2018. Co-transplantation of human neurotrophic factor secreting cells and adipose-derived stem cells in rat model of multiple sclerosis. Cell J. 20, 46–52.

Riedel, T., Brynda, E., Dyr, J.E., Houska, M., 2009. Controlled preparation of thin fibrin films immobilized at solid surfaces. J. Biomed. Mater. Res. A 88, 437–447.

Riis, S., Stensballe, A., Emmersen, J., Pennisi, C.P., Birkelund, S., Zachar, V., Fink, T., 2016. Mass spectrometry analysis of adipose-derived stem cells reveals a significant effect of hypoxia on pathways regulating extracellular matrix. Stem Cell Res Ther 7, 52.

Roberts, R.L., Sandra, A., 1993. Apical-basal membrane polarity of membrane phosphatases in isolated capillary endothelium: alteration in ultrastructural localisation under culture conditions. J. Anat. 182, 339–347.

Rohringer, S., Hofbauer, P., Schneider, K.H., Husa, A.M., Feichtinger, G., Peterbauer-Scherb, A., Redl, H., Holnthoner, W., 2014. Mechanisms of vasculogenesis in 3D fibrin matrices mediated by the interaction of adipose-derived stem cells and endothelial cells. Angiogenesis 17, 921–933.

Rony, I.K., Baten, A., Bloomfield, J.A., Islam, M.E., Billah, M.M., Islam, K.D., 2015. Inducing pluripotency in vitro: recent advances and highlights in induced pluripotent stem cells generation and pluripotency reprogramming. Cell Prolif. 48, 140–156.

Ross, C.L., Siriwardane, M., Almeida-Porada, G., Porada, C.D., Brink, P., Christ, G.J., 2015. Harrison BS. The effect of low-frequency electromagnetic field on human bone marrow stem/progenitor cell differentiation. Stem Cell Res. 15, 96–108.

Safaeijavan, R., Soleimani, M., Divsalar, A., Eidi, A., Ardeshirylajimi, A., 2014. Comparison of random and aligned PCL nanofibrous electrospun scaffolds on cardiomyocyte differentiation of human adipose-derived stem cells. Iran J. Basic. Med. Sci. 17, 903–911.

Salgado, A.J., Reis, R.L., Sousa, N.J., Gimble, J.M., 2010. Adipose tissue derived stem cells secretome: soluble factors and their roles in regenerative medicine. Curr. Stem Cell Res. Ther. 5, 103–110.

Sánchez-Muñoz, I., Granados, R., Holguín Holgado, P., García-Vela, J.A., Casares, C., Casares, M., 2015. The use of adipose mesenchymal stem cells and human umbilical vascular endothelial cells on a fibrin matrix for endothelialized skin substitute. Tissue Eng. Part A. 21, 214–223.

Sauer, H., Bekhite, M.M., Hescheler, J., Wartenberg, M., 2005. Redox control of angiogenic factors and CD31-positive vessel-like structures in mouse embryonic stem cells after direct current electrical field stimulation. Exp. Cell Res. 304, 380–390.

Schosserer, M., Reynoso, R., Wally, V., Jug, B., Kantner, V., Weilner, S., Buric, I., Grillari, J., Bauer, J.W., Grillari-Voglauer, R., 2015. Urine is a novel source of autologous mesenchymal stem cells for patients with epidermolysis bullosa. BMC Res. Notes. 8, 767.

Shekkeris, A.S., Jaiswal, P.K., Khan, W.S., 2012. Clinical applications of mesenchymal stem cells in the treatment of fracture non-union and bone defects. Curr. Stem Cell. Res. Ther. 7, 127–133.

Shishatskaya, E.I., Nikolaeva, E.D., Vinogradova, O.N., Volova, T.G., 2016. Experimental wound dressings of degradable PHA for skin defect repair. J. Mater. Sci. Mater. Med. 27, 165.

Singh, V.K., Kumar, N., Kalsan, M., Saini, A., Chandra, R., 2015. Mechanism of induction: induced pluripotent stem cells (iPSCs). J. Stem Cells. 10, 43–62.

Sivan, U., Jayakumar, K., Krishnan, L.K., 2014. Constitution of fibrin-based niche for in

vitro differentiation of adipose-derived mesenchymal stem cells to keratinocytes. Biores Open Access. 3, 339–347.

Sivan, U., Jayakumar, K., Krishnan, L.K., 2016. Matrix-directed differentiation of human adipose-derived mesenchymal stem cells to dermal-like fibroblasts that produce extracellular matrix. J. Tissue Eng. Regen. Med. 10, E546–E558.

Slepicka, P., Slepickova Kasalkova, N., Siegel, J., Kolska, Z., Bacakova, L., Svorcik, V., 2015. Nano-structured and functionalized surfaces for cytocompatibility improvement and bactericidal action. Biotechnol. Adv. 33, 1120–1129.

Slepickova Kasalkova, N., Slepicka, P., Bacakova, L., Kolska, Z., Svorcik, V., 2017. Interaction of Stem Cells with Polymer Substrate. Chem. List. 111, 439–444.

Sterodimas, A., de Faria, J., Nicaretta, B., Pitanguy, I., 2010. Tissue engineering with adipose-derived stem cells (ADSCs): current and future applications. J. Plast. Reconstr. Aesthet. Surg. 63, 1886–1892.

Succar, P., Medynskyj, M., Breen, E.J., Batterham, T., Molloy, M.P., Herbert, B.R., 2016. Priming adipose-derived mesenchymal stem cells with hyaluronan alters growth kinetics and increases attachment to articular cartilage. Stem Cells Int. 2016, 9364213.

Tajiri, N., Acosta, S.A., Shahaduzzaman, M., Ishikawa, H., Shinozuka, K., Pabon, M., Hernandez-Ontiveros, D., Kim, D.W., Metcalf, C., Staples, M., Dailey, T., Vasconcellos, J., Franyuti, G., Gould, L., Patel, N., Cooper, D., Kaneko, Y., Borlongan, C.V., Bickford, P.C., 2014. Intravenous transplants of human adipose-derived stem cell protect the brain from traumatic brain injury-induced neurodegeneration and motor and cognitive impairments: cell graft biodistribution and soluble factors in young and aged rats. J. Neurosci. 34, 313–326.

Takahashi, K., Tanabe, K., Ohnuki, M., Narita, M., Ichisaka, T., Tomoda, K., Yamanaka, S., 2007. Induction of pluripotent stem cells from adult human fibroblasts by defined factors. Cell 131, 861–872.

Taléns-Visconti, R., Bonora, A., Jover, R., Mirabet, V., Carbonell, F., Castell, J.V., Gómez-Lechón, M.J., 2006. Hepatogenic differentiation of human mesenchymal stem cells from adipose tissue in comparison with bone marrow mesenchymal stem cells. World J. Gastroenterol. 12, 5834–5845.

Tan, Y., Ooi, S., Wang, L., 2014. Immunogenicity and tumorigenicity of pluripotent stem cells and their derivatives: genetic and epigenetic perspectives. Curr. Stem Cell Res. Ther. 9, 63–72.

Tashiro, S., Nishimura, S., Iwai, H., Sugai, K., Zhang, L., Shinozaki, M., Iwanami, A., Toyama, Y., Liu, M., Okano, H., Nakamura, M., 2016. Functional recovery from neural stem/progenitor cell transplantation combined with treadmill training in mice with chronic spinal cord injury. Sci. Rep. 6, 30898.

Teong, B., Wu, S.C., Chang, C.M., Chen, J.W., Chen, H.T., Chen, C.H., Chang, J.K., Ho, M.L., 2018. The stiffness of a crosslinked hyaluronan hydrogel affects its chondro-induction activity on hADSCs. J Biomed Mater Res B Appl Biomater 106, 808–816.

Thakkar, U.G., Vanikar, A.V., Trivedi, H.L., 2014. Co-infusion of autologous adipose tissue derived neuronal differentiated mesenchymal stem cells and bone marrow derived hematopoietic stem cells, a viable therapy for post-traumatic brachial plexus injury: a case report. Biom. J. 37, 237–240.

Thakkar, U.G., Trivedi, H.L., Vanikar, A.V., Dave, S.D., 2015. Insulin-secreting adipose-derived mesenchymal stromal cells with bone marrow-derived hematopoietic stem cells from autologous and allogenic sources for type 1 diabetes mellitus. Cytotherapy 17, 940–947.

Thakkar, U.G., Vanikar, A.V., Trivedi, H.L., Shah, V.R., Dave, S.D., Dixit, S.B., Tiwari, B.B., Shah, H.H., 2016. Infusion of autologous adipose tissue derived neuronal differentiated mesenchymal stem cells and hematopoietic stem cells in post-traumatic paraplegia offers a viable therapeutic approach. Adv. Biomed. Res. 5, 51.

Thamm, O.C., Theodorou, P., Stuermer, E., Zinser, M.J., Neugebauer, E.A., Fuchs, P.C., Koenen, P., 2015. Adipose-derived stem cells and keratinocytes in a chronic wound cell culture model: the role of hydroxyectoine. Int. Wound J. 12, 387–396.

Tian, G., Zhou, J., Wang, J., Xu, B., Li, L., Zhu, F., Han, J., Li, J., Zhang, S., Luo, X., 2012. Neuronal differentiation of adipose-derived stem cells and their transplantation for cerebral ischemia. Neural Regen. Res. 7, 1992–1999.

Tincer, G., Mashkaryan, V., Bhattarai, P., Kizil, C., 2016. Neural stem/progenitor cells in Alzheimer's disease. Yale J. Biol. Med. 89, 23–35.

Tirkkonen, L., Haimi, S., Huttunen, S., Wolff, J., Pirhonen, E., Sándor, G.K., Miettinen, S., 2013. Osteogenic medium is superior to growth factors in differentiation of human adipose stem cells towards bone-forming cells in 3D culture. Eur. Cell Mater. 25, 144–158.

Tobita, M., Orbay, H., Mizuno, H., 2011. Adipose-derived stem cells: current findings and future perspectives. Discov. Med. 11, 160–170.

Tremblay, J.R., LeBon, J.M., Luo, A., Quijano, J.C., Wedeken, L., Jou, K., Riggs, A.D., Tirrell, D.A., Ku, H.T., 2016. In Vitro Colony Assays for Characterizing Tri-potent Progenitor Cells Isolated from the Adult Murine Pancreas. J. Vis. Exp. 112.

Trottier, V., Marceau-Fortier, G., Germain, L., Vincent, C., Fradette, J., 2008. IFATS collection: Using human adipose-derived stem/stromal cells for the production of new skin substitutes. Stem Cells 26, 2713–2723.

Vaikkath, D., Anitha, R., Sumathy, B., Nair, P.D., 2016. A simple and effective method for making multipotent/multilineage scaffolds with hydrophilic nature without any postmodification/treatment. Colloids Surf. B: Biointerfaces 141, 112–119.

Van Pham, P., Truong, N.C., Le, P.T., Tran, T.D., Vu, N.B., Bui, K.H., Phan, N.K., 2016. Isolation and proliferation of umbilical cord tissue derived mesenchymal stem cells for clinical applications. Cell Tissue Bank. 17, 289–302.

Varghese, J., Griffin, M., Mosahebi, A., Butler, P., 2017. Systematic review of patient factors affecting adipose stem cell viability and function: implications for regenerative therapy. Stem Cell Res Ther 8, 45.

Visvader, J.E., Clevers, H., 2016. Tissue-specific designs of stem cell hierarchies. Nat. Cell Biol. 18, 349–355.

Vojtassák, J., Danisovic, L., Kubes, M., Bakos, D., Jarábek, L., Ulicná, M., Blasko, M., 2006. Autologous biograft and mesenchymal stem cells in treatment of the diabetic foot. Neuro Endocrinol. Lett. 27 (Suppl. 2), 134–137.

Wainstein, C., Quera, R., Fluxá, D., Kronberg, U., Conejero, A., López-Köstner, F., Jofre, C., Zarate, A.J., 2018. Stem cell therapy in refractory perineal Crohn's disease: long-term follow-up. Color. Dis. http://dx.doi.org/10.1111/codi.14002. (in press).

Wan, Q., Yeung, S.S., Cheung, K.K., Au, S.W., Lam, W.W., Li, Y.H., Dai, Z.Q., Yeung, E.W., 2016. Optimizing. Am. J. Phys. Med. Rehabil. 95, 28–38.

Wang, C., Yin, S., Cen, L., Liu, Q., Liu, W., Cao, Y., Cui, L., 2010. Differentiation of adipose-derived stem cells into contractile smooth muscle cells induced by transforming growth factor-beta1 and bone morphogenetic protein-4. Tissue Eng. Part A. 16, 1201–1213.

Weissman, I.L., 2000. Stem cells: units of development, units of regeneration, and units in evolution. Cell 100, 157–168.

Weissman, I.L., 2015. Stem cells are units of natural selection for tissue formation, for germline development, and in cancer development. Proc. Natl. Acad. Sci. U. S. A. 112, 8922–8928.

Witkowska-Zimny, M., Walenko, K., Wałkiewicz, A.E., Pojda, Z., Przybylski, J., Lewandowska-Szumieł, M., 2012. Effect of substrate stiffness on differentiation of umbilical cord stem cells. Acta Biochim. Pol. 59, 261–264.

Xiong, B., Tan, Q.W., Chen, Y.J., Zhang, Y., Zhang, D., Tang, S.L., Zhang, S., Lv, Q., 2018. The effects of platelet-rich plasma and adipose-derived stem cells on neovascularization and fat graft survival. Aesthet. Plast. Surg. 42, 1–8.

Yu, J., Vodyanik, M.A., Smuga-Otto, K., Antosiewicz-Bourget, J., Frane, J.L., Tian, S., Nie, J., Jonsdottir, G.A., Ruotti, V., Stewart, R., Slukvin, I.I., Thomson, J.A., 2007. Induced pluripotent stem cell lines derived from human somatic cells. Science 318, 1917–1920.

Zhan, W., Tan, S.S., Lu, F., 2016. Adipose-derived stem cell delivery for adipose tissue engineering: current status and potential applications in a tissue engineering chamber model. Stem Cell Rev. 12, 484–491.

Zhang, Y., Khan, D., Delling, J., Tobiasch, E., 2012. Mechanisms underlying the osteo- and adipo-differentiation of human mesenchymal stem cells. Sci. World J. 2012, 793823.

Zhang, T., Lin, S., Shao, X., Shi, S., Zhang, Q., Xue, C., Lin, Y., Zhu, B., Cai, X., 2018a. Regulating osteogenesis and adipogenesis in adipose-derived stem cells by controlling underlying substrate stiffness. J. Cell. Physiol. 233, 3418–3428.

Zhang, X., Jiang, W., Liu, Y., Zhang, P., Wang, L., Li, W., Wu, G., Ge, Y., Zhou, Y., 2018b. Human adipose-derived stem cells and simvastatin-functionalized biomimetic calcium phosphate to construct a novel tissue-engineered bone. Biochem. Biophys. Res. Commun. 495, 1264–1270.

Zhou, Z., Chen, Y., Zhang, H., Min, S., Yu, B., He, B., Jin, A., 2013. Comparison of mesenchymal stromal cells from human bone marrow and adipose tissue for the treatment of spinal cord injury. Cytotherapy 15, 434–448.

Zhou, X., Tao, Y., Chen, E., Wang, J., Fang, W., Zhao, T., Liang, C., Li, F., Chen, Q., 2018. Genipin-cross-linked type II collagen scaffold promotes the differentiation of adipose-derived stem cells into nucleus pulposus-like cells. J. Biomed. Mater. Res. A (in press). https://doi.org/10.1002/jbm.a.36325.

Zou, T., Fan, J., Fartash, A., Liu, H., Fan, Y., 2016. Cell-based strategies for vascular regeneration. J. Biomed. Mater. Res. A 104, 1297–1314.

Zuba-Surma, E.K., Wojakowski, W., Ratajczak, M.Z., Dawn, B., 2011. Very small embryonic-like stem cells: biology and therapeutic potential for heart repair. Antioxid. Redox Signal. 15, 1821–1834.

Cellulose Mesh with Charged Nanocellulose Coatings as a Promising Carrier of Skin and Stem Cells for Regenerative Applications

Julia Pajorova,*,# Anne Skogberg,*,# Daniel Hadraba, Antonin Broz, Martina Travnickova, Marketa Zikmundova, Mari Honkanen, Markus Hannula, Panu Lahtinen, Maria Tomkova, Lucie Bacakova,* and Pasi Kallio*

Cite This: _Biomacromolecules_ 2020, 21, 4857−4870

Read Online

ACCESS | Metrics & More | Article Recommendations | Supporting Information

ABSTRACT: Engineering artificial skin constructs is an ongoing challenge. An ideal material for hosting skin cells is still to be discovered. A promising candidate is low-cost cellulose, which is commonly fabricated in the form of a mesh and is applied as a wound dressing. Unfortunately, the structure and the topography of current cellulose meshes are not optimal for cell growth. To enhance the surface structure and the physicochemical properties of a commercially available mesh, we coated the mesh with wood-derived cellulose nanofibrils (CNFs). Three different types of mesh coatings are proposed in this study as a skin cell carrier: positively charged cationic cellulose nanofibrils (cCNFs), negatively charged anionic cellulose nanofibrils (aCNFs), and a combination of these two materials (c+aCNFs). These cell carriers were seeded with normal human dermal fibroblasts (NHDFs) or with human adipose-derived stem cells (ADSCs) to investigate cell adhesion, spreading, morphology, and proliferation. The negatively charged aCNF coating significantly improved the proliferation of both cell types. The positively charged cCNF coating significantly enhanced the adhesion of ADSCs only. The number of NHDFs was similar on the cCNF coatings and on the noncoated pristine cellulose mesh. However, the three-dimensional (3D) structure of the cCNF coating promoted cell survival. The c+aCNF construct proved to combine benefits from both types of CNFs, which means that the c+aCNF cell carrier is a promising candidate for further application in skin tissue engineering.
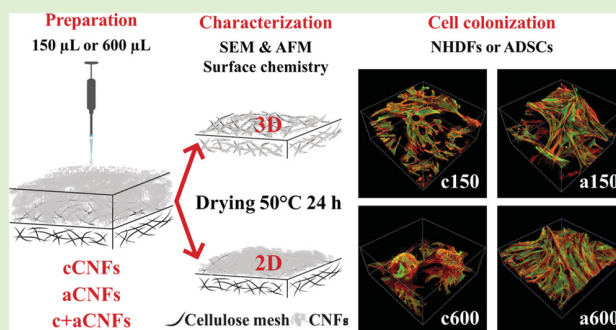
1. INTRODUCTION

Cellulose is frequently used in the production of biomaterials as a scaffold material to carry other molecules, supporting cell adhesion and promoting cell proliferation. Cellulose is an affordable biocompatible material that can be processed into cellulose nanofibrils (CNFs) and nanocellulose-based matrices with precisely controlled physical and chemical properties.

Wood-derived CNFs are manufactured from wood pulp using mechanical techniques alone or in combination with chemical and enzyme-assisted pretreatments.[1] The physicochemical parameters of CNFs, such as swelling, are affected by hydrogen bonding and can be tuned by modifying the CNF dimensions or the charge density.[2,3] The common length of CNFs is within the micrometer range, whereas the width of CNFs is in the nanometer range,[2,4] which mimics the dimensions of extracellular matrix (ECM) components, such as collagen fibrils.[5] Moreover, CNFs form multiple types of solids, such as hydrogels, aerogels, and films with the stiffness range of the dermis and epidermis.[3] These materials absorb significant quantities of water, which is a desired property of wound dressings. The surface properties of wound dressings also have an effect on cellular behavior. The CNF surface has a

weak negative charge in an aqueous solution in the unmodified form, which is not optimal for the growth of mammalian cells.[6] To enhance the cell−surface interactions, the CNF surface can be chemically modified to adjust the hydrophilicity or the surface charge, depending on the requirements of different cell types.[6−8] It has been reported that the modifications of CNFs with cationic or anionic functional groups promoted cell adhesion, proliferation,[6,9] cytocompatibility,[10,11] cell growth directionality,[12] water solubility, and bonding of other bioactive molecules,[7] such as collagen[13] and other peptides and proteins.[6] The beneficial effect of CNF hydrogels is especially emphasized in three-dimensional (3D) cell cultivation.[11,14,15] The application of CNFs as a wound dressing has also recently reached the clinical evaluation phase,[16] and it
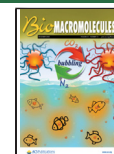
has been examined as a promising scaffold under *in vitro* conditions.[9,17,18]

There are two common chemical modifications that change the charge of the cellulose chain: (1) grafting of anionic 2,2,6,6-tetramethylpiperidine-1-oxyl (TEMPO) oxidation[19] and (2) grafting of cationic glycidyltrimethylammonium chloride (GTMAC).[6] The benefit of these modifications is in adjusting the desired surface properties of CNFs, e.g., for controlled adsorption of bioactive molecules, which can be further stabilized by cross-linking, driven by chemical functional groups introduced into the cellulose molecule.[7] TEMPO-mediated oxidation also allows low-energy mechanical disintegration of oxidized fibers.[19] TEMPO-oxidized anionic CNFs (aCNFs) promote cell adhesion and growth.[12] GTMAC-modified cationic CNFs (cCNFs) effectively adsorb negatively charged compounds,[10,20] including cell adhesion-mediating proteins,[6,21] mediate the binding and the release of hydrophobic drugs,[22] have an antimicrobial effect,[23] and facilitate cell attachment through electrostatic interactions.[8] The attachment of anchorage-dependent cells to CNFs is essential for a newly developed skin cell carrier. The cell adhesion can be regulated by modulating the roughness and the stiffness,[24,25] the surface chemistry,[24,26] the wettability,[3,27] or the electrostatic forces of the substrate.[26]

The present work enhances knowledge about the behavior of cells on promising charged CNF coatings of commercial, economical, and environmentally friendly cellulose meshes. To find an appropriate cell carrier for tissue engineering and wound healing applications, 3D and two-dimensional (2D) coatings of cationic (cCNF), anionic (aCNF), and combined (c+aCNF) nanocellulose were deposited on commercially available cellulose meshes. Since the proposed materials are to be used for skin applications, the CNF-coated meshes were tested *in vitro* with normal human dermal fibroblasts (NHDFs) and with hypodermal human adipose-tissue-derived stem cells (ADSCs).

2. MATERIALS AND METHODS

2.1. Production of Cellulose Nanofibrils. The CNF production and characterization were performed according to the study by Skogberg et al.[12] Both anionic and cationic CNF grades were produced from once-dried bleached birch kraft pulp. Anionic CNFs (aCNFs) were produced using TEMPO-mediated oxidation, as described by Saito et al.;[28] see Supporting Methods (S1.1). Cationic CNFs (cCNFs) were produced by introducing a positive charge using 2,3-epoxypropyl trimethylammonium chloride (EPTMAC; Raisacat, Chimagate, Lapua, Finland); the protocol is described in detail in our earlier study.[12] CNF materials were received from VTT Technical Research Centre (Espoo, Finland).

2.2. Preparation of CNF-Coated Meshes. PurCotton highly pure spunlace nonwoven cotton fabric (Winner Industrial Park, Shenzhen, China) was cut into 1.5×1.5 cm^2 samples (further referred to as "noncoated meshes"). The meshes were fixed into CellCrown inserts (Scaffdex Ltd., Tampere, Finland), which were inserted into 24-well cell culture plates (TPP, Trasadingen, Switzerland).

The CNF gels were diluted to a 0.15% (w/v) solution in Milli-Q water, sonicated for 2 min at 20% amplitude, and centrifuged at 10 000g for 60 min.[12] The CNF-coated meshes were prepared using either 150 or 600 μL of cCNF and aCNF supernatants (further referred to as "c150, c600, a150, a600") and by a combination of these supernatants (c+a), as described in Supporting Methods (S1.2). A pristine noncoated mesh was used as the control. The CNF-coated samples were dried for 24 h in a laboratory dryer (Binder, Tuttlingen, Germany) at 50 °C (Scheme 1). The sterilization included UV-C

Scheme 1. Schematic Picture of the Preparation of the Different Coating Topographies on the Cellulose Meshes Using cCNF and aCNF Solutions
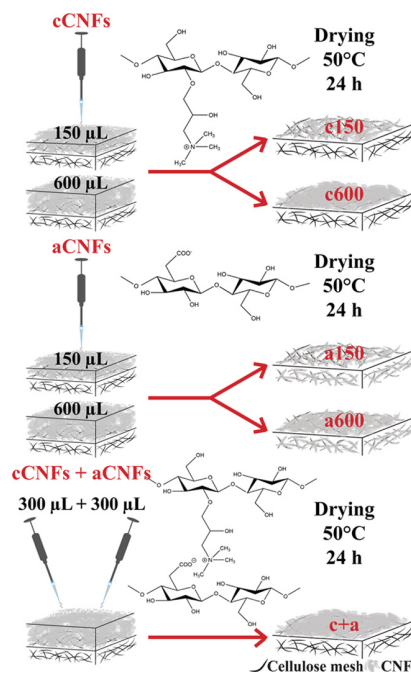
irradiation of both sides of the sample in a flow box for 20 min. The samples were sterilized twice in inserts in a sterile Petri dish before the CNF coatings were prepared and then after the CNF coatings had been dried.

2.3. Characterization of the Noncoated and CNF-Coated Meshes. The CNF-coated meshes were characterized by scanning electron microscopy (SEM; Section 2.3.1) and atomic force microscopy (AFM; Section 2.3.3). Noncoated meshes were also imaged by microCT (S1.3). In addition, the physicochemical properties, i.e., the wettability (S1.4), the swelling ratio (Section 2.3.2), and the surface stiffness (Section 2.3.3), were studied.

2.3.1. Topography of CNF-Coated Meshes Using SEM. Front and side views of the CNF-coated meshes (c150, c600, a150, a600, and c+a) and noncoated meshes were acquired using SEM (ULTRAplus, Carl Zeiss, Oberkochen, Germany). The samples were attached to aluminum SEM stubs using a carbon tape and carbon-coated to avoid charging during the SEM studies. The front view was scanned from the surface of the CNF-coated or noncoated meshes, while the side view was scanned from the cut edges.

2.3.2. Swelling Ratio Measurements. The swelling ratio was measured either on a600, c600, and c+aCNF-coated and noncoated meshes ($n = 3$) or the corresponding glass coverslips (600 μL, $n = 3$). The initial dry weight (W_0) was measured before the samples were immersed in deionized water (dH$_2$O) or in Dulbecco's modified Eagle medium (DMEM) at 37 °C. The swollen samples were weighed (W_s) at two time points: after 20 min and after 20 h. After being weighed at time point 1 (20 min), the samples were returned into dH$_2$O or DMEM and incubated at 37 °C. The water uptake, subsequently referred to as the swelling ratio (SR), was determined as SR = (W_s − W_0)/W_0. The data was presented as the arithmetic mean ± standard deviation (SD) from three parallel samples for each experimental group.

2.3.3. Surface Mapping and Characterization of Mechanical Properties Using AFM. AFM data were acquired only for the samples coated with c600, a600, and c+a. The coatings were prepared by gradual application of 600 μL of CNF solution on both sides of the cellulose mesh. The first step is described in Supporting Methods (S1.2). 3D printed tubes fitted on the CellCrown inserts from the outer side were utilized for applying the CNF solution in the second

step. Young's modulus and the surface arithmetic average roughness (R_a) were determined on the coating from the outer side of the samples. The samples in the inserts were mounted into a custom holder and mapped using an Olympus IX 81 camera (Japan) linked with a JPK NanoWizard 3 AFM microscope (JPK, Berlin, Germany).

Roughness maps of the dry samples were mapped in the hybrid acquisition mode (Quantitative Imaging mode, QI) with an SNL-10A probe (tip radius 2 nm, cantilever spring constant 0.361 N/m, sensitivity 15.4 nm/V; Bruker AFM Probes, Billerica, MA). QI images were acquired. The dry samples were further examined for their mechanical properties in the same setup as the roughness mapping but with an MPP-12120-10 probe (tip radius 8 nm, cantilever spring constant 5.05 N/m, sensitivity 13.1 nm/V; Bruker AFM Probes, Billerica, MA); for details, see Supporting Methods (S1.5).

The mechanical properties of the wet samples were probed at time points of 20 min and 17 h after immersion in Dulbecco's modified Eagle's medium (DMEM; Sigma-Aldrich Co., St. Louis, MO, Cat. no. D2902). In addition, the probe was replaced by a CP-qp-CONT-SiO colloidal probe (tip diameter 6.62 μm, cantilever spring constant 0.391 N/m, sensitivity 45.23 nm/V; NanoAndMore, Wetzlar, Germany); see Supporting Methods (S1.5).

All measurements were preceded by a calibration process. Two parallel samples (eight measurements in total) were used for each experimental group, and the data were presented as the median (Mdn) and the interquartile range.

2.4. Evaluation of Cell Behavior on CNF-Coated Meshes.
Two cell types (Section 2.4.1) were cultured on meshes coated with each of the CNF coatings and on the noncoated meshes (Section 2.4.2) to compare the dependence of the cell behavior on the parameters of the sample. The proliferation (Section 2.4.3), the morphology (Section 2.4.4), and the protein-mediated adhesion (Sections 2.4.5, 2.4.6, and S1.12) of the cells were evaluated.

2.4.1. Cell Models and Culture Conditions. Neonatal normal human dermal fibroblasts (NHDFs, Lonza, Basel, Switzerland, Cat. no. CC-2509) were cultivated in the DMEM medium with 10% fetal bovine serum (FBS; Thermo Fisher Scientific, Gibco, Waltham, MA, Cat. no. 10270-106) and 40 μg/mL gentamicin (LEK, Ljubljana, Slovenia). Adipose-tissue-derived stem cells (ADSCs) were isolated from lipoaspirates after donors' confirmed written informed consent had been obtained, in compliance with the Declaration of Helsinki, and under ethical approval by the Ethics Committee at Na Bulovce Hospital in Prague. The isolation procedure for the ADSCs was performed according to Estes and co-authors,[29] with slight modifications as previously described.[30,31] The pooled ADSCs (for details, see Supporting Methods S1.6) were cultured in the DMEM medium and supplemented with 10% FBS, 40 μg/mL gentamicin, and 10 ng/mL recombinant human basic fibroblast growth factor (FGF2; GenScript, Piscataway, NJ).

2.4.2. Cultivation of Cells on CNF-Coated Meshes. The CNF-coated and noncoated meshes, fixed into CellCrown inserts and placed into 24-well cell culture plates (see above), were seeded with NHDFs and ADSCs in passage 3 at a density of 20 000 cells/insert (i.e., approx. 25 000 cells/cm^2) in 1 mL/well of the cell culture medium. An amount of 0.5 mL/well was added after 2 h of cultivation into the final volume of 1.5 mL/well. The cells were cultivated for 7 days in a cell incubator at 37 °C in a humidified air atmosphere with 5% CO$_2$. The behavior of the cells was evaluated in three time intervals (days 1, 3, and 7), and the culture wells of 24-well polystyrene plates (PS) were used as a control material.

2.4.3. Metabolic Activity of the Cells on CNF-Coated Meshes (Resazurin Assay). The level of metabolic activity of the NHDFs and ADSCs on cellulose meshes with all CNF coatings was measured as an indirect marker of the cell number in three time intervals (days 1, 3, and 7) using the conversion of resazurin sodium salt (Sigma-Aldrich Co., St. Louis, MO, Cat. no. R7017) into resorufin by mitochondrial enzymes (for details, see Supporting Methods S1.7). Four parallel samples were used for each experimental group and each time interval. The data were presented as the arithmetic mean ± standard deviation and were used for constructing growth plots to view the overall growth dynamics of the cells.

2.4.4. Fluorescence Staining and SEM Imaging of the Cells on CNF-Coated Meshes. The morphology of NHDFs and ADSCs seeded on the cellulose meshes with all CNF coatings was visualized in three time intervals (days 1, 3, and 7) by staining filamentous actin (F-actin) and vinculin, an important protein of focal adhesion plaques. Vinculin was stained to indicate the level of specific receptor-mediated cell adhesion and cell spreading. The detailed staining protocol and the imaging setup are presented in Supporting Methods (S1.8).

The morphology of the cells on the CNF-coated and noncoated meshes was further assessed by SEM on day 3 after cell seeding. The dehydrated samples, see Supporting Methods (S1.8) for details, were fixed on aluminum stubs using a carbon tape, followed by gold coating.

2.4.5. Protein Adsorption on CNF-Coated Meshes (Pierce BCA Protein Assay Kit). The investigated materials were preadsorbed with proteins derived from blood serum—FBS or bovine serum albumin (BSA)—which modulate the cell adhesion. The total amount of these proteins adsorbed on the CNF-coated (c600, a600, c+a) and noncoated meshes was evaluated by the Pierce BCA Protein Assay Kit (Pierce BCA Protein Assay, Rockford, IL); for details, see Supporting Methods (S1.9). Four parallel samples (eight measurements in total) were used for each experimental group, and the data were presented as the arithmetic mean ± standard deviation of the adsorbed proteins (mg/sample), calculated from the BSA calibration curve according to the manufacturer's protocol. The data were further expressed as the ratio of the adsorbed proteins (mg/sample) to the concentration of the total proteins in 1.5 mL of added FBS and BSA solutions and given as a percentage.

2.4.6. Cell Adhesion on cCNF Coatings Preadsorbed with Proteins. To explain the cell behavior on cCNF coatings, meshes (see S1.10) and glass coverslips (see S1.11) with cCNF coatings were used for evaluating the dependence of the cell adhesion on the composition of the preadsorbed proteins. The initial cell adhesion on the c600 coatings was observed by fluorescence staining of the cells, as described above (Section 2.4.4). The treated group of cCNF coatings was preadsorbed with proteins for 2 h before cell seeding, while the cCNF coating control group was seeded with cells and proteins simultaneously (Scheme S1).

2.5. Statistical Analysis.
The statistical significance of the data measured by AFM was evaluated using the nonparametric analysis of variance (Kruskal–Wallis), with Tukey's posthoc test for pairwise comparison. Values of $p \leq 0.05$ were considered significant. If not stated otherwise, the data postprocessing and statistical testing were performed in Matlab 2019a (MathWorks Inc., Natick, MA). The parametric data from the measurements of the swelling ratio, the cell metabolic activity, and the protein adsorption were evaluated using parametric analysis of variance (ANOVA) with Tukey's posthoc test for pairwise comparison. Values of $p \leq 0.05$ were considered significant.

3. RESULTS

3.1. Structural Characterization of the Noncoated and CNF-Coated Meshes.
According to the MicroCT analysis (Figure S1), the average fiber thickness of the noncoated mesh was 7.2 ± 1.97 μm (max. 16.1 μm), while the average void thickness was 44.3 ± 36.3 μm. The noncoated mesh possessed high porosity of 84.9%.

The topography of the noncoated and CNF-coated meshes was analyzed using SEM (Figure 1). Depending on the volume applied on the surface of the cellulose mesh and on the charge of the CNFs, the CNF solutions either penetrated into the pores of the mesh, mimicking the 3D structure of the mesh, or formed an almost flat layer on top of the mesh (Figure S1). The CNF solutions with a volume of 150 μL (a150, c150) covered the individual fibers of the mesh and filled the pores between them (see the first column in Figures 1 and S1), while a volume of 600 μL (c600, a600) formed a thin film on the
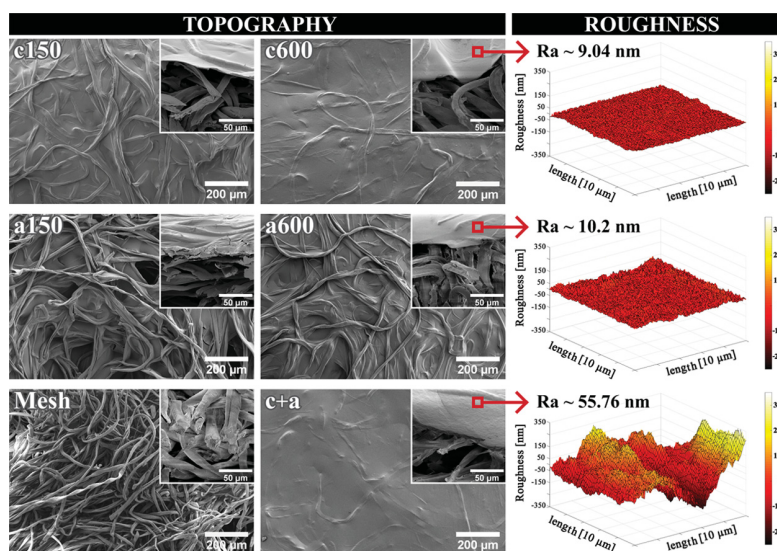
Figure 1. Topography and roughness. Front view and side view (inset image) of SEM images of c150, c600, a150, a600, and c+aCNF-coated and noncoated meshes (left and center). The roughness of the c600, a600, and c+aCNF-coated meshes was measured by AFM (right).

surface of the mesh (see the second column in Figures 1 and S1). At the same time, the cCNFs, mainly c600 and c+a, showed a tendency to form a flat, 2D film-like coating on the mesh surface, while the aCNFs, predominantly a150, covered the individual mesh fibers and filled the pores between them, which created a more pronounced 3D microtopography. As a result, the best-developed 3D microtopography was obtained using 150 μL of aCNFs, and the most pronounced film-like 2D microtopography was observed when 600 μL of cCNFs or c+aCNFs was used (Figures 1 and S1).

The surface roughness was determined using AFM. The results show that the R_a median of a600 was 9.04 nm and the R_a median of c600 was 10.20 nm The R_a median of c+a was 55.76 nm (Figure 1). Groups c600 and a600 were significantly different from group c+a (p = 0.025) (Figure S1).

3.2. Swelling Ratios and Contact Angles of CNF Coatings. The swelling ratios of the noncoated and c600, a600, and c+aCNF-coated meshes were determined after 20 h in deionized water (dH$_2$O) and DMEM. The highest swelling ratio was measured in dH$_2$O in the c600 coatings. However, there was no significant difference between CNF-coated and noncoated meshes in DMEM (Figure 2A). Due to the considerable water uptake of the underlying meshes, the CNF coatings were prepared on glass coverslips and the swelling ratio in DMEM was measured (Figure 2B). The swelling ratio of the c600 coatings was significantly higher than those of the a600 and c+a coatings after 20 min in DMEM, but after 20 h, there was no additional water uptake by the c600 coatings (Figure 2B). However, the water uptake by the a600 coatings increased with time, and the values after 20 h were significantly higher (p = 0.03) than the values after 20 min (Figure 2B). The swelling ratio of the c+a coatings increased slightly between 20 min and 20 h (Figure 2B). The swelling ratios of the noncoated meshes in DMEM and dH$_2$O were comparable (Figure 2A), and they remained relatively unchanged during the incubation period in DMEM (Figure 2B). The measured contact angles are reported in the Supporting Information (Figure S2).

3.3. Stiffness of the CNF Coatings Measured Using AFM. The average stiffness values (arithmetic mean ± SD) of

c600, a600, and c+aCNF-coated meshes in the dry state were 0.572 ± 0.24 GPa (Mdn = 0.640), 0.683 ± 0.45 GPa (Mdn = 0.538), and 0.315 ± 0.10 GPa (Mdn = 0.275), respectively. Although there was a significant difference in coating stiffness between a600 and c+a (p = 0.034), the mean Young moduli reached the same order of magnitude, and the confidence interval demonstrated only a negligible difference (Figure 2C).

The average stiffness values of the CNF-coated meshes after wetting in DMEM for 20 min were 121 ± 16 kPa (Mdn = 116), 342 ± 101 kPa (Mdn = 326), and 241 ± 83 kPa (Mdn = 230) (Figure 2D—0 h). Young's moduli in the wet state (Figure 2D) are, on an average, three orders of magnitude lower than that in the dry state (Figure 2C), which indicates considerable softening of the materials after wetting. The c600 coatings were significantly (p = 0.002) softer than the a600 coatings, while the stiffness of the c+a coatings was between them after 20 min in DMEM (Figure 2D, 0 h).

The average stiffness values of the CNF-coated meshes after 17 h in DMEM were 131 ± 37 kPa (Mdn = 121), 173 ± 117 kPa (Mdn = 194), and 219 ± 174 kPa (Mdn = 221), respectively (Figure 2D, 17 h). Although the median values of a600 and c+a stiffness were higher than the c600 stiffness values, no significant difference between the tested groups was found (Figure 2D, 17 h). There was a significant difference (p = 0.034) within the a600 coatings, depending on the time scale, while Young's moduli of the c600 (p = 0.999) and c+a (p = 0.848) coatings did not differ significantly after 17 h from the situation after 20 min. The stiffness of the a600 coatings decreased with time (Figure 2C), while the water uptake increased with time (Figure 2A), which means that a600 coatings become softer during incubation in DMEM.

3.4. Cell Behavior on CNF-Coated Meshes. *3.4.1. Overall Growth Dynamics of Cells on CNF-Coated Meshes.* The growth of NHDFs and ADSCs on the CNF-coated and noncoated meshes was evaluated at three time intervals by measuring the cell metabolic activity using the resazurin assay. The values of the cell metabolic activity—an indicator of the cell number—were used for constructing growth plots to evaluate the overall growth dynamics of the cells within a 1-week period (Figure S3).
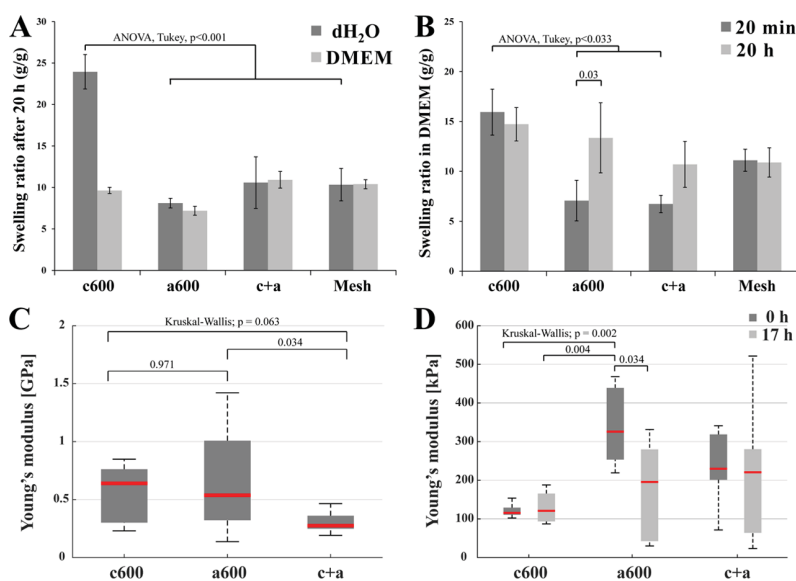
Figure 2. Swelling ratio and stiffness. Swelling ratio of CNF-coated meshes after 20 h in dH$_2$O and DMEM (A). Swelling ratio of CNF-coated glass coverslips after 20 min in DMEM and after 20 h in DMEM (B). Arithmetic mean ± SD from three independent samples, ANOVA, Tukey's method, and statistical significance ($p \leq 0.05$). Young's modulus before wetting with DMEM (dry state; C) and after wetting with DMEM (wet state; 0 h; 17 h; D). Median and interquartile range from eight measurements, Kruskal−Wallis, Tukey's method, and statistical significance ($p \leq 0.05$).

The dynamics of the cell growth on meshes coated with aCNFs or c+aCNFs were comparable to the dynamics on standard tissue culture PS, while on the cCNF-coated meshes, it was similar to the dynamics on the noncoated meshes. Interestingly, these differences were more apparent in NHDFs than in ADSCs (Figure S3). This motivated a deeper analysis of the mechanisms behind these phenomena. The initial adhesion of the two cell types on the CNF-coated and noncoated meshes (Figure 3) and the adsorption of serum-derived proteins (Figure 4) were characterized on day 1 after cell seeding. The proliferation and the morphology of the cells were observed on day 3 when the cells were fully spread and their morphology was well developed (Figures S5 and 5). The final status of the colonization of the CNF-coated cellulose meshes with cells was evaluated on day 7 (Figures S6 and 6).

3.4.2. Day 1: Initial Adhesion of Cells on CNF-Coated Meshes. We observed that the metabolic activity and the morphology of the NHDFs and the ADSCs on the cCNF-coated and aCNF-coated meshes differed (Figure 3). The metabolic activity of the NHDFs was significantly lower on the cCNF coatings than that on the aCNF and c+aCNF coatings (Figure 3A). Conversely, the metabolic activity of ADSCs on the cCNF coatings was mostly similar to, or even slightly better than, on the aCNF coatings (Figure 3B). The cell metabolic activity of both cell types on c+a coatings reached almost the same level as on polystyrene (PS = 100%; Figure 3A,B).

Similarly, the visualization of the cell morphology revealed that NHDFs on c600 coatings was often rounded and nonspread (Figure 3C), while the adhesion and spreading of ADSCs were almost the same as those on the a600 and c+a coatings (Figure 3D). The 3D topography of the a150 CNF-coated meshes supported the attachment and physiological elongation of both cell types. The flat c600, a600, and c+a coatings were more suitable for cell spreading into a polygonal shape, as they provided the cells with a more homogeneous flat area (Figure 3C,D). Vinculin was homogeneously dispersed

throughout the cells, and no distinct focal adhesion sites were observed in the cells on any type of the CNF coating (Figure 3C,D), even at higher magnification (objective 40×; data not shown).

3.4.3. Day 1: Adsorption of Serum-Derived Proteins on CNF-Coated Meshes. To explain the differences in the initial cell attachment and spreading on the CNF-coated meshes on day 1, c600, a600, c+a and noncoated meshes were preadsorbed with serum-derived proteins modulating cell adhesion (Figure 4). When the samples were pretreated with 1.5 mL of 10% FBS in DMEM, a significantly greater amount of proteins was adsorbed on the c600 and c+a coatings than that on the a600 coatings and on the noncoated meshes (Figure 4A). To estimate the adsorption of non-cell-adhesive BSA from 10% FBS, the samples were pretreated with 1.5 mL of 0.25% BSA in DMEM, which theoretically corresponds to the average concentration of BSA in 10% FBS. Interestingly, the absolute amount of adsorbed BSA on the c600 coatings was lower than that of the absolute amount of proteins adsorbed from 10% FBS (Figure 4A). However, the percentage of BSA (15.6%) adsorbed on c600 from the BSA solution was higher than the percentage of proteins (13.1%) adsorbed from 10% FBS (Figure 4B). In contrast, the percentage of BSA (5.5%) adsorbed from the BSA solution on the a600 coatings was lower than that of the percentage of proteins (6.9%) adsorbed from the 10% FBS (Figure 4B). On the c+a coatings, the BSA (12.4%) adsorbed from the BSA solution in a similar proportion to the proteins (12.5%) adsorbed from the 10% FBS (Figure 4B). These results indicate that the c600 and c+a coatings adsorbed more non-cell-adhesive BSA from the FBS than the a600 coatings and noncoated meshes adsorbed. This may explain the lower cell adhesion on the cCNF coatings than that on the aCNF coatings.

3.4.4. Day 1: Adhesion of Cells on cCNF Coatings preadsorbed with Serum-Derived Proteins. Due to the differences in attachment between the cells on cCNFs (Figure
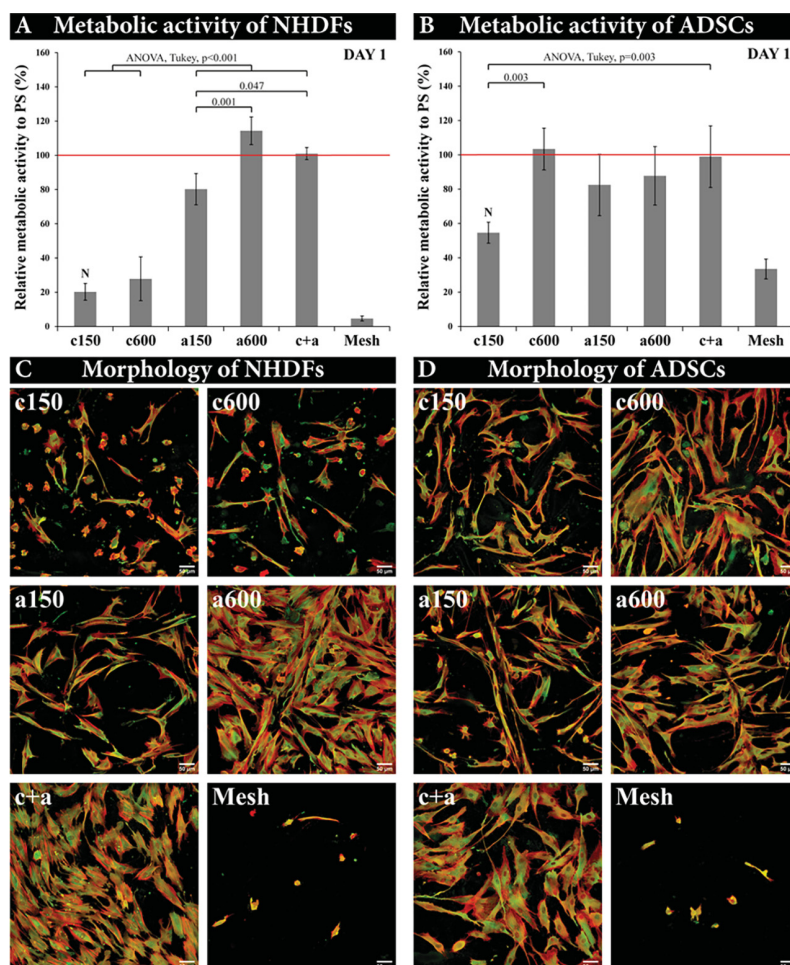
Figure 3. Metabolic activity (A, B) and the morphology (C, D) of NHDFs and ADSCs on CNF-coated and noncoated meshes on day 1 after cell seeding. (A, B) Metabolic activity of the cells on CNF-coated and noncoated meshes is displayed as a value relative to the metabolic activity of the cells on polystyrene (PS = 100%; red lines). Arithmetic mean ± SD from eight measurements made on four independent samples, ANOVA, Tukey's method, and statistical significance ($p \leq 0.05$). N, No significant difference in comparison with the noncoated mesh (mesh). (C, D) F-actin in the cell cytoskeleton is stained in red and vinculin is stained in green. A confocal microscope with an objective magnification of 20×. Scale bar = 50 μm.

3) and due to the adsorption of the serum-derived proteins predominantly on the cCNFs (Figure 4A,B), the initial adhesion of cells on preadsorbed serum-derived proteins was studied only on the cCNF coatings.

On the cCNF-coated meshes preadsorbed with FBS, the ADSCs and NHDFs adhered in low numbers, and their shape after 24 h was abnormal and nonphysiological (Figure 4C,D). However, when the cells were seeded in DMEM supplemented with FBS on pure cCNF-coated meshes, the adhered ADSCs were almost confluent and were well-spread after 24 h. In contrast, the number of adhered NHDFs remained low, and their morphology was comparable with the NHDFs on the cCNF coatings preadsorbed with FBS. Similar results were observed in BSA, although this protein is nonadhesive for cells. On meshes preadsorbed with BSA, both cell types were unable to spread after 2 h. However, when the cells were seeded on pure cCNF-coated meshes in DMEM supplemented with BSA, the ADSCs adhered in greater numbers than the NHDFs and showed some tendency to spread after 2 h of cultivation (Figure 4C,D).

In addition to the investigation into cCNF-coated meshes, the response of NHDFs and ADSCs to the preadsorbed

proteins was investigated on cCNF-coated glass coverslips to eliminate the effect of the underlying mesh and to enable live-cell imaging. The results were basically similar to those obtained on the cCNF-coated meshes, i.e., (1) poor adhesion and spreading of both cell types on glass coverslips preadsorbed with FBS or BSA, (2) almost equally poor adhesion and spreading of NHDFs seeded on pure glass coverslips in a medium supplemented with FBS or BSA, but (3) relatively good adhesion and spreading of ADSCs seeded on glass coverslips in a medium with FBS or BSA (Figure S4).

These results suggest that ADSCs adhere more quickly than NHDFs; that is, mostly before the adsorption of non-cell-adhesive albumin, which is contained in FBS. This assumption was confirmed by live-cell imaging using cell trackers. Simultaneous seeding of NHDFs (red) and ADSCs (green) on a cCNF-coated glass substrate in DMEM with 10% FBS revealed that the attachment and spreading of ADSCs was quicker than the attachment of NHDFs, which were much slower in their attachment and were not able to spread properly (Supporting Video).

3.4.5. Day 3: Proliferation and Morphology of Cells on CNF-Coated Meshes. Measurements of cell metabolic activity
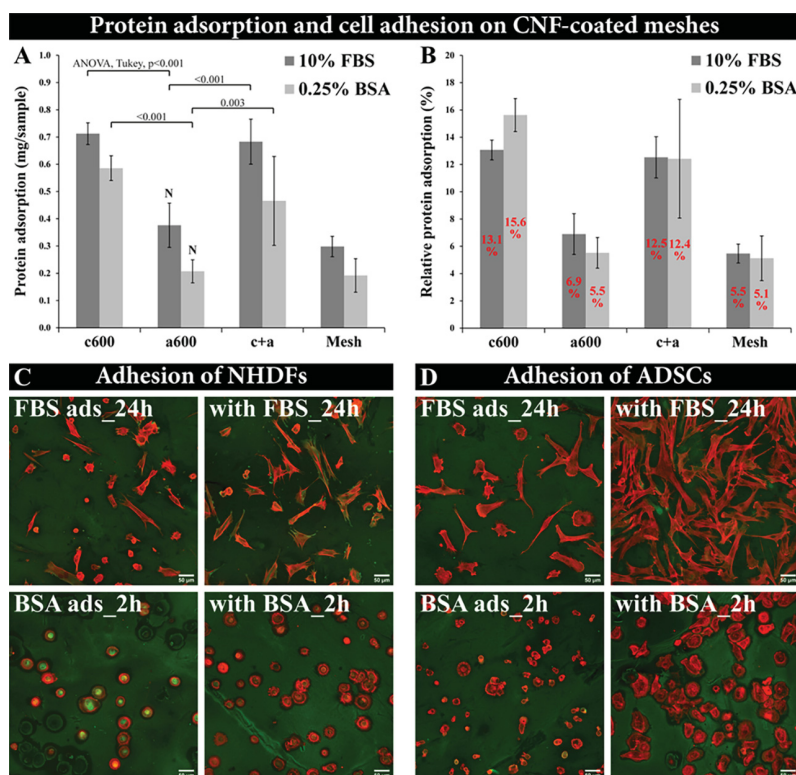
Figure 4. Adsorption of proteins on the cCNF-coated meshes measured by the Pierce BCA Protein Assay Kit (A, B), and initial adhesion of NHDFs and ADSCs on the cCNF-coated meshes with and without preadsorbed proteins (C, D). (A) Adsorption of 1.5 mL of 0.25% BSA (2.5 mg/mL) and 10% FBS (3.64 mg/mL of proteins) displayed in mg/sample. (B) Relative adsorption of 0.25% BSA (3.75 mg = 100%) and 10% FBS (5.46 mg = 100%) displayed as a percentage. Arithmetic mean ± SD from eight measurements made on four independent samples, ANOVA, Tukey's method, and statistical significance ($p \leq 0.05$). N, No significant difference compared to the noncoated mesh (mesh). Adhesion and spreading of NHDFs (C) and ADSCs (D) on cCNF-coated meshes with (FBS ads_24h and BSA ads_2h) and without (with FBS_24h and BSA_2h) preadsorbed proteins after 2 h and 24 h of cell cultivation. F-actin in the cell cytoskeleton is stained in red. Nonspecific binding of the secondary antibody on cCNF coatings and vinculin in the cells are indicated by green. A confocal microscope with an objective magnification of 20×. Scale bar = 50 μm.
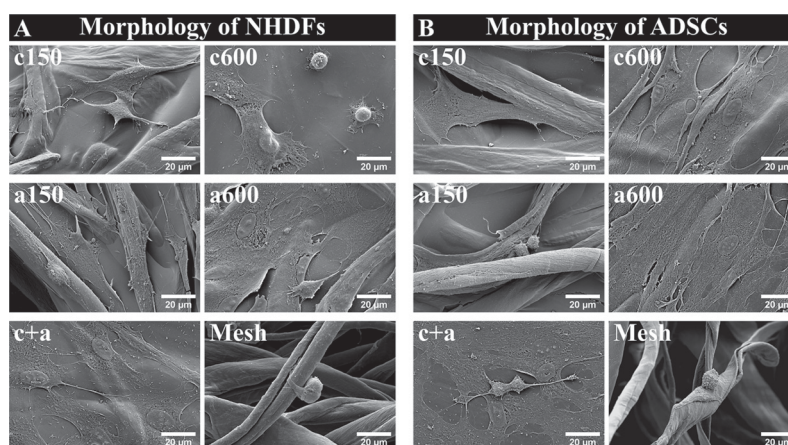
Figure 5. Morphology of NHDFs (A) and ADSCs (B) on CNF-coated and noncoated meshes on day 3 after cell seeding, acquired by SEM. Scale bar = 20 μm.

after 3 days of cultivation (Figure S5A,B) revealed that aCNF-coated meshes (a150, a600) significantly increased the proliferation capacity of both cell types compared to the noncoated meshes (mesh) and the cCNF-coated meshes (c150, c600). The metabolic activity of NHDFs on cCNF-coated meshes (c150, c600) was almost at the same level as on noncoated meshes, and it remained at almost the same level as

on day 1 (cf. Figures S5A and 3A). The negative influence of cCNFs on cell behavior started to be visible also in ADSCs (Figure S3). However, the metabolic activity of the ADSCs was still slightly higher on the c150 and c600 coatings than the metabolic activity of the NHDFs (Figure S5A,B). Similarly to day 1 (Figure 3A,B), the metabolic activity of both cell types on the c+aCNF-coated meshes was comparable with the values
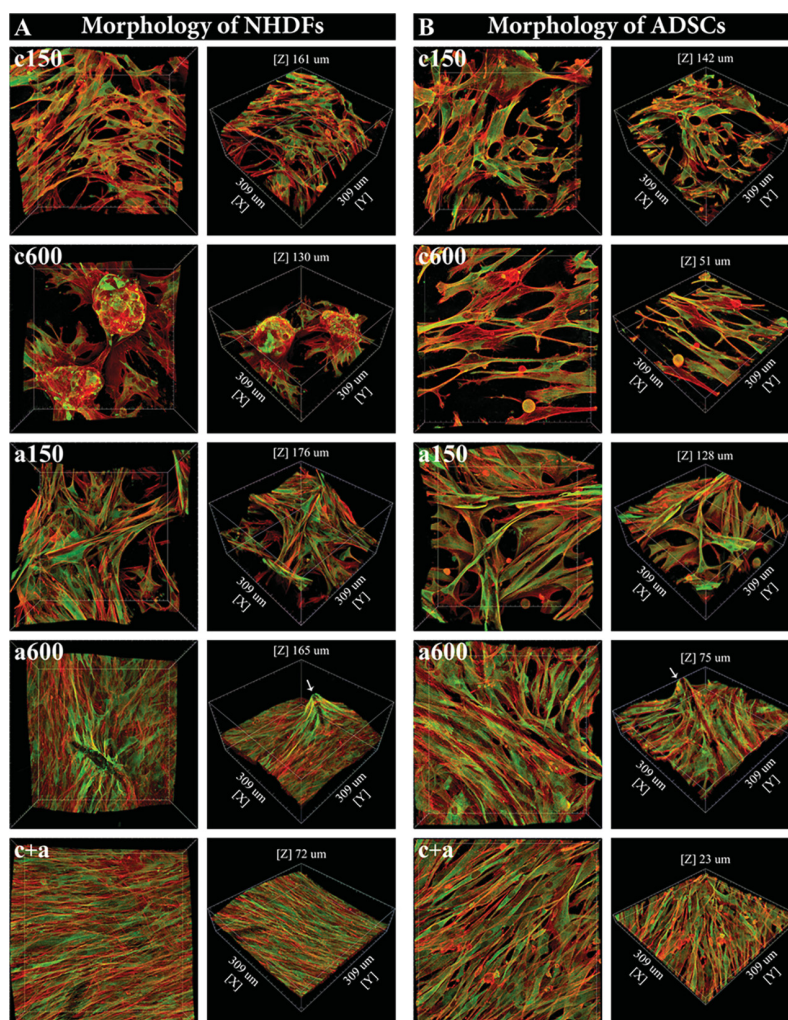
Figure 6. Morphology of NHDFs (A) and ADSCs (B), guided by the topography of the CNF-coated meshes after 7 days of cultivation. 3D projection of microscopy images (front view and side view) of the cells on CNF-coated meshes. F-actin of the cell cytoskeleton is stained in red, and vinculin in the cells is stained in green. A confocal microscope with an objective magnification of 40×.

on the control polystyrene (PS = 100%) but was significantly lower than the values on the a600 CNF-coated meshes (Figure S5A,B).

After 3 days of cultivation, the cells were mostly spread, and the morphology and the orientation of both cell types were guided by the surface topography of the CNF-coated meshes. The flat 2D surface of the c600 coatings markedly supported the growth of ADSCs (Figure 5B), while the NHDFs were poorly spread and started to detach from the c600 coatings (Figure 5A). However, this rounded morphology of the NHDFs was slightly improved by the 3D topography of the c150 coatings, where the cells acquired a more physiological spindle-like morphology (Figure 5 and S5C). Similarly, although the number of both cell types was higher on the 2D surfaces of the a600 coatings, more elongated cells were observed on the 3D surface of the a150 coatings. The cells on noncoated meshes were round and were barely attached (Figures 5 and S5C,D).

3.4.6. Day 7: Final Colonization of the CNF-Coated Meshes with Cells. The metabolic activity of ADSCs on all types of tested materials was generally lower than the metabolic activity of the NHDFs (Figure S3). However, the

proliferation of both cell types on the cCNF-coated and noncoated meshes was significantly lower than that on the aCNF- and c+aCNF-coated meshes. Despite the overall low growth capacity of the cells on the cCNF coatings, the numbers of both cell types were higher on c150 than those on c600 (Figure S6A,B). On a600 and c+a, both cell types reached confluence and colonized almost the entire surface (Figure S6C,D). On day 7, the cell growth capacity on the 3D surface of a150 was equalized with the cell growth capacity on a600 and on c+a, especially in the case of NHDFs (Figure S6).

The 3D projections of microscopy images of cells on the CNF-coated meshes revealed that the 2D coatings (a600 and c+a) enhanced the proliferation and spreading of both cell types only in the *xy* directions, while the 3D coatings (a150) supported elongation of the cells on the mesh fibers and between them in all *xyz* directions (Figure 6). Therefore, the 3D surface of the a150 coatings provided more space for cell elongation and proliferation (Figures 6 and S6). The negative effect of cCNF, mainly of c600 coatings, on cell attachment was manifested by the formation of clusters of ADSCs and spheroids of NHDFs (Figures 6 and S6).

The interaction of the cells with the material surface topography and the formation of vinculin-containing focal adhesion sites were evaluated from 3D projections of microscopy images (Figure 6). During 1 week of cultivation, the interactions between the cells and the surface topography features were established, and a positive effect of the 3D topography of the a150 coatings and also of the c150 coatings on cell growth was observed (Figures 6 and S6C,D). The cells detaching from the c600 CNF-coated meshes showed vinculin dispersed throughout the cell without creating any focal adhesions, except for the spheroidal structures, where vinculin seems to be located in the cell−cell contacts. On the c150 CNF-coated meshes, vinculin was more visible in the cells, but only a few barely detected focal adhesions were observed (Figure 6). On the aCNF-coated meshes, the cells were spread in all three dimensions and grew along the directions of the mesh fibers, and focal adhesions were clearly visible (see a150 in Figure 6). On the predominantly 2D surface of the a600 coatings, a higher vinculin signal was observed in the cells that were migrated upward to the top of the protruding aCNF-coated mesh fibers (see a600—arrows in Figure 6).

4. DISCUSSION

4.1. Properties of CNF-Based Coatings. In this study, we prepared nanocellulose-based coatings on a microfibrous cellulose mesh to improve its properties as a cell carrier in skin tissue engineering and wound healing applications.

Based on the amount of the CNF solutions that was applied, two different coating microtopographies were formed. A greater volume of the CNF solution (600 μL) resulted in the formation of a flat film-like coating on the surface of the cellulose mesh, while a lower suspension volume (150 μL) resulted in a coating that covered the individual fibers of the mesh. Although the topographies can be regulated by the volume of the solutions, the cCNF solution predominantly formed a film-like coating on the surface of the cellulose mesh, while the solution of aCNFs leaked into the mesh pores more easily and predominantly covered the individual mesh fibers (Figures 1 and S1). This behavior can be explained by the presence of larger fibrils in the cCNF solution than in the aCNF solution.[32,33] The larger cCNF fibrils were accumulated on top of the mesh fibers and prevented further penetration of the cCNF solution into the mesh pores, which resulted in a thin film on the mesh surface. This phenomenon was utilized in the preparation of the c+aCNF coatings, where the cCNF solution was first applied on the mesh followed by the application of aCNF and then by mixing of the two solutions. The larger cCNF fibrils blocked the pores and prevented penetration of the aCNFs. The aCNFs formed ionic cross-linking with the oppositely charged sidechains of the cCNFs, as the trimethylammonium ($-N(CH_3)_3^+$) group of cCNFs can form ionic bonding with carboxyl ($-COO^-$) groups of aCNFs.[34]

To describe the functionality of the CNF coating at the cell perception level, the surface roughness of the CNF coating was measured. The roughnesses of the c600 ($R_a \sim 9.04$ nm) and a600 ($R_a \sim 10.2$ nm) 2D coatings were similar (Figures 1 and S1). The greater variation in the roughness of c600 is probably due to the locally distributed larger fibers present in the cCNF solution.[12,33] The greater roughness of c+a ($R_a \sim 55.76$ nm) could be due to strong ionic cross-linking between the anionic $-COO^-$ and cationic $-N(CH_3)_3^+$ groups that probably formed the local aggregation of the nanofibrils.

The different surface chemistries of the CNF coatings influence the wettability and the water uptake, which results in the different swelling properties and the different softening dynamics of the coatings. The more hydrophilic surface of aCNFs presents $-COO^-$ and hydroxyl ($-OH$) functional groups that enable hydrogen bonding.[23] Thus, the aCNF coating binds more water on the surface, resulting in a lower contact angle ($31°$) with water than that on the surface of the cCNFs, which contains not only hydrophilic $-OH$ groups but also more hydrophobic methyl ($-CH_3$) groups. The $-CH_3$ groups do not form hydrogen bonds.[23] This renders the cCNF surface more hydrophobic, resulting in a higher contact angle on cCNFs ($65°$) with water. The hydrogen-bonding capacity may also influence the penetration of the fibrils into the mesh pores, as discussed above. The cellulose mesh has more hydrogen-bonding sites for $-COO^-$ and $-OH$ groups of aCNFs than those for the $-CH_3$ of the cCNFs.[23] HPTMA functionalization of the $-OH$ group in C2 of the cCNF cellulose backbone[23,35] resulted in a larger functionalized moiety than that in the case of the smaller COO^--functionalized $-OH$ group in C6 of aCNFs. Thus, the cCNFs form a more branched and spongier structure (see the structures in Chaker and Boufi[23]), which enables cCNFs to take up more water[36] than aCNFs. The positively charged $-N(CH_3)_3^+$ groups interact with dipolar substituents,[37] enabling solvation even though the $-CH_3$ groups make the cCNFs more hydrophobic.

The swelling ratio and the changes in surface stiffness were measured with time. The surface stiffness of all wetted CNF coatings was dramatically reduced in comparison with the coatings in a dry state. The greater stiffness of the aCNF coatings in comparison with that of the cCNF coatings at the beginning can be explained by the capacity of oxidized nanofibrils to build up a strong network held together by hydrogen bonding,[23] while the presence of the 2-HPTMA chloride moiety of the cCNFs reduces hydrogen bonding and thus weakens the cohesion of the network.[23] The softening of aCNFs with time could also be due to displacement of the hydrogen bonding between the $-COO^-$ and $-OH$ groups by the hydrogen bonding between the $-COO^-$ and H_2O molecules. In addition, the charged groups of CNFs should also increase the hydrophilicity of the material. It has been reported that TEMPO oxidation increases the negative charge, resulting in electrostatic repulsion between the fibrils in a wet state; thus, the high negative charge of TEMPO-oxidized CNFs causes low water resistance[38] and high swelling.[28] The surface charges of our aCNF and cCNF coatings are probably similar to the reported ζ-potential values for the corresponding grades of CNFs, which were −69.5 mV (for aCNFs) and +41 mV (for cCNFs).[33,39] The negative surface charge, in combination with hydrogen bonding to the water molecules, could explain the swelling and softening of aCNF coatings over time, while the branched sponge-like structure of $-N(CH_3)_3^+$ groups could contribute to the higher total water uptake of cCNF coatings. The swelling of cCNFs decreased slightly, while the mean stiffness increased slightly. This is particularly apparent during the immersion of cCNFs in DMEM. The ions present in DMEM may enable ionic cross-linking to some extent, which reduces the water uptake and increases the strength of the material, which was observed for cCNFs over time. In summary, the general trend in stiffness follows the general trend of the swelling of the coatings. There was a significant difference in swelling of c600 between water and

DMEM (Figure 2A). Unlike the deionized water used in our experiments, DMEM contains a variety of ions that can interact with the positively charged moieties of c600, and subsequently, fewer water molecules are occupied around these sites, resulting in less water uptake than that in the case of the samples soaked in deionized water (Figure 2A).

The microtopographical structure of the c+a combination is similar to that of the cCNFs, while the contact angle, swelling, and stiffness properties more closely resemble those measured on the aCNF coatings. The roughness of the c+aCNF coating differs from the roughness of both cCNFs and aCNFs. The values of contact angle and the swelling of c+aCNFs are closer to the values of aCNFs than to the values of cCNFs. This is probably due to strong ionic cross-linking between c+aCNFs, which prevents the water from penetrating into the structure. However, the c+aCNF coating contains more hydrophilic hydrogen-bonding groups than the cCNF coatings, which may also have an effect on the swelling and stiffness. The stiffness of the c+aCNFs coating did not decrease over time, as was observed with the aCNF coatings. This can be explained by strong ionic cross-linking, which can reduce the interactions of hydrogen-bonding groups with water molecules. The c+aCNF combination, therefore, offers an interesting set of properties, which might be further adjusted to create not only film-like coatings for cell cultivation but also 3D cross-linked CNF gels for cell embedding and for 3D printing.

4.2. Cell Behavior Influenced by the Properties of CNF Coatings.

A comparison was made between two coating microtopographies—the 2D film-like topography and the 3D coating topography—for differences in cell–material interactions. Our results suggest that the flat substrates of c600, a600, and c+a, where the cells formed monolayers, can be suitable for cell sheet technology. This technology enables the creation of self-standing, mechanically resistant, continuous cell sheets that can be replanted on other substrates, such as tissue-engineered skin constructs *in vitro* or wound beds *in vivo*. The cell sheets can be released from cellulose substrates by cellulase enzymes, which are not cytotoxic. In addition, unlike proteolytic enzymes such as trypsin or collagenase, they preserve the cell-to-cell connections and the ECM proteins within the sheets.[40] The 3D substrates of c150 and a150, where the cells penetrated into the material, are also promising for tissue engineering and for future clinical applications. 3D substrates made of a CNF-coated cellulose mesh might provide sufficient space for the cells for *in vitro* long-term cell cultivation and might allow for better diffusion of nutrients than the widely used hydrogels.[41]

Not only the microtopography of the material but also the cell–material interactions can also be modulated by the elasticity, roughness, and surface chemistry of the material. The elasticity of natural tissues varies from 0.2 to 1 kPa for soft tissues, such as brain or fat, via medium-soft tissues such as skin (10−30 kPa), to hard tissues of more than 10^5 kPa, e.g., for bone.[42,43] The stiffness of our CNF coatings is close to the stiffness of native tissues such as fibrotic tissue (100 kPa), cartilage, and tendon (approaching 10^3 kPa).[25,42] By comparison, Kummala et al. introduced 0.1 mm thick CNF films with Young's modulus between 1 and 60 kPa.[3] Although the CNF substrates used in this study were much softer than the conventional cell culture substrates (GPa),[42] they can be considered as relatively stiff substrates at the cell perception level. For example, Achterberg et al. determined Young's modulus of native human dermis using AFM between 0.1 and 10 kPa, depending on the location, which is at least 10 times softer than our CNF substrates.[44]

Not only the stiffness but also the roughness is important at the cell perception level, especially for initial cell attachment, because the cell focal adhesions are in the nanoscale range from 2 to 200 nm.[45] Alterations in material surface roughness can influence the adhesion and further proliferation of fibroblasts, as described by Bourkoula et al., and also the spreading and differentiation of mesenchymal stem cells, as observed by Hou et al.[46,47] While the aCNF and cCNF coatings showed relatively low roughness, the c+aCNF combination showed a rougher surface (see $R_a \sim 55.76$ nm in Figure 1), which corresponds to the least rough surface measured by Hou et al.[47] These authors revealed that the substrates with the lowest studied roughness ($R_a \sim 31.49$ nm) supported cell adhesion and spreading, but the cell−substrate tension and osteogenesis were only moderate in comparison with the substrates with intermediate roughness ($R_a \sim 183.16$ nm).[47]

Although the studied CNF surfaces differ in many parameters, including the microtopography, roughness, swelling ratio, and Young's modulus, we assume that the main cell adhesion-modulating factor is the surface chemistry of CNFs, which governs the surface charge and wettability. The surface chemistry can determine the composition of proteins adsorbed on CNF surfaces and the speed with which various serum proteins are adsorbed and the cells are adhered.[24] It is generally known that cells adhere to material substrates through the proteins adsorbed to the material surface from the biological fluids. Adhesion-mediating proteins, such as fibronectin, vitronectin, collagen, and laminin, contain specific amino acid sequences (e.g., RGD) that can be recognized by integrin receptors on cells, while albumin is nonadhesive for cells due to the lack of these specific adhesion sequences in its molecule. However, albumin can improve the geometric conformation of the cell adhesion-mediating proteins for binding by cell adhesion receptors.[21] Based on the Vroman effect—i.e., the dynamics with which proteins adsorb and interchange in time—we can assume that the NHDFs and ADSCs adhered to a layer of proteins that differ in their composition.[48]

We have demonstrated that cCNFs with positively charged $-N(CH_3)_3^+$ tails adsorb more proteins, predominantly BSA, than aCNFs with negatively charged −COO functional groups (Figure 4). Similar results were achieved by Attwood et al.[50] with well-defined positively charged $-N(CH_3)_3^+$- and −COO⁻-terminated self-assembled monolayers (SAMs) and also by Courtenay et al., who quantified the proteins adsorbed from FBS, specifically BSA, on positively charged GTMAC-modified cCNF scaffolds.[49,50] They revealed increasing protein adsorption with increased cationization. The greater affinity of BSA to positively charged surfaces could be due to the negative character of the BSA at the physiological pH of DMEM.[51,52] We could expect that the negatively charged proteins in FBS, such as fibronectin, vitronectin, and BSA, have the same electrostatic affinity to the positively charged surfaces at the physiological pH of DMEM due to their similar theoretical isoelectric points.[26] However, the concentration of BSA at a level between 35 and 50 mg/mL in FBS is 100−1000 times higher than the concentration of other proteins,[26,27] which makes BSA the most abundant adsorbed protein on positively charged substrates. Furthermore, Hoshiba et al.[26] revealed that the absolute amount of adsorbed proteins on chemically

modified charged methacrylates (MA) is less important than the protein composition of the most superficial layer. In their study, positively charged −N(CH$_3$)$_2$$^+$-terminated MA adsorbed more proteins from FBS than were absorbed by negatively charged −COO$^-$-terminated MA. However, the most superficial layer of −COO$^-$-terminated MA contained more cell adhesion-mediating proteins, mainly vitronectin, and also fibronectin in its more suitable conformation for cell adhesion.[26] In general, the positive effect of negatively charged −COO$^-$ termination on cell adhesion, spreading, and proliferation of various substrates has been confirmed by many other research groups.[6,26,53]

The abundant yields of BSA on the surface of the cCNF-coated meshes probably reduced the amount of attached NHDFs, but it did not influence the attachment of the ADSCs. Based on Courtenay et al.'s work, we hypothesize that the ADSCs were attracted by the positive charge on the surface of the cCNFs, and their attachment can be classified as protein-independent electrostatically mediated adhesion.[6,8] Unlike Courtenay et al., we observed this phenomenon with ADSCs not only in a serum-free medium but also in a serum-containing medium (Figure S4 and the Supporting Video).[8] This could be due to a higher adhesion speed of ADSCs than that of NHDFs, which enabled them to adhere before the adsorption of BSA took place. This was clearly visible especially on the ADSCs that were not able to adhere to the cCNF coatings, which were preadsorbed with FBS or nonadhesive BSA (Figure 4). Although ADSCs adhered to the cCNF coatings in large numbers, their cell adhesion forces were rather weak, as was manifested by the suppression of proliferation and by the formation of clusters and spheroids. Courtenay et al. reported similar findings, revealing that there was greater cell adhesion on cationic nanocellulose than on anionic nanocellulose in the serum-free medium, while the cells in the serum-containing medium responded in the opposite way.[6] This confirms that the cells in a serum-free medium adhered to positively charged substrates via integrin-independent electrostatic interactions, while cell adhesion was suppressed in the serum-containing medium by the adsorption of the proteins in an inappropriate spectrum and conformation. Negatively charged substrates therefore seem to be more suitable for cells due to the presence of stronger protein-mediated integrin-dependent adhesions and also weak electro-static cell−material interactions.[26,53] In addition, this specific integrin-mediated cell adhesion is capable of delivering appropriate signals to cells, ensuring the viability, proliferation, and other functions of the cells.

The adsorption of proteins and further cell adhesion is also mediated by the hydrophilicity or hydrophobicity of the surfaces.[27,50,53] Although both CNF coatings were expected to be hydrophilic due to the charged −COO$^-$ and −N(CH$_3$)$_3$$^+$ functional groups,[50] the cCNFs (contact angle 65°) were more hydrophobic than the aCNFs (contact angle 31°). The presence of neutral −CH$_3$ groups on the surface of cCNFs probably reduced the hydrophilicity, which made the surface less attractive than the surface of aCNFs for the cells in a serum-containing medium. Similar results were achieved by McClary et al. and Faucheux et al. with −CH$_3$- and −COO$^-$-terminated SAMs.[53,54] In addition, Arima and Iwata[27] described how moderately hydrophilic SAMs enhanced cell adhesion even though they were preadsorbed with BSA, while hydrophobic SAMs preadsorbed with BSA inhibited cell adhesion. This was due to the strongly adsorbed BSA on hydrophobic SAMs, which cannot be replaced by cell adhesion-mediating proteins as effectively as on hydrophilic SAMs, where the proteins interchanged due to the Vroman effect.[27,48] We could assume that both aCNFs and c+aCNFs were suitable for cell adhesion and growth due to their hydrophilic surface character. Although the level of adsorbed BSA on c+aCNFs was comparable to the level of less hydrophilic cCNFs (Figure 4), the hydrophilic surface character of c+aCNFs probably enabled BSA to be replaced by the cell adhesion-mediating proteins in the most superficial layer of the adsorbed proteins. However, the less adhesive cCNF coatings for cells can also occupy an important place in tissue engineering. As indicated by Figures 6 and S6, these surfaces can be used for generating three-dimensional multicellular spheroids, similar to the albumin-coated surfaces in a study by Okuyama et al.[55]

5. CONCLUSIONS AND FURTHER PERSPECTIVES

In this study, we have developed novel electroactive coatings on a cellulose mesh based on cationic nanofibrils (cCNFs) or based on anionic cellulose nanofibrils (aCNFs) or based on a 1:1 mixture of both types of nanofibrils (c+aCNFs). When seeded with normal human dermal fibroblasts (NHDFs) or human adipose-tissue-derived stem cells (ADSCs), the negatively charged aCNFs, and also the mixture of c+aCNFs, appeared to provide better substrates for cell adhesion and growth than the positively charged cCNFs. This was demonstrated mainly with NHDFs. The most likely explanation for this finding is that the positively charged cCNFs were more hydrophobic and they preferentially adsorbed albumin, which is nonadhesive for cells. However, negatively charged aCNFs and combined c+aCNFs were hydrophilic, and they adsorbed more serum proteins mediating cell adhesion, such as vitronectin and fibronectin. In addition, cCNFs attracted the cells via electrostatic forces, and this non-integrin-mediated cell adhesion is less efficient in maintaining the viability and the growth activity of cells. Nevertheless, all three types of CNF coatings can be utilized in specific biomedical applications, e.g., in skin tissue replacement, using cell sheet technology in the case of aCNFs and c+aCNFs, and the generation of cell spheroids, in the case of cCNFs. In addition, c+aCNFs provide an interesting combination of the properties of cCNFs and aCNFs: the microtopographical structure is similar to that of cCNFs, while the contact angle, swelling, and stiffness properties more closely resemble the values for aCNF coatings. In the future, the properties of the c+aCNF combination can be further adjusted to create not only film-like coatings for cell cultivation but also 3D cross-linked CNF gels for cell embedding and 3D printing.

■ ASSOCIATED CONTENT

Ⓢ Supporting Information

The Supporting Information is available free of charge at https://pubs.acs.org/doi/10.1021/acs.biomac.0c01097.

Supporting methods and figures (PDF)

Adhesion and spreading of NHDFs (red tracker) and ADSCs (green tracker) in coculture on cCNF-coated glass (phase contrast) during the first 22 h after cell seeding (Supporting Video) (AVI)

■ AUTHOR INFORMATION

Corresponding Authors

Julia Pajorova − *Department of Biomaterials and Tissue Engineering, Institute of Physiology of the Czech Academy of Sciences, 14220 Prague, Czech Republic; 2nd Faculty of Medicine, Charles University, 15006 Prague, Czech Republic;* ⓘ orcid.org/0000-0001-5545-0031; Email: Julia.Pajorova@fgu.cas.cz

Anne Skogberg − *BioMediTech Institute and Faculty of Medicine and Health Technology (MET), Tampere University, 33720 Tampere, Finland;* Email: Anne.Skogberg@tuni.fi

Lucie Bacakova − *Department of Biomaterials and Tissue Engineering, Institute of Physiology of the Czech Academy of Sciences, 14220 Prague, Czech Republic;* Email: Lucie.Bacakova@fgu.cas.cz

Pasi Kallio − *BioMediTech Institute and Faculty of Medicine and Health Technology (MET), Tampere University, 33720 Tampere, Finland;* ⓘ orcid.org/0000-0001-6698-774X; Email: Pasi.Kallio@tuni.fi

Authors

Daniel Hadraba − *Department of Biomathematics, Institute of Physiology of the Czech Academy of Sciences, 14220 Prague, Czech Republic*

Antonin Broz − *Department of Biomaterials and Tissue Engineering, Institute of Physiology of the Czech Academy of Sciences, 14220 Prague, Czech Republic*

Martina Travnickova − *Department of Biomaterials and Tissue Engineering, Institute of Physiology of the Czech Academy of Sciences, 14220 Prague, Czech Republic; 2nd Faculty of Medicine, Charles University, 15006 Prague, Czech Republic*

Marketa Zikmundova − *Department of Biomaterials and Tissue Engineering, Institute of Physiology of the Czech Academy of Sciences, 14220 Prague, Czech Republic*

Mari Honkanen − *Tampere Microscopy Center, Tampere University, 33720 Tampere, Finland*

Markus Hannula − *BioMediTech Institute and Faculty of Medicine and Health Technology (MET), Tampere University, 33720 Tampere, Finland*

Panu Lahtinen − *VTT Technical Research Center of Finland, 02150 Espoo, Finland*

Maria Tomkova − *Faculty of Biotechnology and Food Sciences, Slovak University of Agriculture in Nitra, 94976 Nitra, Slovak Republic*

Complete contact information is available at:
https://pubs.acs.org/10.1021/acs.biomac.0c01097

Author Contributions

[#]J.P. and A.S. contributed equally to this work. The manuscript was written through the contribution of all authors. All authors have approved the final version of the manuscript. J.P. and A.S. planned, performed, and analyzed the experimental work, with the exception of the microCT imaging and analysis (M. Hannula) and the AFM scanning and analysis (D.H.). A.B., M.Z., and M. Tomkova helped with the cell experiments and microscopy imaging. M. Travnickova and J.P. performed the ADSC isolations. M. Honkanen performed SEM scanning. P.L. contributed to the CNF preparation. P.K. and L.B. contributed to the conception of the study, coordination of the work, and structuring and editing the manuscript.

■ REFERENCES

(1) Nechyporchuk, O.; Belgacem, M. N.; Bras, J. Production of cellulose nanofibrils: A review of recent advances. *Ind. Crops Prod.* **2016**, *93*, 2−25.

(2) Zhang, Y. X.; Nypelo, T.; Salas, C.; Arboleda, J.; Hoeger, I. C.; Rojas, O. J. Cellulose Nanofibrils: From Strong Materials to Bioactive Surfaces. *J. Renewable Mater.* **2013**, *1*, 195−211.

(3) Kummala, R.; Xu, W. Y.; Xu, C. L.; Toivakka, M. Stiffness and swelling characteristics of nanocellulose films in cell culture media. *Cellulose* **2018**, *25*, 4969−4978.

(4) Dufresne, A. Nanocellulose: a new ageless bionanomaterial. *Mater. Today* **2013**, *16*, 220−227.

(5) Ling, S.; Chen, W.; Fan, Y.; Zheng, K.; Jin, K.; Yu, H.; Buehler, M. J.; Kaplan, D. L. Biopolymer nanofibrils: structure, modeling, preparation, and applications. *Prog. Polym. Sci.* **2018**, *85*, 1−56.

(6) Courtenay, J. C.; Johns, M. A.; Galembeck, F.; Deneke, C.; Lanzoni, E. M.; Costa, C. A.; Scott, J. L.; Sharma, R. I. Surface modified cellulose scaffolds for tissue engineering. *Cellulose* **2017**, *24*, 253−267.

(7) Weishaupt, R.; Siqueira, G.; Schubert, M.; Tingaut, P.; Maniura-Weber, K.; Zimmermann, T.; Thony-Meyer, L.; Faccio, G.; Ihssen, J. TEMPO-Oxidized Nanofibrillated Cellulose as a High Density

Carrier for Bioactive Molecules. *Biomacromolecules* **2015**, *16*, 3640–3650.

(8) Courtenay, J. C.; Deneke, C.; Lanzoni, E. M.; Costa, C. A.; Bae, Y.; Scott, J. L.; Sharma, R. I. Modulating cell response on cellulose surfaces; tunable attachment and scaffold mechanics. *Cellulose* **2018**, *25*, 925–940.

(9) Kummala, R.; Veliz, D. S.; Fang, Z. Q.; Xu, W. Y.; Abitbol, T.; Xu, C. L.; Toivakka, M. Human Dermal Fibroblast Viability and Adhesion on Cellulose Nanomaterial Coatings: Influence of Surface Characteristics. *Biomacromolecules* **2020**, *21*, 1560–1567.

(10) Hua, K.; Carlsson, D. O.; Alander, E.; Lindstrom, T.; Stromme, M.; Mihranyan, A.; Ferraz, N. Translational study between structure and biological response of nanocellulose from wood and green algae. *RSC Adv.* **2014**, *4*, 2892–2903.

(11) Rashad, A.; Mustafa, K.; Heggset, E. B.; Syverud, K. Cytocompatibility of Wood-Derived Cellulose Nanofibril Hydrogels with Different Surface Chemistry. *Biomacromolecules* **2017**, *18*, 1238–1248.

(12) Skogberg, A.; Maki, A. J.; Mettanen, M.; Lahtinen, P.; Kallio, P. Cellulose Nanofiber Alignment Using Evaporation-Induced Droplet-Casting, and Cell Alignment on Aligned Nanocellulose Surfaces. *Biomacromolecules* **2017**, *18*, 3936–3953.

(13) Xiong, G. Y.; Luo, H. L.; Zhang, C.; Zhu, Y.; Wan, Y. Z. Enhanced biological behavior of bacterial cellulose scaffold by creation of macropores and surface immobilization of collagen. *Macromol. Res.* **2015**, *23*, 734–740.

(14) Lou, Y. R.; Kanninen, L.; Kuisma, T.; Niklander, J.; Noon, L. A.; Burks, D.; Urtti, A.; Yliperttula, M. The Use of Nanofibrillar Cellulose Hydrogel As a Flexible Three-Dimensional Model to Culture Human Pluripotent Stem Cells. *Stem Cells Dev.* **2014**, *23*, 380–392.

(15) Xu, W. Y.; Zhang, X.; Yang, P. R.; Langvik, O.; Wang, X. J.; Zhang, Y. C.; Cheng, F.; Osterberg, M.; Willfor, S.; Xu, C. L. Surface Engineered Biomimetic Inks Based on UV Cross-Linkable Wood Biopolymers for 3D Printing. *ACS Appl. Mater. Interfaces* **2019**, *11*, 12389–12400.

(16) Koivuniemi, R.; Hakkarainen, T.; Kiiskinen, J.; Kosonen, M.; Vuola, J.; Valtonen, J.; Luukko, K.; Kavola, H.; Yliperttula, M. Clinical Study of Nanofibrillar Cellulose Hydrogel Dressing for Skin Graft Donor Site Treatment. *Adv. Wound Care* **2020**, *9*, 199–210.

(17) Kiiskinen, J.; Merivaara, A.; Hakkarainen, T.; Kaariainen, M.; Miettinen, S.; Yliperttula, M.; Koivuniemi, R. Nanofibrillar cellulose wound dressing supports the growth and characteristics of human mesenchymal stem/stromal cells without cell adhesion coatings. *Stem Cell Res. Ther.* **2019**, *10*, 1–13.

(18) Bacakova, L.; Pajorova, J.; Bacakova, M.; Skogberg, A.; Kallio, P.; Kolarova, K.; Svorcik, V. Versatile Application of Nanocellulose: From Industry to Skin Tissue Engineering and Wound Healing. *Nanomaterials* **2019**, *9*, 1–39.

(19) Isogai, A.; Saito, T.; Fukuzumi, H. TEMPO-oxidized cellulose nanofibers. *Nanoscale* **2011**, *3*, 71–85.

(20) Voisin, H.; Bergstrom, L.; Liu, P.; Mathew, A. P. Nanocellulose-Based Materials for Water Purification. *Nanomaterials* **2017**, *7*, 1–19.

(21) Bacakova, L.; Filova, E.; Parizek, M.; Ruml, T.; Svorcik, V. Modulation of cell adhesion, proliferation and differentiation on materials designed for body implants. *Biotechnol. Adv.* **2011**, *29*, 739–767.

(22) Jackson, J. K.; Letchford, K.; Wasserman, B. Z.; Ye, L.; Hamad, W. Y.; Burt, H. M. The use of nanocrystalline cellulose for the binding and controlled release of drugs. *Int. J. Nanomed.* **2011**, *6*, 321–330.

(23) Chaker, A.; Boufi, S. Cationic nanofibrillar cellulose with high antibacterial properties. *Carbohyd. Polym.* **2015**, *131*, 224–232.

(24) Syverud, K. Tissue Engineering Using Plant-Derived Cellulose Nanofibrils (CNF) as Scaffold Material. *ACS Symp. Ser.* **2017**, *1251*, 171–189.

(25) Discher, D. E.; Janmey, P.; Wang, Y. L. Tissue cells feel and respond to the stiffness of their substrate. *Science* **2005**, *310*, 1139–1143.

(26) Hoshiba, T.; Yoshikawa, C.; Sakakibara, K. Characterization of Initial Cell Adhesion on Charged Polymer Substrates in Serum-Containing and Serum-Free Media. *Langmuir* **2018**, *34*, 4043–4051.

(27) Arima, Y.; Iwata, H. Effect of wettability and surface functional groups on protein adsorption and cell adhesion using well-defined mixed self-assembled monolayers. *Biomaterials* **2007**, *28*, 3074–3082.

(28) Saito, T.; Nishiyama, Y.; Putaux, J. L.; Vignon, M.; Isogai, A. Homogeneous suspensions of individualized microfibrils from TEMPO-catalyzed oxidation of native cellulose. *Biomacromolecules* **2006**, *7*, 1687–1691.

(29) Estes, B. T.; Diekman, B. O.; Gimble, J. M.; Guilak, F. Isolation of adipose-derived stem cells and their induction to a chondrogenic phenotype. *Nat. Protoc.* **2010**, *5*, 1294–1311.

(30) Bacakova, L.; Zarubova, J.; Travnickova, M.; Musilkova, J.; Pajorova, J.; Slepicka, P.; Kasalkova, N. S.; Svorcik, V.; Kolska, Z.; Motarjemi, H.; Molitor, M. Stem cells: their source, potency and use in regenerative therapies with focus on adipose-derived stem cells - a review. *Biotechnol. Adv.* **2018**, *36*, 1111–1126.

(31) Travnickova, M.; Pajorova, J.; Zarubova, J.; Krocilova, N.; Molitor, M.; Bacakova, L. The Influence of Negative Pressure and of the Harvesting Site on the Characteristics of Human Adipose Tissue-Derived Stromal Cells from Lipoaspirates. *Stem Cells Int.* **2020**, *2020*, No. 1016231.

(32) Lahtinen, P.; Liukkonen, S.; Pere, J.; Sneck, A.; Kangas, H. A Comparative Study of Fibrillated Fibers from Different Mechanical and Chemical Pulps. *BioResources* **2014**, *9*, 2115–2127.

(33) Pöhler, T.; Lappalainen, T.; Tammelin, T.; Eronen, P.; Hiekkataipale, P.; Vehniäinen, A.; Koskinen, T. M. In Influence of fibrillation method on the character of nanofibrillated cellulose (NFC). International Conference on Nanotechnology for the Forest Products Industry. TAPPI Press: Espoo, Finland, 2010; pp 437–458.

(34) Montazer, M.; Harifi, T. In 5 - Nanosurface Activation. *Nanofinishing of Textile Materials*; Montazer, M.; Harifi, T., Eds.; Woodhead Publishing, 2018; pp 65–82.

(35) Pahimanolis, N.; Salminen, A.; Penttila, P. A.; Korhonen, J. T.; Johansson, L. S.; Ruokolainen, J.; Serimaa, R.; Seppala, J. Nano-fibrillated cellulose/carboxymethyl cellulose composite with improved wet strength. *Cellulose* **2013**, *20*, 1459–1468.

(36) Zhang, K.; Barhoum, A.; Xiaoqing, C.; Li, H.; Samyn, P. In Cellulose Nanofibers: Fabrication and Surface Functionalization Techniques. *Handbook of Nanofibers*; Barhoum, A.; Bechelany, M.; Makhlouf, A. S. H., Eds.; Springer International Publishing: Cham, 2019; pp 409–449.

(37) Headley, A. D.; Mcmurry, M. E. The Influence of Solvents on the Basicity of Dipolar Amines. *J. Phys. Org. Chem.* **1994**, *7*, 63–67.

(38) Orelma, H.; Filpponen, I.; Johansson, L. S.; Osterberg, M.; Rojas, O. J.; Laine, J. Surface Functionalized Nanofibrillar Cellulose (NFC) Film as a Platform for Immunoassays and Diagnostics. *Biointerphases* **2012**, *7*, 1–12.

(39) Sneck, A.; Atsushi, T.; Meyer, V.; Kreztzschmar, J. In Advanced characterization techniques to evaluate the structure of nanofibrillated cellulose, SUNPAP Project – Final Conference, Milan, Italy, 2012.

(40) Sakai, S.; Ito, S.; Ogushi, Y.; Hashimoto, I.; Hosoda, N.; Sawae, Y.; Kawakami, K. Enzymatically fabricated and degradable micro-capsules for production of multicellular spheroids with well-defined diameters of less than 150 mu m. *Biomaterials* **2009**, *30*, 5937–5942.

(41) Duval, K.; Grover, H.; Han, L. H.; Mou, Y.; Pegoraro, A. F.; Fredberg, J.; Chen, Z. Modeling Physiological Events in 2D vs. 3D Cell Culture. *Physiology* **2017**, *32*, 266–277.

(42) Skardal, A.; Mack, D.; Atala, A.; Soker, S. Substrate elasticity controls cell proliferation, surface marker expression and motile phenotype in amniotic fluid-derived stem cells. *J. Mech. Behav. Biomed. Mater.* **2013**, *17*, 307–316.

(43) Yang, Y. J.; Wang, L. Y.; Yan, F.; Xiang, X.; Tang, Y. J.; Zhang, L. Y.; Liu, J. B.; Qiu, L. Determination of Normal Skin Elasticity by Using Real-time Shear Wave Elastography. *J. Ultrasound Med.* **2018**, *37*, 2507–2516.

(44) Achterberg, V. F.; Buscemi, L.; Diekmann, H.; Smith-Clerc, J.; Schwengler, H.; Meister, J. J.; Wenck, H.; Gallinat, S.; Hinz, B. The

Nano-Scale Mechanical Properties of the Extracellular Matrix Regulate Dermal Fibroblast Function. *J. Invest. Dermatol.* **2014**, *134*, 1862−1872.

(45) Kim, D. H.; Provenzano, P. P.; Smith, C. L.; Levchenko, A. Matrix nanotopography as a regulator of cell function. *J. Cell Biol.* **2012**, *197*, 351−360.

(46) Bourkoula, A.; Constantoudis, V.; Kontziampasis, D.; Petrou, P. S.; Kakabakos, S. E.; Tserepi, A.; Gogolides, E. Roughness threshold for cell attachment and proliferation on plasma micro-nanotextured polymeric surfaces: the case of primary human skin fibroblasts and mouse immortalized 3T3 fibroblasts. *J. Phys. D: Appl. Phys.* **2016**, *49*, No. 304002.

(47) Hou, Y.; Xie, W. Y.; Yu, L. X.; Camacho, L. C.; Nie, C. X.; Zhang, M.; Haag, R.; Wei, Q. Surface Roughness Gradients Reveal Topography-Specific Mechanosensitive Responses in Human Mesenchymal Stem Cells. *Small* **2020**, *16*, No. 1905422.

(48) Vroman, L.; Adams, A. L.; Fischer, G. C.; Munoz, P. C. Interaction of High Molecular-Weight Kininogen, Factor-Xii, and Fibrinogen in Plasma at Interfaces. *Blood* **1980**, *55*, 156−159.

(49) Courtenay, J. C.; Filgueiras, J. G.; deAzevedo, E. R.; Jin, Y.; Edler, K. J.; Sharma, R. I.; Scott, J. L. Mechanically robust cationic cellulose nanofibril 3D scaffolds with tuneable biomimetic porosity for cell culture. *J. Mater. Chem. B* **2019**, *7*, 53−64.

(50) Attwood, S. J.; Kershaw, R.; Uddin, S.; Bishop, S. M.; Welland, M. E. Understanding how charge and hydrophobicity influence globular protein adsorption to alkanethiol and material surfaces. *J. Mater. Chem. B* **2019**, *7*, 2349−2361.

(51) Beykal, B.; Herzberg, M.; Oren, Y.; Mauter, M. S. Influence of surface charge on the rate, extent, and structure of adsorbed Bovine Serum Albumin to gold electrodes. *J. Colloid Interf Sci.* **2015**, *460*, 321−328.

(52) Phan, H. T. M.; Bartelt-Hunt, S.; Rodenhausen, K. B.; Schubert, M.; Bartz, J. C. Investigation of Bovine Serum Albumin (BSA) Attachment onto Self-Assembled Monolayers (SAMs) Using Combinatorial Quartz Crystal Microbalance with Dissipation (QCM-D) and Spectroscopic Ellipsometry (SE). *PLoS One* **2015**, *10*, No. e0141282.

(53) Faucheux, N.; Schweiss, R.; Lutzow, K.; Werner, C.; Groth, T. Self-assembled monolayers with different terminating groups as model substrates for cell adhesion studies. *Biomaterials* **2004**, *25*, 2721−2730.

(54) McClary, K. B.; Ugarova, T.; Grainger, D. W. Modulating fibroblast adhesion, spreading, and proliferation using self-assembled monolayer films of alkylthiolates on gold. *J. Biomed. Mater. Res.* **2000**, *50*, 428−439.

(55) Okuyama, T.; Yamazoe, H.; Mochizuki, N.; Khademhosseini, A.; Suzuki, H.; Fukuda, J. Preparation of arrays of cell spheroids and spheroid-monolayer cocultures within a microfluidic device. *J. Biosci. Bioeng.* **2010**, *110*, 572−576.

Supporting Information

Cellulose Mesh with Charged Nanocellulose Coatings as a Promising Carrier of Skin and Stem Cells for Regenerative Applications

Julia Pajorova,[1,3,#,] and Anne Skogberg,[2,#,*] Daniel Hadraba,[1†] Antonin Broz,[1] Martina Travnickova,[1,3] Marketa Zikmundova,[1] Mari Honkanen,[4] Markus Hannula,[2] Panu Lahtinen,[5] Maria Tomkova,[6] Lucie Bacakova[1,*] and Pasi Kallio[2,*]*

[1]Department of Biomaterials and Tissue Engineering, [1†]Department of Biomathematics, Institute of Physiology of the Czech Academy of Sciences, Videnska 1083, 14220 Prague, Czech Republic

[2]BioMediTech Institute and Faculty of Medicine and Health Technology (MET), Tampere University, Korkeakoulunkatu 3, 33720 Tampere, Finland

[3]2nd Faculty of Medicine, Charles University, V Uvalu 84, 15006 Prague, Czech Republic

[4]Tampere Microscopy Center, Tampere University, Korkeakoulunkatu 3, 33720 Tampere, Finland

[5]VTT Technical Research Center of Finland, Tietotie 4E, 02150 Espoo, Finland

[6] Faculty of Biotechnology and Food Sciences, Slovak University of Agriculture in Nitra, Tr. A. Hlinku 2, 94976 Nitra, Slovak Republic

[#]*These authors contributed equally*

[*]*Corresponding authors*

1 Supporting Methods

S1.1 Production of cellulose nanofibrils

Before the TEMPO and EPTMAC chemical pretreatments, the pulp was disintegrated and cleaned using mild alkaline washing and autoclaving. Alkaline washing was performed twice using 0.1 M NaOH. The pulp was autoclaved and then washed with MilliQ water.

The TEMPO-modified oxidation was carried out for 100 g pulp batch, which was suspended in water containing 2.09 g (0.13 mmol) of TEMPO and 47.84 g (4.65 mmol) of NaBr at 1% consistency. Then, 178.7 mL (240 mmol) of NaClO was slowly added while stirring at room temperature. The pH was kept at 10.3 by adding 1 M NaOH during the reaction. When the pH stopped decreasing, the reaction was stopped by adding 350 mL ethanol into the oxidized pulp suspension. Finally, the pH was adjusted to 6.5 by adding 1 M HCl. The oxidized pulp was washed with deionized water by filtration and stored in a fridge before further fibrillation.

S1.2 Preparation of CNF-coated meshes

The dry weight of the CNF supernatants (Section 2.1.2) was determined from the freeze-dried aCNF and cCNF solutions, and it reached the values of 0.147% (w/v) and 0.145% (w/v), respectively. These CNF supernatants were used for preparation of the CNF-coated meshes (further referred to as "c150, c600, a150, a600, c+a"). A volume of 150 µL (c150, a150) was pipetted on the top of the mesh to create three-dimensional (3D) coating, and a volume of 600 µL (c600, a600) was used in order to form two-dimensional (2D) film-like coating (Scheme 1). In the case of the cCNFs and aCNFs combination (c+a), a volume of 300 µL of cCNFs was firstly applied to the mesh surface and 300 µL of aCNFs was subsequently added. The cCNF and aCNF solutions were immediately mixed directly on the mesh surface by pipetting both solutions several times. The c+a coatings were prepared only in the final volume of 600 µL. The pristine noncoated mesh was used as the control group (Scheme 1).

S1.3 Characterization of noncoated meshes using microCT

The noncoated meshes were imaged with X-ray microtomography (microCT) at MicroXCT-400 (X-ray tube voltage of 40 kV and a current of 250 µA; Carl Zeiss X-ray Microscopy, Inc., Pleasanton, CA). The 3D microCT images were reconstructed from 1601 projections with a 4-sec exposure time (20× objective, binning 2, pixel size 1.15 µm) using the microCT software

tool XMReconstuctor. 3D image stacks were manually thresholded for the 3D analysis. The mean fiber thickness and the mean void thickness with standard deviations, volume fraction, and porosity were calculated by BoneJ Fiji plugin.[1,2] The data visualization was realized using Avizo 2019.3 software (Thermo Fisher Scientific, Waltham, MA).

S1.4 Wettability of CNF layers

The wettability of dry aCNF, cCNF and c+aCNF layers was measured on the layers prepared on microscopy glass coverslips (n = 3). The volume of 600 µL of CNF solution was spread on a glass coverslip and evaporated (up to 24 h at 60°C). The wettability was then analyzed by the sessile drop method using an OCA-15 plus optical goniometer (Dataphysics Instruments GmbH, Filderstadt, Germany). A 2 µL drop of deionized water (dH$_2$O) or Dulbecco's modified Eagle medium (DMEM) was dispensed on the CNF surfaces and the side profile photographs of the resulting droplets were captured with the goniometer for 15 sec at 0.2-sec intervals to determine the static contact angle. The average of approximately 5-sec periods was taken as the final value.

S1.5 Surface mapping and characterization of mechanical properties using AFM

The QI images of dry samples were acquired at randomly selected places after visual inspection for artefacts (Olympus IX 81, Tokyo, Japan). The size of each scanned area was 10 x 10 µm^2 with the resolution of 128 x 128 pixels. The curves were post-processed in Gwyddion software ver. 2.44 to obtain roughness maps represented by the Ra parameter.[3]

The force-distance curves of dry samples were acquired by changing the mode to force spectroscopy mapping and scanning the samples at the grid size of 25 x 25 µm^2, with a resolution of 8 x 8 pixels.

The set point value for mechanical measurements of wet samples was 50 nN relative to the baseline value, and the speed of the probe was set to 10 µm/s. The absolute value of Young's modulus was determined[4] by fitting the force-distance approaching curves using the Maugis model[5] in AtomicJ software.[6]

For all measurements, the laser was set to maximize the reflection sum followed by centering the laser detector. The thermal noise method was used to return the cantilever stiffness. The data were recorded with the active closed loop at the 5 kHz sample rate.

S1.6 Characterization of isolated adipose-tissue-derived stem cells (ADSCs)

In order to decrease the variability in the cell behavior between individual donors, the ADSCs from 10 female patients (age 26 – 47), harvested from lipoaspirates obtained from thighs under negative pressure of -200 mmHg, were mixed in passage 1. The pooled ADSCs were characterized in passage 2 by a flow cytometry analysis (Accuri C6 Flow Cytometer, BD Biosciences, San Jose, CA) for the positivity of the CD surface markers specific for adult mesenchymal stem cells; that is, CD105 (98.9%), CD90 (98.7%), CD73 (99.9%) and CD29 (99.6%), and for the negativity of endothelial and hematopoietic markers, such as CD146 (1.5%) and CD45 (2.5%). Other endothelial and hematopoietic markers CD34 and CD31 were analyzed in cells from individual donors only, and the average values from all 10 donors were 2% for CD34 and 0.5% for CD31.

S1.7 Metabolic activity of cells on the CNF-coated meshes (Resazurin Assay)

The stock solution of resazurin (40 mM) was diluted in a DMEM medium without phenol red, supplemented with 10% fetal bovine serum (FBS), to a final concentration of 40 μM according to the manufacturer's protocol. The CNF-coated and noncoated meshes (n = 4) in CellCrown™ inserts were transferred to fresh 24-well plates in order to avoid interference of additional metabolic activity of cells growing on the well bottoms around and under the samples. After washing with phosphate-buffered saline (PBS; Sigma-Aldrich Co., St. Louis, MO), 1 mL of the resazurin solution of was added into each well. The cells were incubated with resazurin solution for 4 h at 37°C. Then 100 μL of this solution was pipetted into a 96-well plate in duplicates, and the fluorescence (Ex/Em = 530/590 nm) was measured by a spectrophotometer (Synergy™ HT Multi-Mode Microplate reader; BioTek, Winooski, VT). Background noise of the resazurin solution was removed based on the signal from each control sample without cells.

S1.8 Fluorescence staining of cells on the CNF-coated meshes

The cells were fixed with 4% paraformaldehyde (Sigma-Aldrich Co., St. Louis, MO) at room temperature for 20 min. Then, the solution of 0.1% Triton X-100 (Sigma-Aldrich Co., St. Louis, MO), diluted in PBS, was applied on samples at room temperature for 20 min in order to permeabilize the cell membrane by dissolving its lipid component. The nonspecific binding sites for antibodies on the samples were blocked with a solution of 1% bovine serum albumin and 0.1% Tween 20 in PBS (all chemicals from Sigma-Aldrich Co., St. Louis, MO) at room

temperature for 20 min. The cells were stained with a primary antibody to human vinculin (monoclonal mouse antibody, clone hVIN-1, Sigma-Aldrich Co., St. Louis, MO, Cat. no. V9131) diluted in a blocking solution (1% albumin and 0.1% Tween 20 in PBS) at a ratio of 1:200. The primary antibody was incubated with the samples at 37°C for 1 h. After washing, the samples were incubated for 1 h at room temperature with a secondary antibody; that is, goat anti-mouse F(ab')2 fragments of IgG (H+L) conjugated with Alexa Fluor® 488 (Thermo Fisher Scientific, Molecular Probes, Waltham, MA, Cat. no. A11017), diluted in the blocking solution at a ratio of 1:400. Finally, cytoskeletal F-actin was stained with phalloidin conjugated with tetramethylrhodamine isothiocynate (TRITC) fluorescent dye (Sigma-Aldrich Co., St. Louis, MO, Cat. no. P1951), diluted in PBS to a final concentration of 5 µg/mL, at room temperature for 1 h. The incubations with fluorescent dyes were performed in the dark; for example, in samples covered with aluminum foil. PBS was used for washing the samples between each individual step. The samples were imaged with a spinning disk confocal system Dragonfly 503 (Andor, Belfast, UK) with Zyla 4.2 PLUS sCMOS camera (Andor, Belfast, UK), mounted on a microscope Leica DMi8 (Leica Microsystems, Wetzlar, Germany) with objective HC PL APO 20×/0.75 IMM CORR CS2; Free Working Distance = 0.66 mm or HC PL APO 40×/1.10 W CORR CS2; Free Working Distance = 0.65 mm.

For scanning electron microscopy (SEM) imaging, the cells on samples were fixed in 4% paraformaldehyde in PIPES buffer (pH ~ 7, Sigma-Aldrich Co., St. Louis, MO). The samples were dehydrated in the standard gradient of ethanol solutions (30 min in each concentration of 30%, 50%, 70%, 96%, and 100%). The 100% ethanol was gradually replaced by the following series of drying solutions: 1:1 ethanol/acetone, 100% acetone (Sigma-Aldrich Co., St. Louis, MO), 1:1 acetone/hexamethyldisilazane (HMDS, Sigma-Aldrich Co., St. Louis, MO), 100% HMDS, with each step taking 30 min. The samples were evaporated in air for 48 h and scanned using SEM (ULTRAplus, Carl Zeiss, Oberkochen, Germany).

S1.9 Protein adsorption on the CNF-coated meshes (Pierce™ BCA Protein Assay Kit)

The noncoated meshes and meshes coated with 600 µL of CNF (c600, a600, c+a) – a volume that ensured homogeneous coatings – were incubated in 1 mL of DMEM without phenol red (Sigma-Aldrich Co., St. Louis, MO). The medium was supplemented either with 10% (v/v) of FBS or with bovine serum albumin (BSA, Sigma-Aldrich Co., St. Louis, MO) in a final concentration of 2.5 mg/mL. The samples in DMEM without any supplements were used as a

control. The total concentration of the proteins in 1.5 mL of DMEM supplemented with 10% (v/v) FBS was 3.64 mg/mL and in 1.5 mL of of DMEM supplemented with 0.25% (v/v) BSA was 2.5 mg/mL. After 24 h of incubation with the proteins at 37°C, the samples were rinsed with PBS in order to wash out the nonadsorbed or only weakly adsorbed proteins. In order to avoid the interactions of the meshes with proteins adsorbed on the CellCrowns™, the samples were cut from CellCrowns™ and placed into a fresh 24-well plate. The final solution of 600 µL of the working reagent and 75 µL of PBS was applied on each sample and incubated for 30 min at 37°C. The volume of 225 µL of the final solution, taken from each sample, was then pipetted into a 96-well plate in two parallels, and the absorbance (562 nm) was measured using a VersaMax ELISA Microplate Reader spectrophotometer (Molecular Devices Corporation, Sunnyvale, CA).

S1.10 Cell adhesion on the cCNF-coated meshes preadsorbed with proteins

The treated group of c600 CNF-coated meshes was preadsorbed with cell adhesion-modulating serum-derived proteins by incubating in DMEM supplemented either with 10% (v/v) FBS or with 0.25% (w/v) BSA (referred to as "FBS ads" and "BSA ads", respectively) for 2 h before the cell seeding. The cells were seeded subsequently at a density of 20 000 cells/insert (that is, approx. 25 000 cells/cm^2) in 1 mL/well of DMEM without any supplements. In the control group of c600 CNF-coated meshes, the cells suspended in DMEM supplemented with 10% FBS or 0.25% BSA (referred to as "with FBS" and "with BSA", respectively), were seeded directly on the meshes at the same time, in the same seeding density and in the same volume of the medium as the cells in the treated group. The samples of both groups with BSA were fixed after 2 h of cultivation, while the samples with FBS were fixed after 24 h of cultivation (Scheme S1).

S1.11 Cell adhesion on the cCNF-coated glass coverslips preadsorbed with proteins

In addition to the cCNF-coated cellulose meshes, the cell adhesion was studied on cCNF-coated glass coverslips to evaluate the effect of pure CNFs on cells without the influence of the underlying cellulose mesh. The adhesion of NHDFs and ADSCs on c600 CNF-coated glass coverslips was compared after 2 h and 24 h of cultivation by fluorescence staining, as described in Section 2.4.4. On glass coverslips, the protein preadsorption and the cell seeding with and without proteins were performed in the same manner as in the experiment with cCNF-coated meshes (see S1.10). In addition, the treated group of c600 CNF-coated glass coverslips was

preincubated in pure DMEM (referred to as "DMEM ads"), and the cells in the control group were seeded directly on the substrate in pure DMEM (referred to as "with DMEM"). All samples with BSA and with pure DMEM were fixed after 2 h, while one half of samples with FBS were fixed after 2 h and the other half after 24 h of cultivation (Scheme S1).
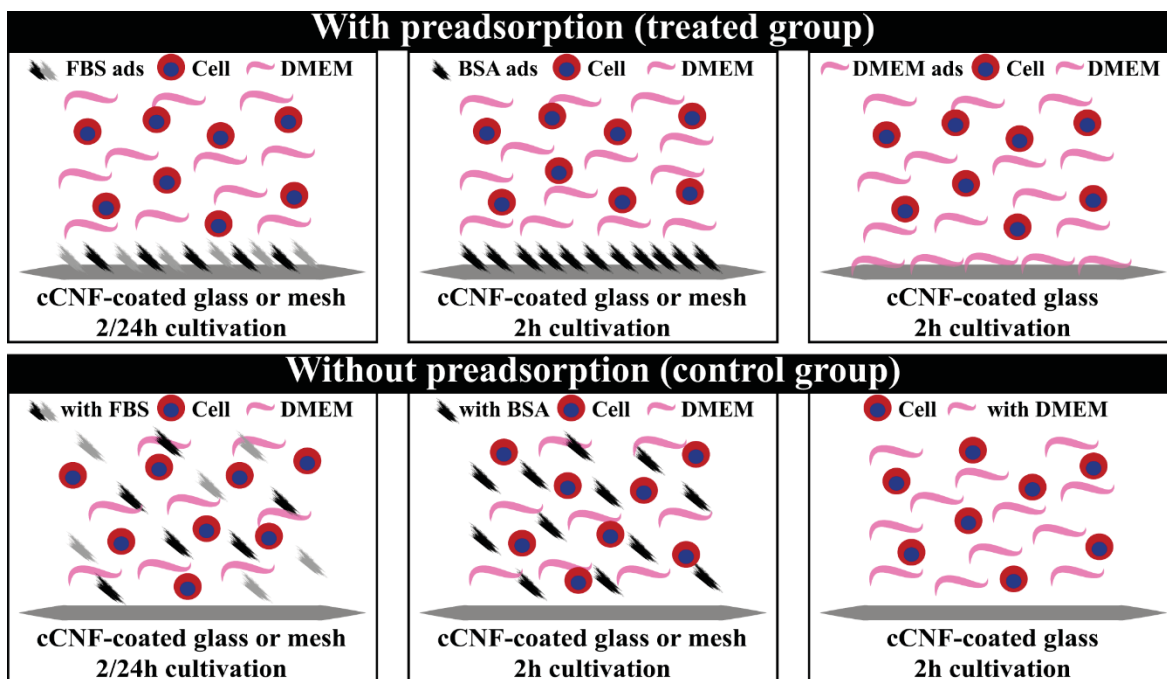
Scheme S1. *Schematic picture of the cell seeding on cCNF coatings with or without preadsorption of serum-derived proteins. The proteins from 10% (v/v) FBS, 0.25% (w/v) BSA and pure DMEM were preadsorbed on cCNF-coated glass coverslips or meshes for 2 h before cell seeding (treated group – FBS ads, BSA ads, DMEM ads, respectively), or were added directly into DMEM with cells (control group – with FBS, with BSA, with DMEM, respectively). The cCNF-coated glass coverslips and meshes were seeded with NHDFs and ADSCs and cultivated for 2 h (all samples) and 24 h (only "FBS ads and with FBS" samples).*

S1.12 Live-cell imaging of NHDFs and ADSCs in coculture on cCNF-coated glass

The speed of adhesion of NHDFs and ADSCs was evaluated on cCNF-coated glass substrate by fluorescence live-cell imaging. The reason for using glass substrates was their transparency, which made it possible to observe the living cells in an inverted microscope. The cCNF coating was prepared on a 20 mm micro-well cover glass of 35 mm glass bottom dish (Cellvis, Mountain View, CA) using 600 µL of cCNF solution. Both cell types, stained by different fluorescent dyes, were seeded simultaneously on a single sample. NHDFs were stained by CellTracker™ Red CMTPX, while ADSCs were stained by CellTracker™ Green CMFDA (both from Thermo Fisher Scientific, Invitrogen, Waltham, MA). The staining procedure was done according to the

manufacturer's protocol before cell seeding. Equal numbers of the stained NHDFs and ADSCs (10^5 cell/0.5 mL for each cell type) were mixed in 1 mL of DMEM supplemented with 10% FBS and seeded directly on the cCNF-coated glass coverslip. The recording of the adhesion and spreading of the cells in coculture was started 10 min after cell seeding, and the images were acquired at 10-min intervals for the first four h, and then at 30-min intervals for the remaining 18 h. Live-cell imaging was performed using Nikon TiE microscope (Nikon, Tokyo, Japan) equipped with a CARVII (Crestoptics S.p.A., Rome, Italy) spinning disk confocal system (in widefield regime), Orca-R2 camera (Hamamatsu, Shizuoka, Japan) and with Nikon ELWD 20× objective (N.A. = 0.45).

Supporting Figures

Figure S1
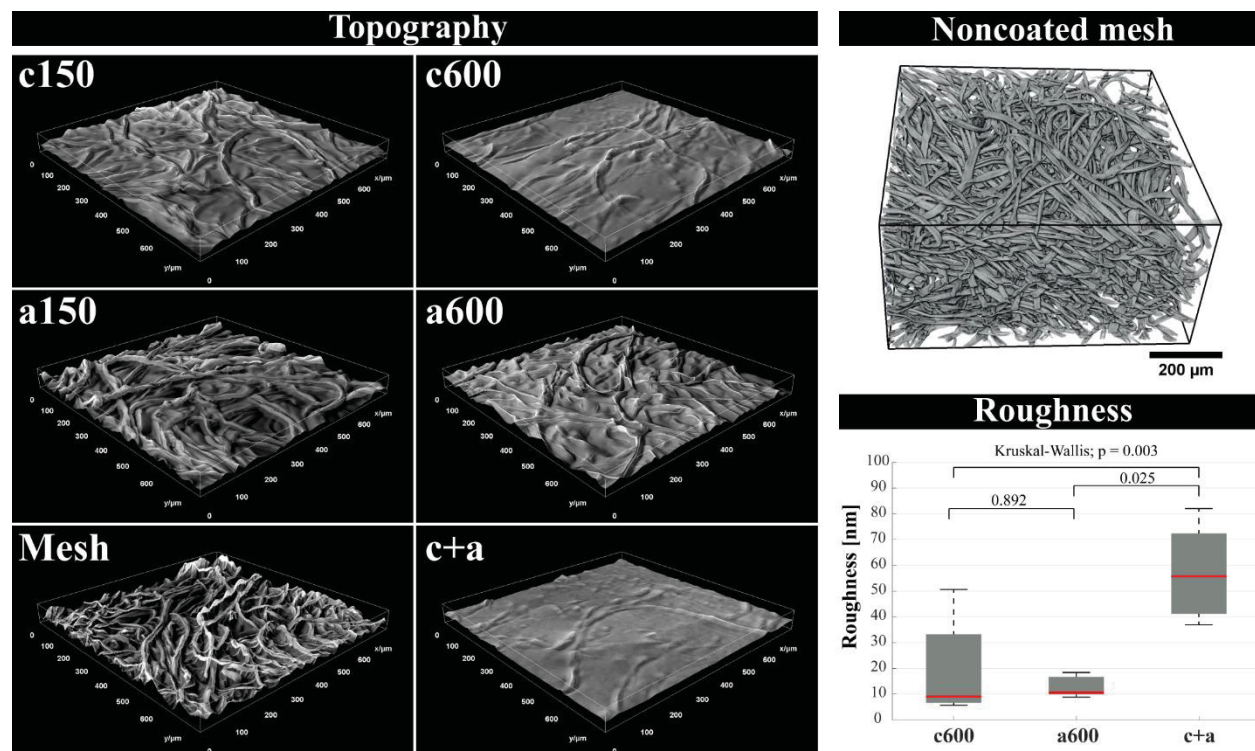
Figure S1. *Topography of noncoated and CNF-coated meshes created by ImageJ (Interactive 3D surface plot) from SEM images, MicroCT image of noncoated mesh and plots of roughness (Ra) values measured by AFM.*

Figure S2

	c600	a600	c+a
dH$_2$O	65°	31°	32°
DMEM	50°	40°	32°

Figure S2. Contact angles of the c600, a600, c+a CNF-coated glass coverslips measured in dH$_2$O and DMEM.
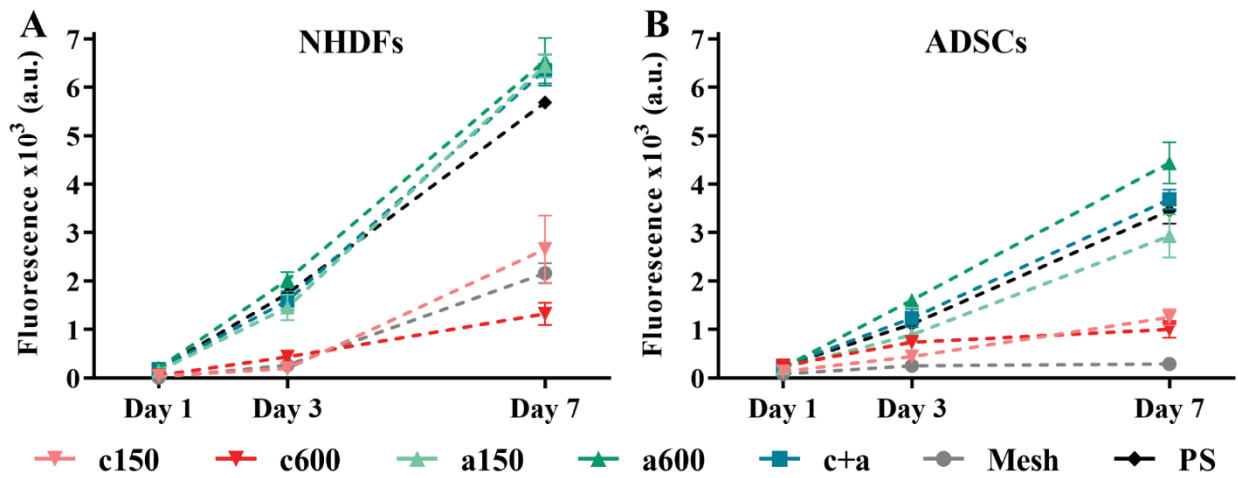
Figure S3

Figure S3. Metabolic activity of NHDFs (A) and ADSCs (B) measured by resazurin on CNF-coated meshes and on noncoated meshes on days 1, 3, and 7 after cell seeding. Arithmetic mean ± SD from eight measurements made on four independent samples for each experimental group and time interval.

Figure S4
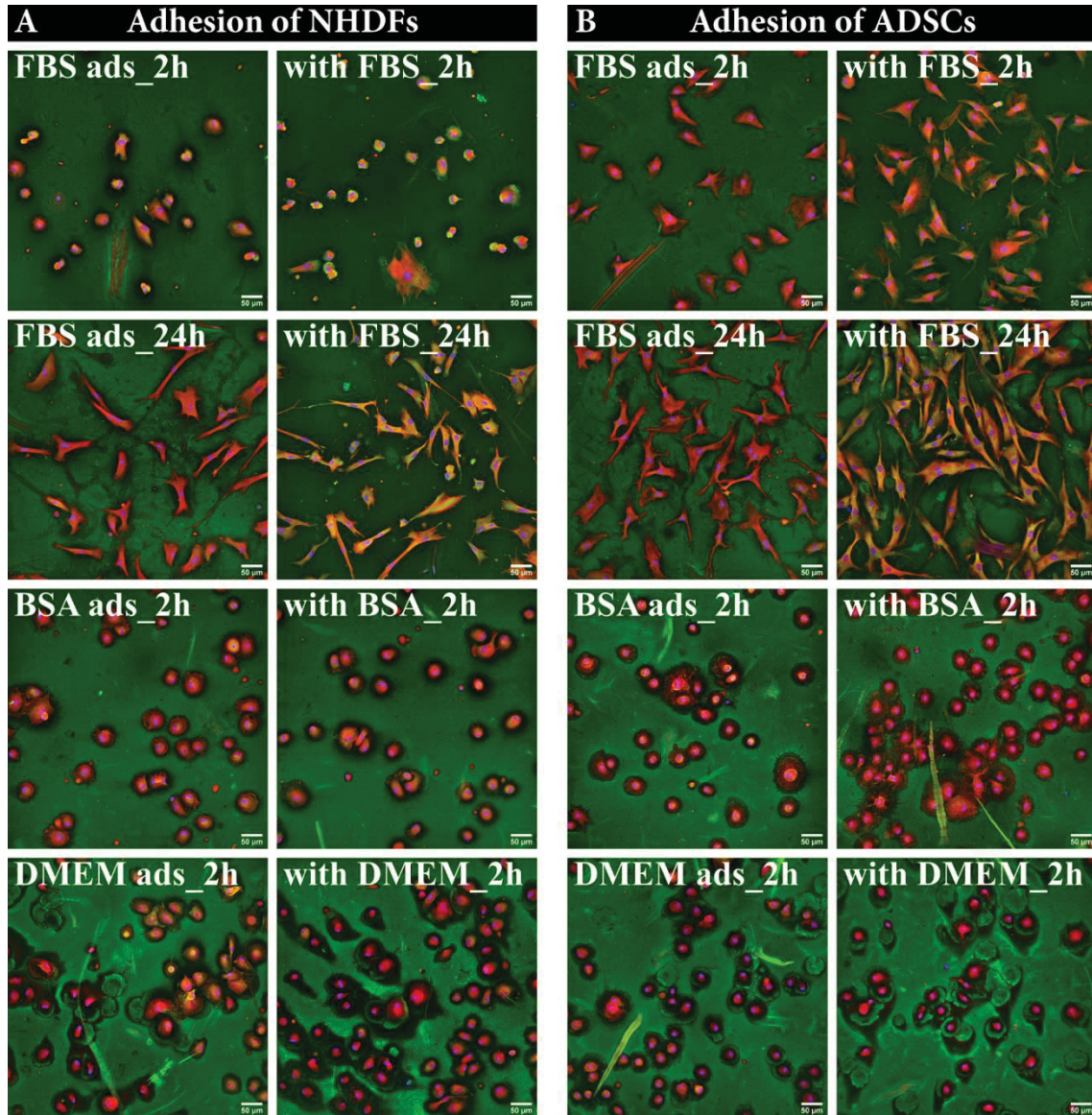
Figure S4. *Adhesion and spreading of NHDFs (A) and ADSCs (B) on cCNF-coated glass coverslips with or without preadsorbed proteins after 2 and 24 h. The treated group of cCNF coatings was preadsorbed with proteins in DMEM (FBS ads_2h, FBS ads_24h and BSA ads_2h) or with pure DMEM (DMEM ads_2h). The control group of cCNF coatings was seeded with cells in DMEM with proteins (with FBS_2h, with FBS_24h and with BSA_2h) or in pure DMEM (with DMEM_2h). F-actin in the cell cytoskeleton was stained with phalloidin-TRITC (red), cell nuclei with DAPI (blue) and the vinculin in the cells was stained by immunofluorescence using a secondary antibody conjugated with Alexa Fluor 488 (green). The cCNF coatings were visualized by nonspecific adsorption of the secondary antibody conjugated with Alexa Fluor 488 (green). A confocal microscope with an objective magnification 20×. Scale bar = 50 μm.*
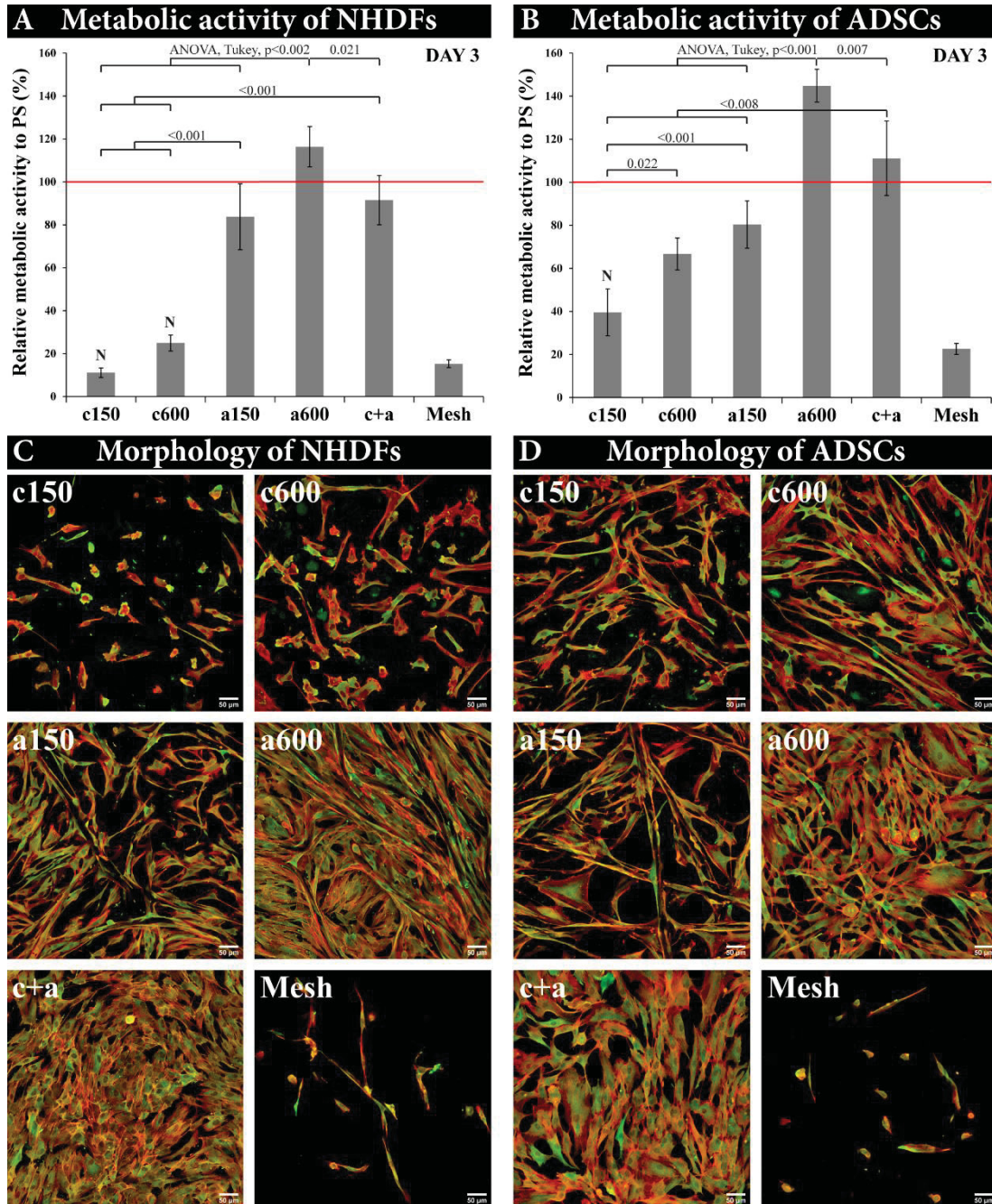
Figure S5

A Metabolic activity of NHDFs

ANOVA, Tukey, p<0.002   0.021   **DAY 3**

<0.001

<0.001

Relative metabolic activity to PS (%)

c150   c600   a150   a600   c+a   Mesh

B Metabolic activity of ADSCs

ANOVA, Tukey, p<0.001   0.007   **DAY 3**

<0.008

<0.001

0.022

Relative metabolic activity to PS (%)

c150   c600   a150   a600   c+a   Mesh

C Morphology of NHDFs

c150   c600
a150   a600
c+a   Mesh

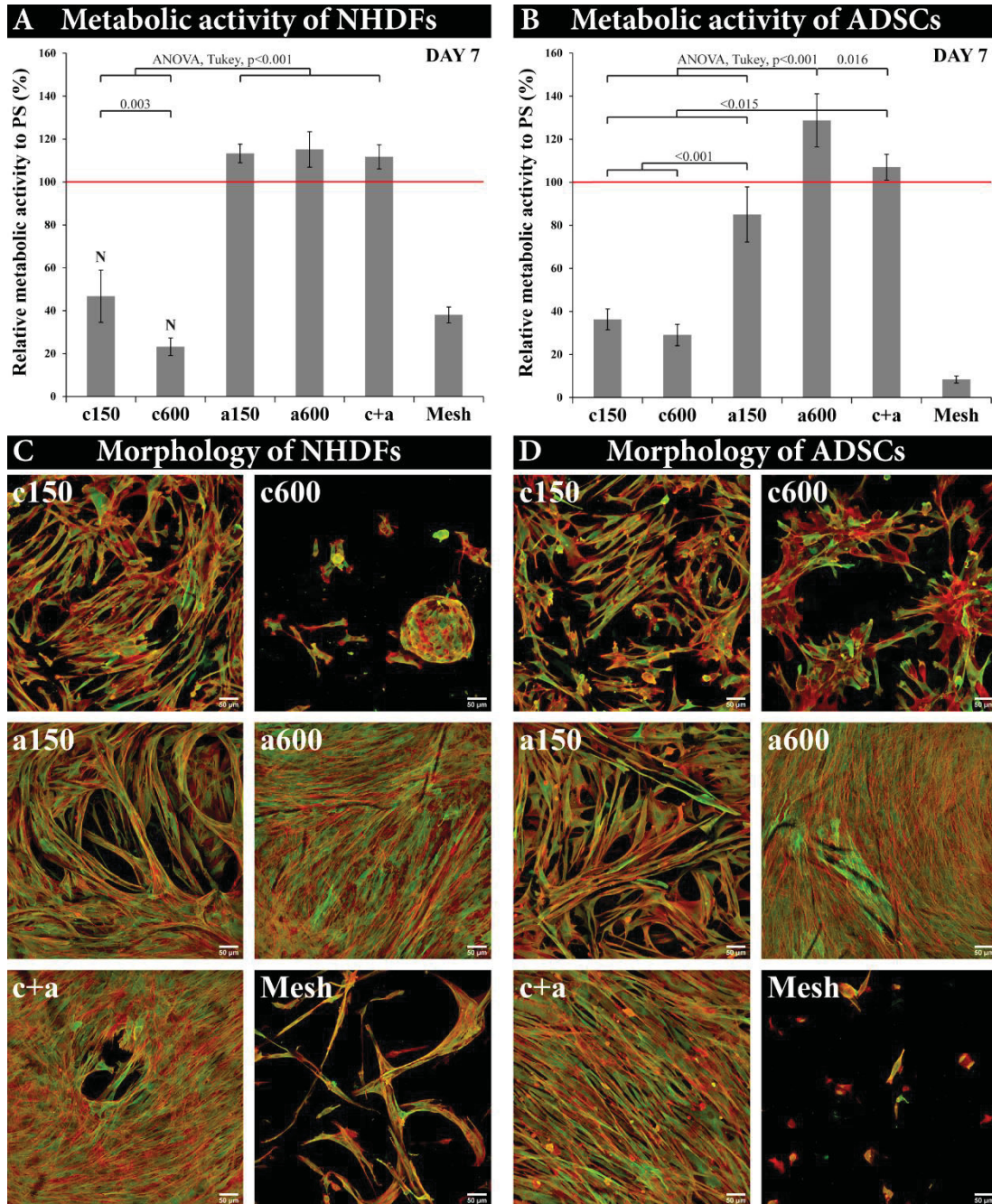**D Morphology of ADSCs**

c150   c600
a150   a600
c+a   Mesh

Figure S5. The metabolic activity (A, B) and the morphology (C, D) of NHDFs and ADSCs on CNF-coated and noncoated meshes on day 3 after cell seeding. (A, B) Metabolic activity of the cells on CNF-coated and noncoated meshes is displayed as a value relative to the metabolic activity of the cells on polystyrene (PS = 100%; red lines). Arithmetic mean ± SD from eight measurements made on four independent samples, ANOVA, Tukey's method, statistical significance (p ≤ 0.05). N, No significant difference in comparison with the noncoated mesh (mesh). (C, D) F-actin in the cell cytoskeleton is stained in red, and vinculin is stained in green. A confocal microscope with an objective magnification 20×. Scale bar = 50 µm.

Figure S6

Figure S6. The metabolic activity (A, B) and the morphology (C, D) of NHDFs and ADSCs on CNF-coated and noncoated meshes on day 7 after cell seeding. (A, B) Metabolic activity of the cells on CNF-coated and noncoated meshes is displayed as a value relative to the metabolic activity of the cells on polystyrene (PS = 100%; red lines). Arithmetic mean ± SD from eight measurements made on four independent samples, ANOVA, Tukey's method, statistical significance (p ≤ 0.05). N, No significant difference in comparison with the noncoated mesh (mesh). (C, D) F-actin in the cell cytoskeleton is stained in red, and vinculin is stained in green. A confocal microscope with an objective magnification 20×. Scale bar = 50 μm.

Video. *Adhesion and spreading of NHDFs (red tracker) and ADSCs (green tracker) in coculture on cCNF-coated glass (phase contrast) during the first 22 h after cell seeding.*

References

(1) Doube, M.; Klosowski, M. M.; Arganda-Carreras, I.; Cordelieres, F. P.; Dougherty, R. P.; Jackson, J. S.; Schmid, B.; Hutchinson, J. R.; Shefelbine, S. J., BoneJ: Free and extensible bone image analysis in ImageJ. *Bone* **2010,** 47, (6), 1076-9.

(2) Schindelin, J.; Arganda-Carreras, I.; Frise, E.; Kaynig, V.; Longair, M.; Pietzsch, T.; Preibisch, S.; Rueden, C.; Saalfeld, S.; Schmid, B.; Tinevez, J. Y.; White, D. J.; Hartenstein, V.; Eliceiri, K.; Tomancak, P.; Cardona, A., Fiji: an open-source platform for biological-image analysis. *Nat. Methods* **2012,** 9, (7), 676-82.

(3) Nečas, D.; Klapetek, P., Gwyddion: an open-source software for SPM data analysis. *Cent. Eur. J. Phys.* **2012,** 10, (1), 181-188.

(4) Caluori, G.; Pribyl, J.; Pesl, M.; Oliver-De La Cruz, J.; Nardone, G.; Skladal, P.; Forte, G., Advanced and Rationalized Atomic Force Microscopy Analysis Unveils Specific Properties of Controlled Cell Mechanics. *Front Physiol* **2018,** 9, 1-11.

(5) Maugis, D., Extension of the Johnson-Kendall-Roberts Theory of the Elastic Contact of Spheres to Large Contact Radii. *Langmuir* **1995,** 11, (2), 679-682.

(6) Hermanowicz, P.; Sarna, M.; Burda, K.; Gabryś, H., AtomicJ: an open source software for analysis of force curves. *Rev. Sci. Instrum.* **2014,** 85, (6), 063703.

materials

MDPI

Fibrin-Modified Cellulose as a Promising Dressing for Accelerated Wound Healing

Marketa Bacakova [1],*, Julia Pajorova [1], Tomas Sopuch [2] and Lucie Bacakova [1]

[1] Department of Biomaterials and Tissue Engineering, Institute of Physiology of the Czech Academy of Sciences, 14220 Prague, Czech Republic; julia.pajorova@fgu.cas.cz (J.P.); lucie.bacakova@fgu.cas.cz (L.B.)

[2] Holzbecher, Ltd.-Bleaching & Dyeing Plant in Zlic, 55203 Zlic, Czech Republic; tomas.sopuch@holzbecher.net

* Correspondence: marketa.bacakova@fgu.cas.cz; Tel.: +420-241-063-765

check for updates

Abstract: Dermal injuries and chronic wounds usually regenerate with scar formation. Successful treatment without scarring might be achieved by pre-seeding a wound dressing with cells. We aimed to prepare a wound dressing fabricated from sodium carboxymethylcellulose (Hcel® NaT), combined with fibrin and seeded with dermal fibroblasts in vitro. We fabricated the Hcel® NaT in a porous and homogeneous form (P form and H form, respectively) differing in structural morphology and in the degree of substitution of hydroxyl groups. Each form of Hcel® NaT was functionalized with two morphologically different fibrin structures to improve cell adhesion and proliferation, estimated by an MTS assay. Fibrin functionalization of the Hcel® NaT strongly enhanced colonization of the material with human dermal fibroblasts. Moreover, the type of fibrin structures influenced the ability of the cells to adhere to the material and proliferate on it. The fibrin mesh filling the void spaces between cellulose fibers better supported cell attachment and subsequent proliferation than the fibrin coating, which only enwrapped individual cellulose fibers. On the fibrin mesh, the cell proliferation activity on day 3 was higher on the H form than on the P form of Hcel® NaT, while on the fibrin coating, the cell proliferation on day 7 was higher on the P form. The Hcel® NaT wound dressing functionalized with fibrin, especially when in the form of a mesh, can accelerate wound healing by supporting fibroblast adhesion and proliferation.

Keywords: fibrin; sodium carboxymethylcellulose; wound dressing; wound healing; dermal fibroblasts; skin

1. Introduction

Cellulose-based materials have been widely applied in clinical practice as a wound dressing for treating acute and chronic wounds (for a review, see [1]). Cellulose is a biopolymer suitable for medical use due to its biocompatibility, non-cytotoxicity, low cost and good availability [2]. Cellulose can be modified into several forms, e.g., regenerated cellulose, oxidized cellulose, acetate cellulose, methylcellulose, hydroxypropylcellulose, carboxymethylcellulose and others, which differ in physicochemical properties [3,4]. Carboxymethylcellulose is prepared by carboxymethylation of any of the three hydroxyl groups in the glucose molecule. The average number of substituted hydroxyl groups is referred to as the degree of substitution. The degree of substitution influences the ability of the material to absorb water and to form a hydrogel. In addition, in the body, the degree of substitution and the molecular weight affect the absorbability of the material. The higher the degree of substitution of the material, the greater the amount of water that the material can absorb, and the longer the time that the water absorption takes [5]. Carboxymethylcellulose, or carboxymethylcellulose in the form of a sodium salt, successfully supports wound healing, prevents infection and promotes homeostasis [5–7].

Although a wide range of tools are available for wound treatment nowadays, scientists are still aiming to achieve faster and less painful healing with better aesthetic outcomes. In clinical practice, carboxymethylcellulose wound dressings are applied only to cover a healing wound, without seeding of the skin cells. However, successful healing is ensured by the cells migrating from the wound edge, producing specific growth factors and synthesizing extracellular matrix (ECM) proteins [8,9]. In the case of deep wounds, the natural healing process can be limited. The result may be a chronic non-healing wound, or extensive scar formation. Pre-seeding the wound dressing with skin cells can contribute to successful healing [10–13]. The colonization of a scaffold with cells depends strongly on the physical and chemical properties of the materials. In their pristine state, many synthetic and natural polymers used as carriers of skin cells fail to provide sufficient support for cell adhesion, growth and ECM deposition [14]. These materials can be combined with biomolecules physiologically present in the natural skin tissue (e.g., collagen, fibronectin), or occurring during wound healing (fibrin), in order to enhance colonization of the material with cells.

Fibrin is a protein resulting from the coagulation cascade. Blood plasma contains fibrinogen, a soluble protein which is converted to insoluble protein fibrin after an injury. This conversion is catalyzed by the enzyme thrombin. Fibrin forms a network in which the blood platelets and immune cells are trapped, and they form a blood clot together [14]. By producing growth factors (mainly platelet-derived growth factor), the platelets stimulate the fibroblasts to migrate into the wound, to proliferate and to form a new ECM composed mainly of collagen I and fibronectin [15,16]. In current clinical practice, fibrin is widely used to support wound healing in the form of a glue, a gel or a sealant seeded by dermal fibroblasts [16]. Promisingly, fibrin can also be used in the form of micro- and nanostructures. Micro- or nanostructured scaffolds mimic better the natural matrix environment for cell life. However, a fibrin scaffold as a self-supporting matrix for cells has weak mechanical strength and a fast rate of degradation. The mechanical stability of a fibrin scaffold can be improved by combining fibrin with other natural or synthetic polymers [17]. In our previous studies, we deposited fibrin on degradable polylactide nanofibers, and we observed improved adhesion and proliferation of dermal fibroblasts and enhanced synthesis of ECM proteins by these cells [18–20].

The aim of this study is to improve a clinically used carboxymethylcellulose wound dressing (Hcel® NaT) by coating with fibrin and pre-seeding with dermal fibroblasts in order to create a cell carrier with potential to deliver skin cells into skin wounds. This novel cell-enriched wound dressing is expected to improve the healing ability of deep wounds.

The Hcel® NaT was prepared in two forms that differed in structural morphology and degree of substitution. We functionalized these materials with fibrin of two different structures. The first fibrin structure, referred to as the fibrin mesh, coated the material fibers and formed a fine mesh among the fibers. The second structure, referred to as the fibrin coating, only coated the cellulose fibers. The purpose of our study was to investigate the effect of Hcel® NaT morphology on cell proliferation and on the preparation of the fibrin structures, and also to evaluate the effect of fibrin and its structures on the adhesion and growth of primary human dermal fibroblasts. We supposed that the properties of Hcel® NaT would influence the formation of the fibrin structures on the material and the behavior of dermal fibroblasts. We further expected an enhancing effect of fibrin functionalization on cell adhesion and proliferation. Moreover, we hypothesized that different morphology of fibrin structures would result in distinct cell behavior.

2. Materials and Methods

2.1. Material Preparation

A nonwoven textile made of sodium carboxymethylcellulose was prepared at the Holzbecher Bleaching & Dyeing Plant in Zlic (Zlic, Czech). This material is a commercially available product known as Hcel® NaT. The highly pure cotton product PurCotton® in a hydroentangled (i.e., spunlaced) textile structure was carboxymethylated and converted to a sodium salt. Two nonwoven textile forms

with different structural morphologies and properties (molecular weight, degree of hydroxyl group substitution (DS) and pH of the aqueous extract) were prepared, namely the P form, containing visible pores, and the homogeneous H form, without visible pores. The textiles were sterilized by 25 kGy of γ-radiation and were packed in sterile Tyvek®-PE packaging (Wipak, Lahti, Finland). The samples were fixed into CellCrowns™ inserts (Scaffdex Ltd., Tampere, Finland) in order to prevent the sample floating in the cell culture medium during cell cultivation.

2.2. Characterization of the Properties of Hcel® NaT

The molecular weight of the P and H forms of Hcel® NaT was determined by size exclusion chromatography (SEC). Sodium carboxymethylcellulose separation was performed in an asymmetric-flow AF4 system (Eclipse AF4, Wyatt Technology, Santa Barbara, CA, USA), using Long Channel (LC, 275 mm), a 350-μm spacer, and a 30 kg.mol^{-1} Regenerated Cellulose (RC) semipermeable membrane. The online concentration was detected by an RI detector (Optiplab T-rEX, Wyatt Technology, Santa Barbara, CA, USA). Angular dependent light scattering was detected by the MALS instrument (Dawn Heleos II, Wyatt Technology, Santa Barbara, CA, USA). The molar mass, the RMS radius (Rg) and other operations were calculated from the scattering and concentration data with the use of Astra software (version 6.1, Wyatt Technology, Santa Barbara, CA, USA). Berry formalism was used for the molar mass and RMS radius calculations. 100 μL of 3g/L sodium carboxymethylcellulose in 100 mmol/L NaCl was injected per single AF4 run. Dn/dc = 0.159 was used, in accordance with Melander and Vuorinen [21].

The degree of substitution was determined by titration of the sodium carboxymethylcellulose solution with an NaOH solution to pH change, in accordance with the European Pharmacopoeia and the American Pharmacopoeia.

To determine the pH of aqueous extracts of two forms of Hcel® NaT, 1 g of the material was shaken in 100 mL of deionized water for 5 min. Then the pH of the Hcel® NaT extract was measured.

The morphology of the P and H forms of Hcel® NaT was studied by scanning electron microscopy (SEM). The Hcel® NaT fibers were sputter-coated with gold in argon background gas. Images were captured by a Quanta 450 scanning electron microscope (SEM) (FEI, Hillsboro, OR, USA) in a high vacuum (10^{-4} Pa). Detection was mediated by an Everhart-Thornley detector in secondary electrons mode in an accelerating voltage of 30 kV. The fiber width and the fiber thickness, and also the size of the void spaces among the fibers, were measured on SEM images of Hcel® NaT of the P form and the H form in the ImageJ Fiji program. The fiber width and thickness data were presented as the arithmetic mean ±standard deviation (S.D.) in μm. The area of the void spaces among the fibers was expressed as the range from the minimum value to the maximum value in μm^2. The data were calculated from 24 measurements per SEM image of the P form or H form.

2.3. Hcel® NaT Functionalization with Fibrin

Two different structures of fibrin modifications (fibrin mesh and fibrin coating) were prepared in this study. The fibrin mesh formed a coating around the cellulose fibers, and additionally a fine mesh among the cellulose fibers. The fibrin coating covered only the cellulose fibers. The principle for preparing the fibrin structures is based on the physiological process of hemocoagulation, when soluble fibrinogen is converted by thrombin to insoluble fibrin [22]. The two fibrin structures, fibrin coating and fibrin mesh, were prepared in accordance with our previously published work [20]. Fibrinogen (EMD Millipore, Billerica, MA, USA, Cat. No. 341576) was dissolved in a Tris Buffer (consisting of 50 mM Tris-HCl, 100 nM NaCl and 2.5 mM CaCl$_2$) to a final concentration of 10 μg/mL and it was left for 1 h to adsorb on the Hcel® NaT fibers. The Hcel® NaT was rinsed with Tris Buffer. Then thrombin (Sigma-Aldrich Co, St Louis, MO, USA, Cat. No. T6884) with a final concentration of 2.5 U/mL in Tris Buffer was added for 15 min. In the case of the fibrin coating, the samples were rinsed properly in Tris Buffer for 30 min. After rinsing, a solution of 200 μg/mL of fibrinogen in Tris Buffer and 0.5 U/mL of antithrombin III (Chromogenix, Milano, Italy) in deionized water was added to the Hcel® NaT

fibers for 1 h. In the case of the fibrin mesh, the solution of fibrinogen and antithrombin III was added to the samples immediately after thrombin catalysis, without the rinsing step in Tris Buffer. Finally, the samples were rinsed with Tris Buffer and with phosphate-buffered saline (PBS, Sigma-Aldrich Co., St. Louis, MO, USA).

2.4. Cell Culture Conditions

The Hcel® NaT samples were seeded with neonatal human dermal fibroblasts (Lonza Group, Basel, Switzerland, Cat. No. CC-2509) in passage 3–5 at a concentration of 15,000 cells/cm^2. The cells were cultured in 1.5 mL of Dulbecco's Modified Eagle's Medium (DMEM; Sigma-Aldrich, USA), supplemented with 10% of fetal bovine serum (FBS; Sebak, Aidenbach, Germany) and 40 μg/mL of gentamicin (LEK, Ljubljana, Slovenia). The cultivation was performed at 37 °C in an air atmosphere with 5% of CO$_2$ and 90% humidity for 3 or 7 days.

2.5. Hcel® NaT Cytotoxicity

The potential cytotoxicity of the Hcel® NaT was tested by evaluating the growth of human dermal fibroblasts in extracts from the tested materials, using the xCELLigence® real-time cell proliferation monitoring system (Roche, Switzerland). The extracts of Hcel® NaT were prepared by sample incubation in DMEM without FBS and without seeded cells at 37 °C in an air atmosphere with 5% of CO$_2$ and 90% humidity for 7 days. Effective extraction was achieved with the use of an SSM1 Mini Orbital Shaker (Stuart; speed 45 rpm). The cells at a concentration of 3000 cells/well in DMEM with 10% of FBS were seeded in a 10 μL suspension into a 96-well E-plate View (ACEA Biosciences, San Diego, USA). After the background impedance had been measured, 180 μL of the sample extract with 10% of FBS was added to the seeded cells. The cell proliferation was measured as the electrical impedance for 168 h with 8-h intervals.

The pure culture medium was used as a control. The real-time proliferation measurement was performed under the same conditions as for cultivation of the cell on Hcel® NaT. The arithmetic mean ± S.D. was determined from four parallel samples for each type of material and time point.

2.6. Morphology of the Fibrin Structures

The morphology of the fibrin mesh and the fibrin coating was observed on freshly prepared samples, and on day 3 and 7 after cell seeding. The fibrin structures were treated with 1% albumin in 0.1% Triton X-100 (Sigma-Aldrich Co., USA) for 15 min, and then with 1% Tween (Sigma-Aldrich Co., USA) for 15 min to block non-specific binding sites. After being rinsed twice with PBS, the fibrin was immunolabeled with primary polyclonal rabbit antibody against fibrinogen (Dako Denmark A/S, Glostrup, Denmark) diluted in PBS in a ratio of 1:200 for 1 h at 37 °C. Then the samples were rinsed twice with PBS and were incubated with a secondary antibody, i.e., goat anti-rabbit F(ab′)2 fragments of IgG (H + L) conjugated with Alexa Fluor® 488 (Molecular Probes, Eugene, OR, USA), diluted in PBS in a ratio of 1:400, for 1 h in the dark. After rinsing with PBS, images of the morphology fibrin structures were taken under a Leica TCS SPE DM2500 confocal microscope (Leica Microsystems, Wetzlar, Germany; obj. 20×/0.70 NA oil, 40×/1.15 NA oil).

2.7. Cell Adhesion and Proliferation

We evaluated the cell attachment, spreading and proliferation by visualizing the cells on days 3 and 7 after seeding. The cells were fixed with 4% paraformaldehyde for 10 min. After fixation, the cell membrane was permeabilized with 0.1% Triton X-100 (Sigma-Aldrich Co., USA) and 1% Tween (Sigma-Aldrich Co., USA). Then the F-actin cytoskeleton was stained with phalloidin conjugated with TRITC fluorescent dye (Sigma-Aldrich Co., USA; diluted in PBS, 5 μg/mL) and the cell nuclei were stained with DAPI (Sigma-Aldrich Co., USA; diluted in PBS, 1 μg/mL), for 1 h in the dark.

The cell pictures were taken under a Leica TCS SPE DM2500 confocal microscope (Leica Microsystems, Germany; obj. 20×/0.70 NA oil, 40×/1.15 NA oil).

The cell proliferation was also evaluated by the CellTiter 96® AQueous One Solution Cell Proliferation Assay (MTS, Promega Corporation, Madison, WI, USA) on days 3 and 7 after cell seeding. The samples were rinsed with PBS and were moved into fresh cell culture wells in order to avoid the influence of the cells adhered to the bottom of the wells. The assay was performed according to the manufacturer's protocol. The formazan dye produced by the cells after 2 h of incubation was quantified by measuring the absorbance using a VersaMax ELISA Microplate Reader spectrophotometer (Molecular Devices Corporation, Sunnyvale, CA, USA). The absorbance was measured with wavelength 490 nm. The measured quantitative data were presented as the arithmetic mean ±S.D. of three independent samples for each experimental group and time interval. The statistical significance was evaluated using the analysis of variance (One Way ANOVA–Tukey method). Values of $p \leq 0.05$ were considered as significant.

3. Results

3.1. Structural Morphology and Chemical Characterization and of Pristine Hcel® NaT

Both forms of Hcel® NaT (P and H forms) had a fibrous morphology with fiber diameter in the microscale. The fiber diameter was characterized by fiber width and thickness (Table 1). The average fiber width was 18 μm, and the average fiber thickness was approximately 6 μm for both forms of Hcel® NaT. The area of the void spaces among the fibers varied approximately from 100 to 8000 μm² (Table 1).

Table 1. Morphological parameters of the P and H forms of Hcel® NaT.

Form of Hcel® NaT	Mean Fiber Width ± S.D. (μm)	Mean Fiber Thickness ± S.D. (μm)	Range of Area of Void Spaces (μm²)
P form	18.1 ± 3.6	5.7 ± 1.7	104–3390
H form	18.0 ± 2.0	6.1 ± 1.3	86–8732

The two prepared forms of Hcel® NaT differed in molecular weight, in the degree of hydroxyl group substitution by carboxymethyl group, and in the pH of their aqueous extracts, as shown in Table 2.

Table 2. Chemical characterization of the P and H forms of Hcel® NaT.

Form of Hcel® NaT	Molecular Weight (kDa)	Degree of Substitution	pH of an Aqueous Extract
P form	262	0.120	8.60
H form	251	0.194	7.07

Moreover, the forms of Hcel® NaT differed in their structural morphology. The P form had visible pores, and the fibers were randomly assembled in a grid shape, whereas the H form had fibers homogeneously distributed over the entire surface (Figure 1).
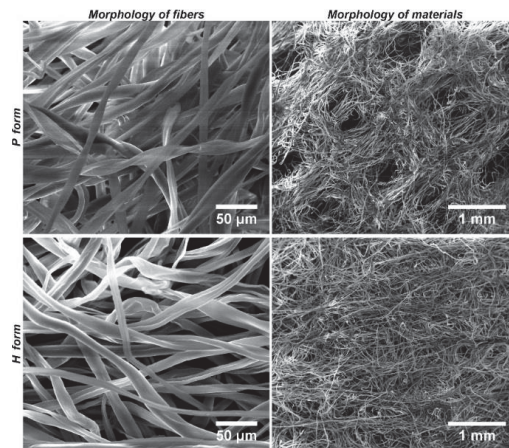
Figure 1. Morphology of the P form and the H form of Hcel® NaT. Quanta 450 scanning electron microscope, original magnification 1000×, scale bar 50 μm; 70×, scale bar 1 mm.

3.2. Morphology of the Fibrin Structures

The P and H forms of the Hcel® NaT were modified with two different fibrin structures (fibrin mesh and fibrin coating). The fibrin mesh coated the material fibers, and in addition it formed a homogeneous fine mesh of nanofibers lying on the membrane fibers and spreading among them. The fibrin nanofibrous mesh homogenously filled the void spaces between membrane fibers which reduced the pore size. The fibrin coating just covered the surface of individual membrane fibers with fibrin nanofibers and did not significantly affect the area of void spaces between fibers of the membrane (Figure 2). In our previous studies performed on nanofibrous polylactide meshes, we found that the fibrin structure was stable for 7 days under cell culture conditions without cells, whereas the fibrin was gradually degraded on the membrane with cells [18,20].
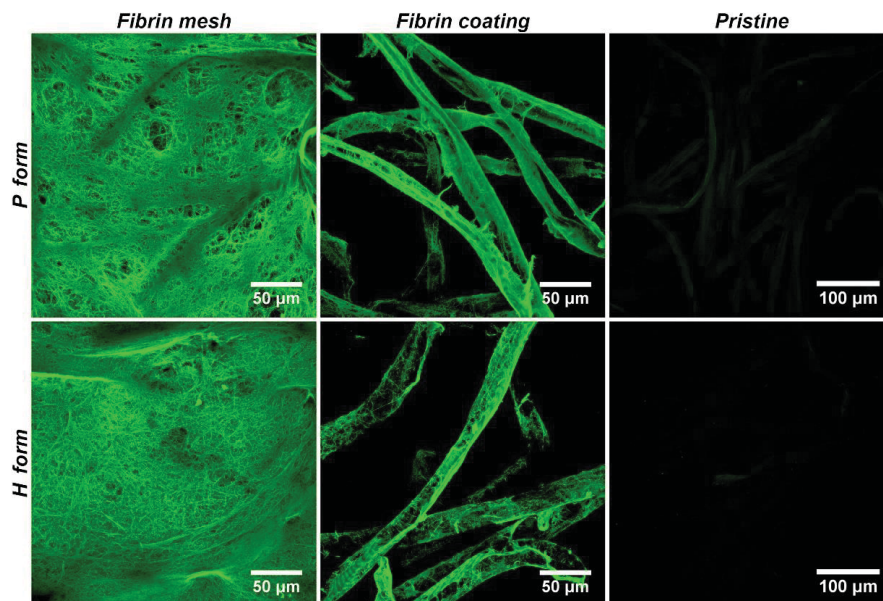
Figure 2. Morphology of the P form and the H form of Hcel® NaT modified with a fibrin mesh or a fibrin coating. The pristine Hcel® NaT of P form and H form were used to show non-specific binding of the antibodies. The fibrin was stained with a primary polyclonal rabbit antibody against fibrinogen and with a secondary antibody conjugated with Alexa 488 (green fluorescence). Leica TCS SPE DM 2500 confocal microscope, magnification 40×/1.15 NA oil or magnification 20×/0.70 NA oil.

3.3. Cell Adhesion and Proliferation on the Pristine Hcel® NaT

The proliferation of human dermal fibroblasts was estimated by measuring the activity of cell mitochondrial enzymes (determined by an MTS assay). The cells did not adhere and proliferate well on either form of the pristine Hcel® NaT. The cell proliferation was significantly lower on both forms of Hcel® NaT on days 3 and 7 after cell seeding than on the bottoms of the control polystyrene culture wells, and this difference increased with the time of cell cultivation. We also observed slightly better cell adhesion and proliferation on the P form than on the H form, with statistical significance on day 7 (Figure 3).
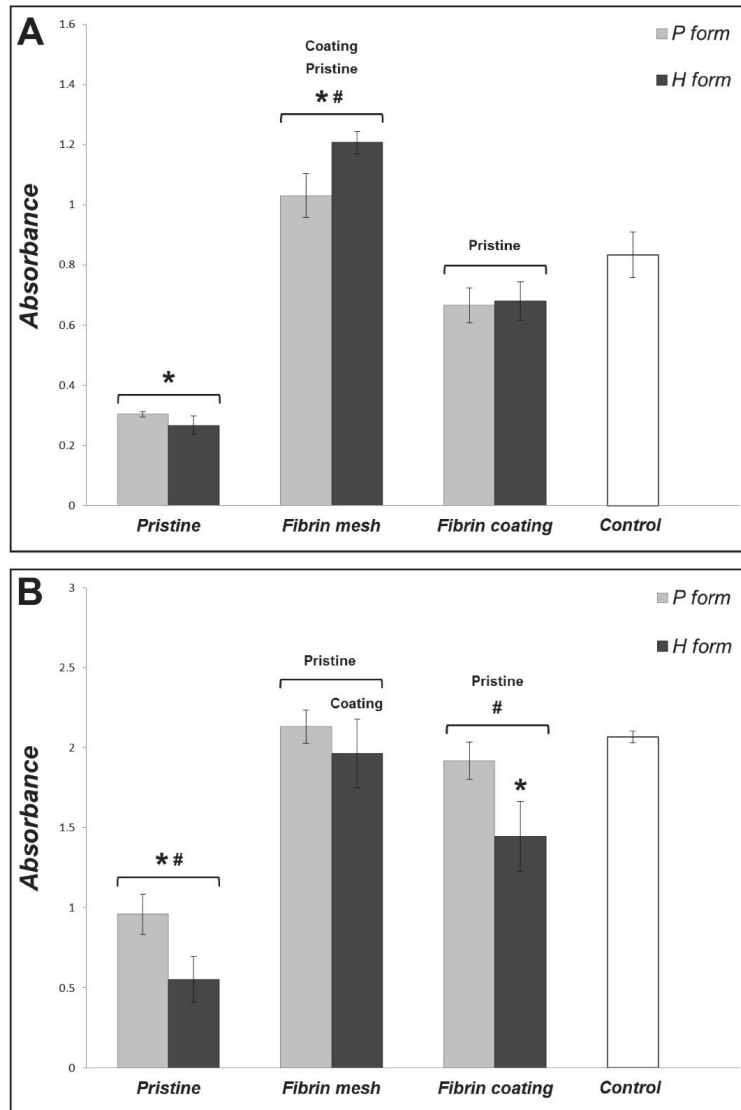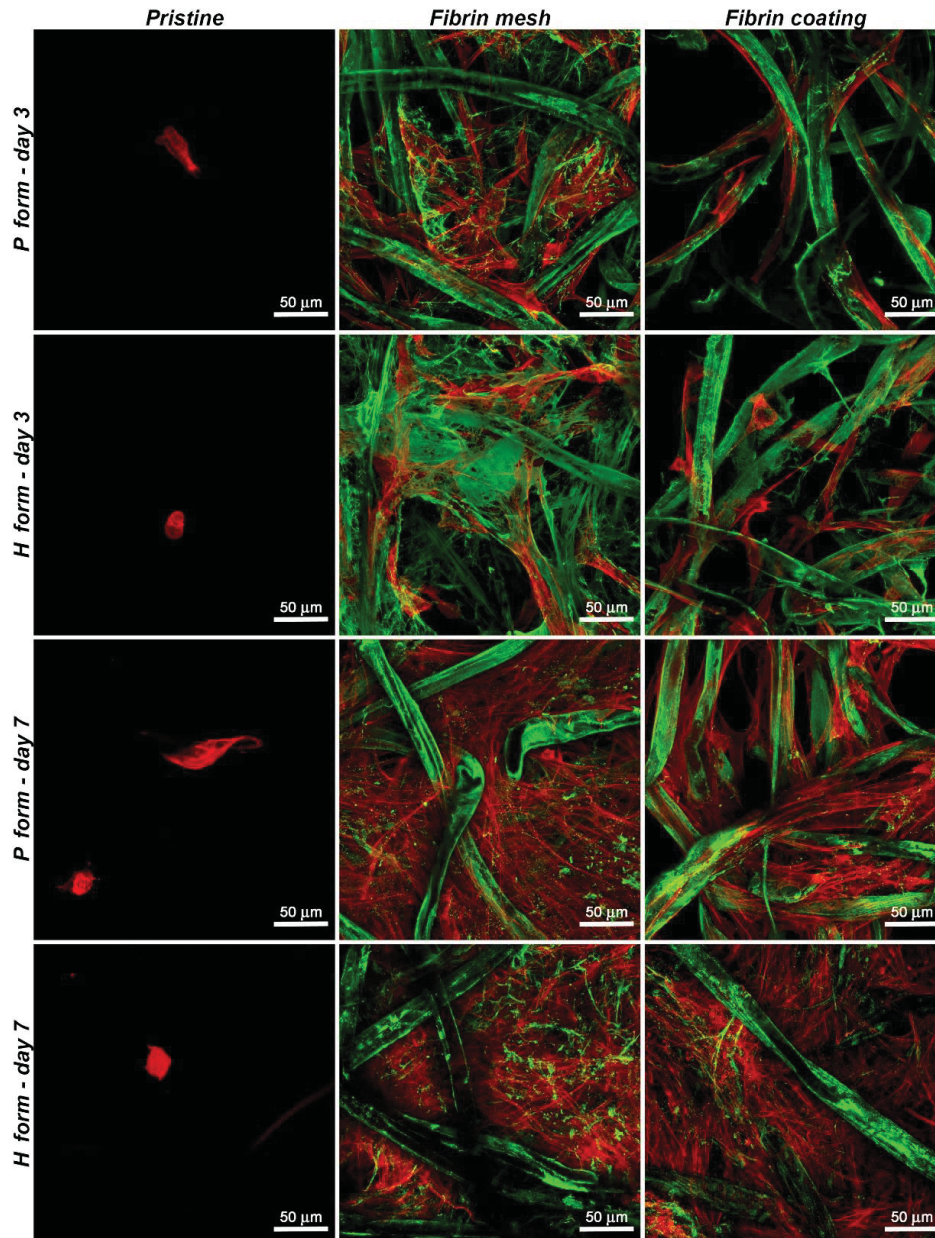

Figure 3. Mitochondrial activity of human dermal fibroblasts on the P form and the H form of Hcel® NaT in pristine state and modified with a fibrin mesh or a fibrin coating, and on the bottoms of the control polystyrene culture wells on day 3 (A) and on day 7 (B) after cell seeding. The absorbance was calculated as the arithmetic mean ± S.D. from three independent samples for each experimental group and time interval. ANOVA, Tukey method, statistical significance ($p \leq 0.05$) above the column on or under the line: * compared with the control polystyrene, # between the P form and the H form, Pristine or Coating compared with Pristine or Fibrin mesh Hcel® NaT. The labels of statistical significance on the line are for both columns, the labels under the line are for a specific column.

Fluorescence microscopy confirmed the data obtained by the MTS assay. We observed only a small number of adhered cells on both forms of pristine Hcel® NaT. The cells on the P form seemed to be elongated on the fibers. However, the cells on the H form were mostly of rounded shape, which indicates poor cell adhesion. The number of cells increased slightly on the P form on day 7 compared to day 3. However, the number of cells on the control polystyrene was much higher. On the H form, on day 7, the cells still had a rounded shape and the cell density remained similar as on day 3 (Figure 4, 1st column Pristine).

Figure 4. Morphology of human dermal fibroblasts on the P form and on the H form of Hcel® NaT, in pristine state and modified with a fibrin mesh or a fibrin coating on day 3 or day 7 after cell seeding. The fibrin was stained with the primary and secondary antibodies mentioned above (Alexa 488, green), and the F-actin cytoskeleton was stained with phalloidin-TRITC (red). Leica TCS SPE DM 2500 confocal microscope, magnification 40×/1.15 NA oil.

3.4. Cytotoxicity of Hcel® NaT

The poor cell adhesion and proliferation on the pristine Hcel® NaT may have been caused by a release of cytotoxic elements from the material. To determine the potential cytotoxic effect of the material, we cultured cells in the extracts from the material samples using the real-time xCELLigence® monitoring system. The cells proliferated in the material extracts similarly as in the control pure culture medium. The cell density increased with cultivation time, as indicated by the increasing Cell Index values (Figure 5).
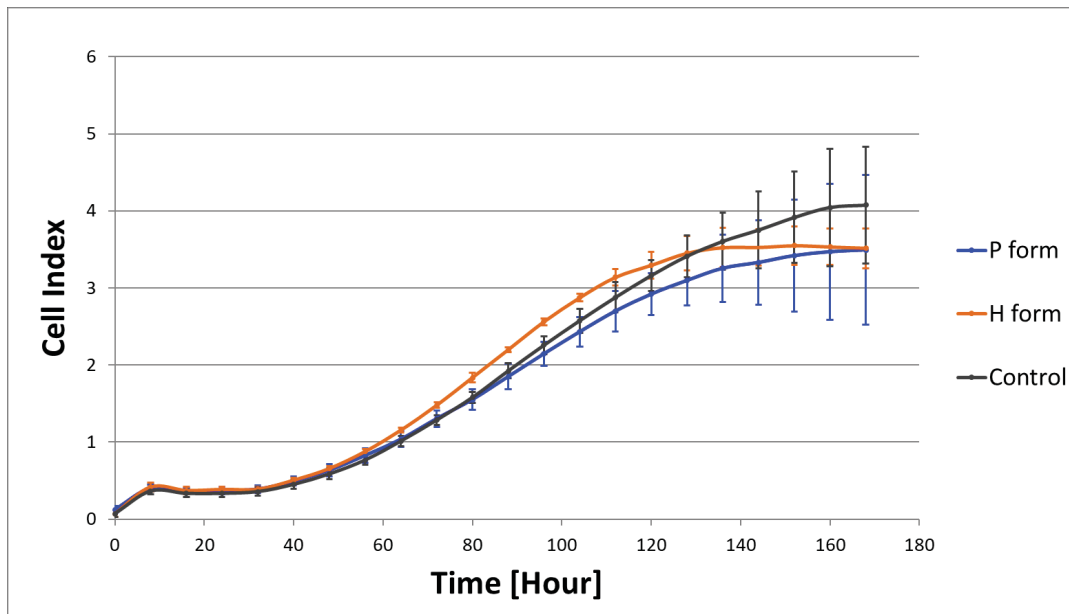
Figure 5. Proliferation of human dermal fibroblasts indicated by the Cell Index in extracts from the P form and the H form of Hcel® NaT, and in the control culture DMEM medium. Measured by the real-time xCELLigence® monitoring system for 168 h with 8-h intervals. Arithmetic mean ±S.D. from four independent samples for each type of material.

3.5. Cell Adhesion and Proliferation on Fibrin-Modified Hcel® NaT

We suggested that the material properties might be improved by modifying them with fibrin of two different structures (fibrin mesh and fibrin coating). The cells grew well on both fibrin structures, and their proliferation, estimated by the cell mitochondrial activity, was significantly higher than on the pristine material in all time intervals. A comparison of the cell behavior on the two different fibrin structures showed that there was higher cell proliferation on the fibrin mesh than on the fibrin coating, mainly on day 3 after seeding (Figure 3). Moreover, the cell proliferation differed slightly on the P and H forms of Hcel® NaT modified with a fibrin mesh or a fibrin coating. Regarding the fibrin mesh structure, we observed significantly higher cell proliferation on the H form than on the P form on day 3. However, on day 7, the cell proliferation on the fibrin mesh tended to be higher on the P form. The fibrin coating significantly increased the cell proliferation on the P form on day 7.

The fluorescence microscopy images (Figure 4) showed that the cells adhered much better to both forms of Hcel® NaT modified with fibrin structures, either the fibrin mesh or the fibrin coating, than on the unmodified materials. The cells were spread through the fibrin mesh covering and interconnecting the cellulose fibers, and tended to be polygonal in shape. By contrast, on the fibrin coating, the cells copied the cellulose fibers and remained in a spindle-like morphology. The number of adhered cells increased with the cultivation time, and the cells achieved a confluent layer on both forms of Hcel® NaT modified with fibrin structures on day 7. The cells progressively degraded and reorganized the fibrin mesh and the fibrin coating during their cultivation. After 7 days of cell cultivation, the thin

homogeneous mesh lying on the fibers and spreading between them was almost completely degraded, whereas the cellulose fibers remained coated with fibrin.

4. Discussion

Cellulose and other polysacharide materials are clinically applied to support wound healing by covering the wound, and also to release drugs and other bioactive molecules into wounds. For example, Tamer et al. (2018) prepared membranes composed of chitosan and high-molar-mass hyaluronan loaded with a gradually releasing mitochondrially targeted antioxidant–Mito Q. The addition of Mito Q antioxidant had beneficial effect on the healing process of injured rabbit and rat skin in vivo, which was due to a suppression of inflammation process caused by reactive oxygen species produced by mitochondria during insufficient oxygen uptake [23]. The application of cellulose as a direct skin tissue substitute with adhered skin cells is still relatively rare. The reason is that this application requires degradability of the cellulose-based material, or spontaneous removal of the material from the wound, in order to prevent inflammation or scar formation. Cellulose can be rendered degradable e.g., by chemical modification or by combining it with other scaffold components. For example, biodegradability has been achieved in a hydroxyethyl cellulose/poly (vinyl alcohol) blend in the form of electrospun fibrous membranes [24], in a cellulose film regenerated from *Styela clava* tunics [25], and in enzyme-digestible cellulose membranes [12]. Another option is to use non-degradable carriers, which can be self-detached from the wound after cell adhesion on the wound bed. These carriers include e.g., a polyurethane wound dressing known as HydroDerm [10], a porous dressing made of a copolymer of hydrophilic polyethylene glycol terephthalate soft segments and polybutylene terephthalate hard segments [11], electrospun mats consisting of polycaprolactone (PCL) and polyvinyl alcohol (PVA) [26], and a composite hydrogel consisting of bacterial cellulose and acrylic acid [13]. The carboxymethylcellulose scaffolds developed in our study are further potential non-degradable carriers for cell delivery into damaged skin sites.

Cellulose in its pristine state does not normally allow sufficient colonization of the material by cells, due to its inappropriate physicochemical properties. The properties of the cellulose-based scaffold can be tailored by a variety of modifications, including functionalization with specific chemical groups (e.g., –COOH), bioactive molecules (ECM proteins, growth factors, healing agents) and chemical groups, by combination with other synthetic or natural materials, by creating a nanostructured surface, by mineralization etc. [1,27].

In our study, we prepared a sodium carboxymethylcellulose scaffold (Hcel® NaT) and we functionalized it with fibrin, a provisional ECM molecule, in order to increase its attractiveness for colonization with skin cells, and thus to stimulate better wound healing. We carried out experiments on two forms of Hcel® NaT with different structural morphologies and chemical properties. The P form formed visible pores in its structure which can allow better gas and nutrient exchange during wound healing. This is one of the requirements for wound dressings that will support sufficient wound healing [28]. On the other hand, there is a potential risk of drying of the wound through the pores. Moreover, healing can take place non-homogeneously. This phenomenon was observed when the Biobrane porous wound dressing was used [29]. By contrast, the homogeneous H form can have a greater surface for potential adsorption of remedial substances, e.g., growth factors, antimicrobial agents, drugs, vitamins, hyaluronan, or fibrin [30–32].

The human dermal fibroblasts cultivated on our pristine Hcel® NaT membrane showed low ability to adhere, spread and proliferate. However, the cultivation of cells in the material extracts did not confirm a cytotoxic effect of the material on the cells. For this reason, we attributed the poor cell adhesion and growth to inappropriate material surface properties. Both forms of Hcel® NaT had an average fiber width and thickness in the microscale. Microscale surface roughness is often inappropriate for cell adhesion and spreading. The size of the irregularities (the Hcel® NaT fibers) is similar to the spreading area of the cells. As a result, the cells cannot adhere to the material by whole their spreading area and they try to bridge the irregularities or squeeze between them [33]. Moreover,

the area of void spaces among the fibers was from hundreds to thousands of square micrometers. The non-adhered round cells were about 15 μm in diameter, so it was possible for cells to fall through the void spaces in the material to the bottom of a culture well.

　　The poor cell adhesion on both pristine forms of Hcel® NaT could also be due to the excessively soft surface properties of the material fibers. As Hopp et al. [34] showed, fibroblasts prefer a stiffer surface to a softer surface. The Hcel® NaT fibers tended to form a gel structure in the cell culture medium when the liquid was absorbed into the material. A soft gelling material surface may collapse under the traction forces generated by the adhering cells [35]. It was mentioned above that the degree of substitution of cellulose hydroxyl groups influences the water absorption into the material, resulting in gelling and dissolution of the material [5]. A higher degree of substitution of the H form led to more apparent gelling of the surface of the material fibers. In other words, the H form formed a softer and more collapsible structure than the P form. The cells therefore adhered and grew better on the P form than on the H form. This was manifested by the greater cell density on the P form in all time intervals.

　　We functionalized the Hcel® NaT with two fibrin structures of different morphologies (a fibrin mesh or a fibrin coating) to enhance the attractiveness of the material for the adhesion and proliferation of the cells. The interactions between Hcel® NaT and fibrin are based on the general principle of chemical bonds formation between reactive chemical groups of fibrinogen and carboxymethylcellulose. The fibrinogen is physically adsorbed on the carboxymethylcellulose through non-covalent strong physical interactions. These interactions involve ionic bonds between carboxyl groups of Hcel® NaT and amino groups of fibrinogen, hydrogen bonds between hydroxyl groups of Hcel® NaT and polypeptide backbone of fibrinogen, and hydrophobic interactions between non-polar parts of Hcel® NaT (methyl groups) and non-polar amino acids in fibrinogen molecules. Both types of modifications with fibrin formed a network of fibrin nanofibers and thus altered the material surface roughness from microstructure to nanostructure that is considered as more favorable for cell adhesion and growth. The fibrin mesh formed a homogeneous thin nanostructure lying on the material surface and filling the void spaces among the cellulose fibers, whereas the fibrin coating only covered the cellulose fibers with fibrin nanofibers. The different morphologies of these two fibrin structures on Hcel® NaT were caused by the different preparation methods, as described in our previous study [20]. The fibrin mesh was prepared without washing out the thrombin, while the preparation of the fibrin coating included a step in which the unbound thrombin with Tris Buffer was washed out. The activity and the concentration of thrombin bound to fibrinogen are crucial for the formation of the final fibrin network. Higher concentration of thrombin (above 1U/mL) induces the formation of thin fibrin fibers [36]. In our case, the high concentration of thrombin on the surface of the material enabled the formation of a homogeneous nanofibrous fibrin mesh. In addition, the desirable morphology, thickness and density of fibrin nanostructure can be also tuned by the concentration of fibrinogen and antithrombin III in the solution and by polymerization time [37]. In our study, we applied a solution of high concentrated fibrinogen (200 μg/mL) and antithrombin III of (0.5 U/mL) for 60 min. Under these conditions, we prepared well developed mesh of fibrin nanofibers. Similar results were obtained Riedelova-Reicheltova et al. on a glass surface [37].

　　Both fibrin structures greatly improved the cell adhesion and the subsequent proliferation. The number of adhered cells increased in time, and the cells reached an almost confluent layer on the 7th day of cultivation. As was mentioned above, fibroblasts can bind to fibrin via integrin and non-integrin adhesion receptors, which support fibroblast proliferation and growth factor secretion [15,38]. In our earlier studies, we observed a positive influence of fibrin modification of a nanofibrous polyester membrane on adhesion, proliferation and ECM protein synthesis in the case of dermal fibroblasts. The proliferating cells gradually degraded and reorganized the fibrin, and replaced it by their own ECM, mainly by collagen I and fibronectin, during cultivation [18,19].

　　Our results also revealed that the structure of the fibrin played an important role in cell adhesion and growth. Our previous study performed on polylactide nanofibrous membranes revealed that the fibrin mesh enhanced the cell adhesion, proliferation and synthesis of ECM proteins better than the

fibrin coating [20]. In this study, the Hcel® NaT modified with the fibrin mesh also provided better support for the attachment, proliferation and migration of cells than the fibrin coating. The fibrin mesh homogeneously distributed among the cellulose fibers decreased the area of void spaces between membrane fibers (pore size) and thus prevented the cells falling through the void spaces in the material on the bottom of the culture well. For this reason, there was a higher initial number of cells adhering to the material with the fibrin mesh than on the material modified with a fibrin coating. The overall surface for cell adhesion was also larger than in the case of the fibrin coating. In addition, the fine fibrin mesh formed a continuous nanoscale structure [39]. It is generally accepted that nanostructured materials better mimic the natural cell environment of the ECM, and cell propagation is more successful on these biomimetic scaffolds [39]. In addition, nanostructured materials promote the adsorption of cell adhesion-mediating molecules in an almost physiological spatial conformation, which enables binding between specific amino acid sequences in these molecules, e.g., RGD, and cell adhesion receptors, e.g., integrins [40,41]. In addition, fibroblasts were capable of remodeling a nanofibrous fibrin mesh, which facilitated fibroblast migration and proliferation, and synthesis of ECM [42].

Although the different properties of the P and H forms of Hcel® NaT did not apparently affect the formation of fibrin structures, the cell proliferation differed slightly on these two forms modified with fibrin structures. Whereas in an earlier cell cultivation interval (on day 3) the cells proliferated better on the fibrin-modified H form (in the case of the fibrin mesh), in a later cultivation interval (on day 7), the cell proliferation was higher on the P form (particularly on the fibrin coating). It can be supposed that the H form without visible pores enables the formation of a more homogenous fibrin mesh among cellulose fibers and ensures better support for the cells than the P form in earlier cultivation intervals. However, during cell cultivation, we observed gradual degradation and remodeling of the fibrin structures. After 7 days, the fibrin, mainly the fibrin mesh, was almost degraded, and the Hcel® NaT properties started to have a predominant influence on the cell behavior. As has been discussed above, the H form had less appropriate properties for cell adhesion, due to its greater tendency to form a gel structure. For this reason, in later cell cultivation intervals, the cell tended to proliferate better on the fibrin-modified P form, which has more favorable properties for cell living compared to the H form.

Our newly developed carboxymethylcellulose scaffolds coated with fibrin could be used as carriers for transferring skin cells into skin wounds. The fibrin coating would increase the cell adhesion and proliferation, and this would result in a considerably higher number of cells delivered into the wounds. Low efficiency of cell delivery was a problem with HydroDerm polyurethane wound dressings, where the keratinocytes grew at approximately 15% of the rate observed in cells cultivated on the tissue culture plastic [10]. Similarly, in polycaprolactone/polyvinyl alcohol electrospun scaffolds, the attachment, viability and proliferation of human fibroblasts was markedly improved by coating the scaffolds with fibronectin, especially when the scaffolds were loaded with an antimicrobial silver sulfadiazine agent [26].

After degradation of the fibrin coating by the cells, our cellulose scaffolds would become less attractive than the wound bed for cell adhesion, and therefore a spontaneous release and migration of cells from these scaffolds could be expected. The scaffolds could then be freely removed from the wound. In other words, our fibrin-modified cellulose-based scaffolds could serve as temporary carriers for in vitro expansion and subsequent delivery of cells into skin wounds. A similar phenomenon was observed in human keratinocytes cultured on poly(2-hydroxyethyl methacrylate) sheets, which were applied clinically in the treatment of severe burns [43].

5. Conclusions

In this study, we have compared the behavior of human dermal fibroblasts in cultures on a porous (P) form and a homogeneous (H) form of carboxymethylcellulose wound dressings (Hcel® NaT), which differed in structural morphology and physicochemical properties. Both forms of pristine Hcel® NaT showed low ability to support cell adhesion and proliferation, probably due to inappropriate physicochemical properties and inappropriate morphology of the material surface.

The cell proliferation was slightly increased on the P form of Hcel® NaT. However, the results showed that the cell adhesion and proliferation were greatly improved by modification of Hcel® NaT by fibrin in the form of a mesh and in the form of a coating. Both fibrin structures enhanced the colonization of our wound dressing with the cells. Moreover, the fibrin mesh, resembling the natural ECM, provided better support than the fibrin coating for the adhesion and proliferation of the cells. The Hcel® NaT wound dressing functionalized with fibrin, especially in the form of a mesh filling the void spaces among the cellulose fibers, is a promising tool for faster wound healing with better aesthetic outcomes. Fibrin ensures good cell adhesion and spreading, and can support the migration and the subsequent proliferation of cells in a wound.

References

1. Bacakova, L.; Novotna, K.; Sopuch, T.; Havelka, P. Cell interaction with cellulose-based scaffolds for tissue engineering—A review. In *Cellulose and Cellulose Composites: Modification, Characterization and Applications*; Mondal, I.H., Ed.; Nova Science Publishers, Inc.: New York, NY, USA, 2015; pp. 341–375. ISBN 978-1634835534.

2. Kalia, S.; Dufresne, A.; Cherian, B.M.; Kaith, B.S.; Averous, L.; Njuguna, J.; Nassiopoulos, E. Cellulose-Based Bio- and Nanocomposites: A Review. *Int. J. Polym. Sci.* **2011**, *2011*, 837875. [CrossRef]

3. Klemm, D.; Heublein, B.; Fink, H.P.; Bohn, A. Cellulose: Fascinating biopolymer and sustainable raw material. *Angew. Chem. Int. Ed.* **2005**, *44*, 3358–3393. [CrossRef] [PubMed]

4. Coseri, S. Cellulose: To depolymerize... or not to? *Biotechnol. Adv.* **2017**, *35*, 251–266. [CrossRef] [PubMed]

5. Ohta, S.; Nishiyama, T.; Sakoda, M.; Machioka, K.; Fuke, M.; Ichimura, S.; Inagaki, F.; Shimizu, A.; Hasegawa, K.; Kokudo, N.; et al. Development of carboxymethyl cellulose nonwoven sheet as a novel hemostatic agent. *J. Biosci. Bioeng.* **2015**, *119*, 718–723. [CrossRef] [PubMed]

6. Ramli, N.A.; Wong, T.W. Sodium carboxymethylcellulose scaffolds and their physicochemical effects on partial thickness wound healing. *Int. J. Pharm.* **2011**, *403*, 73–82. [CrossRef] [PubMed]

7. Wong, T.W.; Ramli, N.A. Carboxymethylcellulose film for bacterial wound infection control and healing. *Carbohydr. Polym.* **2014**, *112*, 367–375. [CrossRef] [PubMed]

8. Mutsaers, S.E.; Bishop, J.E.; McGrouther, G.; Laurent, G.J. Mechanisms of tissue repair: From wound healing to fibrosis. *Int. J. Biochem. Cell Biol.* **1997**, *29*, 5–17. [CrossRef]

9. Tracy, L.E.; Minasian, R.A.; Caterson, E.J. Extracellular Matrix and Dermal Fibroblast Function in the Healing Wound. *Adv. Wound Care* **2016**, *5*, 119–136. [CrossRef] [PubMed]

10. Wright, K.A.; Nadire, K.B.; Busto, P.; Tubo, R.; McPherson, J.M.; Wentworth, B.M. Alternative delivery of keratinocytes using a polyurethane membrane and the implications for its use in the treatment of full-thickness burn injury. *Burns* **1998**, *24*, 7–17. [CrossRef]

11. van den Bogaerdt, A.J.; Ulrich, M.M.; van Galen, M.J.; Reijnen, L.; Verkerk, M.; Pieper, J.; Lamme, E.N.; Middelkoop, E. Upside-down transfer of porcine keratinocytes from a porous, synthetic dressing to experimental full-thickness wounds. *Wound Repair Regen.* **2004**, *12*, 225–234. [CrossRef] [PubMed]

12. Johnen, C.; Steffen, I.; Beichelt, D.; Braeutigam, K.; Witascheck, T.; Toman, N.; Moser, V.; Ottomann, C.; Hartmann, B.; Gerlach, J.C. Culture of subconfluent human fibroblasts and keratinocytes using biodegradable transfer membranes. *Burns* **2008**, *34*, 655–663. [CrossRef] [PubMed]

13. Mohamad, N.; Loh, E.Y.X.; Fauzi, M.B.; Ng, M.H.; Mohd Amin, M.C.I. In vivo evaluation of bacterial cellulose/acrylic acid wound dressing hydrogel containing keratinocytes and fibroblasts for burn wounds. *Drug Deliv. Transl. Res.* **2018**, 1–9. [CrossRef] [PubMed]

14. Groeber, F.; Holeiter, M.; Hampel, M.; Hinderer, S.; Schenke-Layland, K. Skin tissue engineering—In vivo and in vitro applications. *Adv. Drug Deliv. Rev.* **2011**, *63*, 352–366. [CrossRef] [PubMed]

15. Laurens, N.; Koolwijk, P.; de Maat, M.P. Fibrin structure and wound healing. *J. Thromb. Haemost.* **2006**, *4*, 932–939. [CrossRef] [PubMed]

16. Reinke, J.M.; Sorg, H. Wound repair and regeneration. *Eur. Surg. Res.* **2012**, *49*, 35–43. [CrossRef] [PubMed]

17. Rajangam, T.; An, S.S. Fibrinogen and fibrin based micro and nano scaffolds incorporated with drugs, proteins, cells and genes for therapeutic biomedical applications. *Int. J. Nanomed.* **2013**, *8*, 3641–3662. [CrossRef]

18. Bacakova, M.; Musilkova, J.; Riedel, T.; Stranska, D.; Brynda, E.; Zaloudkova, M.; Bacakova, L. The potential applications of fibrin-coated electrospun polylactide nanofibers in skin tissue engineering. *Int. J. Nanomed.* **2016**, *11*, 771–789. [CrossRef] [PubMed]

19. Bacakova, M.; Pajorova, J.; Stranska, D.; Hadraba, D.; Lopot, F.; Riedel, T.; Brynda, E.; Zaloudkova, M.; Bacakova, L. Protein nanocoatings on synthetic polymeric nanofibrous membranes designed as carriers for skin cells. *Int. J. Nanomed.* **2017**, *12*, 1143–1160. [CrossRef] [PubMed]

20. Pajorova, J.; Bacakova, M.; Musilkova, J.; Broz, A.; Hadraba, D.; Lopot, F.; Bacakova, L. Morphology of a fibrin nanocoating influences dermal fibroblast behavior. *Int. J. Nanomed.* **2018**, *13*, 3367–3380. [CrossRef] [PubMed]

21. Melander, A.; Vuorinen, T. Determination of the degree of polymerisation of carboxymethyl cellulose by size exclusion chromatography. *Carbohydr. Polym.* **2001**, *46*, 227–233. [CrossRef]

22. Riedel, T.; Brynda, E.; Dyr, J.E.; Houska, M. Controlled preparation of thin fibrin films immobilized at solid surfaces. *J. Biomed. Mater. Res. A* **2009**, *88*, 437–447. [CrossRef] [PubMed]

23. Tamer, T.M.; Collins, M.N.; Valachova, K.; Hassan, M.A.; Omer, A.M.; Mohy-Eldin, M.S.; Svik, K.; Jurcik, R.; Ondruska, L.; Biro, C.; et al. MitoQ Loaded Chitosan-Hyaluronan Composite Membranes for Wound Healing. *Materials* **2018**, *11*, 569. [CrossRef] [PubMed]

24. Zulkifli, F.H.; Hussain, F.S.; Rasad, M.S.; Mohd Yusoff, M. Nanostructured materials from hydroxyethyl cellulose for skin tissue engineering. *Carbohydr. Polym.* **2014**, *114*, 238–245. [CrossRef] [PubMed]

25. Song, S.H.; Kim, J.E.; Lee, Y.J.; Kwak, M.H.; Sung, G.Y.; Kwon, S.H.; Son, H.J.; Lee, H.S.; Jung, Y.J.; Hwang, D.Y. Cellulose film regenerated from Styela clava tunics have biodegradability, toxicity and biocompatibility in the skin of SD rats. *J. Mater. Sci. Mater. Med.* **2014**, *25*, 1519–1530. [CrossRef] [PubMed]

26. Mohseni, M.; Shamloo, A.; Aghababaei, Z.; Vossoughi, M.; Moravvej, H. Antimicrobial Wound Dressing Containing Silver Sulfadiazine with High Biocompatibility: In Vitro Study. *Artif. Organs* **2016**, *40*, 765–773. [CrossRef] [PubMed]

27. Novotna, K.; Havelka, P.; Sopuch, T.; Kolarova, K.; Vosmanska, V.; Lisa, V.; Svorcik, V.; Bacakova, L. Cellulose-based materials as scaffolds for tissue engineering. *Cellulose* **2013**, *20*, 2263–2278. [CrossRef]

28. Broussard, K.C.; Powers, J.G. Wound dressings: Selecting the most appropriate type. *Am. J. Clin. Dermatol.* **2013**, *14*, 449–459. [CrossRef] [PubMed]

29. Ahmadi, H.; Williams, G. Permanent scarring in a partial thickness scald burn dressed with Biobrane. *J. Plast. Reconstr. Aesthet. Surg.* **2009**, *62*, 697–698. [CrossRef] [PubMed]

30. Boateng, J.S.; Matthews, K.H.; Stevens, H.N.; Eccleston, G.M. Wound healing dressings and drug delivery systems: A review. *J. Pharm. Sci.* **2008**, *97*, 2892–2923. [CrossRef] [PubMed]

31. Rodriguez-Merchan, E.C. Local fibrin glue and chitosan-based dressings in haemophilia surgery. *Blood Coagul. Fibrinolysis* **2012**, *23*, 473–476. [CrossRef] [PubMed]

32. Yildirim, S.; Ozener, H.O.; Dogan, B.; Kuru, B. Effect of topically applied hyaluronic acid on pain and palatal epithelial wound healing: An examiner-masked, randomized, controlled clinical trial. *J. Periodontol.* **2018**, *89*, 36–45. [CrossRef]

33. Bacakova, L.; Filova, E.; Kubies, D.; Machova, L.; Proks, V.; Malinova, V.; Lisa, V.; Rypacek, F. Adhesion and growth of vascular smooth muscle cells in cultures on bioactive RGD peptide-carrying polylactides. *J. Mater. Sci. Mater. Med.* **2007**, *18*, 1317–1323. [CrossRef] [PubMed]

34. Hopp, I.; Michelmore, A.; Smith, L.E.; Robinson, D.E.; Bachhuka, A.; Mierczynska, A.; Vasilev, K. The influence of substrate stiffness gradients on primary human dermal fibroblasts. *Biomaterials* **2013**, *34*, 5070–5077. [CrossRef] [PubMed]

35. Engler, A.; Bacakova, L.; Newman, C.; Hategan, A.; Griffin, M.; Discher, D. Substrate compliance versus ligand density in cell on gel responses. *Biophys. J.* **2004**, *86*, 617–628. [CrossRef]

36. Carr, M.E., Jr.; Hermans, J. Size and density of fibrin fibers from turbidity. *Macromolecules* **1978**, *11*, 46–50. [CrossRef] [PubMed]

37. Riedelova-Reicheltova, Z.; Brynda, E.; Riedel, T. Fibrin nanostructures for biomedical applications. *Physiol. Res.* **2016**, *65*, S263–S272. [PubMed]

38. Becker, J.C.; Domschke, W.; Pohle, T. Biological in vitro effects of fibrin glue: Fibroblast proliferation, expression and binding of growth factors. *Scand. J. Gastroenterol.* **2004**, *39*, 927–932. [CrossRef] [PubMed]

39. Gsib, O.; Duval, J.L.; Goczkowski, M.; Deneufchatel, M.; Fichet, O.; Larreta-Garde, V.; Bencherif, S.A.; Egles, C. Evaluation of Fibrin-Based Interpenetrating Polymer Networks as Potential Biomaterials for Tissue Engineering. *Nanomaterials* **2017**, *7*, 436. [CrossRef] [PubMed]

40. Stevens, M.M.; George, J.H. Exploring and engineering the cell surface interface. *Science* **2005**, *310*, 1135–1138. [CrossRef] [PubMed]

41. Bacakova, L.; Filova, E.; Parizek, M.; Ruml, T.; Svorcik, V. Modulation of cell adhesion, proliferation and differentiation on materials designed for body implants. *Biotechnol. Adv.* **2011**, *29*, 739–767. [CrossRef] [PubMed]

42. Mazlyzam, A.L.; Aminuddin, B.S.; Fuzina, N.H.; Norhayati, M.M.; Fauziah, O.; Isa, M.R.; Saim, L.; Ruszymah, B.H. Reconstruction of living bilayer human skin equivalent utilizing human fibrin as a scaffold. *Burns* **2007**, *33*, 355–363. [CrossRef] [PubMed]

43. Dvorankova, B.; Smetana, K., Jr.; Vacik, J.; Jelinkova, M. Cultivation of keratinocytes on poly HEMA and their migration after inversion. *Folia Biol.* **1996**, *42*, 83–86.

FYZIOLOGICKÝ
ÚSTAV AV ČR

Ředitel Fyziologického ústavu AV ČR uděluje

Julii Pajovové

OCENĚNÍ

ZA NEJLEPŠÍ POSTER

VÝJEZDNÍ ZASEDÁNÍ PGS STUDENTŮ

TŘEŠŤ 2015

MUDr. Jan Kopecký, DrSc.
ředitel FGÚ AV ČR, v. v. i.

5. listopadu 2015

VĚDECKÁ KONFERENCE

2. LÉKAŘSKÁ FAKULTA UNIVERZITY KARLOVY 2018

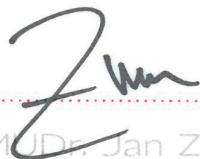### CENU ZA NEJLEPŠÍ POSTER ZÍSKALA

Mgr. Júlia PAJOROVÁ

prof. MUDr. Vladimír Komárek, CSc.
děkan fakulty

prof. MUDr. Jan Trka, Ph.D.
předseda organizačního výboru

doc. MUDr. Jan Zuna, Ph.D.
předseda vědeckého výboru

2. LÉKAŘSKÁ FAKULTA
UNIVERZITA KARLOVA

The 18th congress of the European Burns Association

Poster presentation award

J. Pajórová

A full-thickness skin construct made of a collagen hydrogel strengthened by a fibrin-modified nanofibrous membrane

Clemens Schiestl
EBA President

4-7 September 2019, Helsinki

FYZIOLOGICKÝ ÚSTAV AV ČR

Ředitel Fyziologického ústavu AV ČR uděluje

CENU PAVLA FLACHSE ZA NEJLEPŠÍ PUBLIKACE S AUTORY Z FGÚ ZA ROK 2019

S KORESPONDUJÍCÍM AUTOREM DO 35 LET

Mgr. Julii Pajorové

za publikaci

Bačáková M, Pajorová J, Brož A, Hadraba D, Lopot F, Zavaďáková A, Vištejnová L, Beňo M, Kostič I, Jenčová V, Bačáková L: A two-layer skin construct consisting of a collagen hydrogel reinforced by a fibrin-coated polylactide nanofibrous membrane. *International Journal of Nanomedicine.* 2019, roč. 14, s. 5033-5050. IF: 5,115

MUDr. Jan Kopecký, DrSc.
15. prosince 2020

FYZIOLOGICKÝ ÚSTAV AV ČR

Ředitel Fyziologického ústavu AV ČR uděluje

CENU PAVLA FLACHSE
ZA NEJLEPŠÍ PUBLIKACE
S AUTORY Z FGÚ
ZA ROK 2020
S KORESPONDUJÍCÍM AUTOREM DO 35 LET

Mgr. Julii Pajorové

za publikaci

Pajorová J, Skogeberg A, Hadraba D, Brož A, Trávníčková M, Zikmundová M, Honkanen M, Hannula M, Lahtinen P, Tomková M, Bačáková L, Kallio P: Cellulose Mesh with Charged Nanocellulose Coatings as a Promising Carrier of Skin and Stem Cells for Regenerative Applications. *Biomacromolecules*, 2020, roč. 21, s. 4857-4870. IF: 6,988

MUDr. Jan Kopecký, DrSc.
10. listopadu 2021